



NATIONAL TECHNICAL UNIVERSITY OF ATHENS
SCHOOL OF NAVAL ARCHITECTURE AND MARINE ENGINEERING
SHIPBUILDING TECHNOLOGY LABORATORY

Assessment and Design of Composite Patch Repairing in Marine Applications

by

Vasileios A. Karatzas

PhD Thesis

Athens, May 2016



NATIONAL TECHNICAL UNIVERSITY OF ATHENS
SCHOOL OF NAVAL ARCHITECTURE AND MARINE ENGINEERING
SHIPBUILDING TECHNOLOGY LABORATORY

Assessment and Design of Composite Patch Repairing in Marine Applications

by

Vasileios A. Karatzas

PhD Thesis

Supervisor:

N.G. Tsouvalis, Professor, NTUA

Members of consulting committee:

M. Samuelides, Professor, NTUA

T. Philippidis, Associate Professor, University of Patras

Athens, May 2016

Publication reference data:

Karatzas V.A., *Assessment and Design of Composite Patch Repairing in Marine Applications*, PhD Thesis, National technical University of Athens, School of Naval Architecture and Marine Engineering, May 2016.

Keywords: Composite patches, marine repairs, adhesive bonding, fatigue behaviour, bimaterial fracture mechanics, cohesive zone modelling

Στην οικογένειά μου και τη Χριστίνα

Acknowledgements

A few months after I started my PhD Thesis I was found in the company of some friends. Amongst them was also someone whom I have not met before and who proved to be a young Lecturer in Mechanical Engineering. After the introductions he asked me what is it that I do. I replied that I am a PhD candidate, describing him the topic of my Thesis with the self-importance that characterises most young PhD candidates. He smiled and said almost nostalgically “a PhD is a difficult but above all a wonderful journey, enjoy it!” which, I have to admit, found rather corny at the time. Looking back, I will have to agree with him, and consequently be accused of being corny myself, that a PhD is a journey, and as most memorable journeys, it involved frustration, tiredness, and dead ends but at the same time achievements, personal progress and beautiful moments. Albeit this was a personal endeavour it was far from lonely, and it would have been impossible to bring it to its present form without the support of the following people.

Firstly, I would like to express my deepest gratitude to my advisor Prof. Tsouvalis for offering me the opportunity to pursue a PhD. His support, patience, understanding and the impeccable collaboration we had during my Diploma Thesis and postgraduate studies are greatly treasured. He is largely responsible for shaping my scientific perception and has been a role model for me both as a tutor and as a person.

I also like to thank laboratory technicians Mr. Athanasios Markoulis and Mr. Haris Xanthis for their cooperation and for offering valuable assistance in the experimental activities, and the Co-Patch project partners for their efforts and inputs during the research project.

I am especially and deeply grateful to Dr. Konstantinos Anyfantis, PhD candidate Ilias Zilakos, Dr. Elias Chatzidouros and Mr. Elias Kotsidis for all the discussions we had, their support and their encouragement throughout this endeavour. But foremost for their sincere friendship and everything we shared through all these years.

In addition, my sincere gratitude goes to Associate Prof. Christian Berggreen from the Technical University of Denmark for providing me the opportunity to join his team and for his understanding when I was finalising my Thesis. At the same time, I would like to thank Prof. Leif Carlsson from Florida Atlantic University and PhD student Vishnu Saseendran from the Technical University of Denmark for all the stimulating discussions we had concerning bimaterial fracture mechanics.

Last but not least, I thank my family and my girlfriend Christina for their endless support and encouragement when I needed it most throughout this endeavour and for having them in my life.

Vasileios A. Karatzas

Assessment and Design of Composite Patch Repairing in Marine Applications

by
Vasileios A. Karatzas

Abstract

The current PhD thesis focuses on the investigation of the use of composite patches for the rehabilitation of defected marine steel structures. This work is the result of a combined experimental, numerical and analytical approach aiming at providing insight on the design, inspection and in service performance of such repairs. A design evaluation procedure has been developed based on simple analytical tools which are to be utilized by engineers for the design and analysis of composite patch repairing and other similar adhesively bonded applications.

A series of midscale static tests have been performed in defected steel plates, namely in corroded and notched plates. All plates have been repaired with composite patches and tested in tension. Additionally, different health monitoring and inspection methods have been applied to assess the quality of the repair both after installation and during operating conditions. Moreover, the effect of different aging scenarios has been investigated. Finally, 2D and 3D finite element models have been created using cohesive zone modelling which are in good agreement with the experimental findings.

Simultaneously, cracked plates on which composite patches have been installed were experimentally investigated under fatigue loading. Once again, apart from the efficiency of the repair, health monitoring and the effect of different aging scenarios have been assessed. Additionally, a methodology for the assessment of cracked elements in marine structures and the effectiveness of the investigated repair method is proposed. This methodology is based on the implementation of the common structural rules with the use of user subroutines and finite element modelling.

At the end of this work, emphasis is given in the use of linear fracture mechanics in bimaterial interfaces and a parametric study has been performed to quantify how key parameters affect the adhesive bond between the patch and the steel substrate. Following the parametric study, a simple, time effective design evaluation procedure for this kind of repairs is proposed.

In conclusion, the present PhD thesis shows the potential of composite patch repairing on marine structures, having addressed critical issues associated with their effectiveness and durability, and proposing a simple analytical procedure for their design.

ΠΕΡΙΛΗΨΗ

Η παρούσα διδακτορική διατριβή πραγματεύεται τη χρήση επιθεμάτων από σύνθετα υλικά για την επιδιόρθωση ατελειών που εμφανίζονται σε χαλύβδινες θαλάσσιες κατασκευές. Η εκπονηθείσα διατριβή είναι το αποτέλεσμα του συνδυασμού πειραματικής, αριθμητικής και αναλυτικής προσέγγισης. Στόχος της είναι η εκτίμηση της αποτελεσματικότητας της συγκεκριμένης μεθόδου επισκευής, η διερεύνηση τεχνικών επιθεώρησης της ακεραιότητάς της και τέλος η ανάπτυξη μίας απλής μεθοδολογία ελέγχου για τον ορθό σχεδιασμό αυτής.

Για να επιτευχθούν οι προαναφερθέντες στόχοι πραγματοποιήθηκε μία σειρά στατικών πειραματικών δοκιμών μεσαίας κλίμακας σε χαλύβδινες πλάκες που έφεραν εγκοπή και σε πλάκες που είχαν υποστεί διάβρωση. Όλα τα δοκίμια δοκιμάστηκαν σε εφελκυσμό. Ταυτόχρονα, εφαρμόστηκαν διαφορετικές μέθοδοι ελέγχου και παρακολούθησης για την αξιολόγηση της επισκευής και για τη μελέτη του τρόπου αστοχίας της. Μέσω των πειραμάτων εξετάστηκε και η επίδραση της περιβαλλοντικής γήρανσης λαμβάνοντας υπόψη διαφορετικά σενάρια γήρανσης. Εν συνεχεία αναπτύχθηκαν δισδιάστατα και τρισδιάστατα μη γραμμικά μοντέλα πεπερασμένων στοιχείων με στόχο την αναπαραγωγή των πειραματικών αποτελεσμάτων. Τα αριθμητικά αποτελέσματα ήταν σε καλή συμφωνία με τις πειραματικές μετρήσεις.

Επιπρόσθετα, διεξήχθησαν δοκιμές κόπωσης σε χαλύβδινες πλάκες που έφεραν κεντρική ρωγμή και είχαν επιδιορθωθεί με επιθέματα από σύνθετα υλικά. Αντίστοιχα με τις στατικές δοκιμές, πέραν της αποτελεσματικότητας της μεθόδου, δόθηκε βάρος στην επίδραση της περιβαλλοντικής γήρανσης και στην εφαρμογή μεθόδων μη καταστρεπτικού ελέγχου για την αξιολόγηση του δεσμού μεταξύ του επιθέματος και της πλάκας. Επιπρόσθετα προτάθηκε μία αριθμητική μεθοδολογία αξιολόγησης τόσο της κρισιμότητας ρωγμών σε πλοία μεταφοράς πετρελαίου, καθώς και της μεθόδου επισκευής.

Στο τελευταίο τμήμα της διδακτορικής διατριβής δίνεται έμφαση στη χρήση της γραμμικά ελαστικής θεωρίας θραυστομηχανικής για διεπιφάνειες. Συγκεκριμένα, συνδυάζοντας αριθμητικά μοντέλα και αναλυτικούς τύπους πραγματοποιήθηκε παραμετρική μελέτη για να διερευνηθούν πως το μέτρο ελαστικότητας και το πάχος του επιθέματος σε σχέση με αυτό της μεταλλικής κατασκευής επιδρούν στην αποτελεσματικότητα της επισκευής υπό διαφορετικές φορτίσεις. Κατόπιν, με βάση τα ευρήματα των ανωτέρω εργασιών, αναπτύχθηκε μία απλή μεθοδολογία ελέγχου για τον ορθό σχεδιασμό επιδιορθώσεων αυτού του τύπου.

Εν κατακλείδι, η διδακτορική διατριβή επιδεικνύει τις δυνατότητες της χρήσης επιθεμάτων από σύνθετα υλικά για την επιδιόρθωση θαλάσσιων κατασκευών, έχοντας εξετάσει κρίσιμα ερωτήματα που σχετίζονται με την αποτελεσματικότητα, την ανθεκτικότητα, και τον τρόπο σχεδιασμού αυτών.

Contents

1. COMPOSITE PATCH REPAIRING.....	1
1.1 Introduction.....	1
1.2 Applications of composite patch repairs.....	3
1.3 Main types of damage in marine structures.....	12
Reinforcement of Cross Deck Plating.....	12
Reinforcement in Way of Structural Details.....	13
Defects at Bracket Edges and Bilge Hopper Plates.....	13
Corrosion.....	14
1.4 Fabrication methods of patches.....	15
Adhesively Bonded Patches.....	16
Co-cured Bonded Patches.....	17
Symmetrical and One Sided Configurations.....	17
1.5 Loading / failure and analysis of composite patches.....	18
1.6 Non destructive evaluation, inspection and structural health monitoring.....	21
Strain Gages.....	21
Optical Fibres.....	22
Ultrasounds / Acousto-ultrasonics.....	22
1.7 The Co-Patch project.....	23
1.8 Objectives and layout of PhD thesis.....	24
Experimental and Numerical Investigation of Repaired Corroded and Notched Plates under Static Loading.....	25
Experimental Investigation of Repaired Cracked Plates Subjected to Fatigue Loading.....	25
Numerical Simulations Employing a Three Compartment Model.....	25
Parametric Investigation for the Design of Composite Patches and Design Methodology.....	25
2. INTRODUCTION TO BIMATERIAL LINEAR ELASTIC FRACTURE MECHANICS.....	26
2.1 Introduction.....	26
2.2 Linear elastic fracture mechanics.....	26
2.3 J integral.....	28
2.4 Bimaterial fracture mechanics.....	29
2.5 Cohesive zone modelling.....	33
Introduction.....	33

Cohesive Laws	34
2.6 Experimental procedures for the measuring of the critical energy release rate in bimetals	36
3. EXPERIMENTAL AND NUMERICAL INVESTIGATION OF PATCH REPAIRED CORRODED PLATES UNDER STATIC LOADING	40
3.1 Introduction	40
3.2 General characteristics	40
Specimen Description	40
Materials and Manufacturing Procedure	44
Specimen Instrumentation	46
3.3 Experimental testing and results	47
Test Parameters	47
Results	47
3.4 Numerical modelling	56
Model Description	56
Results	58
3.5 Conclusions	67
4. EXPERIMENTAL AND NUMERICAL INVESTIGATION OF PATCH REPAIRED NOTCHED PLATES UNDER STATIC LOADING	68
4.1 Introduction	68
4.2 General characteristics	68
Specimen Description	68
Specimens Instrumentation	70
4.3 Experimental testing and results	72
Test Parameters	72
Results	73
4.4 Additional testing	83
Specimen Description	83
Manufacturing Procedure and Instrumentation	84
Experimental Testing	86
Results	86
4.5 Numerical simulations	90
4.6 Conclusions	95

5. EXPERIMENTAL INVESTIGATION OF REPAIRED CRACKED PLATES SUBJECTED TO FATIGUE LOADING.....	96
5.1 Introduction.....	96
5.2 General characteristics.....	96
Specimen Description.....	96
Materials and Manufacturing Procedure.....	97
Surface Treatment.....	99
Aging Process.....	99
Specimens Instrumentation.....	101
5.3 Experimental testing and results.....	103
Test Parameters.....	103
Results.....	104
5.4 Patch quality classification.....	114
5.5 Conclusions.....	124
6. NUMERICAL SIMULATIONS EMPLOYING A THREE COMPARTMENT MODEL.....	126
6.1 Introduction.....	126
6.2. Description of Finite Element model.....	127
6.3. Employment of the model for crack assessment.....	130
Description of Studied Cases.....	130
Crack Assessment and Results.....	134
6.4. Crack rectification using composite patches.....	138
Description of the Studied Cases.....	138
Results of Parametric Study.....	142
6.5. Conclusions.....	146
7. PARAMETRIC INVESTIGATION FOR THE DESIGN OF COMPOSITE PATCHES.....	148
7.1. Introduction.....	148
7.2 Crack Surface Displacement Extrapolation method and enhanced Virtual Crack Closure Technique.....	149
Finite Element Formulation: 2-D CSDE Method.....	150
Comparison of the CSDE Method to the Enhanced VCCT.....	154
7.2. Analytical approach.....	155
7.3 General considerations regarding composite patch repairing.....	163
Loading Definition.....	163
Geometrical considerations.....	167

7.4. Parametric study	168
Description of the Study.....	168
Results of the Parametric Study	171
7.5 Design assessment procedure	177
7.6 Implementation of assessment methodology	181
7.7 Conclusions	186
8. CONCLUSIONS AND SCIENTIFIC NOVELTIES	187
9. SUGGESTIONS FOR FUTURE WORK	189
REFERENCES	190
LIST OF PHD PUBLICATIONS	199
APPENDIX A	203
Introduction	203
Test standards applied	203
Nomenclature	204
Hand lay-up carbon/epoxy.....	205
Hand lay-up carbon/vinylester	205
Vacuum infusion carbon/epoxy	205
Vacuum infusion carbon/vinylester	206
Pre-Preg carbon/epoxy.....	207
Material Properties.....	210

List of Figures

Figure 1.1: Example of a carbon fibre patch applied to a defected steel transverse frame.	2
Figure 1.2: Application of a composite patch on site (<i>Grabovac et al, 2009</i>).....	3
Figure 1.3: Patch with structural health monitoring system bonded to F-111 wing (<i>Baker et al, 2009</i>).....	4
Figure 1.4: Reinforcement of concrete bridge using carbon fibres.	5
Figure 1.5: Carbon fibre reinforcement and monitoring system in service (<i>Grabovac et al, 2003</i>).....	6
Figure 1.6: Composite patch configuration (<i>Grabovac et al, 2009</i>).....	6
Figure 1.7: Photos depicting damage and the cut-outs made for welding a life raft support system on the deck (<i>Grabovac et al, 2009</i>).	7
Figure 1.8: Composite patch repairs on lift shafts of Type 42 destroyers.	7
Figure 1.9: Composite patch applied to cargo tank on-board FPSO (<i>Turton et al 2005</i>).....	8
Figure 1.10: Repair on the corridor side of the Bulkhead (<i>McGeorge et al, 2009</i>).	9
Figure 1.11: Glass fibre patching of sensitized aluminium deck.	9
Figure 1.12: Cross-section of patch over sensitized aluminium plate.	10
Figure 1.13: Crack in aluminium superstructure and carbon / epoxy patch.	10
Figure 1.14: Area of damage (pictures a and b), lamination of the repair (c), finished coated repair (d).	11
Figure 1.15: Position of cracks (a), treated surface (b) lamination of the repair (c), finished repair (d).	12
Figure 1.16: Cross deck plating of a bulk carrier.	13
Figure 1.17: Defects in water ballast tank.	13
Figure 1.18: Arrows pointing to fatigue cracks at bracket.	14
Figure 1.19: General corrosion due to coating failure (left) and pitting corrosion (right).	14
Figure 1.20: Prefabricated pultruded carbon strips bonded onto a steel bridge.	16
Figure 1.21: Curing of co-bonded patch.	17
Figure 1.22: Types of failure in composite patch repairing (<i>McGeorge et al, 2009</i>).	18
Figure 1.23: Skewed crack front in one sided repaired specimens (<i>Lee and Lee, 2004</i>).	20
Figure 1.24: Numerical model depicting debonding evolution (<i>Papanikos et al, 2005</i>).	21
Figure 1.25: Commercial wireless sensor nodes.	22
Figure 1.26: Optical Fibre system.....	22
Figure 1.27: Co-Patch project partners.	24
Figure 2.1: Loading modes.	27
Figure 2.2: Stress field near a crack.	27
Figure 2.3: J-Integral schematic.	29
Figure 2.4: Relative displacement at the crack flanks.	30
Figure 2.5: The bilinear traction separation law.	36
Figure 2.6: MMB geometry parameters and test setup (<i>Carlsson 2014</i>).	37
Figure 2.7: Single leg bending tests performed by <i>Lee et al (2010)</i>	38
Figure 2.8: Partial adhesive failure of DCB specimens (<i>Andersen 2005</i>).	38
Figure 2.9: DCB-UBM test rigs.	39
Figure 3.1: P2 plates geometry.	41
Figure 3.2: Six P2D (2 painted and 4 unpainted) specimens after 75 days in the environmental chamber. ...	42
Figure 3.3: Fixture specimen assembly mounted for testing.	44
Figure 3.4: Vacuum infusion setup (figure provided by AS2CON).	45
Figure 3.5: Manufacturing of P2D specimens' patches (figure provided by AS2CON).....	45
Figure 3.6: Instrumentation of specimens P2D1-A, P2D1-B, P2D3-B.	46
Figure 3.7: Instrumentation of P2D2, P2D3 and P2D4 specimens.	46
Figure 3.8: Thickness reduction of the central area of specimens P2A-C and D.	47
Figure 3.9: Force – Displacement curves of P2A specimens.....	48
Figure 3.10: Force – Strain curves (SG-1) of P2A-C and D specimens.....	49
Figure 3.11: Specimen P2D2A being tested on MTS testing machine.	49

Figure 3.12: Qualitative Force – Displacement curves of P2D and P2-A specimens.	50
Figure 3.13: Yielding around the holes during testing.	51
Figure 3.14: Force – Strain curves of P2D1-A specimen.	51
Figure 3.15: Force – Strain curves of P2D2-A specimen.	52
Figure 3.16: Force – Strain curves of P2D3-B specimen.	52
Figure 3.17: Edge debonding of P2D specimens.	53
Figure 3.18: Bondline of the two coated aged specimens after testing.	54
Figure 3.19: Reduction of the effective bonding area due to corrosion in unpainted patched P2 specimens.	55
Figure 3.20: ¼ of the specimen that was modelled in ANSYS.	56
Figure 3.21: Generated finite element model of the P2D1 plates.	57
Figure 3.22: Force displacement curve of the 3D finite element model.	59
Figure 3.23: Plastic strain distribution at 147.00 kN.	59
Figure 3.24: Initiation (left) and development of debonding (right) in the 3D model.	60
Figure 3.25: Experimental versus 3D numerical Force – Strain graph.	60
Figure 3.26: Deflection at 148.06kN (scale factor of 20).	61
Figure 3.27: Generated 2D finite element model and mesh size.	61
Figure 3.28: Force-displacement curves of the 2D and 3D numerical simulations.	62
Figure 3.29: Force strain curves for the experimental and numerical results.	63
Figure 3.30: Von Mises plastic strain at the steel substrate at 151.11 kN.	64
Figure 3.31: Comparison of FE models with different patch length to the experimental results.	64
Figure 3.32: Force – Displacement curves of the undefected, corroded and repaired models.	65
Figure 3.33: Force-displacement of the intact, corroded, and repaired cases with different thickness diminution.	66
Figure 3.34: 2D FE patch model results for steel modelled with and without plasticity.	67
Figure 4.1: P1 plates geometry.	69
Figure 4.2: P1 specimen mounted on the testing machine.	70
Figure 4.3: Instrumentation of specimens P1A-C and P1A-D.	71
Figure 4.4: Instrumentation of P1D1-A, P1D1-B and P1D1-C specimens.	71
Figure 4.5: Instrumentation of P1D2-A and P1D2-B specimens.	72
Figure 4.6: Specimen P1D1-A being tested on MTS testing machine (left) and on INSTRON 300LX testing machine (right).	73
Figure 4.7: Force – Strain curves of P1A-C and P1A-D specimens.	74
Figure 4.8: Force – Displacement (LVDT) curves of P1D1 specimens tested by NTUA.	75
Figure 4.9: Force – Displacement (Crosshead) curves of P1D specimens tested both by NTUA and AIMEN.	76
Figure 4.10: Force – Strain curves of P1D1-A specimen's first loading by NTUA.	76
Figure 4.11: Force – Strain curves of P1D1-A specimen's second loading by NTUA.	77
Figure 4.12: Force – Strain curves of P1D1-C specimen's first loading by NTUA.	77
Figure 4.13: Force – Strain curves of P1D1-C specimen's second loading by AIMEN.	78
Figure 4.14: Existing manufacturing flaw detected during non-destructive evaluation prior to testing.	79
Figure 4.15: Markings denote the debonded/delaminated area after the final testing of specimens.	80
Figure 4.16: Comparison of Force – Strain curves for P1D2-A and P1D2-B specimens.	80
Figure 4.17: Comparison of Force – Strain (SG-3) curves for all P1D specimens.	81
Figure 4.18: Acousto-ultrasonic inspection finding in specimens P1D2-A & B prior to testing.	81
Figure 4.19: Correlation of the outer surface markings to the bondline surface.	82
Figure 4.20: Schematic of specimen P1F.	84
Figure 4.21: Instrumentation of the P1F specimen.	85
Figure 4.22: Positioning of the optical fibres with the aid of laser pointers.	86
Figure 4.23: Force - displacement curve of the reference and P1F specimen.	87
Figure 4.24: Force-strain measurements of P1F specimen.	87

Figure 4.25: Notch at the back side immediately before and after patch debonding.	88
Figure 4.26: P1F specimen after testing.	88
Figure 4.27: Position of optical fibres OF1 (left) and OF-2 (right).	89
Figure 4.28: FE model of the $\frac{1}{4}$ of the specimen.	91
Figure 4.29: Force displacement curves.	92
Figure 4.30: Debonding status at 157 kN.	92
Figure 4.31: Von Mises stress distribution on the unreinforced side (left) and on the reinforced side (right) of the steel plate, at 157 kN.	93
Figure 4.32: Strain gage-1 measurements.	93
Figure 4.33: Strain gage-2 measurements.	94
Figure 4.34: Optical fibre 3 measurements.	94
Figure 4.35: Optical fibre 4 measurements.	95
Figure 5.1: Geometry of P3 plates.	97
Figure 5.2: Specimens' manufacturing (Figure provided by AS2CON).	98
Figure 5.3: Example of needle gun scaler.	99
Figure 5.4: Painted P3 specimens placed into the environmental chamber.	101
Figure 5.5: Position of strain gages on P3 specimens.	102
Figure 5.6: Instrumentation of specimens P3A-C, P3A-D, P3A-E, P3D1-A and P3D-B.	102
Figure 5.7: Instrumentation of specimens P3D1-B and P3D4-A.	102
Figure 5.8: Instrumentation of specimens P3D2-A, B, P3D3-A, B, P3D5-A, B and P3D6-A, B.	102
Figure 5.9: Definition of distances between notch tip and CG-1 and between CG-1 and CG-2.	103
Figure 5.10: Both sides of specimen P3D4-B while tested in fatigue.	104
Figure 5.11: Indicative time strain measurements for specimen P3D1-A.	106
Figure 5.12: α -N curves of the reference P3A specimens.	107
Figure 5.13: α -N curves of P3D specimens.	107
Figure 5.14: Oblique crack propagation that resulted in fewer measurements by CG-2.	108
Figure 5.15: Findings of the initial NDE on the patch surface, for the grit blasted P3 specimens.	109
Figure 5.16: Findings of the initial NDE on the patch surface, for the needle gun treated P3 specimens.	109
Figure 5.17: α -N curves of P3D specimens; comparison of surface preparation method.	110
Figure 5.18: Fatigue life N_{36-83} of all specimens.	110
Figure 5.19: α -N curves of P3D1 and P3D2 specimens.	112
Figure 5.20: α -N curves of specimens P3D3, P3D4, P3D5 and P3D6-A.	113
Figure 5.21: Crack faces of two representative specimens.	113
Figure 5.22: Initial non-destructive evaluation of the patch repair in P3D4-B (left) and evolution of debonding during fatigue testing (right).	114
Figure 5.23: Initial findings (a) projection of findings matching the dry area at the interface (b), dry plies detected by the inspection revealed after cutting the laminate (c).	115
Figure 5.24: Internal and external patch surfaces of P3 grit blasted specimens. The initial findings were marked on the external surfaces.	120
Figure 5.25: Internal and external patch surfaces of P3 needle gunned specimens. The initial findings were marked on the external surfaces.	121
Figure 5.26: Distinction between white and black areas on the internal surface of P3D5-B patch.	122
Figure 5.27: Unpatched side of steel, showing the crack paths.	123
Figure 6.1: Aframax tanker depicting the modelled section.	127
Figure 6.2: Bulkhead stiffeners modelled using shell elements (red) and Euler-Bernoulli beams (green). ..	128
Figure 6.3: Stiffeners' mesh size.	128
Figure 6.4: Distribution of bending moment in the model after the adjustment.	130
Figure 6.5: the FLD (top) and WBD (bottom) conditions.	131
Figure 6.6: Regions where the cracks were introduced.	132
Figure 6.7: Derivation of the U_y displacement analytical field at the hopper floor boundary.	133

Figure 6.8: Distribution of the nodal rotations for the hopper floor boundary.	134
Figure 6.9: Von Mises stress distribution near crack-1 for hogging (left) and sagging (right).	135
Figure 6.10: Distribution of stresses normal to crack-2 edges for hogging (left) and sagging (right).	135
Figure 6.11: Indicative figure showing the crack-2 edge penetration.	136
Figure 6.12: Crack propagation curve of AH36 steel along with the evaluated point for Crack-1.	137
Figure 6.13: Cargo loading considered in the three compartment model.	138
Figure 6.14: Displacement field along the Y (top) and Z (bottom) direction in the shell (left) and the solid (right) sub model.	139
Figure 6.15: Crack locations.	140
Figure 6.16: Von Mises stress in the steel before (left) and after repair (right).	143
Figure 6.17: Stress intensity factor across the thickness.	143
Figure 6.18: Distribution of stress intensity factor in crack-2.	145
Figure 6.19: One sided versus double sided patch configuration.	146
Figure 7.1: Representation of the CSDE method.	150
Figure 7.2: Illustration of the crack region of studied bimaterial interface.	151
Figure 7.3: Mesh size of the FE model for the implementation of the CSDE method.	152
Figure 7.4: Element arrangement and mesh density at the crack tip.	152
Figure 7.5: Extrapolation of the energy release rate.	153
Figure 7.6: Extrapolation of the mode mixity.	154
Figure 7.7: Superposition technique (<i>Suo 1990</i>).	156
Figure 7.8: Moment equilibrium due to contact at the crack tip.	165
Figure 7.9: Axial force and moment equilibrium in a single strap joint.	166
Figure 7.10: Critical energy release rate models as a function of mode mixity.	170
Figure 7.11: Strain energy release rate and mode mixity versus thickness ratio (bending load).	171
Figure 7.12: Strain energy release rate and fracture toughness versus thickness ratio (bending load).	172
Figure 7.13: Strain energy release rate and mode mixity versus bending stiffness ratio (bending load).	172
Figure 7.14: Strain energy release rate and fracture toughness versus bending stiffness ratio (bending load).	173
Figure 7.15: Strain energy release rate and mode mixity versus thickness ratio (axial load).	173
Figure 7.16: Strain energy release rate and fracture toughness versus thickness ratio (axial load).	174
Figure 7.17: Strain energy release rate and mode mixity versus axial stiffness ratio (axial load).	174
Figure 7.18: Strain energy release rate and fracture toughness versus axial stiffness ratio (axial load).	175
Figure 7.19: Strain energy release rate and mode mixity versus axial stiffness ratio (axial load) for the HLU.	176
Figure 7.20: Outline of repair assessment and decision making process (<i>DNV-RP-C301</i>).	178
Figure 7.21: Patch assessment and decision making procedure.	180
Figure 7.22: von Mises stress distribution (top) and longitudinal stresses (σ_z) in defected structure (bottom).	182
Figure 7.23: von Mises stress distribution (top) and longitudinal stresses (σ_z) on the steel structure after the application of a HLU-CE patch.	183
Figure 7.24: von Mises stress distribution (top) and longitudinal stresses (σ_z) on the steel structure after the application of a VI-CE patch.	184
Figure 7.25: Stress distribution in the reinforced and unreinforced sides of the steel at the patch edge.	185
Figure A.1: Vacuum infusion of laminate (provided by AS2CON).	206
Figure A.2: Layer configuration used for each specimen type (provided by UM).	206
Figure A.3: Plies configuration prior to infusion (provided by UM).	207
Figure A.4: Sealing and Vacuum Infusion of laminates (provided by UM).	207
Figure A.5: Set-up of pre-preg prior to curing (provided by NTNU).	208
Figure A.6: PP-C/E-T-0 laminate after curing (provided by NTNU).	209

Figure A.7: PP-C/E-T-0 and PP-C/E-T-90 laminates with tabs prior to tab-adhesive curing (provided by NTNU).....	209
Figure A.8: PP-C/E-T-0 and PP-C/E-T-90 laminates with tabs after tab-adhesive curing (provided by NTNU).	210
Figure A.9: PP-C/E-S laminate after curing (provided by NTNU).....	210

List of tables

Table 3.1: Conditions of one accelerated corrosion cycle.....	41
Table 3.2: Nomenclature of P2 specimens.....	43
Table 3.3: Dimensions of P2 specimens.....	43
Table 3.4: Results of P2A specimens.....	48
Table 3.5: Patch Debonding Loads of P2D specimens.....	53
Table 3.6: Results of P2 plates.....	56
Table 3.7: Average dimensions of the non-aged specimens.....	57
Table 3.8: Cohesive law properties.....	58
Table 4.1: Dimensions of P1 specimens.....	69
Table 4.2: Nomenclature of P1 specimens.....	70
Table 4.3: Yield and maximum loads for P1 reference specimens.....	74
Table 4.4: Results of P1D specimens.....	83
Table 4.5: Results of reference and P1F specimens.....	88
Table 4.6: Patch material properties for the FE model of specimen P1F.....	91
Table 5.1: Specimens' geometry.....	98
Table 5.2: Surface preparation and aging scenarios of P3 specimens.....	100
Table 5.3: Fatigue results of P3D specimens.....	105
Table 5.4: Notch eccentricity measurements.....	115
Table 5.5: Patch eccentricity measurements.....	116
Table 5.6: Specimens characteristics measurements.....	116
Table 5.7: Initial characteristics of patch or bond defects.....	117
Table 5.8: Patch quality classification.....	118
Table 5.9: Comparison of repair characteristics and fatigue life.....	124
Table 6.1: Principal characteristics of study case.....	127
Table 6.2: Value of K and J for the WBD.....	136
Table 6.3: Calculated ΔK and crack growth rate.....	136
Table 6.4: Material properties of resin and steel.....	140
Table 6.5: Patch dimensions.....	141
Table 6.6: Studied cases.....	142
Table 7.1: Crack tip convergence CSDE.....	152
Table 7.2: Comparison of the CSDE to the enhanced VCCT and the J-integral.....	155
Table 7.3: Extraction of ω values for different cases.....	160
Table 7.4: Generalised Dundurs parameters for the studied bimaterial systems.....	161
Table 7.5: ω values table for the reduced formulation.....	162
Table 7.6: ω values table for the full formulation.....	163
Table 7.7: Results for bending moments with different signs.....	166
Table 7.8: Edge versus crack debonding in cracked cases.....	167
Table 7.9: Cases of the parametric study.....	169
Table A.1: Experimentally measured material properties.....	211
Table A.2: Engineering Constants.....	211

1. Composite Patch Repairing

1.1 Introduction

The various structural parts and details of a steel ship are subjected to a plethora of loading conditions during the vessel's operational life. The type and magnitude of these loading conditions vary significantly due to the stochastic nature of sea waves, which are the major cause for the loading applied to a marine structure. For this reason, it is quite usual to notice various types of local defects and failures in a ship structure, like plastic deformations and development of cracks, not forgetting corrosion, which increases the susceptibility of the structure to such local defects. In particular, in the presence of stress concentrations, fatigue loads acting on the structure can generate cracks, which, if not detected and repaired in time, can grow up to a critical length and cause catastrophic failures. Another typical defect of marine structures is corrosion that reduces the plate thickness, causing deterioration of the stiffness of the metal structure. Nowadays the tendency to use high strength steel and the consequent reduction of plate thickness accentuates the problems generated by corrosion. Thus, there are many cases in a steel marine structure where the need arises for local reinforcements or repairs, either permanent or temporary, until the next programmed inspection and maintenance. This need can also be the consequence of requirements for higher load-carrying capacity of the structure, which can in turn be the result of either a problematic initial design (i.e. existence of high stress concentrations which were not initially predicted) or an improper manufacturing or erection procedure, or a change in the operational conditions (i.e. later additional loading). Another very common reason for local repairs is the existence of defects in the steel structure resulting from accidents or overloading. The basic objective of these local reinforcements and/or repairs is the increase of the structure's residual strength in static loading or the elongation of its operational life in cyclic loading.

Composite material patching is a very promising new method for repairing and/or reinforcing steel structures. The technique consists of the application of a patch made of fibrous composite materials on the metal structure to repair or improve static strength (Figure 1.1). The patch is effective due to the fact that part of the applied load acting on the patched structure is transferred from the base metal plate through an adhesive layer to the composite patch, thus reducing the stress levels in the metal substrate under the patch. Thus, in the case of cracked structures, a composite patch decreases the stresses in the area of the crack tip therefore decelerating or under certain conditions completely arresting the crack.

If the damage of a marine structure is not too severe or if the need for improvement is small, the structures are generally repaired or reinforced through the addition of plates (the so-called doubling) or stiffeners by means of welded or bolted joints, or by welding-in the cracks in the case of cracked structural members. In the case of most severe conditions (for example when the damage is widespread over a large part of the structure), the replacement of the whole portion of the structure is necessary. The use of these traditional methods offers several advantages to all stakeholders involved in ship repair/reinforcement business (ship-owners, shipyards, Classification Societies, Authority Flags, etc.). The advantages are

essential due to the fact that being a well tried and trusted practice, the designers do not have excessive difficulties to design the repair/reinforcement, because the use of welded and bolted joints has been widely discussed in many literature papers and is also included in many Rules and Regulations. Furthermore, the Classification Societies usually accept these solutions without further investigations or analyses beyond those already foreseen from standards or regulations. In addition, the availability of qualified personnel able to deal with these methods encourages their use for repair and/or reinforcement. However, welding and bolted joints repair/reinforcement methods have also several disadvantages that in some circumstances make these techniques costly and time-consuming or simply impossible to be used.



Figure 1.1: Example of a carbon fibre patch applied to a defected steel transverse frame.

First of all welding in explosive environment (e.g. in the double bottom of a fuel oil tanker) requires a very complicated and expensive preparation procedure and the repair/reinforcement can be executed only under rigorous safety precautions; furthermore, traditional repair techniques often require the availability of complicated and costly infrastructures (dry-docks, cranes, scaffolding, etc.) and the application of an either welded or bolted joint, if not carefully designed, can generate new stress concentrations that mitigate the effect of the repair/reinforcement. Also the addition of weight caused by the application of welded or bolted doubler plates is a significant drawback that the designer should keep into account in order to avoid excessive weight increase. Another disadvantage, is that welding methods are not directly applicable on structures subject to significant loads (i.e. by their own weight), because welding generates high temperatures that can cause catastrophic collapse of the structures under tension. All the above mentioned drawbacks have negative effect on the cost of the repair/reinforcement, since the ship may stay out of operation for a relatively long period; thus, investigating new solutions alternative to welded and bolted joints can help improve the repair/reinforcement process. From this point of view, the use of composite materials patches appears to be a very promising way to repair/reinforce metal structures, because it overcomes most of the above mentioned drawbacks of the traditional techniques.

Applying a composite patch requires neither hot-work (so they can be used also in explosive environments or in structures subject to significant loads), nor the presence of special infrastructures since the patches are directly applied to the metal with a simple preparation of the surface. Composite patches can

be quickly applied with no geometric or shape restrictions in their application. Furthermore the added weight is very limited. For these reasons the patches can be usually applied 'in situ' while the structure is in service (Figure 1.2). In addition, contrary to the welded or bolted joints, composite patches do not generate stress concentrations on the repaired/reinforced structures.



Figure 1.2: Application of a composite patch on site (*Grabovac et al, 2009*).

Regarding the consequences on the environment and on the climate change, the use of composite patches is not considered to have negative effects. On the contrary, the reduction of downtime for ships or civil structures has positive effects, as there is no need any more to perform many and lengthy traditional repair works; also the minimization of traffic disruption reduces the traffic congestion and therefore positively affects the environment. Since the quantities of material used to fabricate the patches are quite small and the composite recycling technologies are making significant progress, it is possible to state that the influence on the environment is negligible.

All the above mentioned advantages make composite patches a new interesting method that, in several cases, can substitute the techniques involving welded and bolted joints and allows the reduction of the time and cost of the repair/reinforcement of the metal structure.

However, there are some parameters regarding the use of composite patches as a repairing/reinforcing technique that require additional investigation and studies. The most critical aspect concerns the long-term performance of the steel-adhesive-composite system, because it is subjected to the influence of complex external environmental parameters that makes it difficult to predict the behaviour of the patched structure in the long-term period. So far the topic has not been investigated in a satisfying way in the marine field, while the problem has already been widely investigated in the aerospace sector, where nowadays the use of patches is a common and trusted practice.

1.2 Applications of composite patch repairs

As mentioned earlier, composite patch repairing originates from the aerospace industry where boron/epoxy patches have been used to arrest fatigue cracks in the wings and fuselage of military aircrafts

since the 90s (Figure 1.3). The first applications of such repairs have been performed by the Royal Australian Air Force (*Molent 1989, Baker 1984*) with Baker, Rose and Jones being among the pioneers in this field, focusing on the design, monitoring and environmental or operational effects on repaired aluminium structures (*Baker et al 1984, 1988, 1999, 2004, 2009*). *Katnam et al (2013)* provided an extensive literature review of patch repairing of composite structures on the aerospace field.



Figure 1.3: Patch with structural health monitoring system bonded to F-111 wing (*Baker et al, 2009*).

In the civil sector composites have been recently utilized for strengthening or repairing beams, slabs and bridge decks (Figure 1.4) and a limited number of application cases have been reported, mainly in the UK. In civil engineering, bridges might be constructed using reinforced concrete, cast iron, wrought iron, steel and even masonry, as, unlike aerospace and marine applications, bridges are designed with a significantly larger operational life. In fact a recent survey on the age profile and condition of existing European bridges revealed that around 35% from a sample of 220000 bridges were over 100 years old (*Larsen et al 2010*). Bearing this in mind, it is obvious that these structures were considered according to outdated techniques and materials and in order to remain in service they need to be strengthened to accommodate bigger loads or to mitigate the effects of defects and outdated design and construction practices. A review on the application of fibre reinforced plastics with an emphasis on metallic bridges can be found in *Hollaway (2013)*, while *Zhao and Zhang (2007)* provided a state of the art of current research on FRP strengthened steel structures focusing on the strengthening of steel hollow section members and fatigue crack propagation in the FRP–Steel systems.



Figure 1.4: Reinforcement of concrete bridge using carbon fibres.

It would be expected that the technology associated with the bonding of composite materials to different substrates has matured and the experience gained primarily from the aerospace sector would make it easy to implement it also in the marine and offshore structures. This expectation is partially true as, indeed, the potential has been proven in praxis and data of their long term performance are available, but still there are several fundamental differences between the aerospace applications and marine/offshore steel applications which dictate a different approach and further investigation. These differences include the different stiffness of the base metal (stiffer steel versus the more similar to composites flexible aluminium), the completely different geometries involved (significantly thicker plating and larger beams in steel structures), the different loading cases and the different operating and environmental conditions. Furthermore, the operating time is greater for marine structures which in conjunction with their increased complexity and sparser inspection raise questions relatively to the long time performance of such repairs. Last but not least, the regulatory framework related to marine structures is more intricate as flag state regulations, classification societies' requirements and national and international authorities are involved.

In the marine sector, there have been only a handful of documented applications and, as with the aerospace sector, most of them have been performed in military vessels. A first perspective for the development of the composite patch repair technology and its application in big ships was given by *Grabovac et al (1993, 1997, 1999, 2003, 2009)*. In these works a brief description of the developments of the composite patch repair technology in the marine sector is given and an application case is presented in detail, including analysis of the superstructure cracking problem, research and development work, installation of composite reinforcement on board the ship, assessment of reinforcement efficiency, through-life monitoring and maintenance and repair. The application consists of repairing the aluminium deckhouse of a Royal Navy frigate that repeatedly exhibited fatigue cracking (Figure 1.5). The preferable installation procedure according to the authors is to grind out the crack and re-weld, then grind out the weld flat and affix the patch.

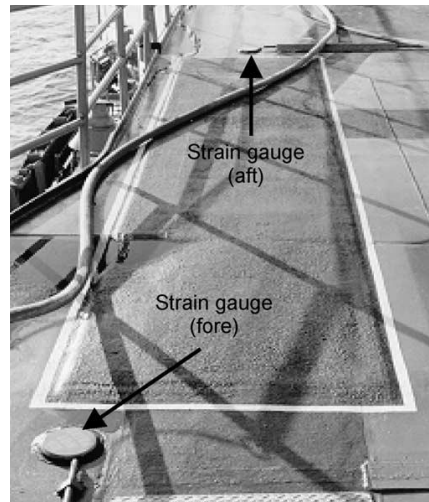


Figure 1.5: Carbon fibre reinforcement and monitoring system in service (*Grabovac et al, 2003*).

During the vessel's service period, seven inspections were made using non-destructive evaluation techniques combined with visual and acoustic tests. A total of four repairs were made during the 15 years of service. One repair was a non-structural restoration involving only the sacrificial edges of the GRP protective layers. The other three interventions were all structural repairs. Of those, two can be classified as dockyard inflicted damage that occurred during the ship maintenance or upgrade activities. The other may be regarded as environment initiated damage affecting the bonding at the overlay/deck interface which went unnoticed over a length of time. That was because the marine system paint failed to provide adequate protection to water ingress at the composite metal interface, and a new approach using an edge sealant was used (Figure 1.6). Additionally a time-cost estimation is given for the repairs. Apart from the repairs, the patch was cut in some locations so as to weld a support frame for the installation of a life raft (Figure 1.7). Although the welding operations were carried out in close proximity to the patch, no visible damage was noted. The installation of composite patches in stress concentration areas where the fatigue crack initiated in the past, led to a 20% reduction of stresses and after 15 years of active service no cracking underneath the patch or in adjacent areas was initiated.

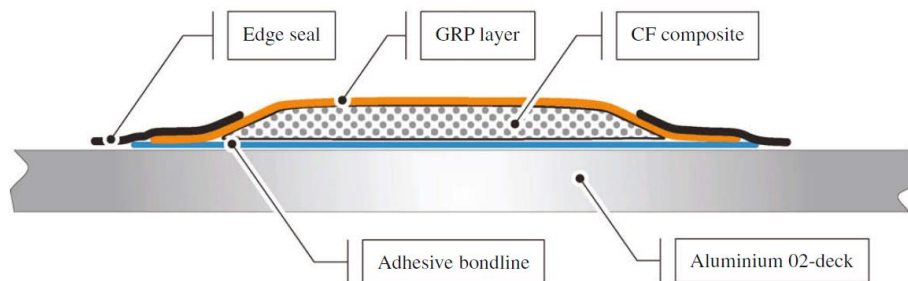


Figure 1.6: Composite patch configuration (*Grabovac et al, 2009*).

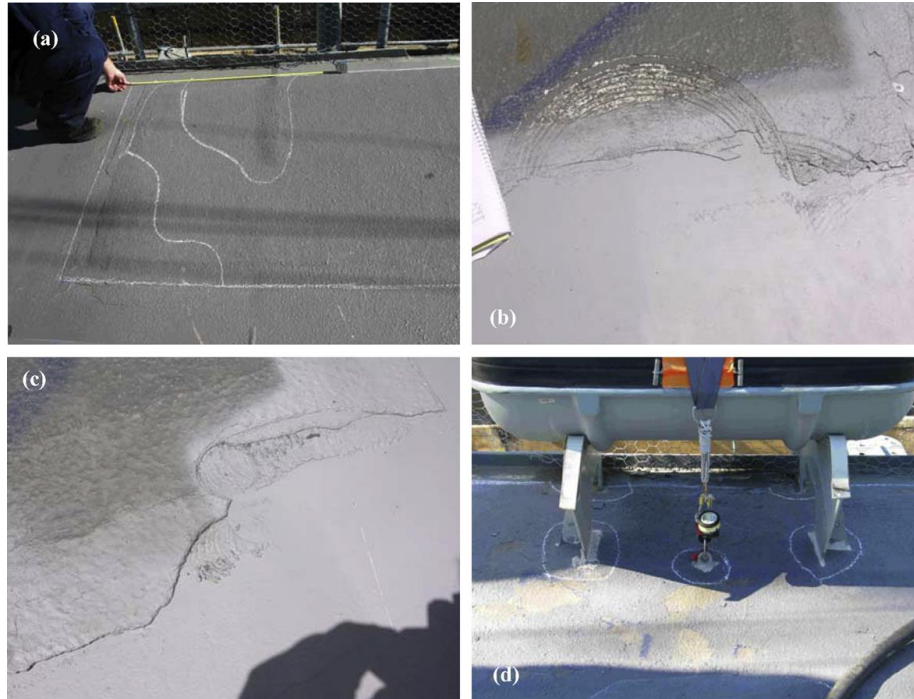


Figure 1.7: Photos depicting damage and the cut-outs made for welding a life raft support system on the deck (Grabovac *et al*, 2009).

Dalzel-Job et al (2003) reference the applications that existed by that time, starting from the composite repairs in the aluminium superstructures of some frigates of the UK Navy performed in the 80s. The same work presents also the results of a corresponding experimental program, where thick (15 mm) steel plates with a central crack were reinforced with carbon/epoxy patches and then subjected to fatigue loading ($\sigma = \pm 100$ MPa). The patch survived without any problem more than 1000000 loading cycles, equivalent to 12 ship years which was defined as the limit. The fatigue life of the plate was extended by at least 3 times, by applying the patch. In a subsequent work (*QinetiQ, 2004*), reference is made to the cases where the composite patch repair technology can or has already been applied in both marine (Figure 1.8) and aviation sectors, highlighting its advantages against traditional methods of repair. A brief description of the health monitoring systems applied in composite patch repairs is also presented. An important remark stated is that better and longer-term repairs are often achieved by laying up the patches and curing them in a continuous operation rather than bonding a pre-manufactured patch to the affected structure.



Figure 1.8: Composite patch repairs on lift shafts of Type 42 destroyers.

In the work by *Turton et al (2005)* a description of the major advantages of this technology against the conventional repair methods is given followed by a brief description of case studies that took place from 1982-2003 in two different types of frigates and a FPSO unit (Figure 1.9). In all aforementioned cases composite patches were installed to arrest the propagation as well as the initiation of fatigue cracks. A qualitative comparative study between three methods for manufacturing the patches namely hand-lay-up, vacuum-infusion and pre-preg is presented. Additional experimental research performed in the same scope showed that composite patch application can increase the fatigue life of a cracked steel plate by a factor of over three times and that a patch has survived fatigue cycling equivalent to at least 12 ship years with no sign of patch delamination. Additionally, four different ultrasonic inspection techniques were examined for the non-destructive evaluation (NDE) of the repair with manual pulse echo contact ultrasonics and tandem pulse-echo ultrasonics being more promising at checking the quality and effectiveness of a composite patch. The alternating current potential difference (ACPD) technique was used for monitoring the crack growth on two field applications on frigates.



Figure 1.9: Composite patch applied to cargo tank on-board FPSO (*Turton et al 2005*).

Another more recent work dealing with the application of composite patch repairs in marine structures is that of *McGeorge et al (2009)* where a procedure for the design and qualification of bonded repairs of floating offshore units used in the oil and gas industry has been developed. The use of this procedure has been demonstrated by two full-scale repairs that were carried out in two different FPSO units. The first repair was carried out in order to arrest a fatigue crack that had developed from the corner of a door (Figure 1.10), while the second one was carried out to restore material loss on a heavily pitted deck floor. The procedure is based on the use of relatively simple design methodologies that are derived from fracture mechanics theory. The two demonstrators have shown the viability of bonded composite repairs to the two most widely

encountered damage scenarios in floating offshore units – fatigue cracking and patch thinning due to corrosion.

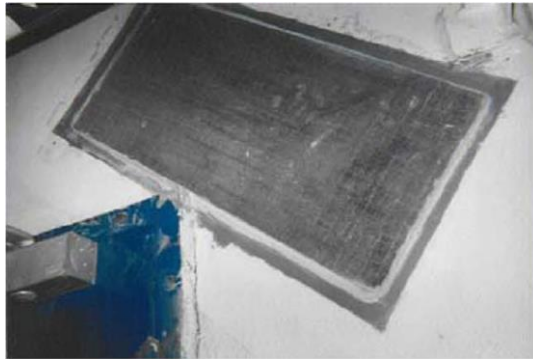


Figure 1.10: Repair on the corridor side of the Bulkhead (*McGeorge et al, 2009*).

The U.S. Naval Warfare Centre, Carderock Division, have used composite patches to cover large areas of sensitized aluminium plate on the superstructure of ships. For unknown reasons, but possibly due to changes in the processing by the aluminium mill, several U.S. Navy ships have suffered sensitization of 5456-H116 aluminium plating. Sensitization is a process where over time with exposure to higher service temperatures the magnesium that had been disbursed throughout the grain structure of the aluminium migrates to the grain boundaries, causing stress-corrosion cracking. Because the sensitization occurs throughout the aluminium plate, weld repairs to cracks are not effective because the plate adjacent to the weld, which is sensitized, will crack from the residual stress of welding. The only solution to the problem appeared to be total replacement of the plating, which would be extremely costly.

To address the problem and, at a minimum, provide watertight integrity, a repair procedure using low-elastic modulus E-fibre glass was used, laying down patches over large areas of the structure, as shown in Figure 1.11. The patches were designed to be of low stiffness so as to not attract more stress in the area that could cause cracking beyond the boundary of the patches. However, it is intended that the patches will reduce the stress intensity at the tips of the cracks under the patches, reducing the rate of fatigue crack propagation.



Figure 1.11: Glass fibre patching of sensitized aluminium deck.

A cross-section through the patch is shown in Figure 1.12. Prior to patching, the surface was prepared by disk grinding. Subsequently it was cleaned using a solvent and a coupling agent was applied. The patch area was vacuum bagged and cured at 60°C (140°F) for eight hours. An epoxy system that would permit curing at a lower temperature was selected to prevent further sensitization of the plate. The edges were sealed with polysulfide to prevent water egress to the patch, taped over to prevent damage from abrasion, and then the entire area was painted over and marked as shown in Figure 1.11 to reduce the risk of inadvertent damage to the patch. The above work was carried out on several ships to cover a total area of about 100 sq. meters.

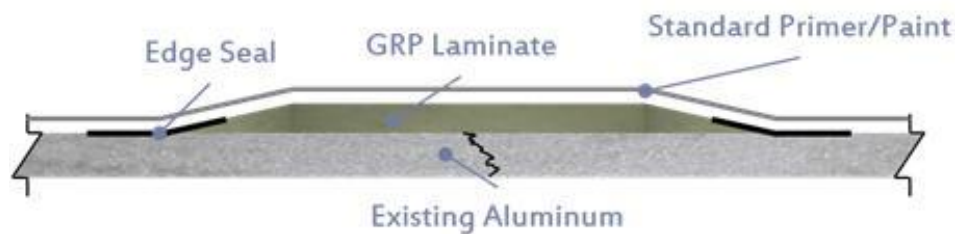


Figure 1.12: Cross-section of patch over sensitized aluminium plate.

The French Navy has used composite patches to repair and prevent cracking in the aluminium superstructure of naval ships. Carbon fibre patches with an epoxy matrix were applied over cracks as shown in Figure 1.13. Temporary shelters were placed around the work area to control the environment. The laminate was vacuum-bagged and cured at 100°C for two hours. These composite patches are expected to extend the service life of the ships by 20 years. The selected application method was grinding of the surface, followed by the application of a primer.



Figure 1.13: Crack in aluminium superstructure and carbon / epoxy patch.

Apart from the examples listed above, the NTUA Shipbuilding Technology Laboratory team had the opportunity to apply composite patch repairing in the field in different applications. Two of them are presented here. The first one consisted of rehabilitating a corroded part at the fore ballast tank of a LPG tanker with a DWT of 9130 t. In particular, due to extensive pitting corrosion a hole was created in the bulkhead separating the ballast tank from the adjacent deep fuel tank. This led to loss of impermeability and therefore to the mixing of water ballast in the fuel tank and to the contamination of water ballast with fuel oil.

The latter was by far more critical as it led to the discharging of fuel oil to the sea each time the ballast tank was emptied, which is a severe violation of the existing regulations. A rotating wire brush has been used for the surface preparation of the area prior to lamination and the achieved roughness was on average $R_z = 45 \mu\text{m}$. The steel and ambient temperature was 31°C and 28°C respectively. The patch consisted of 16 layers of 200 g/m^2 biaxial carbon reinforcement impregnated in epoxy resin in which an additive (KONASIL K-200) has been added to control the viscosity of the resin. A biaxial glass layer has been laminated between the steel plate and the patch to act as an isolating layer and prevent galvanic corrosion of the steel. The patch was laminated using the hand lay-up technique and the repair was successfully completed the same day. After curing, a typical marine coating has been applied in the area (Figure 1.14). The repair has been in service for four years with no reported reoccurrence of the problem and no visible signs of damage in the patch.

The second application case was performed in a vessel of the Hellenic Navy. A cluster of cracks was detected in the aluminium deck plating of one of the vessels as depicted in Figure 1.15. The cracks were formed due to unsuccessful attempts to repair the initial crack by welding, which eventually resulted to the formation of new cracks in the vicinity of the initial one. A carbon fibre patch with epoxy matrix was applied to repair the defects. Holes were drilled at the crack tips to act as crack arrestors and the aluminium surface was grinded using a rotating wire brush and cleaned with the use of a solvent. The first ply consisted of a glass layer to prevent galvanic corrosion between the carbon patch and the metallic substrate. The patch lamination was successfully completed the same day and left to cure at ambient conditions (around 40°C).



Figure 1.14: Area of damage (pictures a and b), lamination of the repair (c), finished coated repair (d).

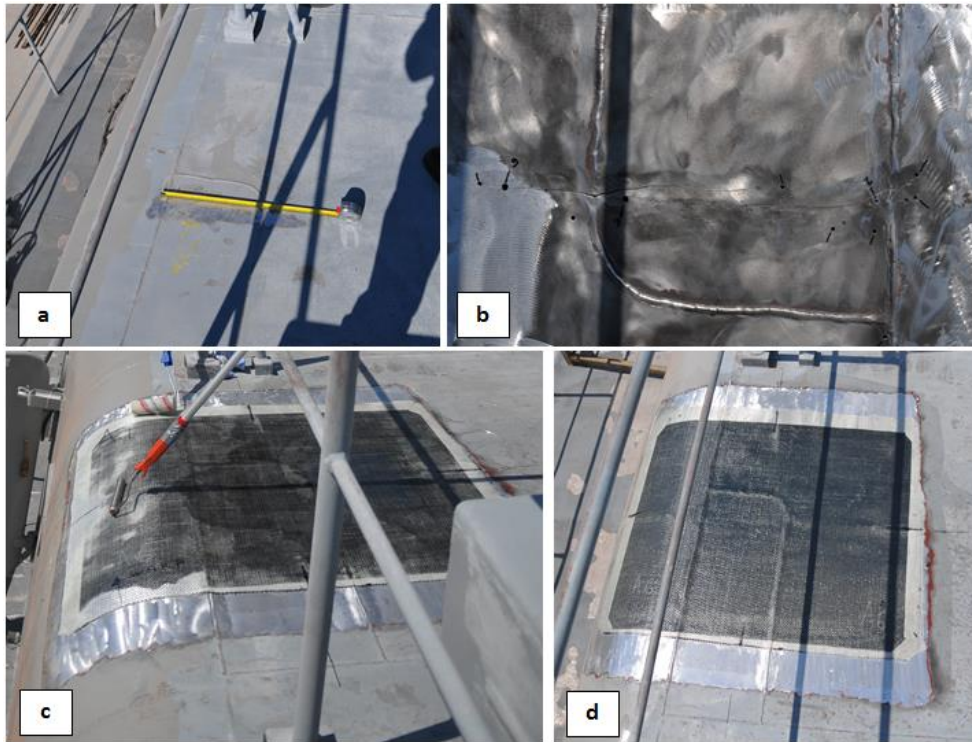


Figure 1.15: Position of cracks (a), treated surface (b) lamination of the repair (c), finished repair (d).

1.3 Main types of damage in marine structures

Ship and offshore structures will invariably face structural damage throughout their operational life. In this section, some of the most common, non-accidental structural defects are listed, in an attempt to identify possible patch repair application cases (*Larsen et al 2010*). The list is focused on typical known defects found on-board bulk carriers, oil tankers and containerships but not necessarily limited to these, as similar defects are prone to appear in other types of ships.

Reinforcement of Cross Deck Plating

In the case of bulk carriers, due to the large open areas produced by cargo hatchways, the main deck which is a primary longitudinal strength component is continuous only at the outer strakes of the deck (Figure 1.16). This dictates that the cross deck plating experiences high loads to compensate for the discontinuity of the deck structure which can result in the buckling of the cross deck plating. This might be the result of sea loads acting directly on it, excessive loading in two adjacent holds, insufficient transverse stiffening or thickness diminution due to corrosion or a combination of the aforementioned. In the case of containerships, buckling might also be caused by the torsional deflection of the ship, as this type of ships are susceptible to torsional loads due to the big hold openings compared to bulk carriers.



Figure 1.16: Cross deck plating of a bulk carrier.

Reinforcement in Way of Structural Details

These types of damage involve typical defects located in way of lightening holes, girders, swash bulkheads and openings such as cut outs designed to allow the passage of stiffeners and other structural components (Figure 1.17). These areas typically introduce stress concentration points and, in combination with high loading and/or aggressive environment and the topology of the area, are prone to fracture, cracks, excessive deformation, corrosion and buckling.



Figure 1.17: Defects in water ballast tank.

Defects at Bracket Edges and Bilge Hopper Plates

Fractures may appear in details such as brackets. It is envisaged that the complex arrangement of some components may render these difficult to access. Cracks or fractures may occur at the connection of the bilge hopper plate and web frames in oil tankers due to stress concentrations along with static and dynamic loads from fluids (Figure 1.18).



Figure 1.18: Arrows pointing to fatigue cracks at bracket.

Corrosion

Corrosion can occur for various reasons including lack of maintenance, interaction of cargo ingredients with steel, unintentional sacrificial protection (such as the hull becoming an anode in the process), stress corrosion or erosion. This application case concerns general and pitting corrosion (Figure 1.19) and it is essential that the cause of the corrosion is determined prior to treatment. Where general or pitting corrosion exists, if the thickness reduction is not significant then blasting of the surface and the application of a new coating is sufficient. In the opposite scenario, rectification measures must be sought. In all cases the Classification Society apply rules which specify acceptable diminution limits of the steel and this must also be considered prior to application of patches in this case. The allowable diminution of a component is usually given as a percentage of the as-fitted thickness of the component, while for pitting corrosion the acceptable diminution is based on a combination of pitting depth (referred to as intensity) and the surface area of the affected steel.



Figure 1.19: General corrosion due to coating failure (left) and pitting corrosion (right).

1.4 Fabrication methods of patches

The joining of dissimilar materials has become a growing research area, as these joints are generally the weakest part of hybrid structures. The most common types of joining methods in composite structures are mechanical joining and bonding. Mechanical fastening rely on mechanical means such as rivets or bolts, which in most cases require drilling holes. Although this method makes the disassembly and the inspection easier, it also leads to undesirable stress concentrations, increase of weight of the structure and non-uniform load transfer through the joint. On the contrary, adhesive joints provide a more uniform load transfer and do not add to the weight of the structure, while rivets or bolts, where stress concentrations appear, are not required. Moreover, it is an ideal method for joining different materials, especially composite materials to metallic ones. For these reasons, adhesively bonded joints are increasingly being utilized substituting traditional methods of bonding such as welding, fastening and bolting. On the other hand, adhesive bonding is sensitive to environmental conditions, both during manufacturing and in service, and the appropriate surface treatment, which depends on the type of the adherents, is crucial for the good performance of the joint. In fact, surface treatment is considered as the weakest link in adhesively bonded structures and it is of paramount importance for the success and efficiency of the repair (*Davis et al 1999*).

Surface preparation includes the cleaning of the substrates from any kind of contaminants such as rust, oil, grease, dust etc. that are detrimental to the bond. At the same time several studies have showed that increasing the surface roughness leads to the enhanced performance of the bond, as a certain degree of mechanical interlocking between the adhesive and the substrate is achieved. This interlocking is connected to the achieved surface roughness of the surfaces of the adherents and can be achieved either by mechanical or by chemical methods. Since immersion of the substrates into a chemical solution is inevitable when using a chemical treatment method, it is impractical to apply such a method to the large scale structures incorporated in the marine industry. In the framework of mechanical treatment methods, polishing, grit blasting and the use of power tools such as rotating wire brushes or emery cloth are the most common techniques utilized for roughening the adherents' surfaces. These techniques depend on the type of the substrate, with grit-blasting being applied on metallic surfaces of metal adherents while polishing is applied to the composite ones. Comparative studies between different mechanical and chemical surface preparation for adhesive bonding have been performed by *Siddaramaiah et al (1998)*, *Grabovac et al (2003, 2009)*, *Dag McGeorge et al (2009)*, *Liu et al (2009)*, *Andersen (2006)* and *Tsouvalis et al (2008)*. In each case, results indicated that grit-blasting led to better results.

Composite patches can be divided in two main categories in terms of the installation method. The first category consists of composite patches that are prefabricated and subsequently transferred and bonded in the defected structure with the use of specialized adhesives. The second approach consists of in situ lamination of the composite patch directly on the structure and curing it on site. In this case, the matrix of the composite acts as the adhesive upon curing. Each method presents advantages and disadvantages and which one is more favorable depends on the application at hand. The two methods are described below.

Adhesively Bonded Patches

This approach presents the advantage that a high quality composite laminate can be achieved as the manufacturing process and curing takes place in a controlled laboratory environment. This allows for the employment of greater range of manufacturing techniques, spanning from the simple hand lay-up technique to more advanced methods such as prepregs, pultrusion and injection moulding. Additionally, the curing cycle can be better controlled and the risk of contamination or inappropriate curing of the laminate is significantly lower compared to the in situ lamination. Another advantage is that the designer is able to choose from a wide variety of specialized industrial adhesives to better suit the needs of each application. On the other hand, the procedure becomes more complicated as the correct application of the adhesive becomes crucial and suitable surface preparation of the composite material is necessary to ensure that adequate bonding is achieved between the patch and the selected adhesive. In addition, prefabricated patches are less versatile in terms of transportation, especially when the damaged area is hard to access or if the geometry of the member to be repaired is complicated. Another challenge is associated with the thickness and quality of the adhesive layer. Studies have been presenting contradicting results on the effect of the adhesive thickness with some claiming that a thick adhesive layer is desired (*Mall 1989, Kawashita 2008*) and others that an increased adhesive thickness is detrimental (*Grant et al 2009, Tamblin et al 2001*). In reality a relatively thick adhesive is susceptible to imperfections caused from voids that might lead to premature failure and in practice, controlling the adhesive thickness and achieving a uniform thickness has proven to be challenging, even more so in cases where the base material surface is uneven. Additionally, the challenge of properly curing the adhesive is not surpassed, if not increased, as the bulk of the material between the substrates is not accessible. This method nevertheless has been used in civil engineering, especially by using pultruded or prepregged unidirectional beams or tapes that are subsequently bonded to bridge deck and girders. Such an application case is illustrated in Figure 1.20.



Figure 1.20: Prefabricated pultruded carbon strips bonded onto a steel bridge.

Co-cured Bonded Patches

In situ curing or alternatively co-cured bonding use the excess resin of the composite system during the curing process as the adhesive, forming bondlines with thicknesses typically less than 0.1 mm. This method presents several advantages compared to adhesively bonded joints where a different adhesive is used, as the design, analysis and manufacturing of these kind of joints is simpler compared to adhesive joints, it requires no surface preparation of the composite adherent and it is considerably faster, as the bonding process is performed simultaneously to the curing process of the composite system. Despite the practicality of this method, only a few studies on co-cured bonding are available studying the behaviour of single lap and double lap joints under static and fatigue loading (*Shin et al 2003, 2006, Park et al 2006, Russo 2011, Song 2010*).

The drawbacks associated with this method are that the manufacturing procedures that can be applied on site are limited mainly to hand lay-up, vacuum bagging and vacuum infusion and careful planning and execution has to be followed in order for them to be successful. Moreover, additional preparation might be necessary to control the ambient conditions on site and mitigate detrimental environmental effects that can lower the efficiency and the life expectancy of the repair. Such measures involve the isolation of the area and position of heaters and dehumidifiers if it is in an enclosed space. Concerning the curing cycles, these can be achieved in a satisfactory way by the use of heating blankets, specialized portable curing devices (Figure 1.21) or even heat induction curing in the case of carbon fibres (*Grabovac 2009*). It is deemed that this bonding technique is better suited for marine applications, as defects in marine structures tend to be located in areas where the topological features of the structure change and access could be limited, especially if these are located inside holds, tanks or at the double bottom of the ships' structure. Additionally, especially in the case of corrosion, the area to be repaired might be considerably large rendering the use of prefabricated patches logistically complicated and more cumbersome (*QinetiQ 2004, McGeorge et al 2009*).



Figure 1.21: Curing of co-bonded patch.

Symmetrical and One Sided Configurations

In terms of configurations, the repair can be either applied to both sides of the defect or to one side. In

fact the most favourable configuration is the installation of a patch symmetrically on both sides of the defect, as this alleviates the secondary bending effects that are manifested in the one sided repair due to the eccentricity of the neutral axis when it is axially loaded. The benefits of a double sided repair become more important in the extension of the fatigue life of cracked components, as it will be discussed later. Nonetheless, in most applications it is simply not possible to install a symmetric configuration, as the area from the other side might be inaccessible, plus a double sided repair increases the time, cost and preparation actions required and might be difficult to be identically replicated from both sides.

1.5 Loading / failure and analysis of composite patches

The possible failure mechanisms in a bonded composite repair are shown schematically in Figure 1.22. Failure can occur either in the metal substrate, in the interface or/and the adhesive between the two different materials, or in the composite laminate. Therefore it is crucial to define prior to the design of the repair, which are the acceptance criteria for each one of the aforementioned types of failure, as, for example, partial debonding does not necessarily denote failure of the repair if the load can still be effectively transmitted from the substrate to the composite. Examples of failure criteria for the metal substrate are yielding, fracture, excessive deformation and failing to arrest the existing crack in the metal substrate. It is paramount that the engineer understands how the repair interacts with the remaining structure, as a wrong design might shift the existing problem or give way to new defects in other adjacent areas.

A well designed bond will rarely fail within the laminate, as this would mean that the strength of the composite is lower than the shear strength of adhesive or the interface. The most common failure types are crack extension in the substrate or/and extensive debonding.

As already stated, the main task of the composite patch is to bear part of the load acting on the steel structure. The load transfer between the substrates is achieved via the adhesive or the bimaterial interface. In other words the loads acting on the repair are governed by the acting load on the underlying steel substrate. As structural elements of marine structures are characterized by small thicknesses compared to their width and length, the loads acting on these are predominantly planar loads induced by axial and shear forces, bending moments and their combinations.

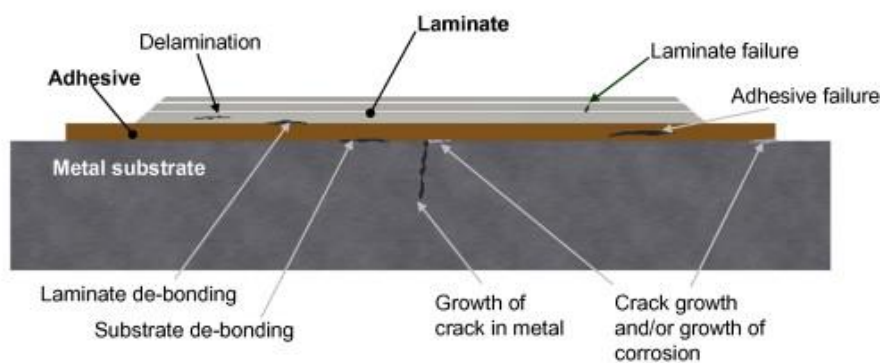


Figure 1.22: Types of failure in composite patch repairing (*McGeorge et al, 2009*).

These forces and moments are the result of loads which are influencing the ship structure in primary, secondary and tertiary level (*Hughes 2010*). Quantification of the exact loading acting on a structural member is a complicated task, as some loads act in more than one level. Furthermore, the loading might be cyclic with frequency and amplitude governed by the location of the repair and the operating conditions. Due to the nature of such loads along with the fact that these will undoubtedly vary during the service life of the vessel, it is impossible to accurately represent them in laboratory conditions. Nevertheless, there has been significant research both experimental and numerical focusing on the durability and failure of bonded composite to metal specimens. These have been mainly emanating from the aerospace industry investigating the effectiveness of composite patches on aluminium but also applications focusing on steel substrates and marine structures exist. In particular, *Lam et al (2010)* and *Liu et al (2007)* have performed research focusing on the proper identification of loading and failure modes with the use of finite element modelling, and the efficiency of patches in rehabilitating corroded plates and extending the fatigue life of cracked steel plates.

The design parameters that have been systematically examined are: the effect of the geometrical parameters of the patch i.e. the shape, thickness, length and width, the role of the stacking sequence and the effectiveness of each configuration in reducing the stress intensity factor (SIF) of the cracks in the metallic component (*Xiong and Shenoi 2008, Hosseini – Toudeshky and Mohammadi 2007*). In all cases it was proven that the patch was able to extend the fatigue life ranging from 2 up to 20 times compared to the unrepaired cracked plate, depending on the experimental configuration (*Chung et al 2003, Seo and Lee 2002*). The results were more prominent in the case of thicker patches and thin plates (*Wang and Pidaparti 2002*) and double sided repairs (*Belhouari et al 2004, Megueni and Lousdad 2008, Liu et al 2009*). This is attributed to the reduction of the stress intensity factor through the crack thickness (*Megueni et al 2003-a, Bachir Bouiadjra et al 2002*) which, in the case of one sided repairs, is not uniform leading to curved crack fronts. This phenomenon revealed the question of defining a representative value of the stress intensity factor for the assessment and design of repairs in cracked components. Researchers dealing with this issue have proposed different modelling and averaging techniques employing finite element modelling (*Bachir Bouiadjra et al 2002, Umamaheswar et al 1999, Seo and Lee 2002, Megueni et al 2003-a*). *Lee and Lee (2004)* used a successive crack front updating technique to capture the skewed crack front with the use of finite element modelling and successfully compared it to experimental results obtained for different metallic plate thicknesses (Figure 1.23). *Toudeshky et al (2006, 2009)* used the obtained mid plane SIF values for thin panels to predict the fatigue life of thin aluminium panels, however this proved to be problematic in the case of thicker plates. A different approach by measuring the SIF in a specific position of the skewed front was suggested by *Hosseini – Toudeshky and Mohammadi (2007)*, based on the results from their experimental campaign.

To better understand the interaction between the crack evolution in the base material and the repair configuration, the debonding effects have to be studied and understood. It has been observed that local debonding occurs in the vicinity of the crack tip, preceding it as the crack grows in the base material. Its extent relies on the given configuration, loading and the achieved quality of the bondline. The debonding around the crack area and the crack growth are interdependent, as the stress concentration and local

plasticity in the crack tips in conjunction with the fact that the patch is more loaded above the crack region leads to the local debonding. This in turns redistributes and gives rise to the stresses acting in the vicinity of the track tip and simultaneously redistributes the load in the repair. This continues until either there is extended or total debonding of the two substrates or until the crack length exceeds the width of the repair. The importance of considering debonding has been highlighted by *Mall and Conley (2009)* and *Papanikos et al (2005, 2007)*, who used progressive damage modelling techniques to simulate these effects (Figure 1.24).

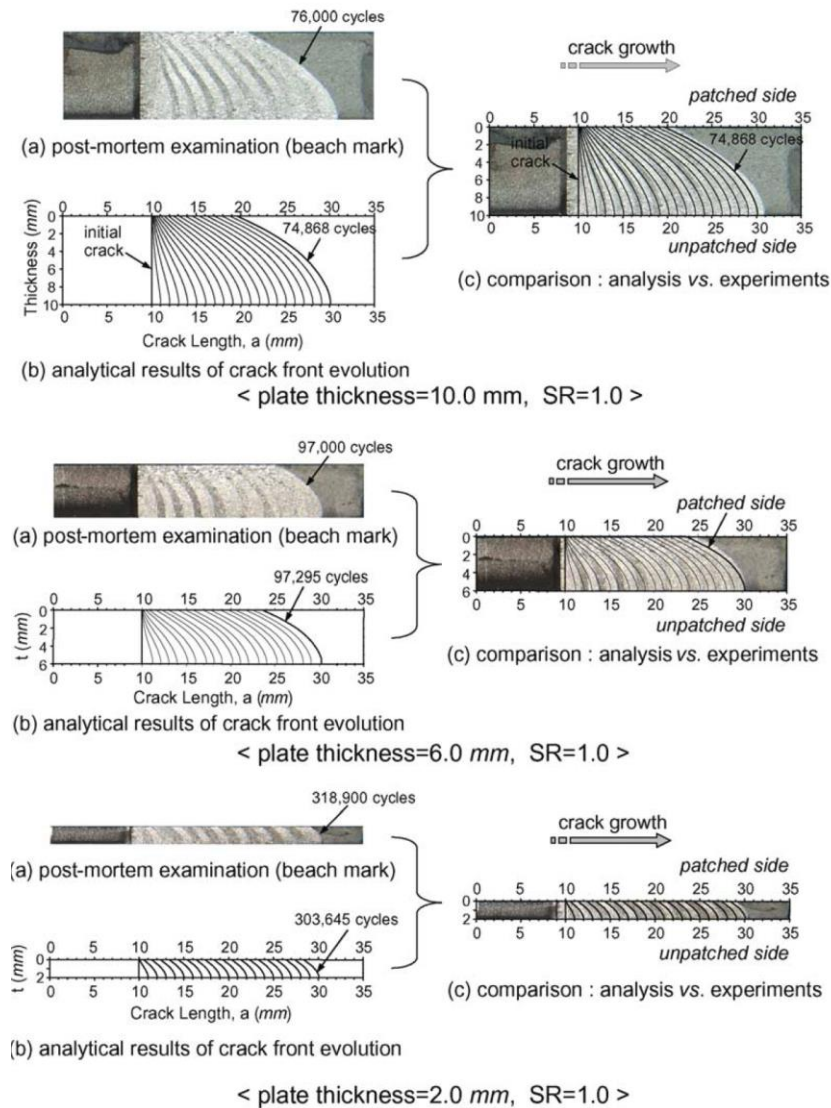


Figure 1.23: Skewed crack front in one sided repaired specimens (*Lee and Lee, 2004*).

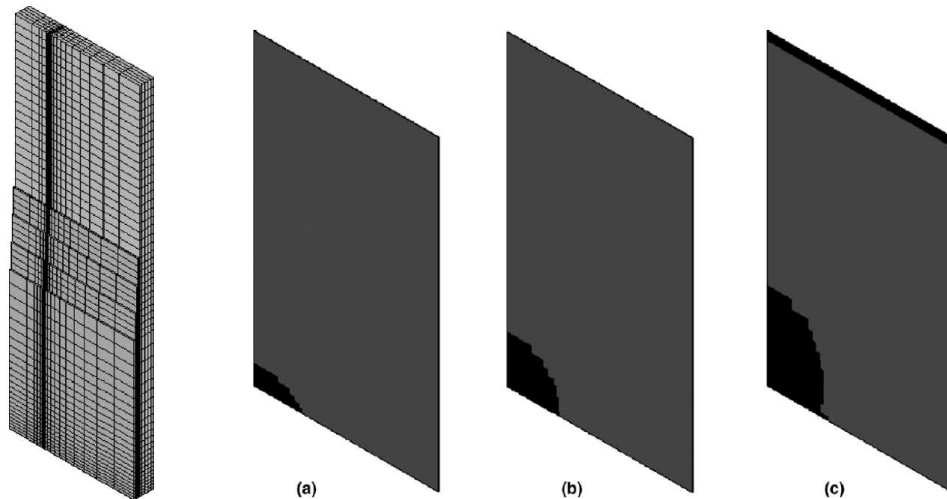


Figure 1.24: Numerical model depicting debonding evolution (*Papanikos et al, 2005*).

1.6 Non destructive evaluation, inspection and structural health monitoring

As only limited in field experience on the long term performance of such repairs in marine applications exists, it is paramount that structural health monitoring and robust inspection techniques are applied to monitor the performance of the repair and possible evolution of damage in the substrate. Another challenge relies to the fact that being a hybrid construction, a practical solution is sought that would enable the monitoring of all involved materials i.e. metal, composite and the bond between these two. Different real time monitoring systems are available and could be employed to monitor the repair offering significant advantage in terms of reliability of the structure and minimizing periodic inspection requirements. There is a plethora of different non-destructive evaluation techniques which enable the monitoring of different types of flaws, however a significant part of these are difficult to implement on the field or not yet possible to form automated solutions.

Strain Gages

Strains are mostly measured with electrical strain gauges. They constitute the simplest and most established solution for structural health monitoring with a broad range of existing commercial solutions to choose from and have been extensively used in laboratories and field applications (*Grabovac 2009*). Almost all strain gauges are glued to the surface of the material; it is theoretically possible to embed them inside a laminate, although there are several challenges associated with that approach, rendering it impractical. One very attractive solution is the combination of the strain-gages with the wireless technology, which counters the problem of extensive wiring that arise with the employment of traditional strain gauges (Figure 1.25). Apart from strain gauges, a variety of sensors can be combined measuring different features simultaneously (for example strains, temperature and acceleration), and special casings allow them to operate in aggressive environmental conditions and in different temperature ranges with substantial autonomy.



Figure 1.25: Commercial wireless sensor nodes.

Optical Fibres

Different optical fibre systems are available but unarguably Fibre Bragg Gratings (FBG) and Fabry-Perot have been more extensively used (Figure 1.26). Optical fibre sensors have a better long-term performance than strain gauges and are less sensitive to environmental attack. In addition, optical fibres can be embedded inside the composite laminate. This allows readings inside the laminate and the adhesive joint but also on the metal substrate. Examples depicting the potential of employing optical fibres for the monitoring of patch repairs are given by *Baker et al (1999, 2009)*, *McKenzie et al (2000)*, *Jones and Galea (2002)* and *Takeda et al (2007)*. Careful consideration must be given to the position of the fibres in order to detect the changes in the strain field that might occur due to damage.

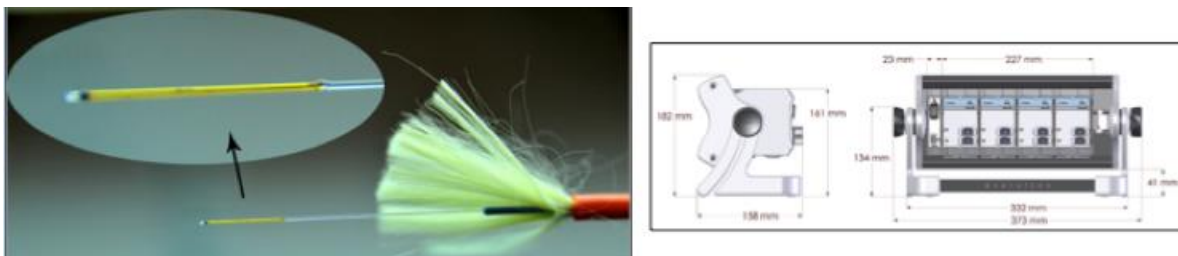


Figure 1.26: Optical Fibre system.

Ultrasounds / Acousto-ultrasonics

Most of the ultrasound systems are used for periodic inspection and they are not permanently installed monitoring systems. However, portable and automated systems based on ultrasounds have been developed for industrial applications (*Gieske et al 1998*). The main principle of ultrasound is that a transducer sends an acoustic wave into the laminate and a receiver at a different position will detect this wave. Damage interrupts or modifies the flow of the acoustic wave and it is detected by a change in the characteristics of the wave or the time of flight. Moving transducer and receiver along the laminate allows scanning of the entire laminate. Moving can be done by hand or it can be automated. Independently of which method is used, the position of transducer and receiver needs to be known to find the position of the damage. Ultrasounds can detect defects/damage in the laminate, as well as cracks in metal substrate; however they are not reliable in detecting debonding in the adhesive.

One of the methods used for the evaluation of the quality of the bond and the patch within the framework of this thesis was based on acousto-ultrasonics. The acousto-ultrasonic inspection is a fairly new technique that can be used to detect debonding. The difference to ultrasonic techniques is that the wave sent through the material has a much lower frequency than ultrasound. This low frequency gives in principle less resolution than the ultrasound method, but it has proven to be a reliable method to detect debonding both at the laminate and the steel/composite interface (*Karatzas et al, 2014*).

1.7 The Co-Patch project

A significant part of the work presented in this PhD thesis has been conducted within the framework of the Co-Patch research project funded from the European Community's Seventh Framework Programme (FP7/2007-2013) under grant agreement n° 233969 (www.co-patch.com). The scope of the project was to investigate the suitability and effectiveness of the composite repair method for the rehabilitation of large steel structures, focusing on marine and civil engineering structures.

The project consortium consisted of fifteen different organizations from eight European countries. These are presented in Figure 1.27. Among these, the following were involved in the specimen preparation, manufacturing and testing for the experimental procedures that will be described in Chapters 3, 4 and 5 of this document.

AS2CON is a research, development and application enterprise based in Croatia. They were responsible for the surface treatment and vacuum infusion of the composite patches for the manufacturing of the specimens subsequently tested under static and fatigue loading.

AIMEN is a research and development centre based in Spain. AIMEN undertook the task of testing the notched specimens in tension whose ultimate load exceeded the capacity of the testing machines available at NTUA's facilities.

For the material characterization of the selected material configurations ENP, NTNU, UM and AS2CON were involved in the production of the specimen. ENP and UM are shipyards focused on the production of composite vessels based in Portugal and Norway respectively. NTNU is the Norwegian University of Science and Technology.

Finally UniS stands for University of Surrey. Among other activities, UniS was responsible for the material characterization of the steel that was used in the project.

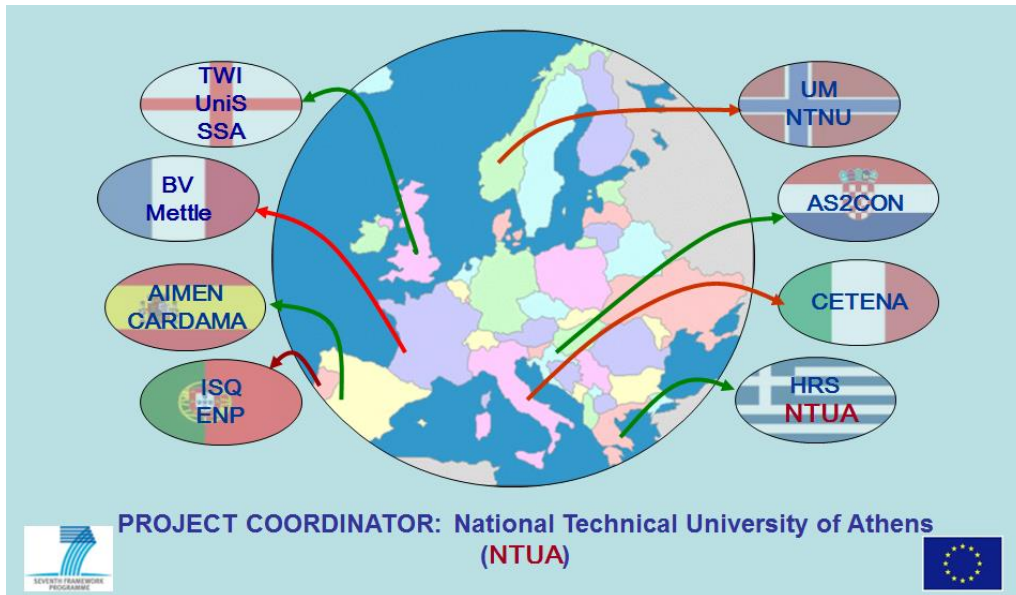


Figure 1.27: Co-Patch project partners.

This dissertation emphasizes in presenting the most conclusive results and does not include all the research activities conducted for the project by the author as a member of the NTUA team in the project.

1.8 Objectives and layout of PhD thesis

The current PhD thesis focuses on the investigation of the use of composite patches for the rehabilitation of typical defects found in marine steel structures namely cracks and corrosion. The main scope is, having demonstrated their potential, to further comprehend how specific parameters govern their efficiency on realistic operating conditions and to propose a straightforward design assessment methodology based on analytical tools, derived from Linear Elastic Fracture Mechanics for bimaterial interfaces. These simple analytical tools are to be utilized by design engineers and researchers for the evaluation, design and analysis of composite patch repairs and other similar adhesively bonded applications.

To achieve the aforementioned goals a combined experimental, numerical and analytical approach has been followed varying from medium scale, i.e. defected steel plates rehabilitated using composites under static and fatigue loading, to large scale study cases, such as the creation and analysis of a three compartment model of an AFRAMAX tanker using the Finite Element Method.

In conclusion, the present PhD thesis shows the potential of composite patch repairing on marine structures having addressed critical issues associated with their effectiveness, durability and inspection methods and a simple analytical design procedure is proposed.

In detail, the research activities carried out within the framework of this PhD thesis can be categorized as follows:

Experimental and Numerical Investigation of Repaired Corroded and Notched Plates under Static Loading

In these chapters, an experimental campaign involving one selected composite material system have been undertaken showing the effectiveness of the repairs. A series of midscale static tests have been performed in defected steel plates, namely in corroded and notched plates. All plates have been repaired with the selected composite material system and were tested in tension. Additionally, different health monitoring and non-destructive evaluation methods have been applied to assess the quality of the repair both after installation and during operating conditions. Moreover, the effect of different aging scenarios has been investigated. Finally, 2D and 3D finite element models have been created using cohesive zone modelling, whose results are in very good agreement with the experimental findings. Results showed that the repair could reinstate the initial state of the structure and that failure was preceded by yielding of the steel substrates.

Experimental Investigation of Repaired Cracked Plates Subjected to Fatigue Loading

Cracked plates on which composite patches have been installed were experimentally investigated under fatigue loading. Two different surface preparation methods have been investigated i.e. sand blasting and treating the surface with a needle gun. Once again, apart from the efficiency of the repair, health monitoring and non-destructive evaluation methods were employed. Additionally, the effect of different aging scenarios has been investigated. Results indicated that grit blasting led to better adhesion between the metallic and the composite substrates significantly extending the fatigue life of the specimens. The needle gun treatment on the other hand was able to extend the fatigue life in most cases but to a smaller extent.

Numerical Simulations Employing a Three Compartment Model

Additionally, a methodology for the assessment of cracked structural elements in marine structures has been proposed. This methodology is based on the implementation of the common structural rules for oil tankers with the use of user subroutines and finite element modelling. Numerical investigations on the ability of the patch repair to reduce the stress intensity factor of cracks in the structure have been performed.

Parametric Investigation for the Design of Composite Patches and Design Methodology

At the end of this work, emphasis is given in the use of linear fracture mechanics in bimaterial interfaces to address the integrity of the repair. By expanding the already existing work on the field an analytical parametric study has been performed to quantify how key parameters affect the adhesive bond between the patch and the steel substrate. Following the parametric study and based on the major findings and knowledge gained throughout this dissertation a simple, time effective design evaluation procedure for this kind of repairs is proposed.

2. Introduction to Bimaterial Linear Elastic Fracture Mechanics

2.1 Introduction

The conventional design criteria are predominantly based on tensile strength, yield strength and buckling loads stemming from the widely known continuum mechanics approach. These criteria are adequate for many engineering structures but despite their usefulness, they are insufficient to interpret the creation and propagation of cracks in structures, hence a different approach should be sought. The field of mechanics concerned with the study of cracks in materials is called fracture mechanics.

The problem of fracture has been concerning mankind since ancient times but it wasn't until the 1920s by the work of Griffith (1921) that a systematic scientific approach was implemented to study the problem. Griffith applied the first law of thermodynamics to the formation of a crack. Namely, a crack can be formed (or an existing crack can grow) only if such a process causes the total energy to decrease or remain constant. Thus the critical conditions for fracture can be defined as the point where crack growth occurs under equilibrium conditions, with no net change in total energy. This approach was able to predict accurately the behaviour of brittle materials that obey Hooke's law, such as glass, but failed to do the same for ductile materials where significant plastic deformation precedes failure. This was later made possible from the expansion of the original Linear Elastic Fracture Mechanics to the Elastic Plastic Fracture mechanics through the work of Irwin (1948) who managed to account for the energy dissipated in the material due to plasticity.

In this chapter basic concepts associated with the analysis and modelling of cracks in bimaterial interfaces that befall the Linear Elastic Fracture Mechanics theory are presented, as several of these have been employed throughout this dissertation.

2.2 Linear elastic fracture mechanics

According to Griffith's theory, a flaw becomes unstable, and thus fracture occurs, when the strain energy change that results from an increment of crack growth is sufficient to overcome the surface energy of the material. Irwin extended this concept and proposed that the energy release rate, G , or the Griffith energy can be expressed as a measure of available energy for crack growth as expressed in Equation 2.1.

$$G = \frac{-d\Pi}{dA} \quad (2.1)$$

where Π denotes the potential energy and dA is the incremental area. When the potential energy becomes equal to the energy required for the creation of new surfaces (W_s), Equation 2.1 expresses the critical energy release rate G_c or Fracture Toughness (Equation 2.2). The energy release rate G is the driving force for fracture, while G_c is the material's resistance to fracture

$$G_c = \frac{-dW_s}{dA} \quad (2.2)$$

For certain cracked configurations subjected to external forces, it is possible to derive closed-form expressions for the stresses in the body, assuming isotropic linear elastic material behaviour. There are three types of loading that a crack can experience (Figure 2.1), namely: Mode I loading, where the principal load is applied normal to the crack plane, opening the crack. Mode II corresponds to in-plane shear loading and tends to slide one crack face with respect to the other. Mode III refers to out-of-plane shear and is not present in 2D analyses. A cracked body can be loaded in any one of these modes, or in a combination of two or three modes.

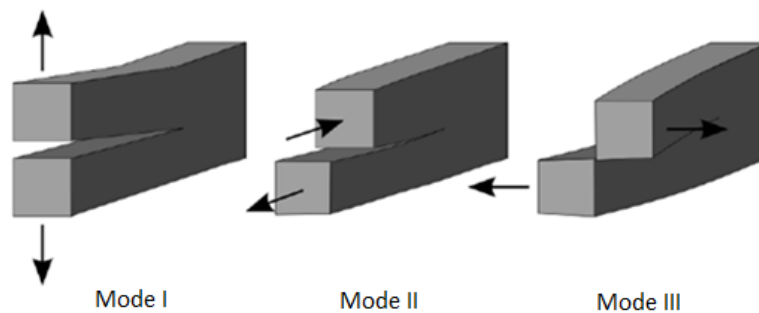


Figure 2.1: Loading modes.

Irwin was also among the first to derive the singular stress field close to a sharp crack tip in 2D problems for a homogeneous isotropic elastic solid. For a polar coordinate axis with the origin at the crack tip, it can be proven that the stress field in any linear elastic cracked body is given by:

$$\sigma_{ij} = \left(\frac{k}{\sqrt{r}}\right) f_{ij}(\theta) + \sum_{m=0}^{\infty} A_m r^{\frac{m}{2}} g_{ij}^{(m)}(\theta) \quad (2.3)$$

where σ_{ij} is the stress tensor, k is a constant and f_{ij} is a dimensional function of θ (see Figure 2.2).

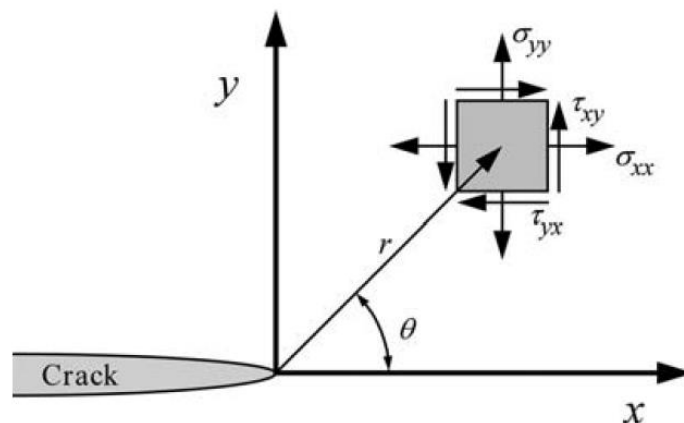


Figure 2.2: Stress field near a crack.

The higher order terms depend on geometry and A_m is the amplitude and $g_{ij}^{(m)}(\theta)$ is a dimensional function of θ for the m th term. In a mixed-mode problem (i.e., when more than one loading mode is present), the individual contributions to a given stress component are additive according to the principle of superposition. The stress intensity factor is equal to the constant k multiplied by $\sqrt{2\pi}$ and is different for each loading mode. The relation between the stress amplitudes and the stress intensity factors for pure mode I ($\sigma_{xy} = 0$) and pure mode II ($\sigma_{yy} = 0$) respectively are listed in Equation 2.4:

$$\sigma_{yy} = \frac{K_I}{\sqrt{2\pi r}}, \quad \sigma_{xy} = \frac{K_{II}}{\sqrt{2\pi r}} \text{ for } \theta = 0 \quad (2.4)$$

The relationship connecting the stress intensity factors to the Griffith-energy is given in Equation 2.5

$$G = \frac{K_I^2 + K_{II}^2}{\bar{E}} \quad (2.5)$$

where \bar{E} is the efficient Young's modulus for plane stress and plane strain conditions defined as $\bar{E} = E$ for plane stress and $\bar{E} = \frac{E}{1-\nu^2}$ for plane strain with E being the Young's modulus of elasticity of the material. The displacement field can be derived in a way similar to the stress field to describe the relative crack opening δ_2 and shearing δ_1 at a given distance behind the crack tip (Equation 2.6).

$$\delta_2 = \frac{8K_I}{\bar{E}} \sqrt{\frac{r}{2\pi}} \quad \text{and} \quad \delta_1 = \frac{8K_{II}}{\bar{E}} \sqrt{\frac{r}{2\pi}} \quad (2.6)$$

2.3 J integral

The J-integral is a path-independent integral for the analysis of cracks developed by *Rice (1968)*. The values of the J-integral denoted as J are the energy release rate around a crack and are equal to the Griffith-energy when the Linear Elastic Fracture Mechanics approach is valid for the given problem (Equation 2.7).

$$J = G = \frac{K_I^2 + K_{II}^2}{\bar{E}} \quad (2.7)$$

The J-integral, for an arbitrary counter clockwise path (Γ) around the crack tip is given by Equation 2.8. A schematic of the J-integral is depicted in Figure 2.3

$$J = \int_{\Gamma} \left(w dy - T_i \frac{\partial u_i}{\partial x} ds \right) \quad (2.8)$$

where:

w = strain energy density

T_i = components of the traction vector

u_i = displacement vector components

ds = length increment along the considered contour Γ

The strain energy density is given by Equation 2.9

$$w = \int_0^{\varepsilon_{ij}} \sigma_{ij} d\varepsilon_{ij} \quad (2.9)$$

and the tractions are defined by Equation 2.10

$$T_i = \sigma_{ij}n_j \quad (2.10)$$

where n_j is normal to the Γ contour around the crack tip.

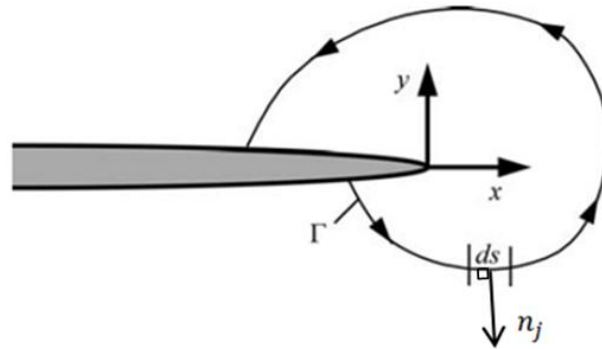


Figure 2.3: J-Integral schematic.

2.4 Bimaterial fracture mechanics

So far, basic concepts associated with Linear Elastic Fracture Mechanics have been described for homogeneous isotropic materials. In this section the expanded theory addressing inhomogeneous materials such as bimetals is described. One important difference between homogeneous and inhomogeneous media should be outlined before proceeding. In the case of homogeneous materials, a crack will predominantly advance under mode I conditions and, even under mixed mode loadings, the crack will try to kink in a path where pure mode I loading exists. This is not the case in interfacial cracks advancing between two dissimilar materials. A crack in a bimaterial interface is restricted to propagating directly or along the interface. In this way it is forced to propagate in different mode mixities and not only under mode I. Consequently, the fracture toughness depends on the mode mixity and different values of fracture toughness are obtained with varying mode mixity. This is attributed to the contribution of mechanisms such as asperity contact which increases with increasing mode mixity. Additionally a high mode mixity tends to make the crack kink away in a microscopic scale which in turn increases the asperity and therefore increases the fracture toughness of the interface. This behaviour makes necessary the fracture toughness characterization for the full range of mode mixities in bimaterial interphase problems.

Among the most important publications in bimaterial fracture mechanics are the ones from Hutchinson and Suo who were the first to establish a firm foundation for the analytical description of bimaterial fracture mechanics by studying debonding of thin films. Nevertheless, the principle described in their work can be applied in different bimaterial problems and is not constrained to that particular application. *Suo and Hutchinson (1988)* analysed interface cracks between dissimilar isotropic linear elastic materials when subjected to bending moments and axial loads using the superposition principle. *Suo (1990)* presented a more general approach studying cracks between dissimilar anisotropic media. A recent study that is worth mentioning is that of *Harvey and Wang (2012)* who presented analytical theories for the mixed mode partitioning of one dimensional delaminations in composite materials, taking into account bending moments, axial forces and shear forces.

The Lekhnitskii-Eshelby-Stroh (LES) formulation (*Lekhnitskii 1963, Eshelby et al 1953 and Stroh 1958*) can be specialized to describe only the opening δ_y and shearing δ_x relative displacements of the crack flanks (Equation 2.11 and Figure 2.4) and in the same manner the σ_{yy} normal and σ_{xy} shear stress in front of the crack tip (Equation 2.12), as follows:

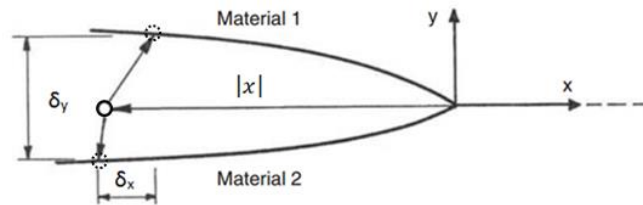


Figure 2.4: Relative displacement at the crack flanks.

$$\sqrt{\frac{H_{11}}{H_{22}}} \delta_y + i\delta_x = \frac{2H_{11}(K_1 + iK_2)|x|^{\frac{1}{2}+i\varepsilon}}{\sqrt{2\pi}(1 + 2i\varepsilon)\cosh\pi\varepsilon} \quad (2.11)$$

$$\sqrt{\frac{H_{22}}{H_{11}}} \sigma_{yy} + i\sigma_{xy} = \frac{K|x|^{i\varepsilon}}{\sqrt{2\pi x}} \quad (2.12)$$

Where H_{11} and H_{22} are material dependent constants, and ε is the oscillatory index defined below. The mathematical expressions of these two parameters are given in Equations 2.15 and 2.16.

$$\lambda = \frac{S_{11}}{S_{22}} \quad (2.13)$$

$$n = \sqrt{\frac{1}{2}(1 + \rho)}, \text{ where } \rho = \frac{2S_{12} + S_{66}}{2\sqrt{S_{11}S_{22}}} \quad (2.14)$$

$$H_{11} = [2n\lambda^{1/4}\sqrt{S_{11}S_{22}}]_1 + [2n\lambda^{1/4}\sqrt{S_{11}S_{22}}]_2 \quad (2.15)$$

$$H_{22} = [2n\lambda^{-1/4}\sqrt{S_{11}S_{22}}]_1 + [2n\lambda^{-1/4}\sqrt{S_{11}S_{22}}]_2 \quad (2.16)$$

The subscripts 1 and 2 of the brackets refer to material 1 and material 2 respectively. S_{11} and S_{22} are components of the compliance matrix and n and λ are non-dimensional orthotropic constants (Equations 2.13 and 2.14). The compliance components differ between plane stress and plane strain conditions, and for plane stress are (Equation 2.17):

$$S_{11} = \frac{1}{E_1}, \quad S_{12} = S_{21} = -\frac{\nu_{12}}{E_1}, \quad S_{22} = \frac{1}{E_2}, \quad S_{13} = S_{31} = -\frac{\nu_{13}}{E_3} \quad \text{and} \quad S_{33} = \frac{1}{G_{12}} \quad (2.17)$$

These can be transformed to plane strain by Equation 2.18:

$$S_{ij}^* = S_{ij} - \frac{S_{i3}S_{j3}}{S_{33}} \quad (2.18)$$

The oscillatory index ε mentioned in Equations 2.11 and 2.12 is given by Equation 2.19:

$$\varepsilon = \frac{1}{2\pi} \ln \left(\frac{1 - \beta}{1 + \beta} \right) \quad (2.19)$$

The term β used for the calculation of the oscillatory index is the second Dundurs parameter for bimetals. *Dundurs (1970)* observed that the elastic moduli dependence of a bimaterial system may be expressed in terms of two parameters α and β . At this point it must be noted that the expressions of the Dundurs parameter are different for an isotropic bimaterial than for an orthotropic one. In the latter these are referred to as the generalized Dundurs parameters and are expressed by Equation 2.20 and Equation 2.21. When both substrates are isotropic the generalized expression of these parameters reduce to their isotropic form

$$a = \frac{[\sqrt{(S_{11}S_{22})_2}/\sqrt{(S_{11}S_{22})_1} - 1]}{[\sqrt{(S_{11}S_{22})_2}/\sqrt{(S_{11}S_{22})_1} + 1]} \quad (2.20)$$

$$\beta = \frac{[S_{12} + \sqrt{S_{11}S_{22}}]_2 - [S_{12} + \sqrt{S_{11}S_{22}}]_1}{\sqrt{H_{11}H_{22}}} \quad (2.21)$$

The first Dundurs parameter measures the mismatch in the plane tensile modulus across the interface. The physical interpretation of the second Dundurs parameter is more complicated compared to the first one, representing a measure of the mismatch in the in-plane bulk modulus. Both parameters vanish when there is no mismatch, and both change signs when the same materials are used but are assigned to the opposite designation. The complex stress intensity factor K in Equation 2.12 is defined as:

$$K = K_1 + iK_2 \quad (2.22)$$

It should be noted at this point that Equations 2.11 and 2.12 are similar to 2.4 and 2.6 defined for homogeneous materials, however the stress intensity factors K_1 and K_2 , unlike the isotropic case, do not represent individual stress amplitudes for mode I and II. This is due to the contribution of the term $|x|^{i\varepsilon}$ which leads to the mix-up of the traditional stress intensity factors (Equation 2.23). As a result of this mix-up, an opening of the crack flanks does not necessarily mean that $K_2 = 0$, but rather that mixed mode condition is present with both K_1 and K_2 having values different from zero.

$$K|x|^{i\varepsilon} = [K_1 \cos(\varepsilon \ln x) - K_2 \cos(\varepsilon \ln x)] + i[K_1 \cos(\varepsilon \ln x) + K_2 \cos(\varepsilon \ln x)] \quad (2.23)$$

The complex intensity factor (Equation 2.21) can be related to the strain energy release rate as (Suo 1990) (Equation 2.24)

$$G = \frac{H_{11}|K|^2}{4 \cosh^2(\pi\varepsilon)} \quad (2.24)$$

Similarly, the strain energy release rate can be expressed in terms of the opening and relative sliding displacements of the crack flanks (Hutchinson et al 1992) as illustrated in Equation 2.25:

$$G = \frac{\pi(1 + 4\varepsilon^2)}{8H_{11}|x|} \left(\frac{H_{11}}{H_{22}} \delta_y^2 + \delta_x^2 \right) \quad (2.25)$$

A way to quantify the mode mixity is by calculating the phase angle; however, there are different definitions of the phase angle depending on the bimaterial system and on the assumptions made by the analyst. The most commonly employed are concentrated in this section. In the case of homogeneous materials the mode mixity is defined based on the stress intensity factors (Equation 2.26)

$$\psi = \arctan \left(\frac{K_{II}}{K_I} \right) \quad (2.26)$$

which, for that particular case, is equivalent to Equation 2.27

$$\psi = \arctan \left(\frac{\delta_x}{\delta_y} \right) \quad (2.27)$$

However in bimaterial fracture mechanics the stress intensity factors do not correspond to pure modes I and II. Therefore Hutchinson and Suo (1990) defined the mode mixity using the expression of Equation 2.28:

$$\psi = \arctan \left[\frac{\text{Im}(Kh^{i\varepsilon})}{\text{Re}(Kh^{i\varepsilon})} \right] \quad (2.28)$$

where h is the characteristic length of the problem. This parameter has no physical meaning and its value is chosen so as the mode mixity $\psi = 0$ corresponds to the minimum value of the Griffith energy, and different

values of this parameter lead to a phase shift. Alternatively to Equation 2.28, the mode mixity can be expressed as a function of the crack flank displacements δ_y and δ_x as follows. This is referred to as the full formulation (Equation 2.29):

$$\psi_{full} = \arctan\left(\sqrt{\frac{H_{22}}{H_{11}}}\frac{\delta_x}{\delta_y}\right) - \varepsilon \ln\left(\frac{|x|}{h}\right) + \arctan(2\varepsilon) \quad (2.29)$$

The phase angle formula can be simplified by setting the oscillatory index $\varepsilon = 0$. In this way, the following reduced form can be assumed (Equation 2.30), which is more practical:

$$\psi_{reduced} = \arctan\left(\sqrt{\frac{H_{22}}{H_{11}}}\frac{\delta_x}{\delta_y}\right) \quad (2.30)$$

The reduced formulation can be rewritten using the Griffith energy mode I and II as shown in Equation 2.31

$$\psi_{reduced} = \arctan\left(\sqrt{\frac{G_2}{G_1}}\right) \quad (2.31)$$

It is obvious that for the same energy release rate, different values of mode mixity can be obtained depending on the selected definition. The difference between the full formulation and the reduced one is in effect a phase shift caused by the presence of the two additional terms that are dependent on the oscillatory index in the full formulation expression. This phase shift makes the interpretation of the phase angle somewhat non intuitive as the physical meaning granted by the first term of Equation 2.29 is obscured by the phase shift. Therefore the reduced formulation is more appealing as it captures better the physics of the problem denoting the ratio of mode II energy release rate to mode I. Interpreting Equation 2.31, it follows that a phase angle of 0° denotes a pure mode I condition and a phase angle of 90° a pure mode II. In the case when the energy release rates for both modes are equal, the phase angle is equal to 45° . Bearing these observation is mind, cases where the phase angle is between 0° and 45° are referred to as mode I dominant as the energy release rate due to mode I loading is greater to the energy release rate caused by mode II loading. Inversely, cases with phase angle values between 45° and 90° are referred to as mode II dominant, meaning that the mode II loading contribution in the total energy release rate is greater than the one due to mode I loading. From the defined mode mixities, the full and reduced formulations have been used throughout this thesis.

2.5 Cohesive zone modelling

Introduction

An advanced modelling technique to simulate the evolution of damage between adhesively bonded

interfaces is cohesive zone modelling which befalls the field of damage mechanics. Damage mechanics permits the simulation of the initiation, progressive damage and fracture at a predefined crack path constituting it ideal for the analysis and simulation of damage in bimaterial interfaces where the crack path is already known. This field is still under intense development regarding more accurate and robust modelling techniques, different models to cover the range of different available adhesive systems and their behaviour, and also to eliminate existing convergence issues. Another advantage of this modelling approach is that it is heavily implemented in commercial finite element software and has become the most widespread method of predicting damage. Additionally cohesive zone modelling can be implemented to model both brittle and ductile behaviour making it an invaluable tool for the latter where Linear Elastic Fracture Mechanics is no longer valid and the elastic plastic fracture mechanics is cumbersome to implement analytically.

The cohesive zone modelling technique consists of establishing traction-separation laws to model the interface behaviour. These laws are established between paired nodes of cohesive elements and can be used to connect superimposed nodes of elements representing the different substrates, simulating a zero thickness interface which is referred to as the local approach, or they can be applied in non-contacting mediums simulating the entire adhesive bond which is referred to as the continuum approach (*Yang et al., 2001, Kafkalidis and Thouless, 2002*).

The use of cohesive zone models (CZM's) coupled to conventional FE analyses is the most widespread method of predicting static or fatigue damage uptake in structures (*Tvergaard and Hutchinson, 1992; Tvergaard and Hutchinson, 1993; Yang et al., 1999; Yang et al., 2000; Yang and Thouless, 2001; Campilho et al., 2005; Campilho et al., 2007*).

Cohesive Laws

The cohesive law, or traction-separation law, relates the tractions σ acting on the two planes of the cohesive elements with the corresponding separations δ for each loading mode; meaning, that the local normal stress σ_I and local shear stresses σ_{II} are associated with the normal crack opening δ_I and with the tangential sliding δ_{II} as follows:

$$\sigma_I = \sigma_I(\delta_I, \delta_{II}) \quad \text{and} \quad \sigma_{II} = \sigma_{II}(\delta_I, \delta_{II}) \quad (2.32)$$

The traction separation law for each mode is defined employing specific experimental procedures. Through these experiments the critical energy release rate can be calculated under pure or mixed mode loadings. By differentiating the critical energy release rate by the normal opening for mode I and by tangential opening for mode II at the precrack tip, the respective pure mode laws are defined. Inversely, this means that the area enclosed by the traction separation law should be equal to the critical energy release rate measured.

In the case of pure mode loading there is no interaction between the cohesive laws, meaning that the normal cohesive stresses depend solely on the normal opening displacement for the case of pure mode I and the shear cohesive stresses depend on the tangential crack opening in the case of mode II loading. The cohesive laws for pure mode I and pure mode II is also what constitutes the required input in most finite

element software. For the mixed mode, the two pure modes are coupled through a failure criterion that gives the critical combination of opening and shear displacements at which the tractions in both modes fail simultaneously. The variation of the fracture energy from mode I fracture to mode II fracture has been demonstrated through mixed-mode fracture specimen (*Banks-Sills and Bortman, 1986*) and delamination testing (*Reeder and Crews, 1990; Benzeggagh and Kenane, 1996*). The most commonly employed mode mixity law is the power law (*Wu and Reuter 1965*) illustrated in Equation (2.33) with superscript values $a_m = a_n = 1$ (linear) and $a_m = a_n = 2$ (quadratic)

$$\frac{G_{equiv}}{G_{equivc}} = \left(\frac{G_I}{G_{IC}}\right)^{a_m} + \left(\frac{G_{II}}{G_{IIC}}\right)^{a_n} \quad (2.33)$$

Different shapes of traction separation laws exist to better render the behaviour of different systems. In general, a cohesive law is described by two parts, a traction strengthening part and a traction softening one following the latter. The most commonly used are of the following shapes: bilinear, exponential and trapezoidal. However it must be pointed out that the shape of the traction separation law does not significantly affect the results of the analysis (*Alfano 2006*). The bilinear law is depicted in Figure 2.5 and its analytical expression is presented in Equation 2.34:

$$\sigma = \begin{cases} K_0 \delta & \text{if } \delta \leq \alpha_0 \\ \frac{\alpha_1 - \delta}{\alpha_1 - \alpha_0} \sigma_0 & \text{if } \alpha_0 \leq \delta \leq \alpha_1 \\ 0 & \text{if } \delta \geq \alpha_1 \end{cases} \quad (2.34)$$

where α_0 and α_1 are given by Equation 2.35

$$a_0 = \frac{\sigma_0}{K_0} \quad , \quad a_1 = \frac{2G_c}{\sigma_0} \quad (2.35)$$

G_c represents the fracture energy dissipated during the complete debonding process and is equal to the area enclosed by the $\sigma - \delta$ curve and K_0 is the initial penalty stiffness.

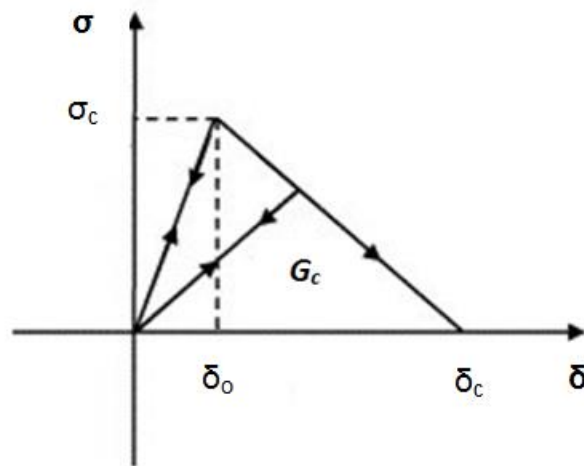


Figure 2.5: The bilinear traction separation law.

Regarding the traction strengthening part, two different approaches exist i.e. the intrinsic and the extrinsic approach, (*Kubair and Geubelle, 2003*). In the intrinsic approach the slope of the initial strengthening part, increases denoting an increasing resistance as the cohesive surfaces move relative to each other. At a given separation δ_o the maximum cohesive traction σ_c is reached. After that point the traction softening starts and tractions reduce following a linear, exponential, or polynomial fashion depending on the shape of the softening law, until the critical separation value δ_c , where the tractions have reached zero which leads to the tractionless separation of the cohesive surfaces simulating in that way a physical crack. Needleman (*1987*) was the first to introduce the intrinsic approach within the context of finite element methods by using a polynomial form for the traction–separation law in the modelling of void nucleation associated with particle debonding.

The extrinsic approach assumes that there is no strengthening part and that the cohesive law consists solely of the traction softening part. Nevertheless, due to numerical purposes a very steep initial strengthening part is included and as it represents a minor fraction of the area under the traction separation law, the represented critical energy release rate is not affected. The most commonly used extrinsic laws are the triangular, linear-parabolic and exponential (*Alfano and Crisfield, 2001*), linear-parabolic (*Allix and Corigliano, 1996*), polynomial (*Chen, 2002*) and exponential (*Chandra et al., 2002*). The CZM has been extensively used for the simulation of adhesively bonded structures. (*Chai, 1988; 1995; Ikeda et al., 2000; Yan et al., 2001; Lee et al., 2004; Pardoen et al., 2005*).

Depending on the adhesive bond under study, the analyst has to consider which approach is the most suitable one to represent the physical problem. In the case of co-cured bonding, the extrinsic local approach is favored, as there is no distinct adhesive layer joining the different substrates.

2.6 Experimental procedures for the measuring of the critical energy release rate in bimaternal

For the implementation of Linear Elastic Fracture Mechanics and cohesive zone modelling experimental testing is required in order to measure the fracture toughness of the bimaterial system. As mentioned earlier,

a crack in a bimaterial interface is restricted to propagating directly or along the interface. In this way it is forced to propagate in different mode mixities and not only under mode I.

Having identified this behaviour, special attention has been paid to develop sound experimental and data reduction techniques for the correct measurement of the fracture toughness of bimetals under different mode mixities using precracked specimens. These have been developed predominantly for the study of delamination in laminates and sandwich structures, where delaminations and debonding between the face skin and the core are prevalent. A few corresponding data reduction techniques are currently available (e.g. the property determination technique, the direct method and the inverse method) that enclose varying degrees of complexity and expected accuracy of the results. Some of the more widely used debonds test specimens include the Double Cantilever Beam (DCB) for measuring mode I, the End Notch Flexure (ENF) for measuring mode II and the Mixed Mode Bending (MMB) tests for measuring different mode mixities. The Mixed Mode Bending tests (Figure 2.6) can be considered as a superposition of the DCB and ENF tests and with a suitable loading lever length, different mode mixity ratios can be achieved.

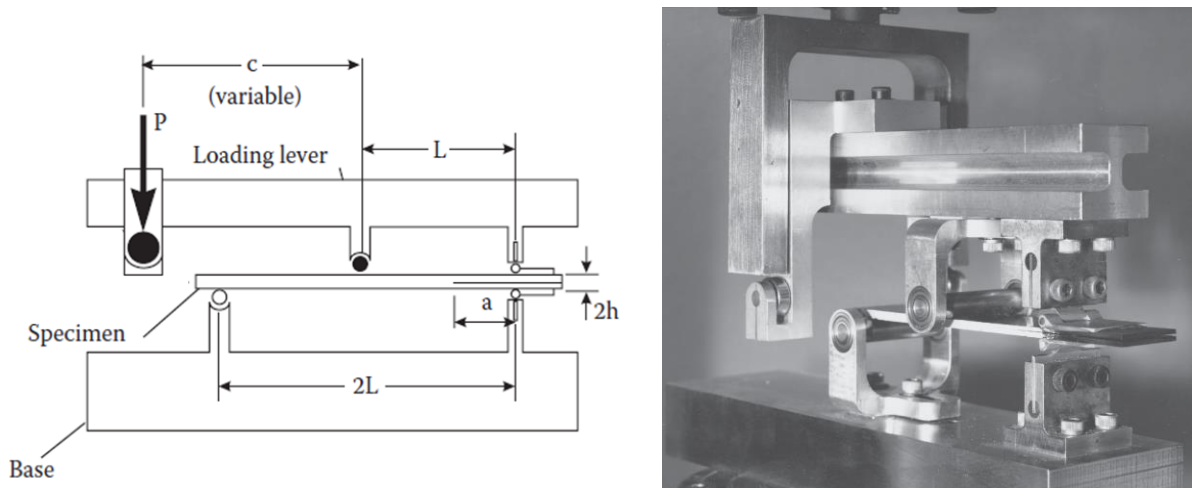


Figure 2.6: MMB geometry parameters and test setup (Carlsson 2014).

However, few data and methods seem to exist for characterizing bonds between dissimilar materials. *Lee et al (2010)* performed Single Leg Bending tests on co-cured specimens under mode I and mode II dominant modes (Figure 2.7) and subsequently extracted the pure mode I and mode II fracture toughness with the use of numerical simulations. The materials used were unidirectional carbon fibres on steel which had been treated with emery cloth before bonding. The values obtained were 140 J/m^2 for pure mode I and 280 J/m^2 for pure mode II. *Andersen and Echtermeyer (2005)* performed DCB and ENF tests to characterize the adhesive bonding between grit blasted steel and a carbon epoxy system with a chop strand mat glass layer in the interface (Figure 2.8). The fracture toughness of the composite system for mode II is in good agreement with the values obtained by *Lee* as it was measured equal to 283 J/m^2 with a standard deviation of 96 J/m^2 . The fracture toughness for mode I was measured equal to 593 J/m^2 with a standard deviation of 108 J/m^2 . At this point it must be noted that examination of the surface after testing for these specimens indicated that there was quite a certain degree of matrix microcracking and delamination between the glass

layer and the carbon laminate and that the debonding was not purely an adhesive one as resin remnants were found on the steel surface. And as such the measured fracture toughness is the resulting contribution of different failure mechanisms.

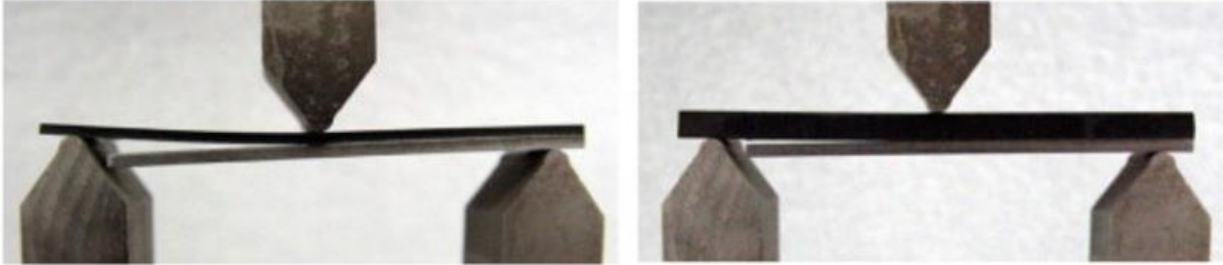


Figure 2.7: Single leg bending tests performed by *Lee et al (2010)*.

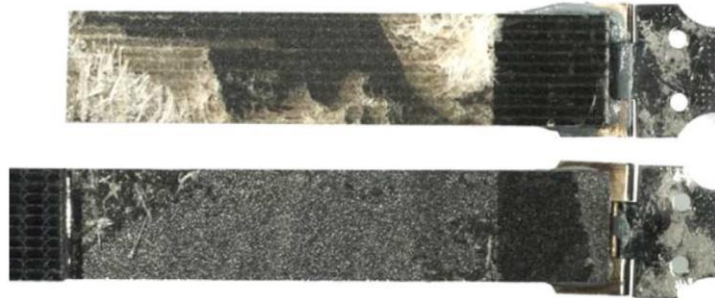


Figure 2.8: Partial adhesive failure of DCB specimens (*Andersen 2005*).

A very promising experimental test is the Double Cantilever Beam with Uneven Bending Moments (DCB-UBM) (*Sørensen et al 2006; Berggreen 2013*). The principle behind this method is to create two different bending moments in the free beams of a DCB-UBM specimen. Two different setups exist, with the main difference being the way the moments are applied to the free beams of the specimen. The first one was developed by Risø national laboratories and employs two different moment arms, one at each side of the specimen. By applying the same loading in these arms, different moment ratios can be achieved (Figure 2.9, left). In the second type, the moment is generated by directly applying rotation with the use of rotational actuators (Figure 2.9, right). In both cases the specimen is restricted from rotation at the uncracked end but can freely move in the longitudinal direction.

The main advantage of the DCB-UBM tests is that the energy release rate can be calculated without the need to measure the crack length during testing, which can be hard to achieve in an accurate way. Moreover, since there are no transverse forces transmitted to the specimen, the friction between the opening faces is reduced. Additionally, the desired mode mixity can be achieved directly from controlling the lever arms or the actuators and therefore, the same specimen can be used for all range of mode mixities.

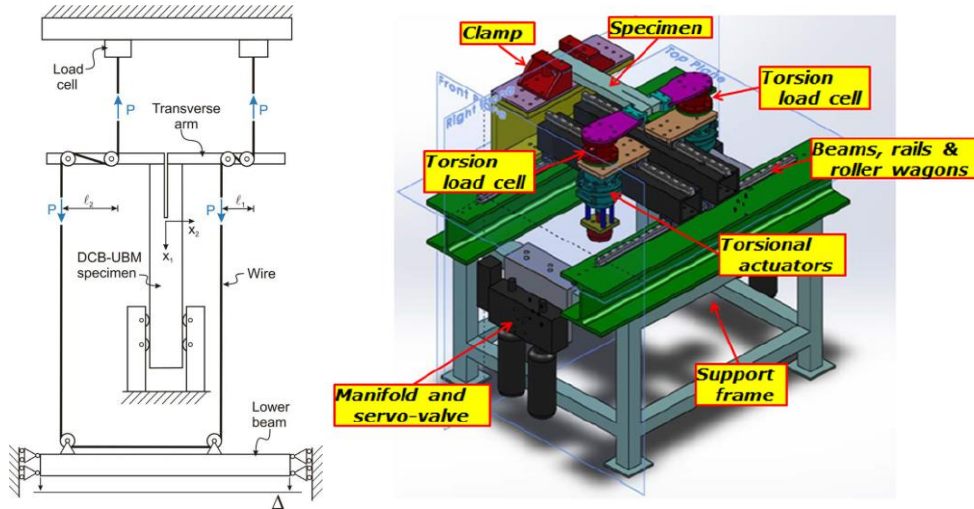


Figure 2.9: DCB-UBM test rigs.

3. Experimental and numerical investigation of patch repaired corroded plates under static loading

3.1 Introduction

The experimental program described in this chapter consists of static testing of plates which have been artificially corroded and subsequently reinforced with a one-sided composite patch. These specimens are referred to as P2 to differentiate them from specimens with different type of defect which are presented subsequently in Chapters 4 and 5 of this dissertation. The main objective is to experimentally prove in a systematic way that the use of a composite patch increases the static strength of a corroded steel structure. Another objective is to provide solid and systematic experimental data, which are used to assess the effectiveness of the repairs. In parallel, the experimental results presented in this report are used to validate the developed finite element models. The tests are categorized in different groups according to the aging scenario. Defected unrepaired plates were also tested to evaluate the effectiveness of the patch.

3.2 General characteristics

Specimen Description

The geometry and main dimensions of the type plates tested are presented in Figure 3.1. The nominal thickness of the steel plates, t_s , is 5 mm. The central orthogonal reference part of the steel specimen has length L_s equal to 400 mm and width W_s equal to 100 mm. A central area on one side of the plate having length 100 mm and width 80 mm has been subjected to artificial corrosion, by partially protecting the plate (using a special nylon sheet and special sealing tape, that can withstand the accelerated corrosion conditions), leaving the 100 x 80 mm area exposed, and subsequently placing the plates in an environmental chamber. The artificial corrosion procedure lasted for 250 cycles (≈ 83 days, see Table 3.1 for the details of each cycle). This time of exposure was deemed adequate for the study of the effects of corrosion and efficient for the time limitations of the project. Corrosion cycles were in accordance with *ISO 14993:2001*. After this procedure the rust was removed and the corroded areas were treated using grit blasting. On top of the corroded area (front side), and after the surface preparation, a central composite patch of thickness t_p , effective length $L_p = 200$ mm and width $W_p = 100$ mm, equal to the specimen's width, was laminated. The total patch length (L_{pt}) is greater, equal to 300 mm, as it additionally includes the tapered edges of the patch.

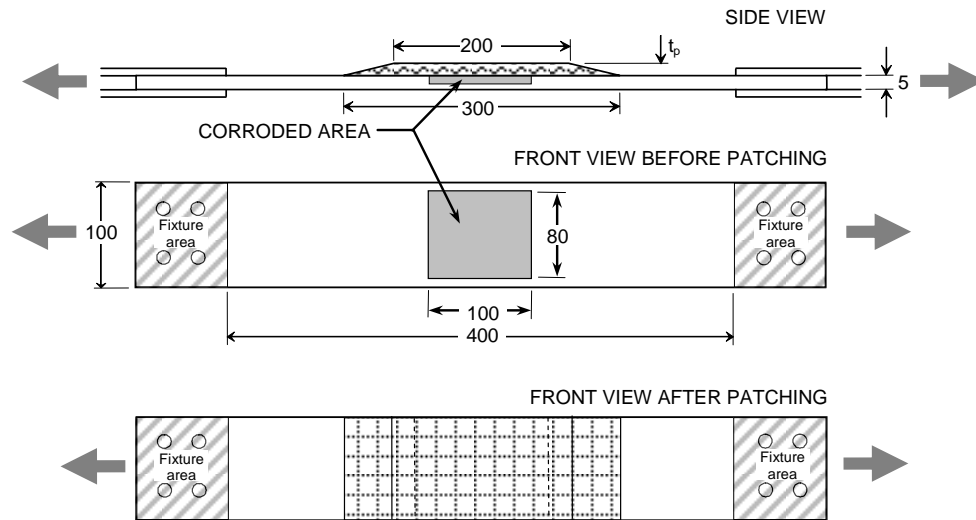


Figure 3.1: P2 plates geometry.

Table 3.1: Conditions of one accelerated corrosion cycle.

1	Salt mist conditions	Duration:	2
	(1) Temperature		35°C ± 2°C
	(2) Salt solution		5% solution NaCl
2	"Dry" conditions	Duration:	4
	(1) Temperature		60°C ± 2°C
	(2) Relative humidity		< 30% RH
3	"Wet" conditions	Duration:	2
	(1) Temperature		50°C ± 2°C
	(2) Relative humidity		> 95% RH

A total of ten (10) specimens were tested in this experimental campaign. Two of them, namely P2A-C and P2A-D were damaged unrepaired specimens. These served as a reference for the investigation of the effectiveness of the repaired cases. The remaining eight specimens were nominally identical from a geometrical and material perspective and were grouped in four pairs denoted as P2D1, P2D2, P2D3 and P2D4.

After the lamination and curing of the patch, specimen groups P2D2, P2D3 and P2D4 were subjected to accelerated aging conditions into an environmental chamber according to *ISO 14993:2001*. The scope was to investigate the effect of the environmental conditions on the integrity of the repair. Sealing tapes were used to protect the edges that were later inserted in the fixtures (Figure 3.2). The specimens subjected to the aging process were exposed for 300 cycles (i.e. 100 days) under cyclic corrosion (including salt mist, dry and wet conditions in different temperatures) and were subsequently tested in tension. This time of exposure was considered satisfactory for the study of the effects of aging, without being overly time demanding.

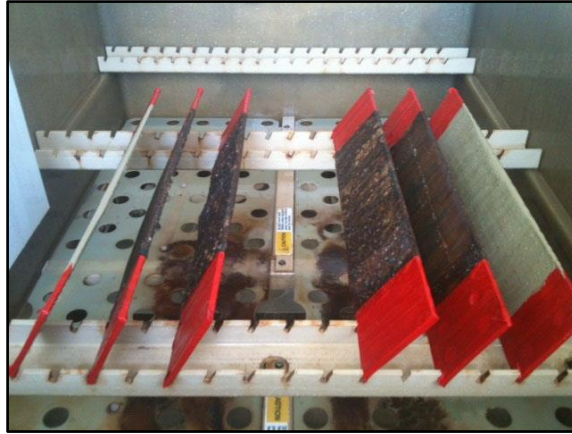


Figure 3.2: Six P2D (2 painted and 4 unpainted) specimens after 75 days in the environmental chamber.

Cyclic aging testing is intended to be an accelerated way to perform salt spray tests than traditional, steady state exposures. Because actual atmospheric exposures usually include both wet and dry conditions, it makes sense to pattern accelerated laboratory tests after these natural cyclic conditions. Research indicates that, with cyclic aging tests, the relative corrosion rates, structure and morphology are more similar to those seen outdoors. Consequently, cyclic tests usually give better correlation to outdoors than conventional salt spray tests. They are effective for evaluating a variety of corrosion mechanisms but there is no direct way to correlate the endured aging cycles with in service conditions.

From the aforementioned groups, specimens P2D3-A and P2D3-B have been painted with typical marine grade paint before being placed into the salt spray chamber. The rationale behind this was to investigate whether the application of a typical marine coating would sufficiently protect the repair from the detrimental environmental conditions. The specimen nomenclature is presented in Table 3.2. Naturally there were some minor variations in the geometry of the specimens from the nominal values presented above. For this reason, the exact geometry of the specimens is presented in Table 3.3 below.

The specimens' width exceeded that of the grips of the testing machine. Therefore, in order to achieve the uniform loading of the specimens along their width, special steel fixtures were designed and manufactured. The specimens were positioned in the fixtures and kept in place with the aid of 16 M16 bolts, through holes specifically opened for this purpose. These friction grip fixtures were designed to accommodate specimens with various thicknesses (from 2 to 20 mm) and widths (from 100 to 300 mm). In order to achieve complete contact between the fixtures and the specimens, steel sheets with various thicknesses (from 1.5 to 5 mm) were used as fillers. The fixture-specimen assembly was subsequently mounted to the testing machine (Figure 3.3).

Table 3.2: Nomenclature of P2 specimens.

Specimen Description	Code	Specimen code	Aging
Unpatched	P2A	P2A-C P2A-D	N/A
	P2D1	P2D1-A P2D1-B	N/A
	P2D2	P2D2-A P2D2-B	Aged 100 days
Patched	P2D3	P2D3-A P2D3-B	Aged-100 days (painted)
	P2D4	P2D4-A P2D4-B	Aged-100 days

Table 3.3: Dimensions of P2 specimens.

Specimen	Dimensions					
	W_s [mm]	L_s [mm]	t_s [mm]	L_{pt} [mm]	L_p [mm]	t_p [mm]
<i>P2A-C</i>	100	400	5.0	- ¹	-	-
<i>P2A-D</i>	100	400	5.0	-	-	-
<i>P2D1-A</i>	100	400	5.3	300	200	3.3
<i>P2D1-B</i>	100	400	5.3	299	198	3.3
<i>P2D2-A</i>	100	400	5.3	-	-	3.3
<i>P2D2-B</i>	100	400	5.2	-	-	3.7
<i>P2D3-A</i>	100	400	5.3	-	-	3.2
<i>P2D3-B</i>	100	400	5.4	-	-	3.3
<i>P2D4-A</i>	100	400	5.2	-	-	3.5
<i>P2D4-B</i>	100	400	5.3	-	-	3.3

¹Not measured.

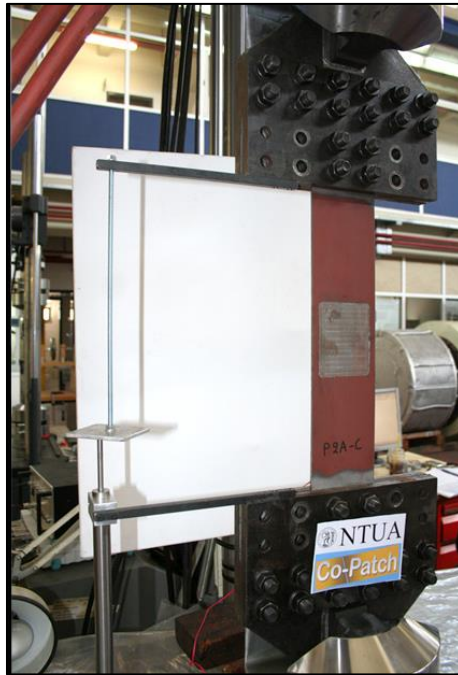


Figure 3.3: Fixture specimen assembly mounted for testing.

Materials and Manufacturing Procedure

The experimentally derived tensile properties of this specific steel were 203 GPa for the Young's modulus and 314.6 MPa for the yield stress. The material characterization tests were performed by UniS (*Zhang and Chryssanthopoulos, 2011*). The composite material system used for the manufacturing of the patches is Carbon/Epoxy using the vacuum infusion method. The mechanical properties of the laminate are listed in Appendix A. The specimens were fabricated in two steps by the Co-Patch project partner AS2CON using CST 200 carbon unidirectional fibres with area density equal to 200 g/m^2 provided by SGL GROUP. The number of layers for each specimen was 16 (made in two stages, 8+8 plies). The resin used was LH 288 Epoxy resin by HAVEL and it was made by mixing Aerosil (hydrophilic Fumed Silica) and micro balloons. A 280 g/m^2 E-glass woven roving, twill weave by AEROGLOSS was used to prevent galvanic corrosion between the carbon fibres and the steel substrate. The epoxy resin hardener was H283 by HAVEL. The mixing ratio of resin and hardener was 100:19. The specimens were produced using the vacuum infusion method. The resin inlet was placed in the middle, and vacuum outlet was placed around the plate as seen in Figure 3.4. . The specimens were produced under the vacuum of -0.75 bar. Prior to infusion, all materials were heated to the production facility room temperature to enhance the curing of the resin, and resin flow. The environmental conditions at the production facility were 35°C and 29% humidity for the first step and 35°C and 34% humidity for the second.

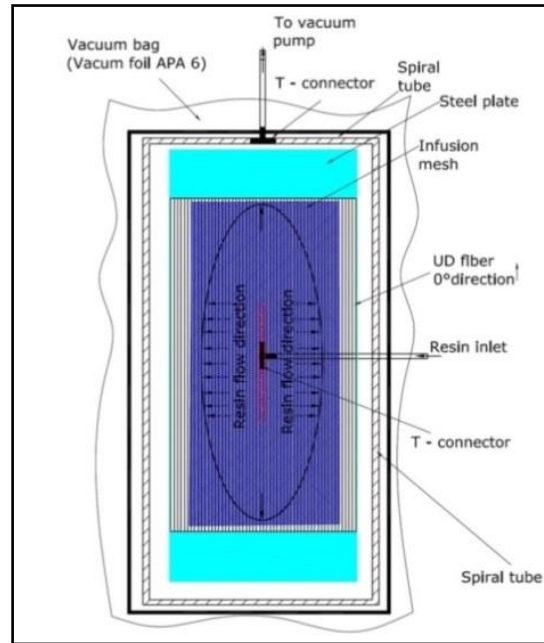


Figure 3.4: Vacuum infusion setup (figure provided by AS2CON).

Prior to the vacuum infusion process, the plates were all grit blasted and laminated immediately with the first E-Glass layer and 8 carbon UD layers. This was done to minimize the exposure of the bare steel to corrosion contamination. In the beginning, the vacuum was tested prior to the infusion process, by opening the vacuum, while the resin inlet was closed. After the successful test, the resin inlet was opened and the infusion started. Resin reached the resin outlet line (spiral tube) and started to fill the resin trap. The resin inlet was then closed and the pump remained operational for several hours. The infusion went without any problems or unexpected events. The same process was used for infusing the last 8 layers on the samples (Figure 3.5).



Figure 3.5: Manufacturing of P2D specimens' patches (figure provided by AS2CON).

Specimen Instrumentation

Strains were recorded during testing with strain gages (SGs) in three locations as shown in Figure 3.6 and Figure 3.7. Strain gages 1 and 2 (SG-1, SG-2) were positioned on the back side of the specimens, 100 mm from the centre of the corroded area of the plates. Strain gages 3 (SG-3) were positioned at the front side and on the centre of the patch for all cases except from the unpatched ones where no SG-3 was attached. Strains were measured with 5 mm gage length SGs.

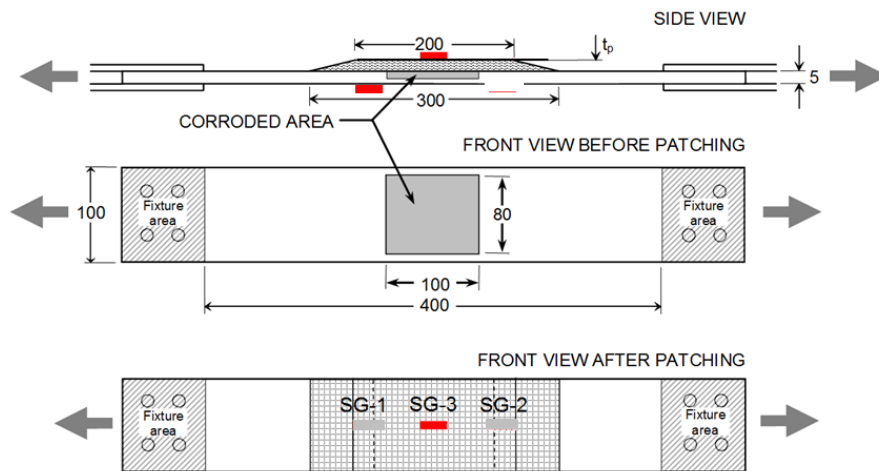


Figure 3.6: Instrumentation of specimens P2D1-A, P2D1-B, P2D3-B.

The instrumentation of specimens P2D1-A, P2D1-B, P2D3-A and P2D3-B is the one described in Figure 3.6. Due to the fact that the unpainted specimens (P2D2-A, P2D2-B, P2D4-A and P2D4-B) had undergone considerable corrosion, it was impossible to place SG's on the metal substrate. Therefore, three SG's were used on the composite patch, in the middle of its width, as shown in Figure 3.7. In order to achieve a better comparison of the results, the same instrumentation was used for the coated specimens (P2D3-A, P2D3-B) as well.

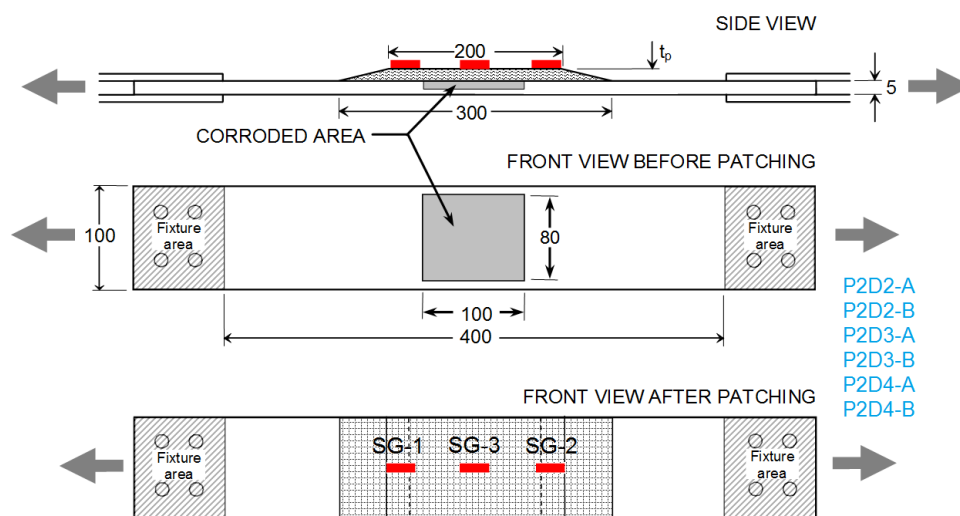


Figure 3.7: Instrumentation of P2D2, P2D3 and P2D4 specimens.

3.3 Experimental testing and results

Reference unpatched specimens (P2A-C and D) were tested to provide a reference for the unrepaired defected case. As it would be overly time consuming to artificially corrode these two specimens in accordance with the procedure described in the beginning of this section, a milling machine was used for the reduction of the plate thicknesses in the specified central area. In this way the desired corrosion thickness reduction was achieved. The thickness diminution was measured as the average of the achieved thickness diminution for the repaired specimens after testing (see Figure 3.8). The average thickness reduction on the central areas of specimens P2A-C and D were 0.3 mm and 0.4 mm, respectively. On specimens P2A-C and D, only one strain gage was used in the position of SG-1, as shown in Figure 3.6.



Figure 3.8: Thickness reduction of the central area of specimens P2A-C and D.

Test Parameters

A MTS hydraulic testing machine with a capacity of 250 kN was used for the tests. A preloading of 25 kN was initially applied to the specimens, in order to minimize the specimen-fixtures assembly tolerances. This preloading was applied as a slow linearly increasing displacement with rate equal to 0.5 mm/min. Then, the specimens were unloaded and afterwards subjected to the final loading in the form of a linearly increasing tensile displacement with the same rate.

The applied force, the total specimen elongation and the longitudinal strains on the specimen were recorded during each test. In order to precisely measure the specimen's elongation, a LVDT transducer was placed alongside the length between the testing machine fixtures (Figure 3.11). For monitoring these parameters, the data acquisition system of the testing machine itself was used, together with an additional external Spider-8 system.

Results

Ten specimens were tested in tension and the results are presented in this section. Out of them, two were

unpatched (namely P2A-C and D), serving as reference specimens, while the rest were reinforced.

The Force – Displacement curves of the reference specimens P2A are presented in Figure 3.9. The reference specimen's response is linear up to approximately 150 kN, followed by yielding in the central plate area as witnessed by the strains response shown in Figure 3.10. The load continued to increase gradually until the end of the tests was decided. The yield load of the reference specimens is listed in Table 3.4 along with the nominal applied stress.

Table 3.4: Results of P2A specimens.

Specimen	Yield Load [kN]	Applied Stress [MPa]
P2A-C	150.8	301.6
P2A-D	151.0	302.0

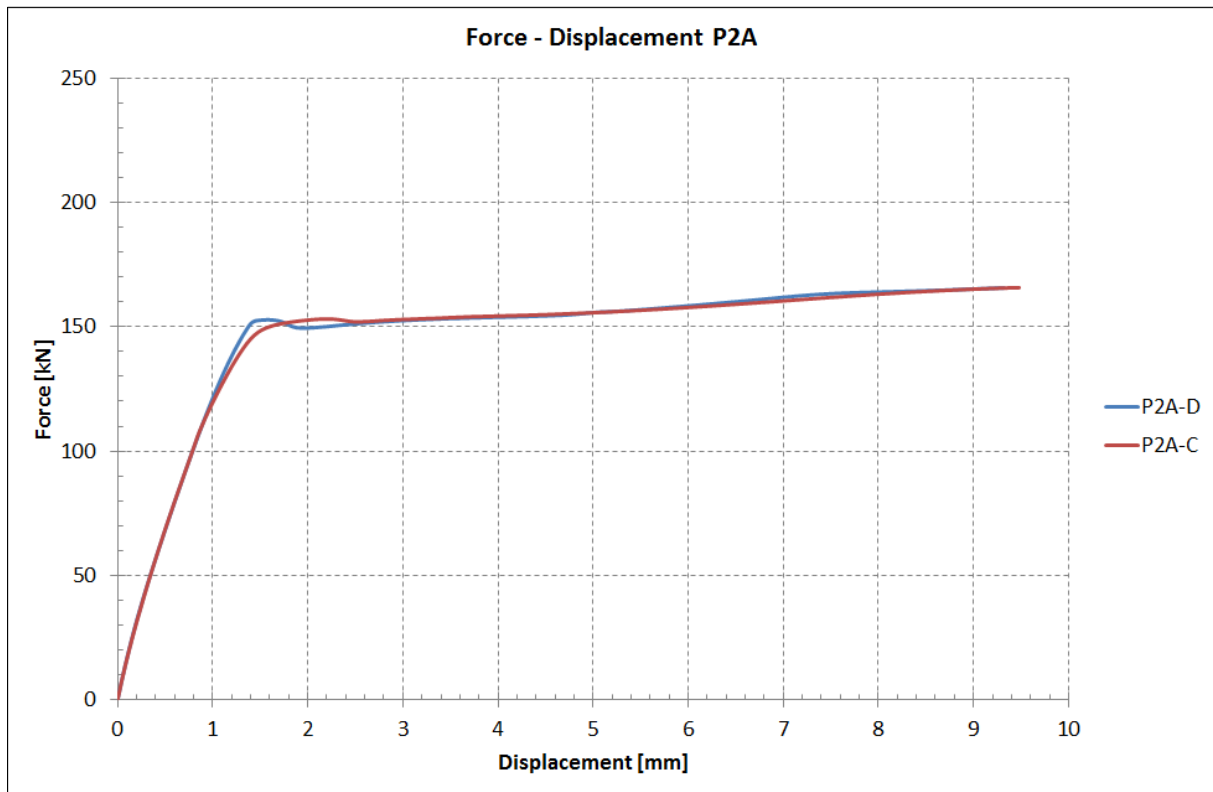


Figure 3.9: Force – Displacement curves of P2A specimens.

The Force – Strain curves of specimens P2A-C and D are presented in Figure 3.10. Strains on the steel (SG-1 position) are increasing linearly until yielding, as expected. The strain measurements exhibit excellent repeatability. Following the testing of the reference specimens, the composite patch repaired specimens were tested (Figure 3.11).

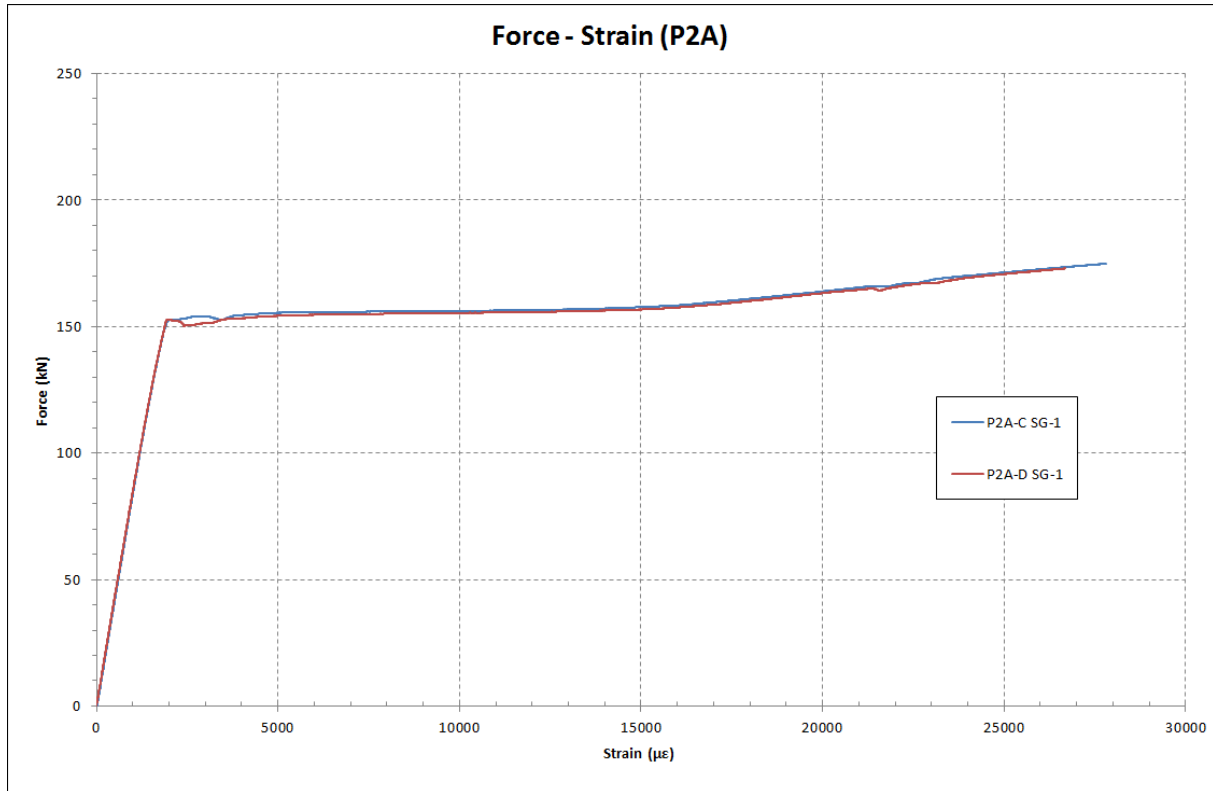


Figure 3.10: Force – Strain curves (SG-1) of P2A-C and D specimens.

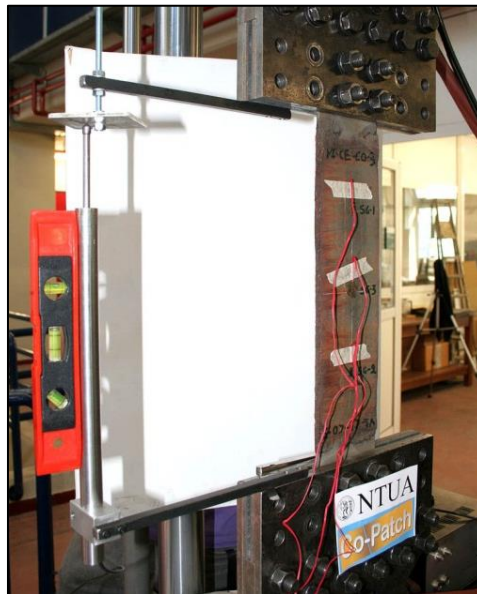


Figure 3.11: Specimen P2D2A being tested on MTS testing machine.

Figure 3.12 depicts the Force–Crosshead displacement curves for the patched and the reference specimens. The majority of the load – displacement curves exhibits a linear response up to approx. 75 kN, followed by a nonlinear behaviour up to the patch debonding load. Exceptions to this behaviour are the P2D1-A, P2D3-A, and P2D1-B specimens, at which yielding occurred at the fixing area at approximately 60 kN. This is attributed to a combination of different factors. In these specimens the diameters of the holes had

to be increased, as the original holes were misaligned and correct positioning of the specimens was not possible. This in turn led to the reduction of the contact area in the grip which allowed slipping of the specimen and ultimately led to the yielding at the holes, as the load was transferred through the bolts in shear and not by friction in the grip area as originally intended. This phenomenon is clearly shown in Figure 3.13, where the ovality of the originally circular holes is evident.

In the same graph it can be observed that there is a deviation of the force - displacement curves between the specimens after 75kN. It was discovered after the end of the experimental campaign that there has been a problem in the LVDT of the MTS testing machine leading to erroneous readings of displacements. Due to this fact, the force - displacement curves have been plotted using the data from the external LVDT transducer used between the grips of the testing machine, which in turn was not able to yield accurate measurements in all occasions.

Regarding the failure mechanisms, in all cases debonding initiated from the edges of the composite patch and gradually progressed to such an extent that the patch did not contribute to the strength of the structure. The first local maximum in the force-crosshead displacement curves was considered as the patch debonding load, as it is at this point that substantial debonding has occurred which significantly affects the load carrying capacity of the specimens. In reality, the patch was still partially bonded to the plate to a certain extent, but it did not contribute to the load bearing capacity of the plate.

In Figure 3.14 to Figure 3.16 indicative Force–Strain curves are depicted along with the revealed interface in the bondline for the cases that underwent aging.

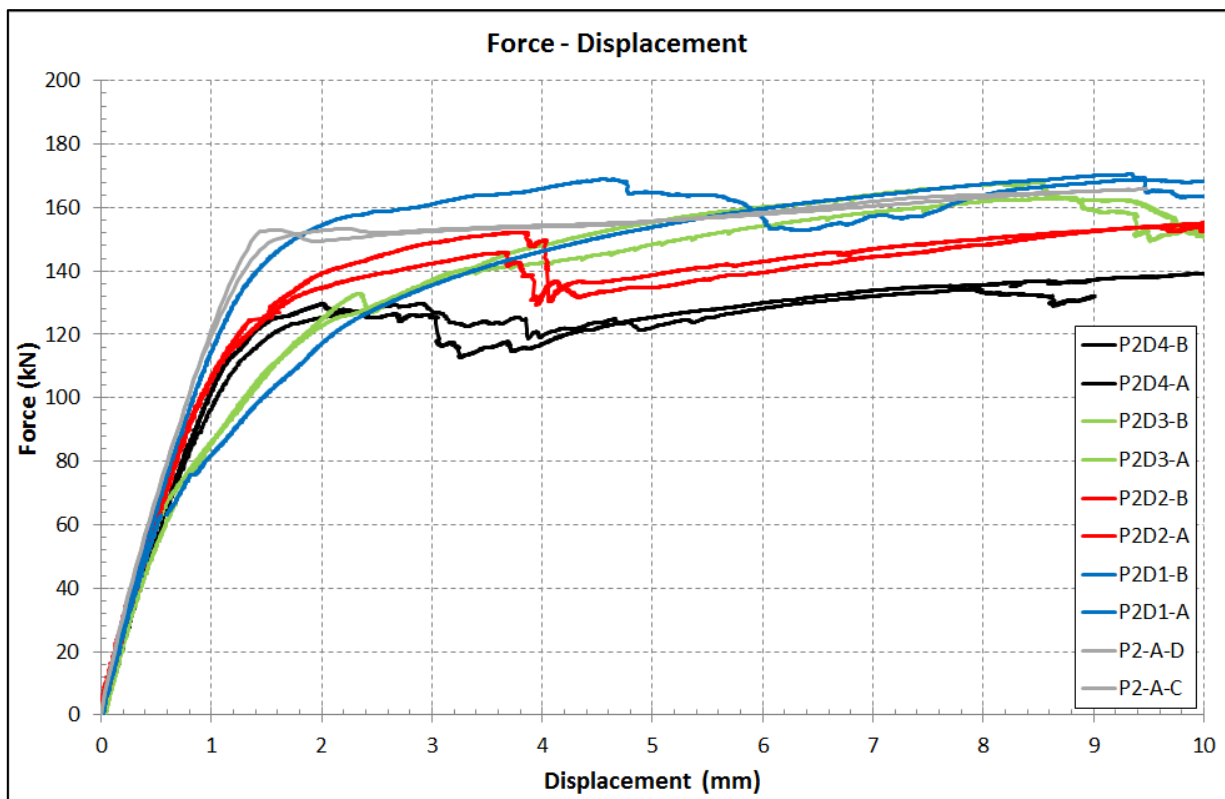


Figure 3.12: Qualitative Force – Displacement curves of P2D and P2-A specimens.

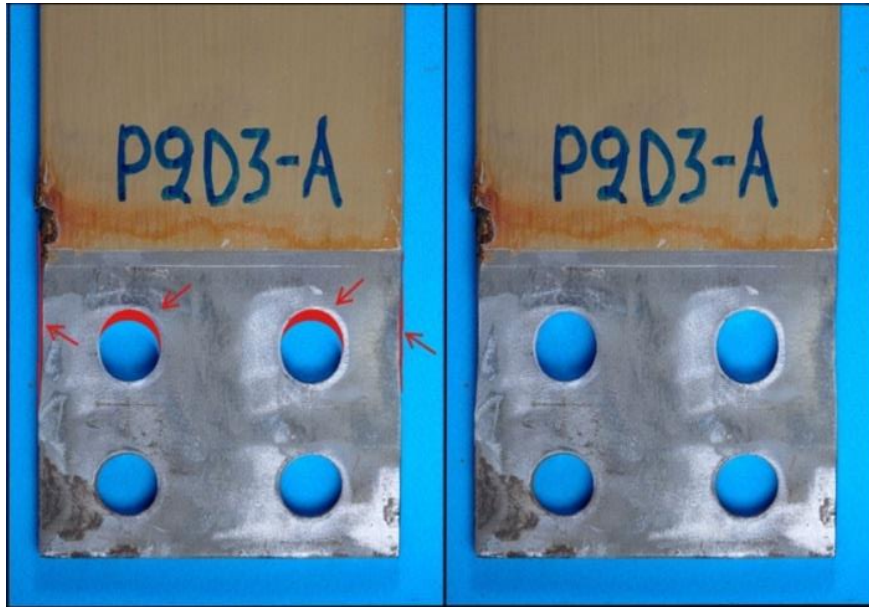


Figure 3.13: Yielding around the holes during testing.

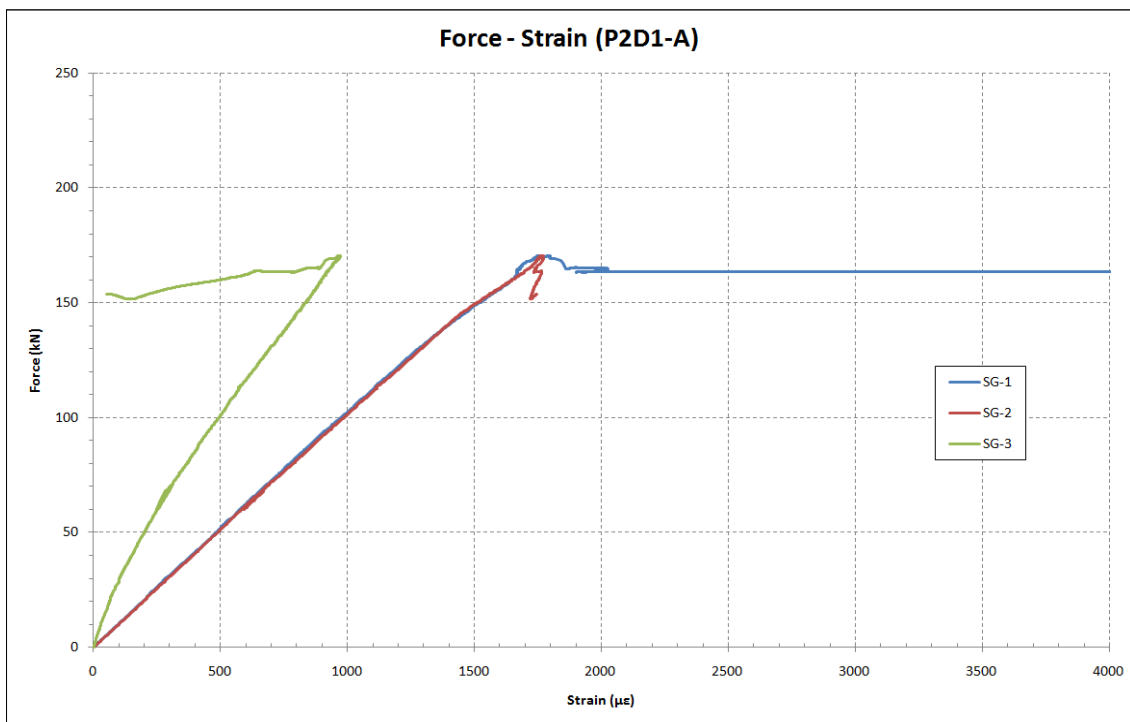


Figure 3.14: Force – Strain curves of P2D1-A specimen.

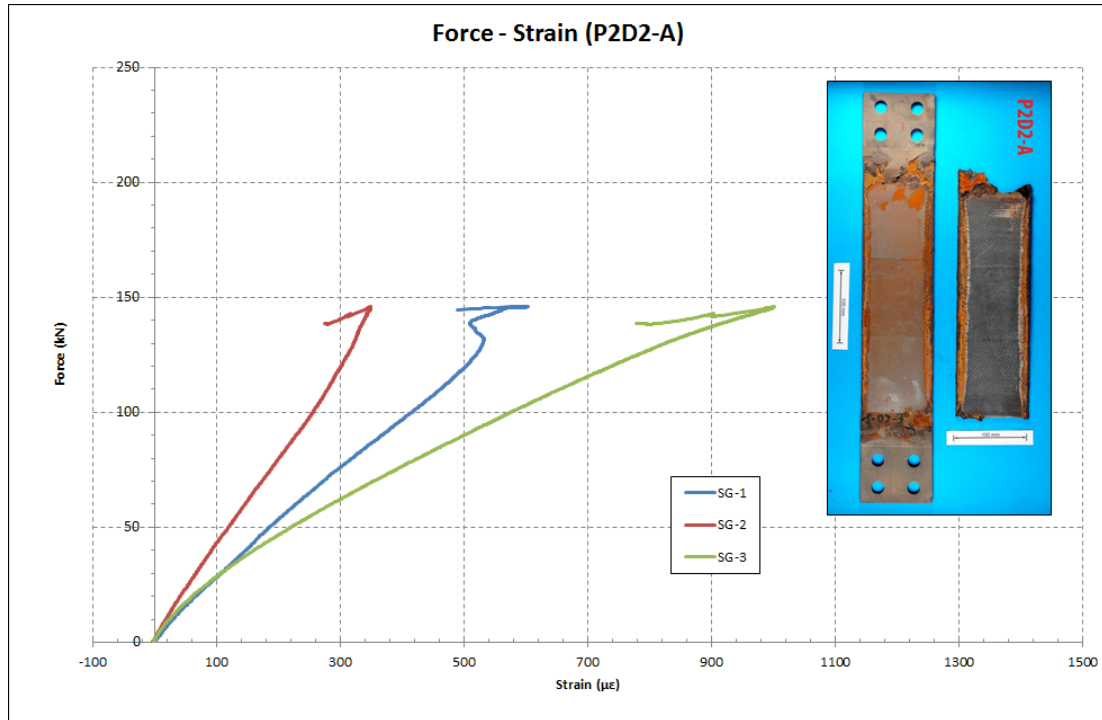


Figure 3.15: Force – Strain curves of P2D2-A specimen.

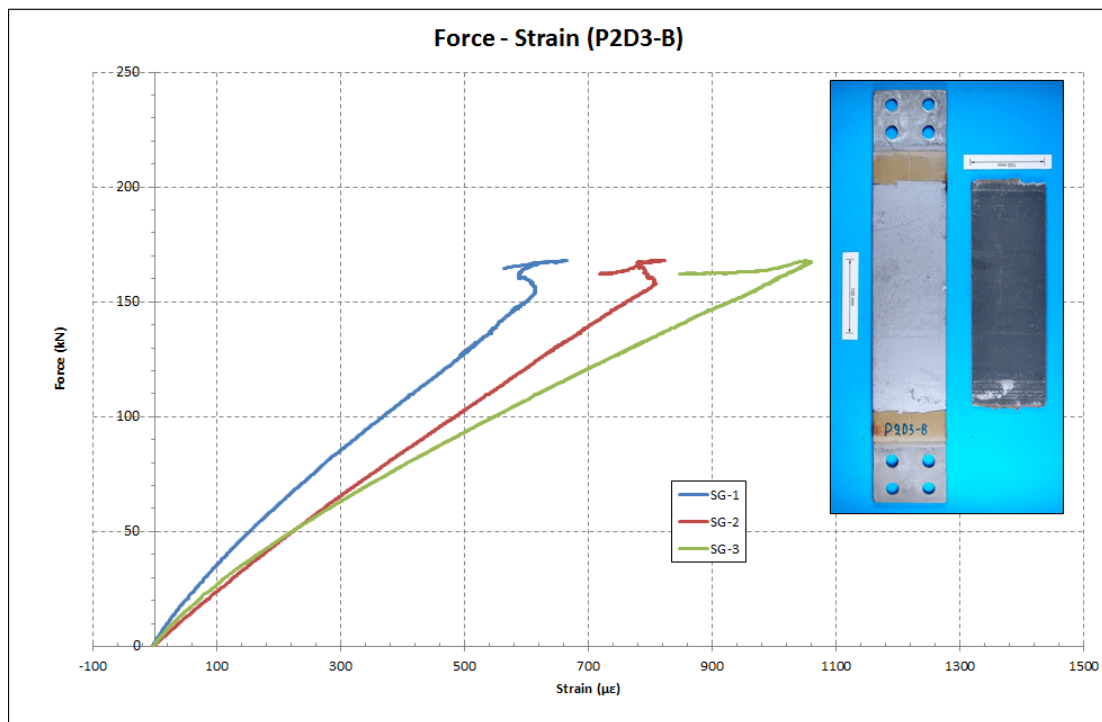


Figure 3.16: Force – Strain curves of P2D3-B specimen.

Regarding the measurements from the strain gages, excellent repeatability of the strains was noted for the non-aged cases (Figure 3.14). Strains measured on the steel (i.e. SG-1 and SG-2) increased linearly

until yielding. The increase of the strains measured at the SG-3 position ensured that there was a proper load transfer from the metal substrate to the patch; however, since SG3 was located at the centre of the patch, it provided no information concerning the initiation and propagation of debonding which started from the edges. In the aged cases, there was a good repeatability of the measured strains. Additionally the inflection point in the strains in positions SG-1 and SG-2 is a sign of debonding propagation in the patch-steel interface, under these sensors. The slightly increased inflection point of the SG-3 curve indicates the difference between the time instance when debonding propagated under the edges of the full thickness patch (i.e. under SG-1 and SG-2) and the time instance when debonding reached the centre of the patch (under SG-3). The patch debonding loads of P2D specimens are shown in Table 3.5 the nominal applied stress listed is based on the specimens average dimension measurements considering the thickness diminution. Figure 3.17 depicts the propagation of debonding during testing.

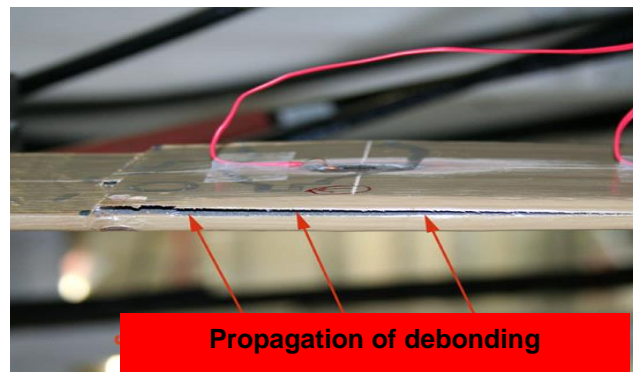


Figure 3.17: Edge debonding of P2D specimens.

Table 3.5: Patch Debonding Loads of P2D specimens.

Specimen	Patch Debonding Load [kN]	Applied Nominal Stress [MPa]
<i>P2D1-A</i>	170.3	321.3
<i>P2D1-B</i>	168.7	318.3
<i>P2D2-A</i>	145.6	327.9
<i>P2D2-B</i>	152.0	357.6
<i>P2D3-A</i>	166.3	313.8
<i>P2D3-B</i>	168.2	311.5
<i>P2D4-A</i>	128.8	340.7
<i>P2D4-B</i>	129.2	337.3

Observing the results, there are some variations concerning the patch debonding loads. The two specimens that did not undergo the aging procedure (P2D1) showed the highest patch debonding load, as expected. Those that had undergone aging without being painted (P2D2 and P2D4) showed the lowest patch debonding load. Apart from the thickness reduction in the unprotected steel substrate in these specimens, some damage was detected in the bimaterial interface. After testing and complete removal of the patch, it was observed that moisture had infiltrated between the patch and the metal substrate, partially corroding the steel surface under the patch. Additionally, in all cases, there was no trace of resin or fibre bridging on the steel surface and no visible damage of the patch, denoting that failure mode was adhesive. This resulted in the reduction of the effective bonding area, shown in Figure 3.19, where the percentage of the intact area of the bondline is also presented, after measuring the extend of the affected area by analysing the pictures. It must be noticed that at the edges of the patch there was no corrosion. This is attributed to the fact that the resin layer (due to the Vacuum Infusion method) extended outside the laminate, covering the steel surface beyond the patch and therefore forbidding the ingress of water in the interface between the two substrates from these sides. By calculating the non-affected areas, it was noticed that specimens P2D2-A and P2D2-B which had the greatest patch debonding loads, had also the largest intact bonding areas.

The average thickness reduction of specimens P2D2-A and B was measured equal to 0.66 mm, while in the P2D2-C and D specimens, the thickness reduction was greater, equal to 1.20 mm. This variation in the material loss between specimens after aging is another reason for the variation noted in the patch-debonding loads. Finally, coated specimen P2D3-A exhibited similar behaviour to the one of the non-aged specimens with a failure load equal to 166.3 kN. Reviewing the force displacement curve of specimen P2D3-B it is implied that the failure load is equal to 132.2 kN which corresponds to the first local maximum. However, examining the force – strain measurements (Figure 3.16) there is no change in the strain measurements at this load. This local maximum is associated with the encountered problems while measuring displacement, which in turn rendered the recorded measurement data questionable. Hence the patch debonding load is taken equal to 168.2 kN which corresponds to the second local maximum in the force displacement graph and is in good accordance with the force strain measurements. Post testing examination of the bond area revealed no visible signs of corrosion in the specimens (Figure 3.18).

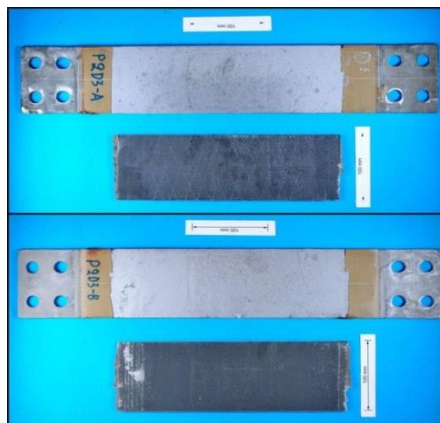


Figure 3.18: Bondline of the two coated aged specimens after testing.

Thus, typical marine coating seems to adequately protect the patch and the bondline from the environmental effects and protect the steel-patch interface from corrosion. The area underneath the patch that was affected from the moisture ingress was 20% of the bond area for the P2D2-A & B specimens, whereas in the P2D2-C & D specimens this percentage was equal to 23%. Although the extent and morphology of the affected bondline area was very similar, the average thickness reduction differed substantially between the specimens (Figure 3.19). These differences are the result of the specimens' position inside the environmental chamber. Detailed measurements of the intact area and the average thickness diminution in the steel are presented in Figure 3.19, where, additionally the failure load of each specimen is also listed. Recapitulating, all results of the P2 specimens' tests are presented in Table 3.6.

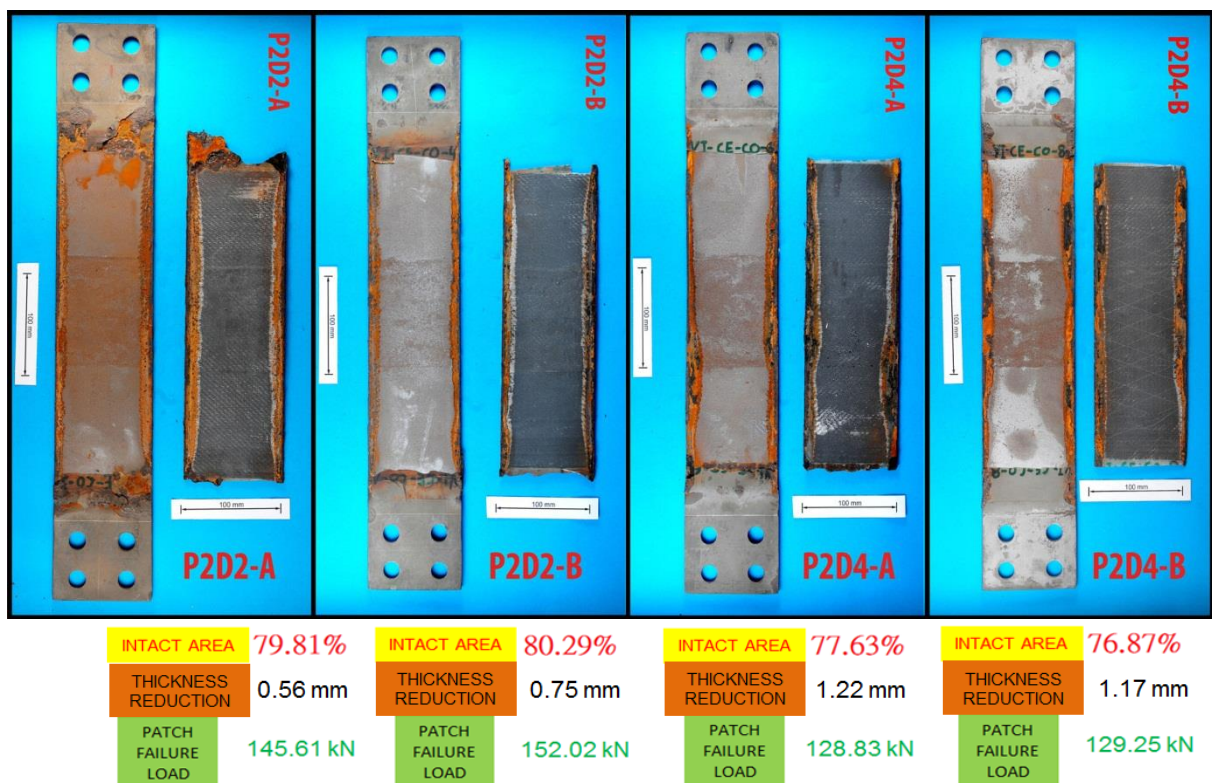


Figure 3.19: Reduction of the effective bonding area due to corrosion in unpainted patched P2 specimens.

Table 3.6: Results of P2 plates.

Specimen Description	Specimen Code	Aging	Patch Debonding Load [kN]
Unpatched	P2A-C	N/A	150.8 ¹
	P2A-D		151.0 ¹
<hr/>			
VI-C/E, GB	P2D1-A	N/A	170.3
	P2D1-B		168.7
	P2D2-A	A-100	145.6
	P2D2-B		152.0
	P2D3-A	A-100 (painted)	166.3
	P2D3-B		168.2
	P2D4-A	A-100	128.8
	P2D4-B		129.2

¹Yield load of the unpatched specimens.

Based on the yield loads of the milled unpatched specimens P2A-C and D, on the average milled thickness of 0.35 mm and on the yield stress of the steel (314.6 MPa), we can estimate that the yield load of the intact (non-corroded) plate would be approx. equal to 160 kN. Comparing this value to the ones listed in Table 3.6 it can be stated that, in the cases of the non-aged specimens (P2C1 and P2D1) and of the properly painted aged specimens (P2D3), the patch application fully reinstated the strength of the corroded plate, providing also a slight strength increase of the order of 5%. Failure at lower loads than the yield load of the original cross section occurred only in the cases of the non protected, aged specimens (P2D2 and P2D4) due to the significant thickness diminution of the exposed steel plate.

3.4 Numerical modelling

Model Description

Following the experiments, finite element models were created using ANSYS 13.0. These models were based on the average dimensions of the non-aged specimens (Table 3.7), as it would be too cumbersome to realistically represent the thickness variation and the non-uniformity of the surface of the aged specimens. Due to symmetry, only ¼ of the specimens was modelled, omitting the area that was inserted in the fixture. The modelled area is depicted with blue in Figure 3.20. In the present model, both material and geometric nonlinearities were taken into account.

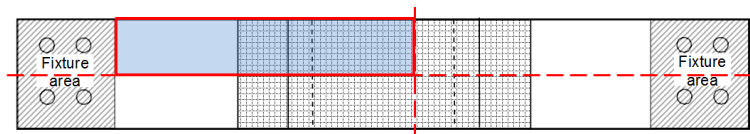
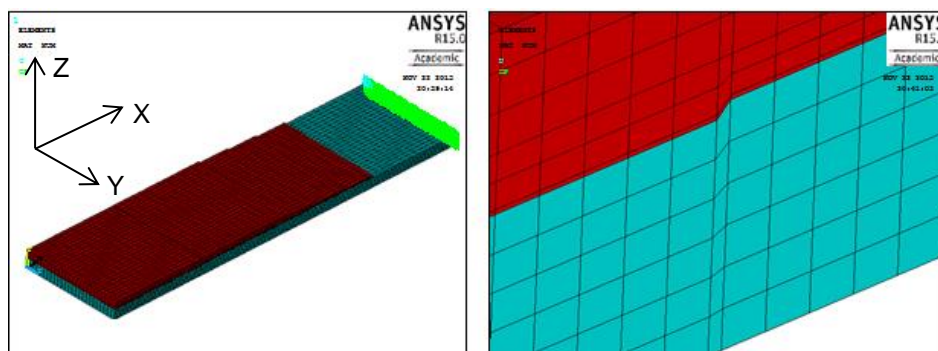


Figure 3.20: ¼ of the specimen that was modelled in ANSYS.

Table 3.7: Average dimensions of the non-aged specimens.

Geometrical parameters	
Width [mm]	100
Depth of corrosion [mm]	0.26
Length full thickness patch [mm]	200
Total length of patch [mm]	300
Total specimen length [mm]	400
Thickness of the steel [mm]	5.07
Thickness of the patch [mm]	3.45

The applied boundary conditions allowed only for translation in the longitudinal X axis, simulating the boundary conditions applied by the fixtures during testing. Symmetry boundary conditions were applied in the planes of symmetry YZ and XZ (Figure 3.21). In order to account for geometrical and material nonlinearities, the Newton-Raphson method has been utilized together with a line search algorithm. A displacement controlled approach is utilized to be in accordance with the one followed in the experimental campaign. Additionally, the displacement control approach is well suited for aiding the convergence of the non-linear solution and avoiding numerical instability issues involved in debonding analyses, where softening behaviour is apparent. SOLID186, which is a higher order 3-D 20-node solid element that exhibits quadratic displacement behaviour, was used for the steel and the composite with an average element edge size of 1mm. 6 elements were used across the thickness of each substrate. Figure 3.21 shows the generated model. The elements that represent the composite patch are depicted in red, while those that represent the steel substrate with cyan. The transition from the full thickness to the corroded area is achieved by a small transitional region inclined by 45° . The composite material was modelled as a linear elastic orthotropic material with material properties equal to the ones of the VI-CE system (Appendix A). Steel was modelled as a bilinear isotropic elastic-plastic material with a hardening equal to 0.015 of the young's modulus of the material to avoid numerical instabilities. The material properties were the ones mentioned earlier in this chapter.

**Figure 3.21:** Generated finite element model of the P2D1 plates.

3D 8-node contact elements CONTA174 and TARGE170 with the option of cohesive surfaces were selected to model the bondline area. ANSYS allows the use of contact elements that can model interface delamination, using the bilinear cohesive zone model which was described in Chapter 2. The contact elements (CONTA174) themselves overlay the solid elements describing the boundary of a deformable body and are potentially in contact with the target surface. This target surface is discretized by a set of target segment elements (TARGE170) and is paired with its associated contact surface.

The interfacial separation is defined in terms of contact gap or penetration and tangential slip distance. The computation of contact and tangential slip is based on the type of contact element and the location of contact detection point. The cohesive zone model can be implemented using the bonded contact option in the contact wizard. For mixed-mode debonding a power law based energy criterion is used to define the completion of debonding. This is also known as the quadratic criterion (Equation 2.33).

The bilinear law is well suited for the modelling of resins and non-ductile adhesives. It is of critical importance to assign the corresponding material properties that characterize the fracture toughness of the bimaterial interface under pure mode and mixed mode conditions. The material properties required to define the cohesive law are: the maximum normal stress, the maximum tangential stress (tractions), the critical fracture energy for normal separation (mode I) and the critical fracture energy for tangential slip (mode II). These properties were taken from the literature (*Lee et al 2010*) and were implemented in the present model (Table 3.8).

Table 3.8: Cohesive law properties.

	Maximum Stress [MPa]	Critical Energy release Rate [N/mm]
Mode I	7.3	0.14
Mode II	53.0	0.28

Results

To check the validity of the model, the numerical results were compared to the experimental ones. Due to the difficulties associated with the acquisition of valid displacement measurements during the experiments, the experimental force displacement graphs were not taken into consideration. The force displacement curve of the 3D FEM is presented in Figure 3.22. Interpreting the graph, the stages associated with the initiation and evolution of the debonding of the patch can be identified. The force displacement curve is linear up to the load of 147.00 kN where the slope changes. This is because the steel substrate which was in the elastic linear region enters plasticity at 147.00 kN (Figure 3.23). At that load the bondline remains undamaged. Debonding starts at 158.68 kN starting from the edge of the laminate. This load is also the maximum load. The debonding increases in size abruptly, reducing the stiffness of the specimen and leading to lower reaction forces (135.64 kN). After that point only a small part of the composite substrate remains bonded to the steel, which does not effectively contribute to the stiffness or to the load bearing capacity of the specimen. With increasing applied displacement, the loading increases and the force displacement curve

corresponds to the yielding of the steel substrate. Figure 3.24 presents the contact elements in the bonded area, where undamaged elements are marked with red colour and the debonded ones with yellow and orange. The left part of this figure shows the initiation of debonding (158.68 kN) while the right part the extent of damage at 139.90 kN right after the maximum load has been reached. Comparing the force strain graphs in Figure 3.25, it is evident that the numerical results are in very good agreement with the experimental results, consolidating the developed model.

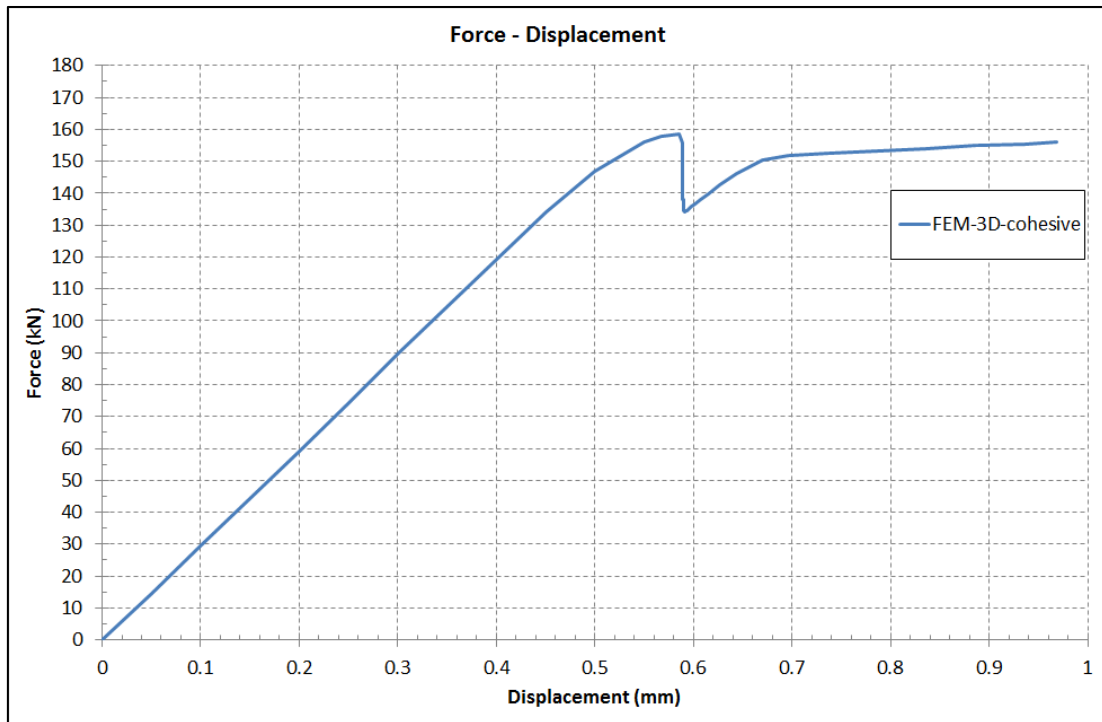


Figure 3.22: Force displacement curve of the 3D finite element model

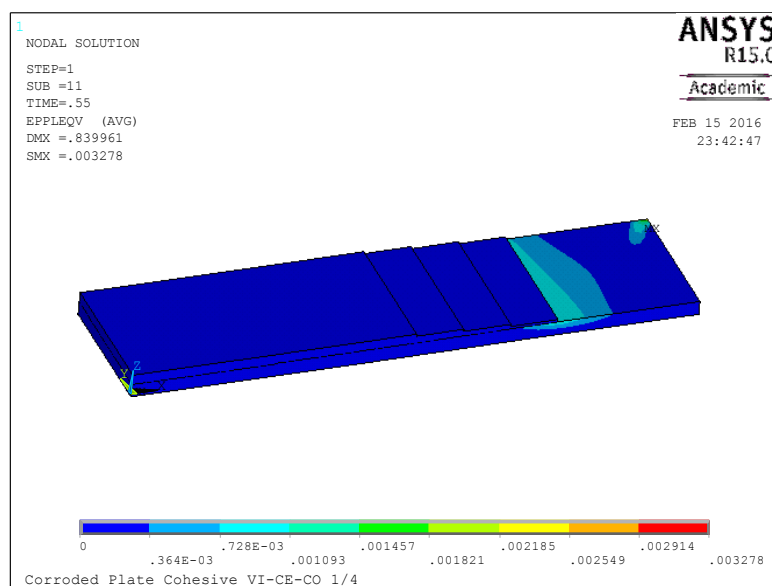


Figure 3.23: Plastic strain distribution at 147.00 kN.

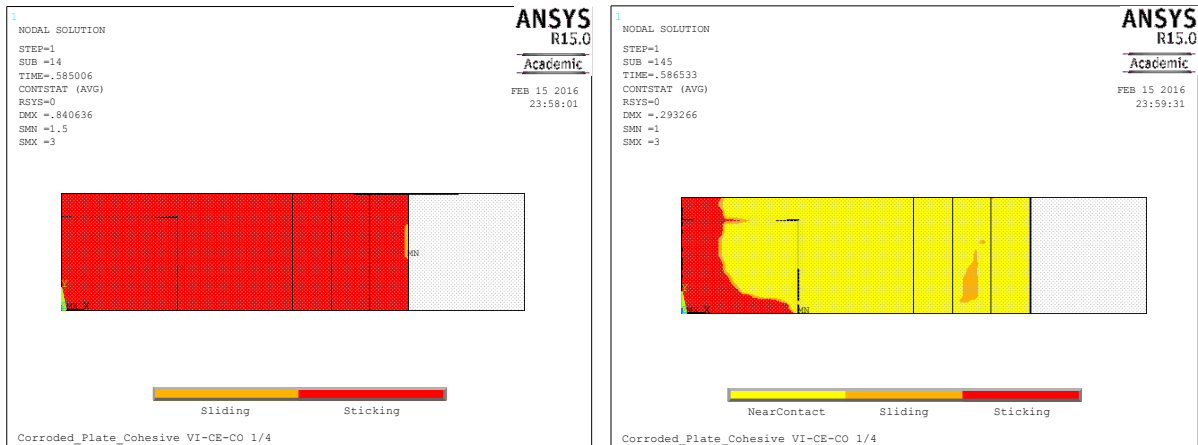


Figure 3.24: Initiation (left) and development of debonding (right) in the 3D model.

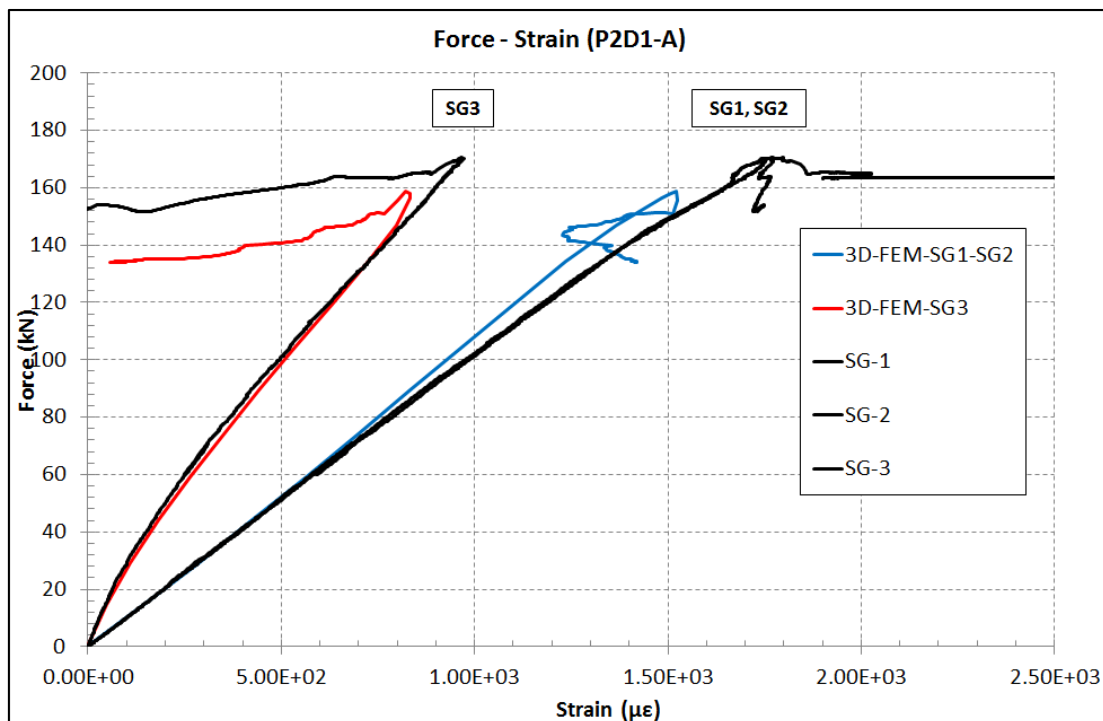


Figure 3.25: Experimental versus 3D numerical Force – Strain graph.

Reviewing the displacement field in the FE model, it can be observed that apart from the displacement in the longitudinal X axis caused by the imposed displacement, deflection in the vertical Z axis is also present (Figure 3.26). The deflection is attributed to the shift of the neutral axis of the specimen from the middle of the steel substrate towards the bimaterial interphase due to the existence of the composite substrate. As it is widely known the position of the neutral axis is dependent on the geometrical features and the material properties that constitute the bimaterial. The distance between the two positions of the neutral axis acts as a lever arm inducing a bending moment to the structure. This effect is referred to as secondary bending and causes the out of plane deflection. This effect is prominent in asymmetric repairs (such as one sided repairs), and should be carefully considered when designing a composite patch repair as it might lead to undesired

deformation and to substantial additional loading.

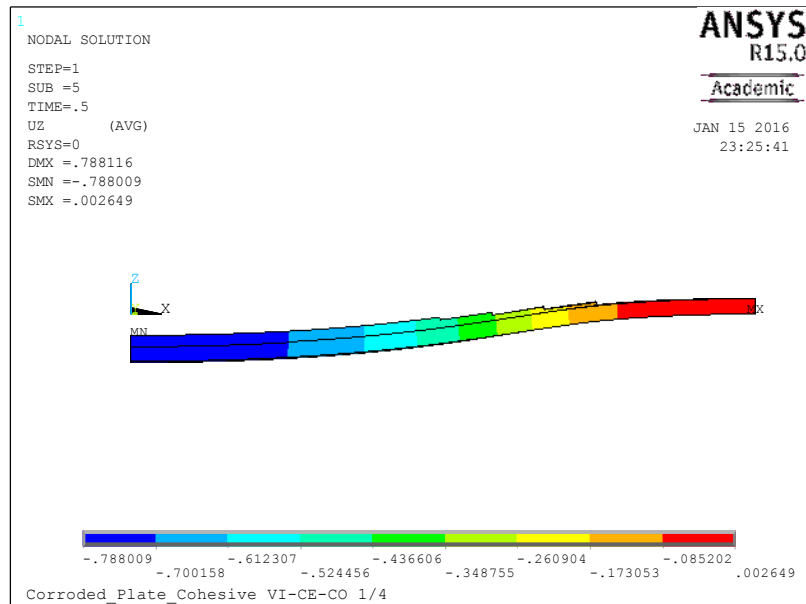


Figure 3.26: Deflection at 148.06kN (scale factor of 20).

The 3D finite element incorporating cohesive elements was able to simulate the conducted experiments; nevertheless increased computational resources were needed for these simulations. In addition, a series of models with different time steps, mesh sizes and solution controls have been investigated before identifying the suitable magnitudes for these parameters that would lead to converged solutions. To minimize the required time in subsequent simulations, a 2D finite element model of the specimens was additionally developed using ANSYS 13.0 software. 2D high order 8-node elements were used to model the steel substrate and the patch; these elements are referred to as PLANE183 by ANSYS. The length of the elements edges was 0.9 mm. Only half of the specimen was modelled due to symmetry to reduce computational time. The generated 2D model and the element size are presented in Figure 3.27.

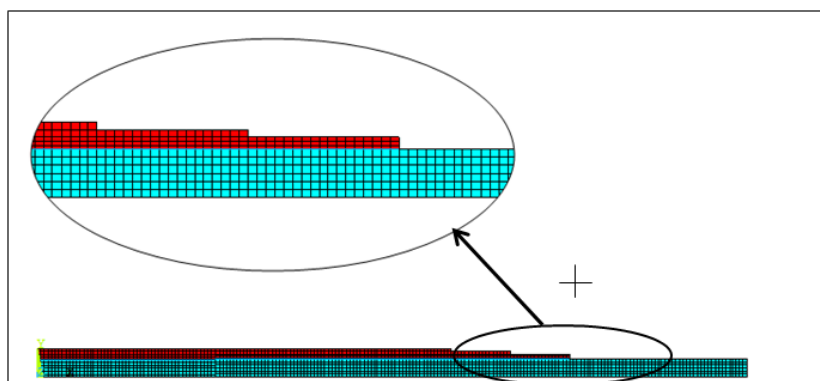


Figure 3.27: Generated 2D finite element model and mesh size

Once again contact elements that can be used to simulate interface fracture using the cohesive zone model were employed to simulate the bondline. Results indicate that the 2D and the 3D models are in excellent agreement between each other in terms of patch debonding load (Figure 3.28), with the difference between the two cases being less than 2.5%. More significantly, the FE results were in very good agreement with the experimental results, capturing the ultimate load and failure mechanisms that were observed in the experiments. Comparing the obtained numerical force displacement curves (Figure 3.28), it appears that there is a difference between the 2D model and the 3D model in the vicinity of the maximum load. More specifically, the 2D simulation exhibits a more progressive development of damage, with debonding gradually expanding as the applied displacement increases. This results in a gradual drop of the reaction forces once the maximum load has been reached and damage has initiated. Subsequently the load increases until a second local maximum is reached, after which a sudden drop is noted corresponding to the full development of the damage. Contrarily, the 3D simulations predict an almost instantaneous evolution of debonding after the onset of damage. It is noteworthy that both behaviours were recorded in the experimental results (Figure 3.12).

The patch debonding load obtained from the 2D FE analysis is 162.39 kN and corresponds to the first local maximum of the force displacement curve. The average experimental patch debonding load for the two non-aged specimens P2D1-A and P2D1-B is equal to 169.51 kN. The deviation between the 2D calculated debonding load and the experimental load is only 4%. In addition, the strains calculated from the numerical model are in perfect agreement with the experimental results, capturing the plastic strains in the steel (SG-2) and the unloading at the centre of the patch due to the evolution in debonding which reduced the load carried by the composite laminate (SG-3) (Figure 3.29).

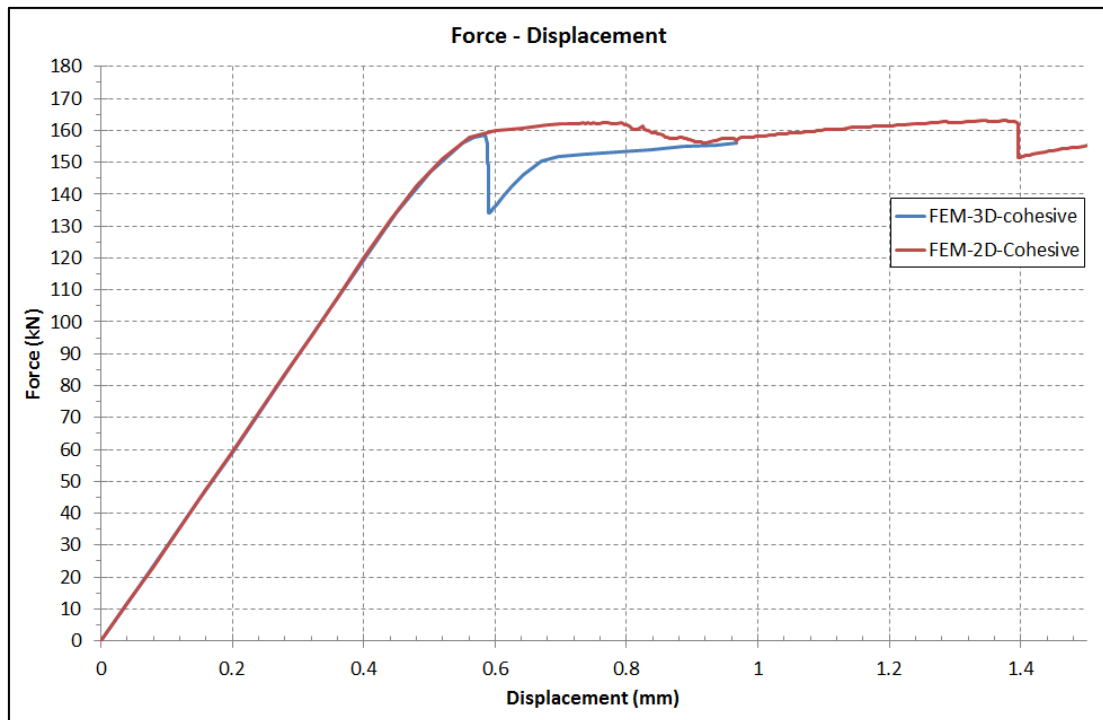


Figure 3.28: Force-displacement curves of the 2D and 3D numerical simulations.

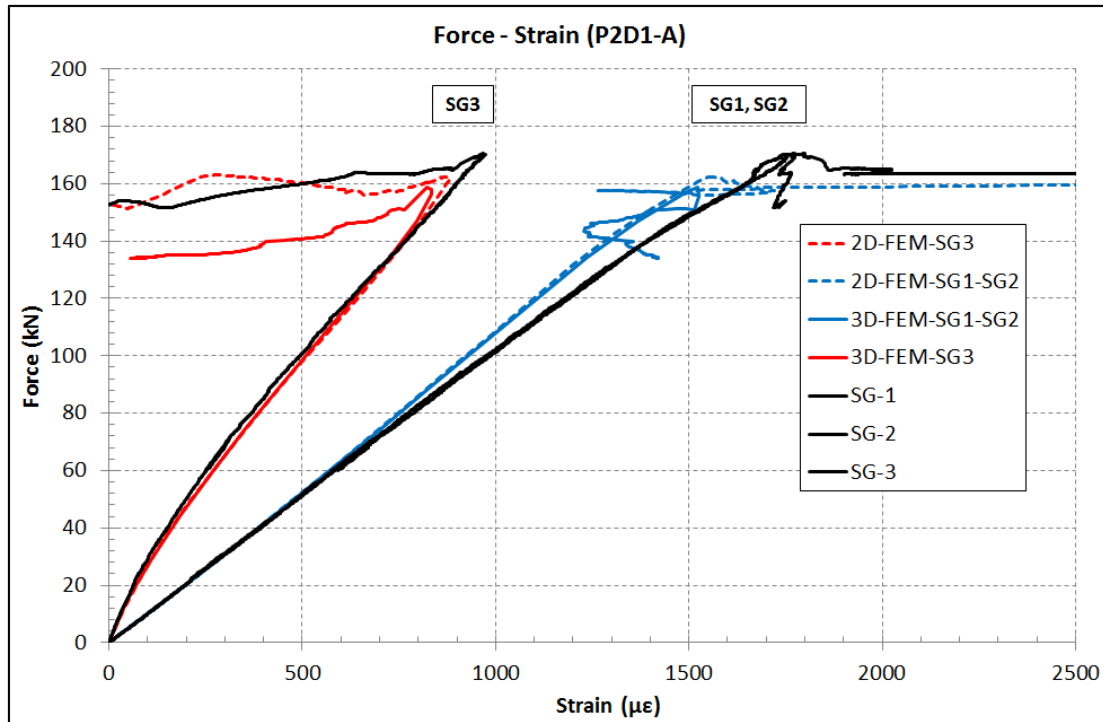


Figure 3.29: Force strain curves for the experimental and numerical results.

Therefore, having proven the validity of the 2D model, it was decided that all subsequent modelling would be carried out using the 2D model to save on computational resources. The 2D FE results showed that yield of the steel initiated in the same area as for the 3D case, i.e. at the patch edge and gradually increased in size extending towards the centre of the plate after debonding has initiated. The von Mises plastic strain at 151.1 kN, prior to debonding is depicted in Figure 3.30. The area of the steel that is bonded to the patch started yielding only after the patch has debonded. To investigate how the length of the patch affects the repair, a different scenario was simulated in which the length of the patch was equal to the length of the steel. The remaining dimensions and material properties were kept the same, along with the mesh size and the boundary conditions. In Figure 3.31 the force – displacement curves of the FE models with varying patch lengths are depicted. The results indicate that increasing the length of the patch does not contribute to the effectiveness of the repair, as the yield of the steel substrate occurs at the same load as for the shorter patch case and the patch debonding load is practically the same. Increasing the patch length affects the stiffness of the specimen as expected, which is reflected in a slight change of the slope at the elastic region of the force - displacement curve. Additionally, it appears that the repair with the full patch was able to deform more before the patch debonding, which occurred almost instantaneously.

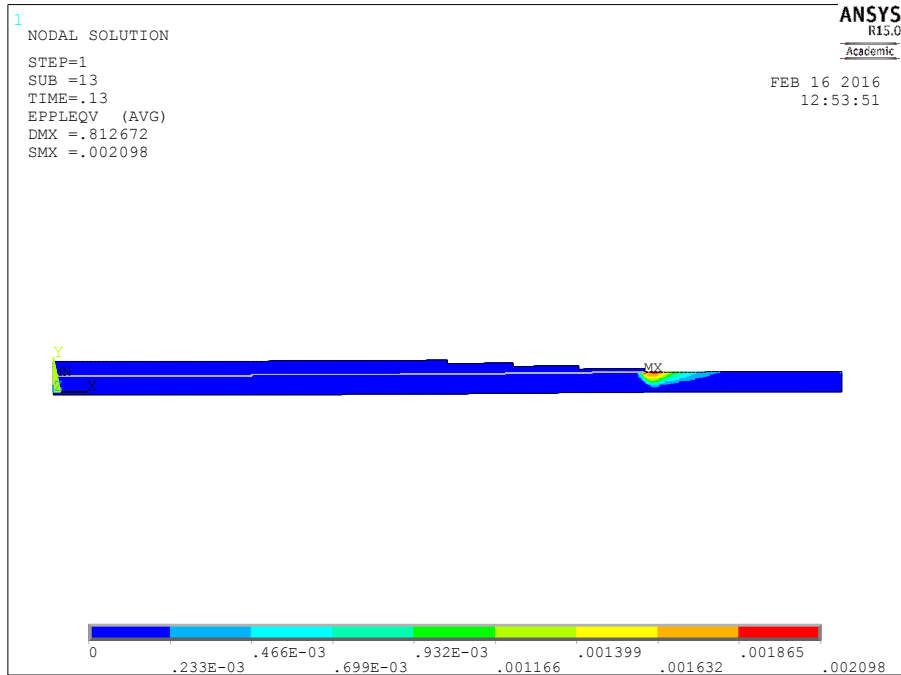


Figure 3.30: Von Mises plastic strain at the steel substrate at 151.11 kN.

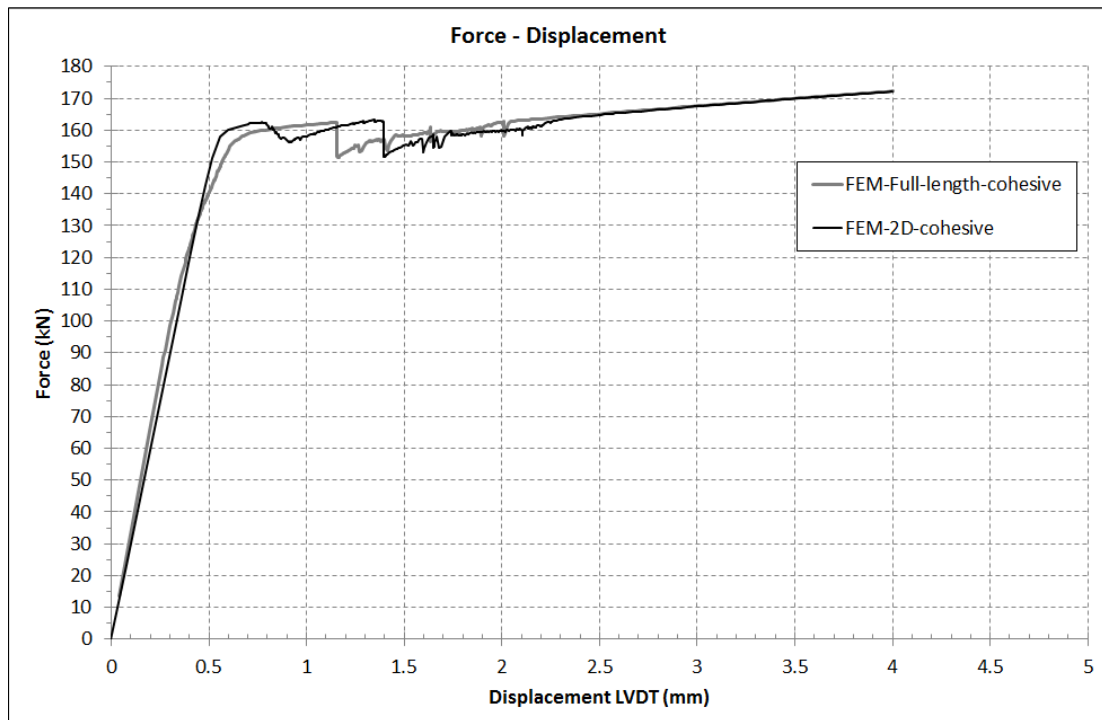


Figure 3.31: Comparison of FE models with different patch length to the experimental results.

Apart from the patched FE model, two additional models were developed, one for the non-defected (non-corroded) plate and one for the corroded but unpatched plate. This was done in order to evaluate the effect of the patch on the response of the corroded plate, as well as to compare the rehabilitated plate to that of the initial, non-defected condition of the plate. The force-displacement results are plotted in Figure 3.32. The patched model exhibits a strength increase compared to the unpatched case, whereas it also reaches the

yield load of the initial non-defected plate. Concerning the yield loads of the three models, as it was expected, the lower yield load is presented in the unpatched, corroded model due to the reduction of the cross sectional area and is equal to 150.0 kN. The yield load is the same for the initial plate and the patched case and is equal to 158.3 kN. This is due to the fact that, in the repaired case, yielding occurs in the steel area that is beyond the patch and since the cross section in this area is the same as the initial non-defected plate, the yield load is the same.

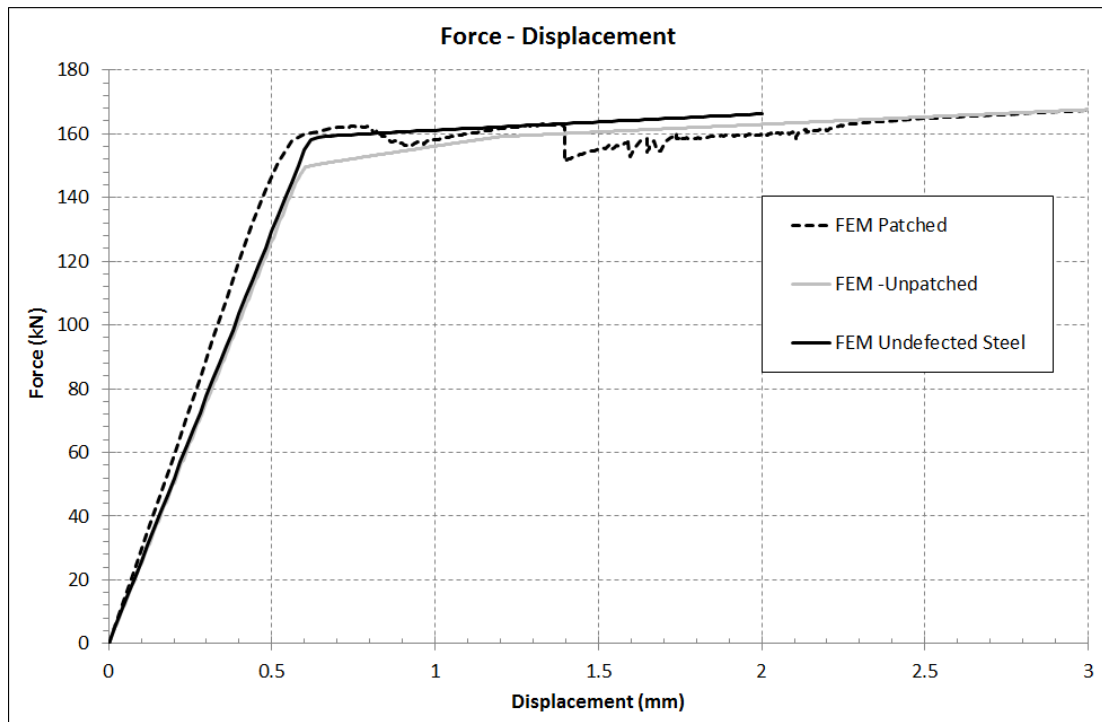


Figure 3.32: Force – Displacement curves of the undefected, corroded and repaired models.

Having validated the numerical models, another case was considered for study. In this case the corrosion thickness was taken equal to 1 mm. This thickness reduction is equal to 20% of the initial nominal steel thickness and is the maximum allowable thickness diminution according to IACS rules (*IACS 2010*). Once again, the patched and the unpatched cases were considered. The geometry, patch and material properties are the same as in the previous cases, apart from the thickness reduction in the corroded area.

The force – displacement curves for the patched and the unpatched cases for thickness reductions equal to 0.26 and 1 mm are presented in Figure 3.33. As it was expected, the unpatched case with 1 mm thickness reduction yielded at lower load (125.0 kN). Once again, the yield load of the patched cases and the non-defected plate was the same (158.3 kN), as yielding occurred in the steel areas beyond the patch for the patched cases. Therefore, the conclusion arises that the presence of the patch moves the location where the steel plate enters plasticity from the reduced, corroded area, to the full thickness area at the vicinity of the patch edges, thus reinstating the original load carrying capacity of the plate. Another significant remark is that the studied corrosion thickness reduction of the patched plates has practically no effect as the patch repaired cases exhibited the same stiffness and practically the same patch debonding load equal to 162.4

kN for the 0.26 mm case versus 162.7 kN for the case with the 1 mm reduction. Therefore, the efficiency of the repair is more pronounced in the case where thickness reduction is 1 mm.

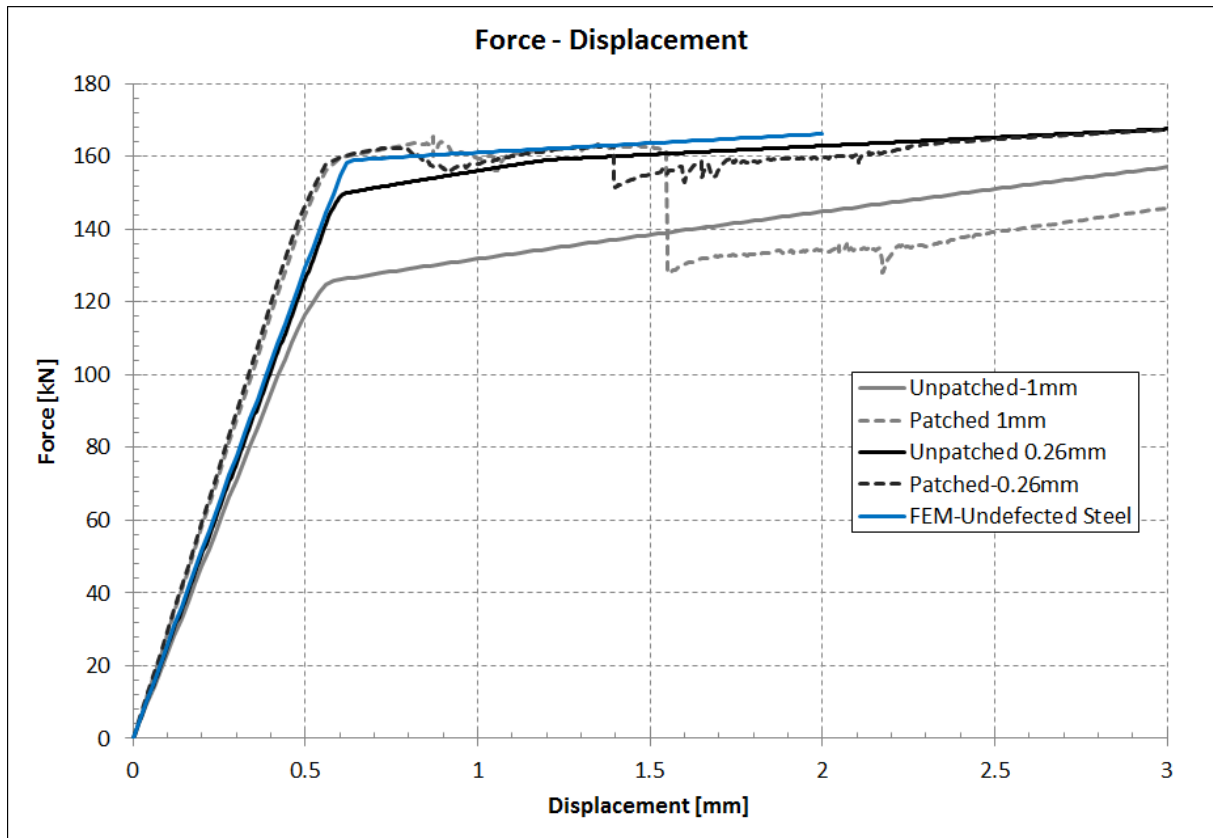


Figure 3.33: Force-displacement of the intact, corroded, and repaired cases with different thickness diminution.

To further study in a larger extent the effect of different parameters, a parametric study has been conducted (Koventarou *et al*, 2013) using the developed 2D model. In this study, the steel thickness diminution along with the thickness, material properties and length of the composite were varied. Additionally, the properties of the cohesive elements were investigated. It was observed that steel yielding at the patch edge preceded debonding in all cases. To enquire further into the effect of plasticity and how it relates to the debonding load, an analysis where steel was modelled as a linear elastic material was carried out and compared to the model considering plasticity. The results are plotted in Figure 3.34. The linear elastic model presents significantly higher debonding loads (at the vicinity of 175 kN) compared to the model where plasticity has been considered. This observation, along with the findings of the parametric study, signifies that the steel substrate entering plasticity is the main governing parameter for the initiation of debonding.

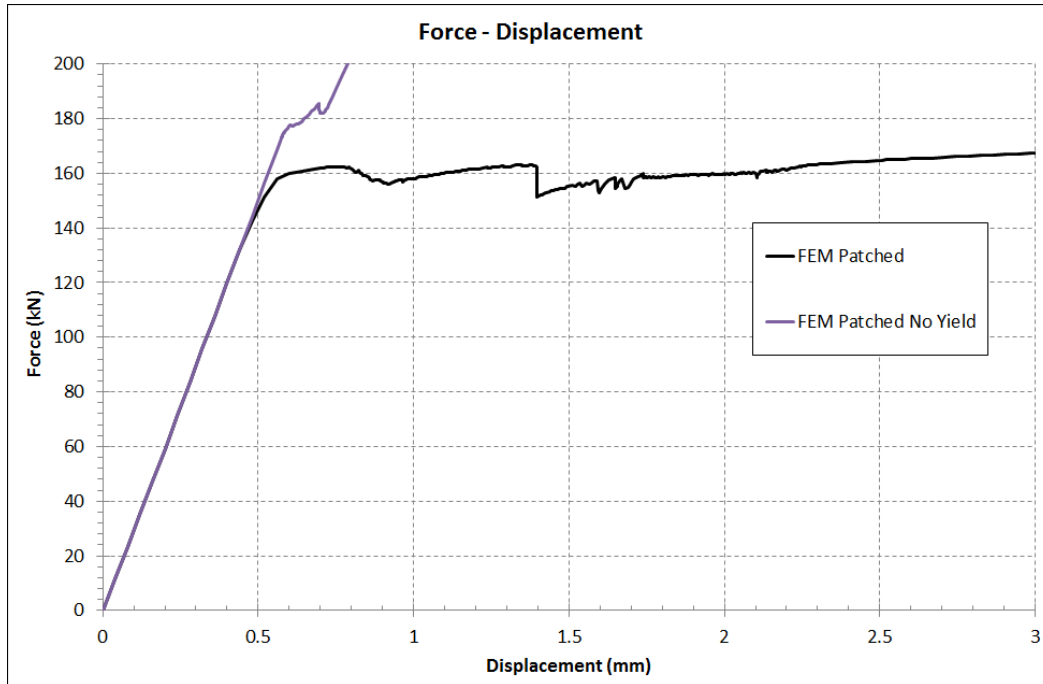


Figure 3.34: 2D FE patch model results for steel modelled with and without plasticity.

3.5 Conclusions

The effectiveness of composite patch repairing of corroded steel members was studied both experimentally and numerically. To this end, corroded steel specimens that were repaired with a CFRP patch were tested in tension. Three different aging scenarios in cyclic corrosion conditions were taken into consideration, i.e. non-aged, aged unpainted and aged painted specimens. Results showed that the unpainted specimens yielded the lower failure loads due to the degradation of the mechanical properties of the patch and the partial ingress of moisture under the patch from the edges. The painted specimens showed the same failure load as the non-aged ones, a fact which simplifies the installation procedure of such repairs, as it appears that a typical marine paint is sufficient to protect the repair from the aggressive marine environment. Yielding of the steel was observed prior to patch debonding, a fact which was later on validated with the FE simulations.

The numerical simulations encompassing interface elements with a bilinear mixed-mode cohesive law proved capable of accurately predicting the initiation and propagation of debonding in the patch-steel interface, as well as the corresponding patch failure load. The numerical simulation results are in very good agreement with the experimental ones. The repaired case was also numerically compared to the non-defected and the corroded unrepaired steel case. Additionally, a second scenario with a corrosion thickness reduction of the steel plate equal to 20% was investigated numerically. Results showed that composite patch repairing was able to rehabilitate the defected steel plates and reinstate the original, non-defected condition in all cases, with the repair being more effective for the case where the thickness reduction of the steel was equal to 20%. Concerning the length of the patch, a numerical investigation of a model with an increased patch length showed that the length did not affect the ultimate load of the repair for the studied case study.

4. Experimental and numerical investigation of patch repaired notched plates under static loading

4.1 Introduction

This experimental program includes static testing of notched steel plates, which were reinforced with a one-sided composite patch. This series of specimens was named P1. The main objective is to experimentally prove in a systematic way that the use of a composite patch increases the static strength of a notched steel structure. In parallel part of the experimental results presented in this report are used to validate the developed finite element models. In general, the tests are categorized considering the type of the plate's defect, the aging scenario and finally the surface preparation method. Additionally, the effectiveness of embedding optical fibres in the bimaterial interface and between the composite plies as a structural health monitoring method is investigated.

4.2 General characteristics

Specimen Description

The geometry and main dimensions of the P1 type plates tested are presented in Figure 4.1. The materials were the same as in the P2 plates, meaning that the patch consisted of unidirectional carbon plies in epoxy, laminated using the vacuum infusion method. The steel had a Young's modulus of 203 GPa and yield stress equal to 314.6 MPa. The nominal thickness of the steel plate, t_s , is 5 mm. The central orthogonal reference part of the steel plate has length L_s equal to 400 mm and width W_s equal to 200 mm. The total length of the plate is equal to 554 mm, which includes the fixtures areas. At the centre of this plate, there is a through thickness initial notch, having length 2α equal to 140 mm which has been opened using a wire electric discharge machining (EDM). On one of its sides (front side) the plate has a central composite patch with thickness t_p , effective length L_p equal to 200 mm and width W_p equal to 200 mm. The total patch length is equal to 300 mm, since it additionally includes the tapered edges of the patch. These specimens have been manufactured by the Co-Patch project partner AS2CON and the material lay-out and manufacturing procedure are exactly the same to those described in Section 3.2 for the P2 corresponding plates. Once again the surfaces were grit blasted to SA 2½ prior to lamination. The conditions during the manufacturing of the specimens were 35°C and 30% humidity for the first step and 35°C and 33% humidity for the second. In total five patched specimens were produced; in addition two unpatched notched specimens were tested as reference to examine the effectiveness of the repair (P1C and P1D). The actual dimensions of the fabricated specimens are shown in Table 4.1 below. As in the P2 series, the specimens' width exceeded that of the grips of the testing machine. Therefore, the steel fixtures described in the previous chapter were used once again (Figure 4.2).

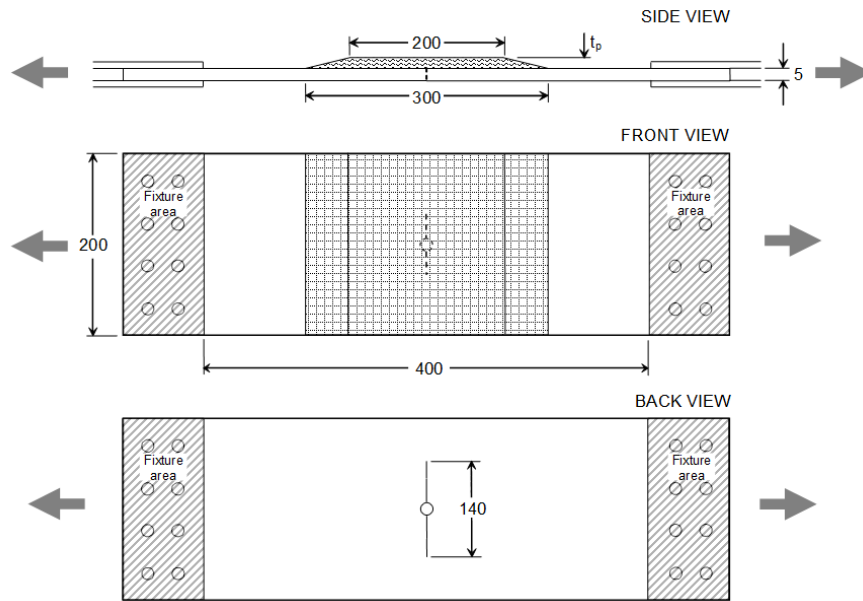


Figure 4.1: P1 plates geometry.

Table 4.1: Dimensions of P1 specimens.

Specimen	Dimensions					
	W_s [mm]	L_s [mm]	t_s [mm]	L_{pt} [mm]	L_p [mm]	t_p [mm]
P1A-C	199.0	400	5.0	-	-	-
P1A-D	198.0	400	5.0	-	-	-
P1D1-A	200.6	399	5.1	300.3	200.6	3.5
P1D1-B	201.0	400	5.1	300.3	204.2	3.2
P1D1-C	200.9	400	5.1	301.1	201.9	3.3
P1D2-A	201.0	400	5.1	300.9	201.1	3.6
P1D2-B	201.0	400	5.1	300.8	202.1	3.6

Similar to the P2 plates, some of the manufactured P1 plates were subjected to accelerated aging conditions into an environmental chamber according to *ISO 14993:2001*. Sealing tapes were used to protect the edges that were later inserted in the fixtures; apart from that, the whole specimens were exposed so as to investigate the effect of aging on the integrity of the repair and on the specimens' load bearing capacity. The specimens subjected to the aging process were exposed for 300 cycles (100 days) under cyclic corrosion (including salt mist, dry and wet conditions in different temperatures) and were subsequently tested in tension. Once again, to further inquire the effectiveness of typical marine coatings as a protection method, two of the specimens, namely P1D2-A and P1D2-B, were painted with common marine grade paint and

afterwards placed into the salt spray chamber where they were subjected to cyclic aging conditions for 300 cycles (100 days).

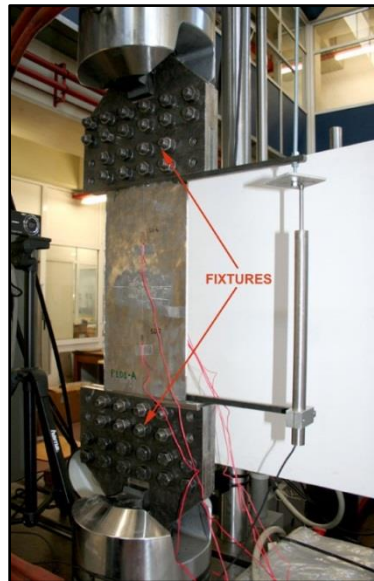


Figure 4.2: P1 specimen mounted on the testing machine.

Table 4.2 shows the code names of all specimens for their identification in this document. Each specimen has its own code name depending on the category to which it belongs. The table below also includes the case of the applicable (A-100) or not applicable (N/A) aging procedure.

Table 4.2: Nomenclature of P1 specimens.

Specimen Description	Code	Specimen code	Aging
Unpatched	P1A	P1A-C P1A-D	N/A
VI-C/E, GB	P1D1	P1D1-A P1D1-B P1D1-C	N/A
	P1D2	P1D2-A P1D2-B	A-100 (painted)

Specimens Instrumentation

During the tests, the force and crosshead displacement were recorded in all specimens. In addition, strain gages were used to record strains at different locations. In specimens P1A-C and D only one 5mm strain gage was used which was placed in the middle of the plate's width, 100 mm from the notch, as shown in Figure 4.3.

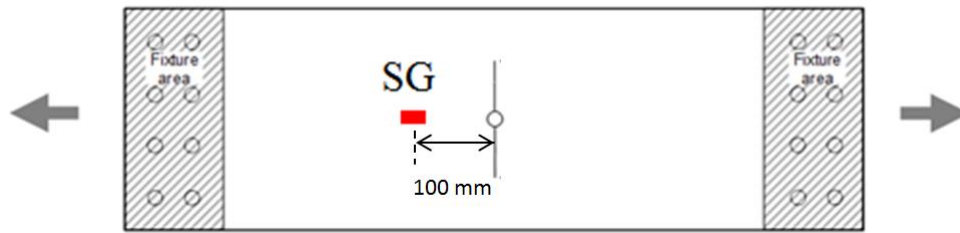


Figure 4.3: Instrumentation of specimens P1A-C and P1A-D.

The instrumentation of specimens P1D1-A, P1D1-B and P1D1-C is depicted in Figure 4.4. Two strain gages, denoted as SG-1 and SG-5 with gage length 2 mm, were placed at the patch edges in an attempt to record the debonding initiation at the edges of the patch. Two strain gages, SG-2 and SG-4 with gage length 5 mm, were placed at the edges of the maximum thickness of the patch in order to record the propagation of damage from the patch edges. Two more strain gages, SG-6 and SG-7 with gage length 5 mm, were placed on the steel plate, back to back to gages SG-2 and SG-4, respectively, in order to evaluate the possible differences of the axial strains between the steel plate and the patch. Gage SG-3 was located in the centre of the patch so as to evaluate the behaviour of the patch debonding. For the instrumentation of specimens P1D2-A and P1D2-B, a different approach was followed, as can be seen in Figure 4.5. Based on experience from the P1D1 tests, four strain gages were positioned in total. Gages SG-3 and SG-6 remained at the same position, while gages SG-8 and SG-9 were positioned on the patch, next to SG-3, at a distance of 70 mm and 80 mm, respectively. These two gages (SG-8 and SG-9) are expected to derive further information about the patch debonding process.

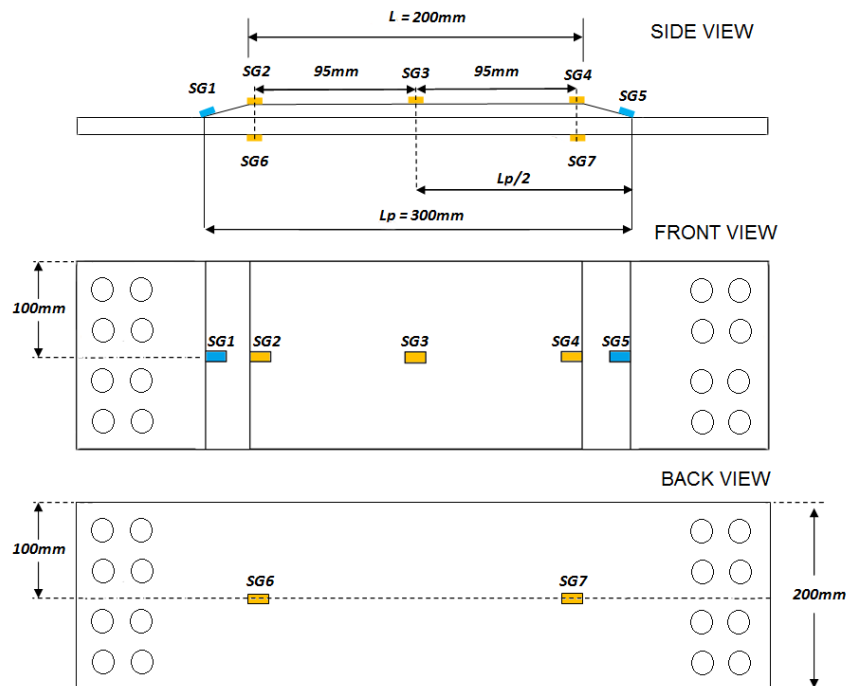


Figure 4.4: Instrumentation of P1D1-A, P1D1-B and P1D1-C specimens.

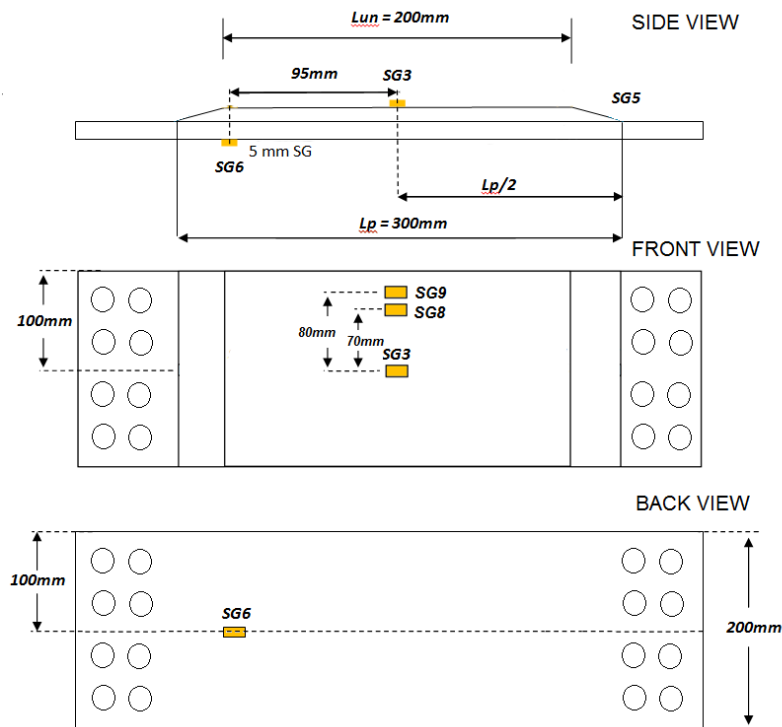


Figure 4.5: Instrumentation of P1D2-A and P1D2-B specimens.

4.3 Experimental testing and results

Test Parameters

A MTS hydraulic testing machine with a capacity of 250 kN was used for the tensile tests. A preloading of 25 kN was initially applied on the specimens in order to minimize the specimen-fixtures assembly tolerances. This preloading was applied as a linearly increasing displacement with rate equal to 0.5 mm/min. Specimens were subsequently unloaded and afterwards tested up to failure with the same displacement rate. However, after testing one of the patched specimens, it was proven that the load bearing capacity of the testing machine was not enough for the specimen's failure. For this reason, an INSTRON 300 LX testing machine with a capacity of 320 kN was used.

The applied force, the total specimen elongation and the longitudinal strains at various locations on the specimen were recorded during each test. In order to precisely measure the specimen's elongation, a LVDT transducer was placed alongside the length between the testing machine fixtures. For monitoring these parameters, the data acquisition system of the testing machine itself was used, together with an additional Spider-8 system, synchronized with each other.

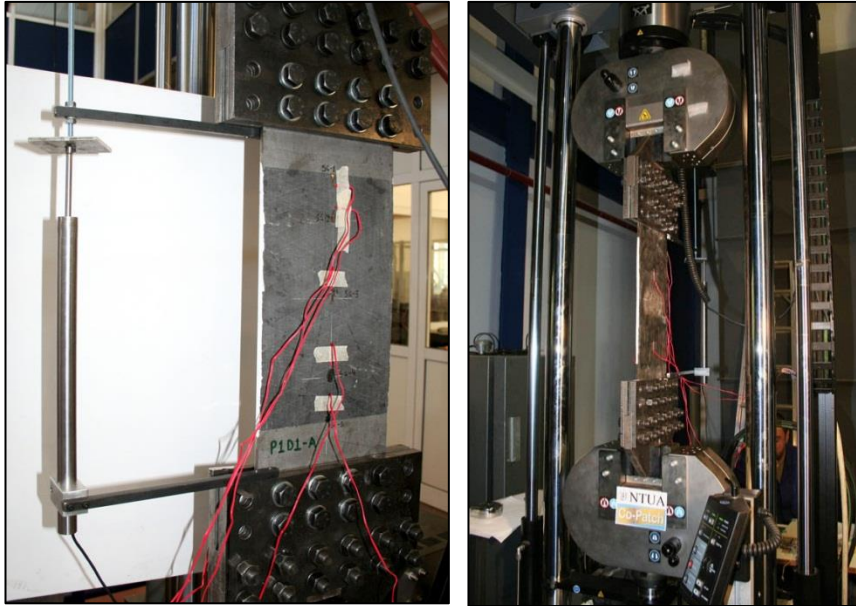


Figure 4.6: Specimen P1D1-A being tested on MTS testing machine (left) and on INSTRON 300LX testing machine (right).

Seven specimens in total were tested in tension. Specimen P1D1-A was initially tested at NTUA's lab with the MTS testing machine up to a 250 kN load, at which it didn't fail. Therefore, a second test attempted with the INSTRON machine up to 315 kN (machine's maximum load capacity), however once again the specimen did not fail. Specimen P1D1-C was also tested by the INSTRON machine but it did not fail either. For this reason, all P1D1 and P1D2 specimens were sent to the Co-Patch project partner AIMEN's facilities in O Porriño, Spain, for further testing, where a HOYTOM testing machine with a capacity of 600 kN was used. That being said, specimen P1D1-A was tested three times (twice at NTUA and once at AIMEN), specimen P1D1-C two times (once at NTUA and once at AIMEN), while the remaining specimens only once at AIMEN. On tests that took place in AIMEN, only four strain gages could be recorded at a time, thus in corresponding Force – Strain figures of P1D1-A,B and C specimens only four curves are shown. These strain curves correspond to positions SG-2,3,4,6 of Figure 4.4.

In addition, an inspection for patch debonding and delamination detection took place before testing, by using an acousto-ultrasonic instrument (BONDMASTER 1000e) to assess if the patch was correctly infused and bonded to the plate. The BONDMASTER findings prior to the static testing were marked with a marker. In this way, an evaluation of the quality of the bond and the composite patches was made in all P1D2 specimens. As it will be shown in the following, this instrument proved its effectiveness and trustworthiness as well as its limitations, by comparing the initial non-destructive inspection findings with the actual state which was revealed after the full debonding of the patch. These findings were very helpful in understanding and analyzing the test results.

Results

Both reference specimens P1C and P1D exhibited the expected behaviour, with an initial linear elastic

deformation, followed by plasticity. The loads at which the specimens enter plasticity and the maximum loads are shown in Table 4.3. Yield loads have been defined from the load-displacements response. Figure 4.7 shows the global response of the reference specimens, in the form of total elongation versus applied tensile force.

Table 4.3: Yield and maximum loads for P1 reference specimens.

Specimen	Yield Load [kN]	Maximum Load [kN]	Nominal applied Maximum stress [MPa]
P1A-C	98.3	110.6	110.6
P1A-D	93.4	106.6	106.6

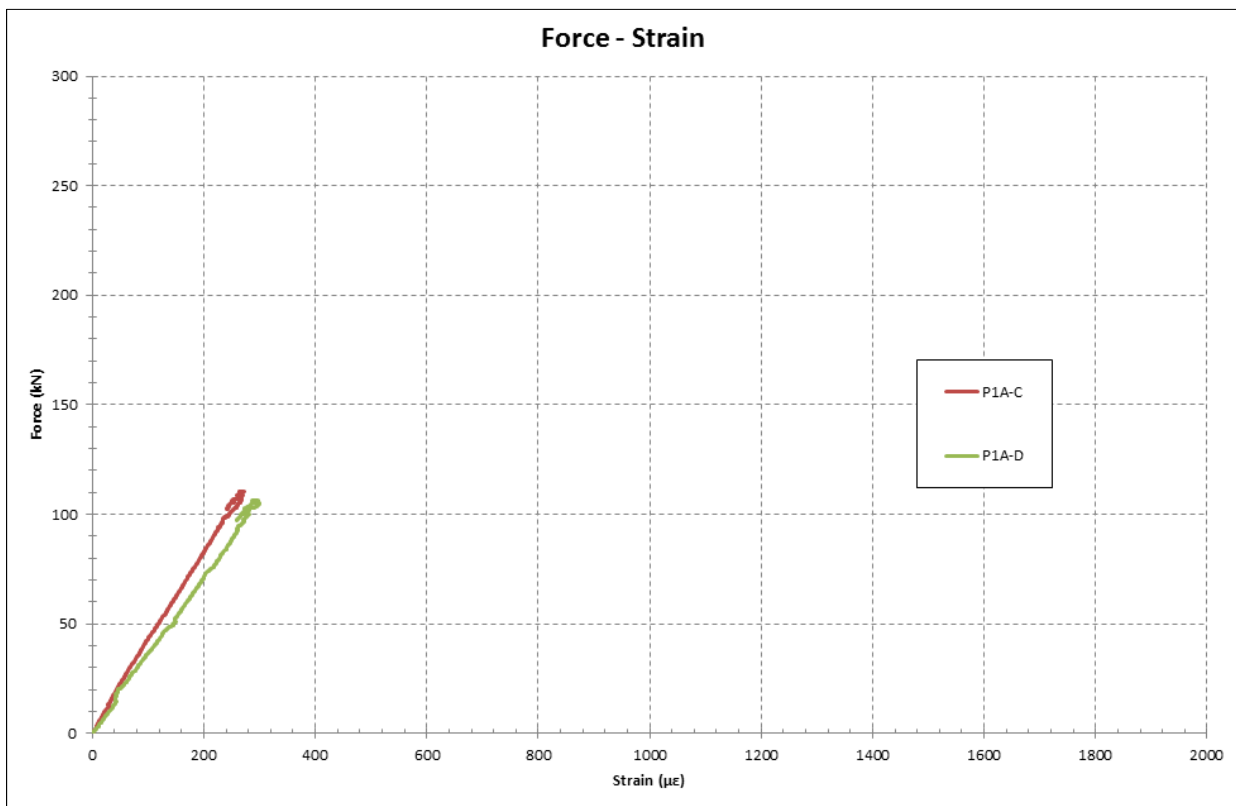


Figure 4.7: Force – Strain curves of P1A-C and P1A-D specimens.

The static tests results of the P1D specimens are presented below. The load-displacement responses of specimens P1D1-A and P1D1-C (tested at NTUA) are shown in Figure 4.8. The specimens exhibited a linear response which was followed by a non-linear behaviour up to the testing machines capacity. This non-linearity occurred after approx. 250 kN and was the result of yielding in the bolted fixture areas around the holes of the specimens. This yielding was also the main reason that specimen P1D1-C was not tested to the limits of the INSTRON machine. Yielding at the specimens' fixture areas occurred mainly due to two reasons. The first one was the unexpectedly high strength of the patched plate and the second one due to poor initial

manufacturing quality, some of the bolt holes were enlarged beyond their initial nominal diameter of 16 mm in order for the specimens to fit into the test fixture. This enlargement reduced the effective cross section of the specimen at the gripping area, resulting in insufficient gripping and slipping of the specimen. Further increasing the applied load led to the shearing of the holes by the bolts which is reflected in the test results. Indicative graphs depicting the measured force-displacement and force-strain curves of the P1D1 specimens are presented in Figure 4.9 to Figure 4.13. A very good repeatability of the force displacement curves of the specimens P1D1-A and P1D1-C is noticed for the tests that have been performed at NTUA's facilities. However the recorded behaviour of the force displacement curves differs significantly from the ones of the tests performed at AIMEN's facilities. The reason behind this was the incorrect placing of the specimens in the fixture from AIMEN, as no filler plates were used. This affected the load transmission path from the grip to the specimens as, instead of the load being transmitted through friction through the filler plates, it was transmitted directly from the M16 bolts through shear.

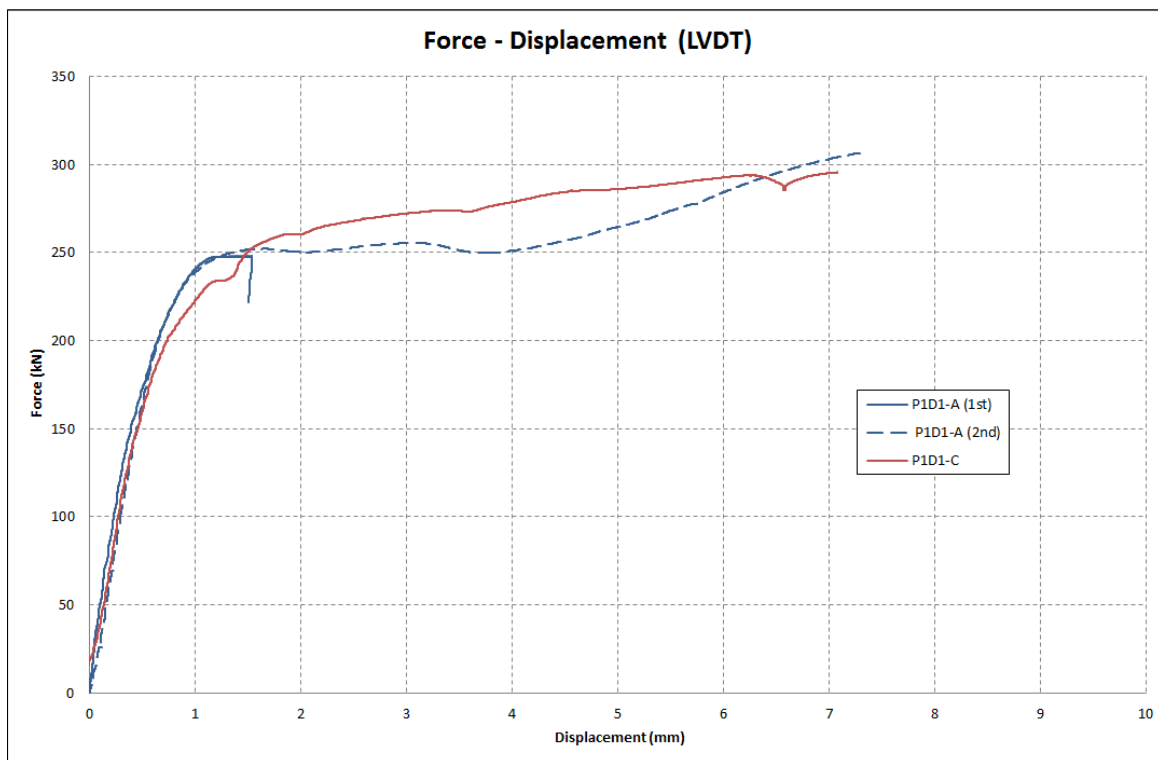


Figure 4.8: Force – Displacement (LVDT) curves of P1D1 specimens tested by NTUA.

In Figure 4.9 the typical Force - Crosshead Displacement curves for each specimen (tested both at NTUA and AIMEN) are depicted. The differences between the curves were mainly due to usage of different testing machines and preloading procedures. Unlike the non-aged specimens, patch debonding did occur at aged specimens as it can be seen by the sudden change of slope of the respective curves. In general, all P1D1 specimens exhibited a very good performance, reaching maximum loads that are higher than two times the loads reached by the reference unpatched P1A specimens.

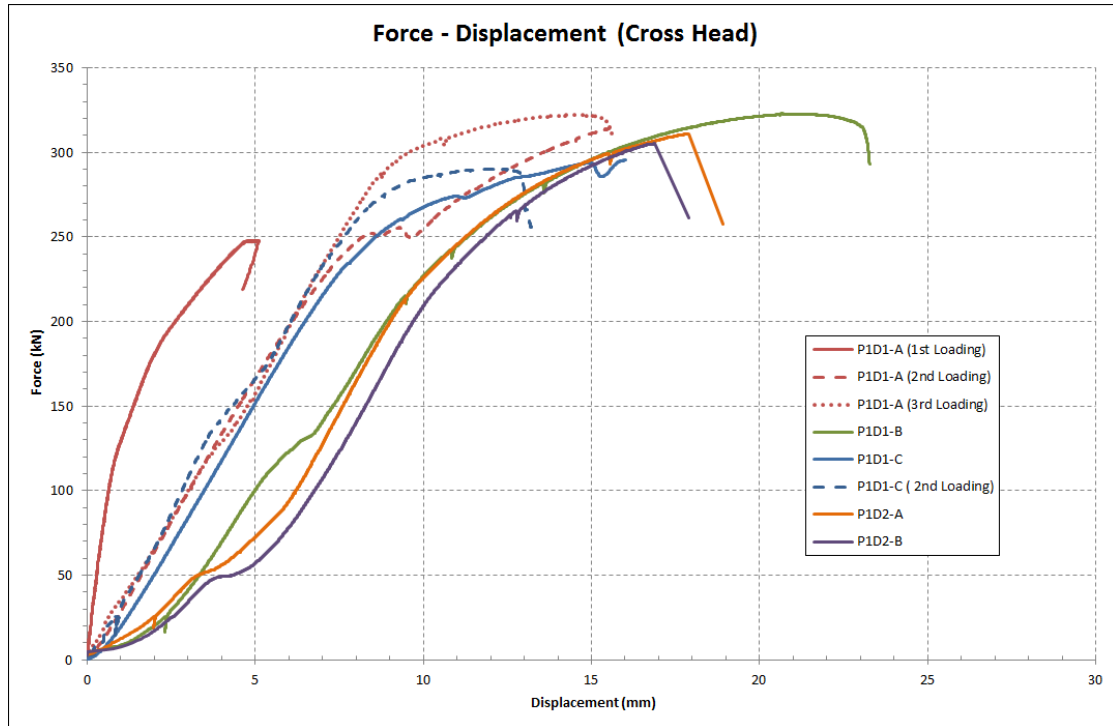


Figure 4.9: Force – Displacement (Crosshead) curves of P1D specimens tested both by NTUA and AIMEN.

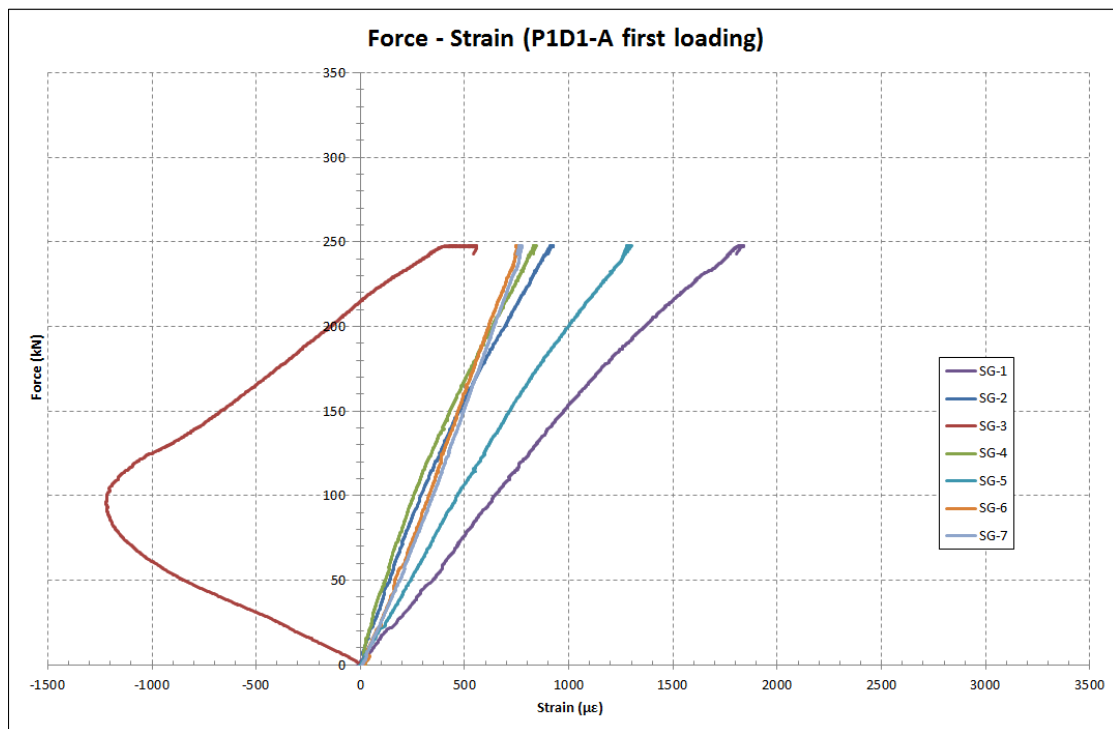


Figure 4.10: Force – Strain curves of P1D1-A specimen's first loading by NTUA.

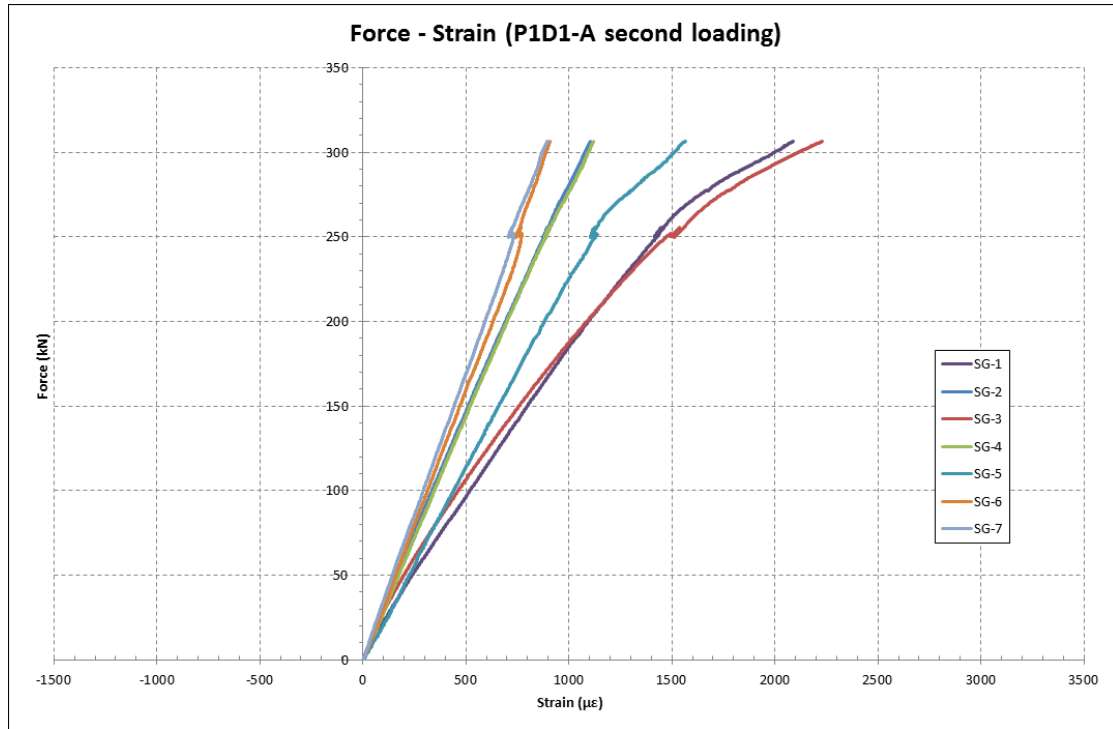


Figure 4.11: Force – Strain curves of P1D1-A specimen's second loading by NTUA.

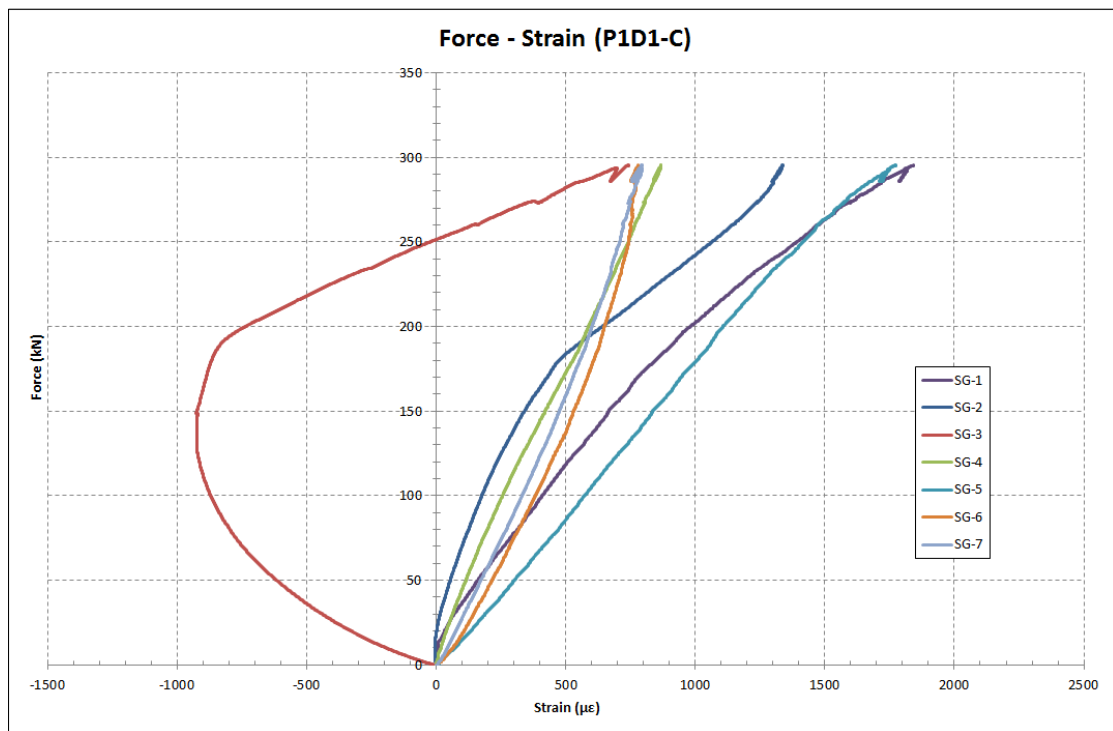


Figure 4.12: Force – Strain curves of P1D1-C specimen's first loading by NTUA.

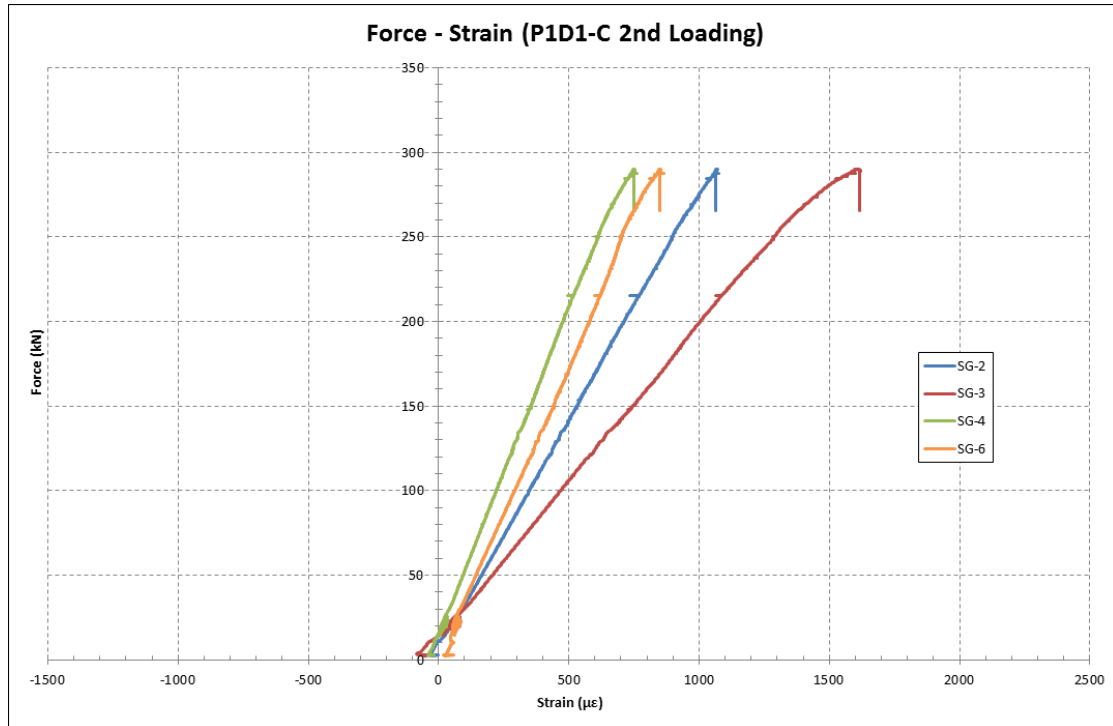


Figure 4.13: Force – Strain curves of P1D1-C specimen's second loading by AIMEN.

Figure 4.10 and Figure 4.11 show a very good repeatability of strain measurements among the two different loadings of specimen P1D1-A, for the edge strain gages on the patch (SG1, SG2, SG4 and SG5) and for the steel strains (SG6 and SG7). In particular, the strain measurements at the edge of the patch (SG1 and SG5) slightly differ between each other after 20kN. This is to be expected as the edge of the tapering length is prone to geometrical imperfections that may lead to localized debonding. However, apart from local damage, it is important to note that no sudden change in the behaviour of these curves is depicted, which signifies that damage did not initiate from the edges of the patch. In the second loading of the P1D1-A, a discontinuity in the measurements of the SG positioned on the patch is present at around 250kN. This is attributed to the evolution of damage in the interface or between the plies of the composite. Similar results were obtained for the P1D1-C specimen (Figure 4.12 and Figure 4.13), with the exception of SG-2 which exhibits a divergent non-linear behaviour from the first loading. This non-linearity is attributed to existing flaws during the laminate infusion process, as revealed by the acousto-ultrasonic inspection. More specifically, a poorly bonded area was detected exactly at the area where SG-2 was located, as shown in Figure 4.14.

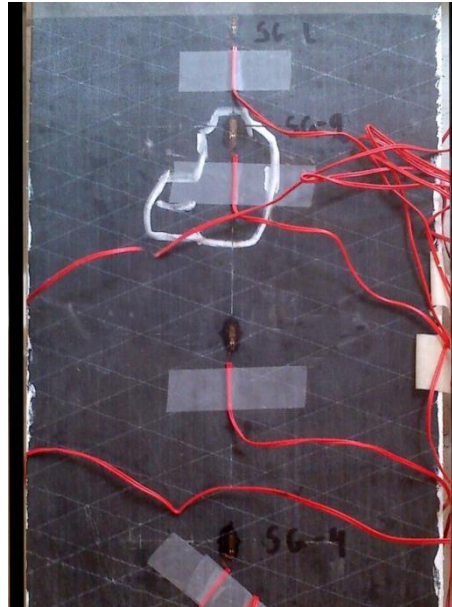


Figure 4.14: Existing manufacturing flaw detected during non-destructive evaluation prior to testing.

Contrarily to the good agreement exhibited for the aforementioned strain gages between the two tests, the behaviour of the central patch gage SG3 was significantly different. At the first loading of specimens P1D1-A and P1D1-C, compressive strains were initially measured, which gradually changed to tensile ones after a certain loading. This pattern was not repeated at the subsequent loadings of the specimen, where SG3 strains were tensile right from the start of the loading. The cause of the initial compressive strains at the centre of the patch (which were measured in all P1D1 specimens) is the secondary bending. This bending owes to the eccentricity of the centre of the cross section of the patched plate with respect to the axis of loading, and has two components, a global bending and a local one just above the notch due to the fact that the cross section has lower bending stiffness at that location. As the load increases, the patch starts to debond locally at the notch area and the load is redistributed in such a way that reduces the bending stresses in the patch. In the subsequent (beyond the first) tensile tests of specimens P1D1-A and P1D1-C, there is already an existing flaw at the central area around the notch and, therefore, SG3 strains become tensile right from the start of the test, since the bending effect of the patch has been significantly reduced. This was also verified from the findings of the acousto-ultrasonic inspection, which are depicted in Figure 4.15. As mentioned earlier, the P1D2 specimens were protected by the use of typical marine coating and were inserted in the environmental chamber to undergo aging before being tested. Moreover, the instrumentation differed from the one employed for the testing of the P1D1 series. These specimens were tested only one time at AIMEN's facilities. The obtained force - strain results are plotted in Figure 4.16.

In the P1D2 series, the trend of the strains measured on the patch (i.e. SG3 SG8 and SG9) is more complex than the one measured in the P1D1 tests. Nevertheless, the results exhibited satisfactory repeatability. SG-6 exhibits identical behaviour with the strains measured in the P1D1 specimens, being tensile and increasing with increasing load. Concerning SG-3, in the case of the aged specimens P1D2-A and B, the strains behaviour at the centre of the patch differed from the one described earlier. The

compressive strains at the start of the test are much lower, which means that a noticeable smaller local bending is taking place for these two specimens. This is the result of inadequate bonding between the patch and the plate around the notch or due to extended unwetted fibres in the patch which has been detected from the non-destructive evaluation prior to testing (see markings in Figure 4.18 and Figure 4.19) and verified from the strain gage measurements. Correlating the markings to the bondline, it was deduced that these refer principally to poor wetting of the carbon fibre plies during the infusion process, as the extent of the dry areas in the bondline (marked in green) was considerably smaller compared to the original markings. This signifies that the major extent of the detected flaws correspond to dry fibres in the laminate. The delamination of the insulating layer at the edges of the patch in Figure 4.19 was caused during the complete removal of the patch from the steel plate after the completion of the tests.

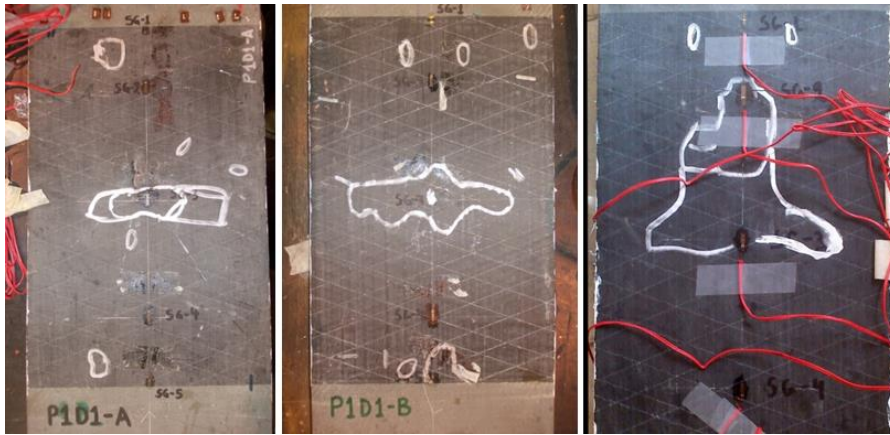


Figure 4.15: Markings denote the debonded/delaminated area after the final testing of specimens.

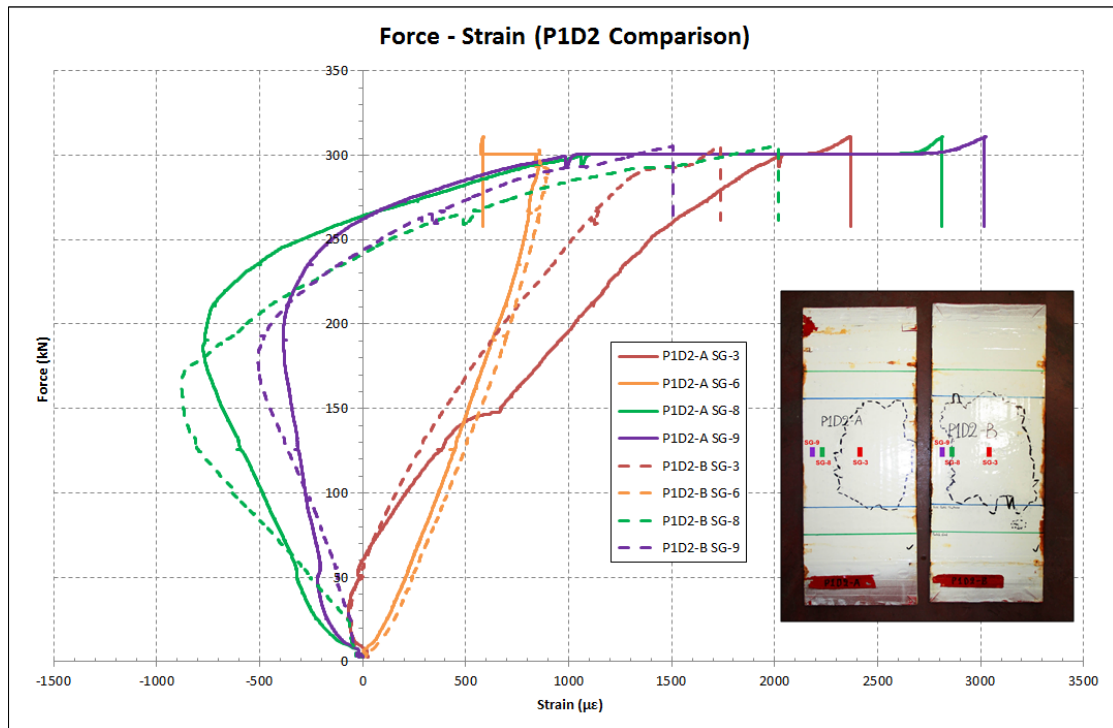


Figure 4.16: Comparison of Force – Strain curves for P1D2-A and P1D2-B specimens.

The effect of secondary bending has been captured also by SG8 and SG9, with SG8 exhibiting higher compressive strains. This is to be expected as the strain gage is positioned exactly above the notch tip and therefore the bending stiffness is at this point is lower compared to the one in SG9 where the steel section is present. It is expected that if it were not for the delamination in the central area of the laminate, SG3 would record even larger compressive strains.

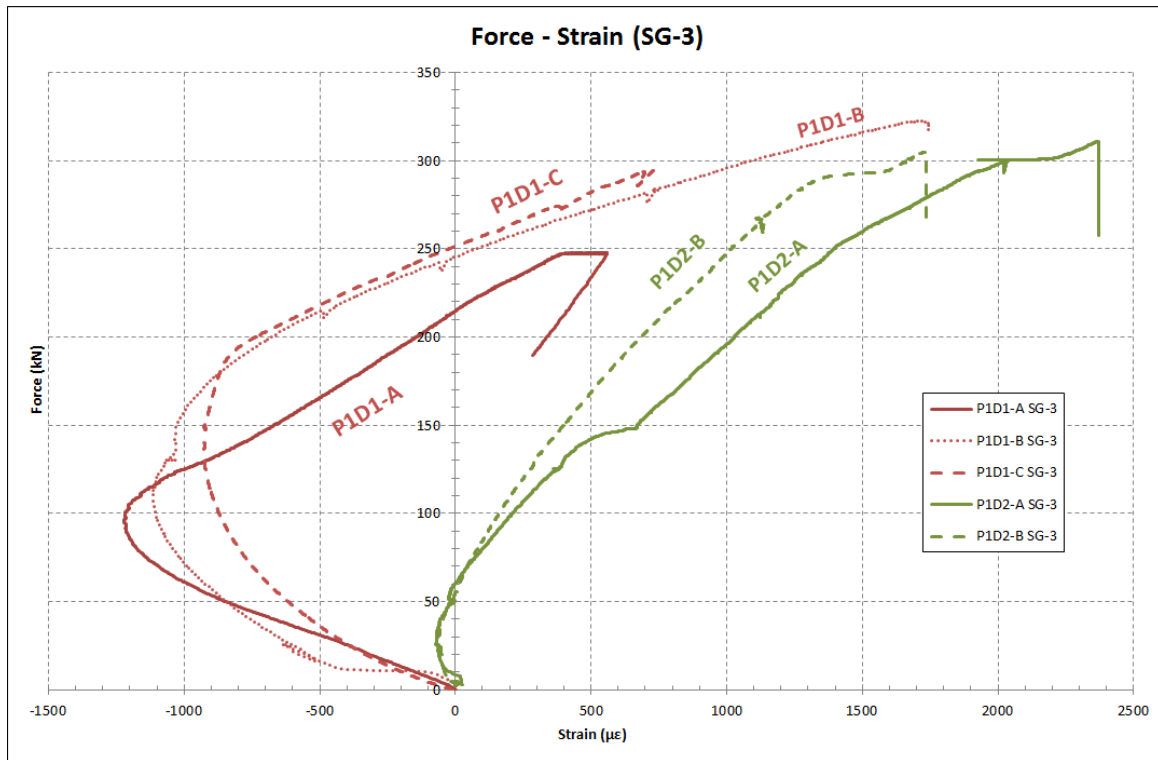


Figure 4.17: Comparison of Force – Strain (SG-3) curves for all P1D specimens.

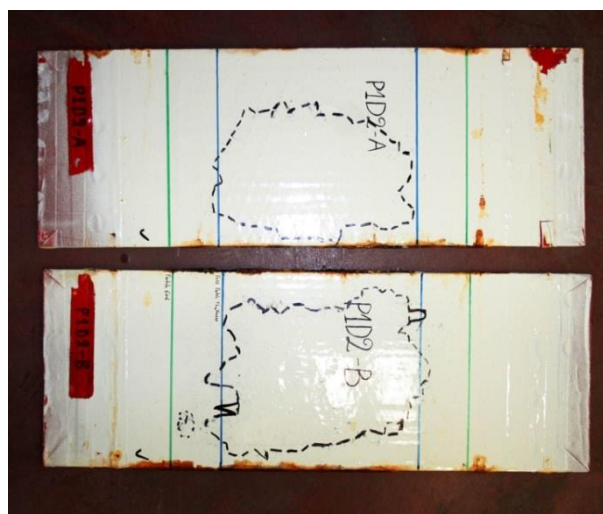


Figure 4.18: Acousto-ultrasonic inspection finding in specimens P1D2-A & B prior to testing.

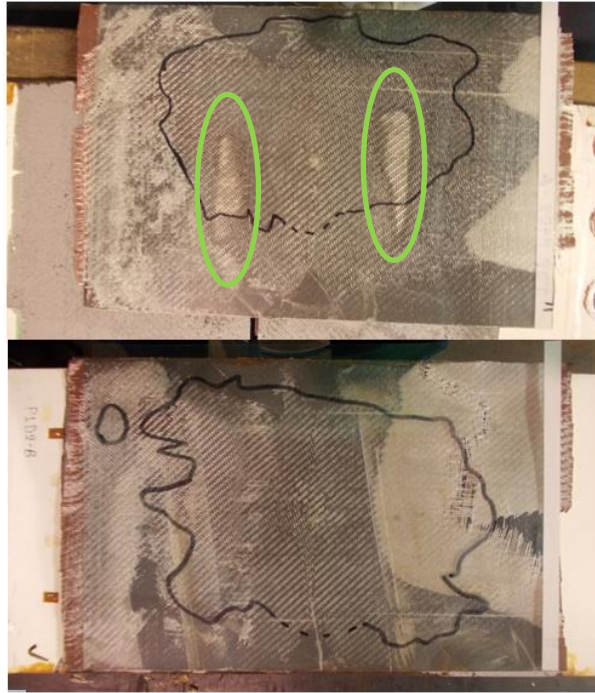


Figure 4.19: Correlation of the outer surface markings to the bondline surface for P1D2-A (left) and P1D2-B (right).

The patch debonding loads of the P1 specimens are listed in Table 4.4. The patch debonding loads are defined as the loads at which the patch ceases to contribute to the load bearing capacity of the specimens. Typically this is reflected in the results by a local maximum after which a sudden drop in the recorded force takes place. This sudden change occurred only in specimens P1D2, while on specimens P1D1 steel failure at bolt holes preceded and therefore the sudden change was not observed. As mentioned earlier, the maximum loads achieved by the vacuum infusion carbon/epoxy patched specimens are almost three times higher than the maximum load achieved by the reference unpatched specimens (approx. 108.6 kN on average). Comparing the results listed in Table 4.4, the lower patch debonding load is greatly influenced by the poor manufacturing quality of the specimens and hence no safe conclusion can be made on the effect of aging and the effectiveness of the coating on these repairs. Nevertheless inspection of the P1D2 specimens after testing revealed no sign of corrosion in the bondline, indicating that the coating provides at least partial protection. As a final conclusion regarding the effectiveness of the patches on the static strength of cracked plates, it can be stated that it can be significant, if a good bond is achieved and proper protection from the environment is applied. More specifically, the patch was still functional at loads three times higher than the yield load of the reference specimens. The problems encountered with yielding of the specimen inside the grips along with the varying manufacturing quality of the patches undoubtedly interfered with the repeatability of the tests. Nevertheless, they were reflected and correctly interpreted in the experimental results. Moreover, the fact that some of the test specimens had to be tested multiple times introduced new variables and further affected the repeatability of the tests.

Table 4.4: Results of P1D specimens.

Specimen	Yield Load [kN]	Patch Debonding Load [kN]	Nominal Applied [MPa]
P1A-C	98.3	-	98.3
P1A-D	93.4	-	93.4
P1D1-A	-	>322.1 ¹	322.1 ¹
P1D1-B	-	>323.1 ¹	323.1 ¹
P1D1-C	-	>295.6 ¹	295.6 ¹
P1D2-A	-	311.1	311.1
P1D2-B	-	305.3	305.3

¹ Failure at the bolt holes. Not patch debonding load.

4.4 Additional testing

Due to the aforementioned reasons, it was decided to perform one additional test with an altered design to account for the factors that interfered with the repeatability of the obtained results. Additionally, this allowed the implementation of optical fibres, which was not possible in the previous tests due to challenges associated with logistic complications and the vacuum infusion process. Based on this design, one additional specimen was manufactured and tested at NTUA's facilities (Kotsidis, 2012). In this case, a steel plate with a narrower tapered width outside the grip area was considered to avoid yielding at the grips. Moreover, the hand lay-up method was used to ensure that there would be no dry spots in the laminate or in the interface between the steel and the patch. The work described in this section was carried out within the framework of the MSc Diploma Thesis of E. Kotsidis, under main supervision and guidance from the author. Two unrepaired notched steel plates with identical geometry to the repaired notch plate were tested in a preceding experimental campaign (Mirisiotis et al, 2007) and served as a reference to quantify the efficiency of the repair.

Specimen Description

The geometry and main dimensions of the steel plates are presented in Figure 4.20. The nominal thickness, t_s , is 4 mm. The central orthogonal reference part has length L_s equal to 400 mm and width W_s equal to 140 mm. The total length of each plate is equal to 662 mm, which includes the transitional and fixtures areas. At their centre, a through thickness initial notch, having length 2α equal to 80 mm was machined using a plasma cutting equipment. In one of the steel plates, on one of its sides (front side) a central composite patch with thickness t_p equal to 5.3 mm, effective length L_p equal to 200 mm and width W_p equal to 200 mm was laminated. The total patch length, including the tapered edges is equal to 300 mm. The

patched specimen is referred to as P1F. The notched steel plates which comprised the reference specimens are referred to as S-C-1 and S-C-2.

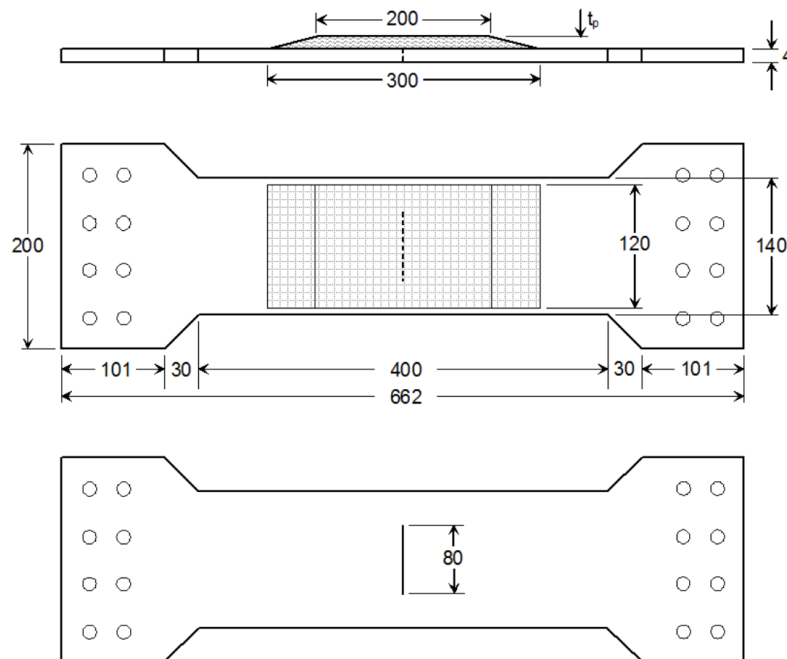


Figure 4.20: Schematic of specimen P1F

The steel plates used for the specimens were provided by ELEFSIS shipyards with Young's modulus equal to 200 GPa and yield stress equal to 348 MPa. The patch consisted of plain weave carbon fibre in epoxy matrix laminated using the hand lay-up method. In total 16 plies of 0/90 plain weave carbon fibres with areal weight equal to 240 g/m² were used. Unlike previous cases, a glass isolating layer was not positioned between the steel and the patch.

Manufacturing Procedure and Instrumentation

Prior to manufacturing, the positions where strain readings would be measured had to be decided. After careful consideration, four Fabry-Perot optical fibres and two 5mm KYOWA strain gages were used to monitor the test. The position of each sensor along with the rationale for choosing it is described in detail below.

- Optical fibre 1 (OF-1) was positioned at the interface between the patch and the steel surface, in the middle of the specimens width, 5 mm from the patch edge.
- Optical fibre 2 (OF-2) was positioned in the interface between the patch and the steel surface, in the middle of the width, 50 mm from the patch edge towards the centre of the specimen
- Optical fibre 3 (OF-3) was embedded between the fourth and the fifth ply of the patch, in the middle of the length of the specimen, 10 mm from the notch edge
- Optical fibre 4 (OF-4) was embedded once again between the fourth and the fifth ply of the patch, in

the middle of the length and the width of the laminate, right above the centre of the crack .

- SG-1 was positioned on top of the patch, exactly at its centre
- SG-2 was positioned on the back face in the centre of the specimens' length, 10 mm from the notch tip.

The optic fibres embedded in the steel/patch interface aim at providing more insight on the evolution of debonding and how the change in the bondline condition is reflected to the sensors in the laminate. The sensors on the surface of the patch and the steel surface are placed for the validation of the numerical models that were developed after the experiments. The P1F instrumentation is illustrated in Figure 4.21.

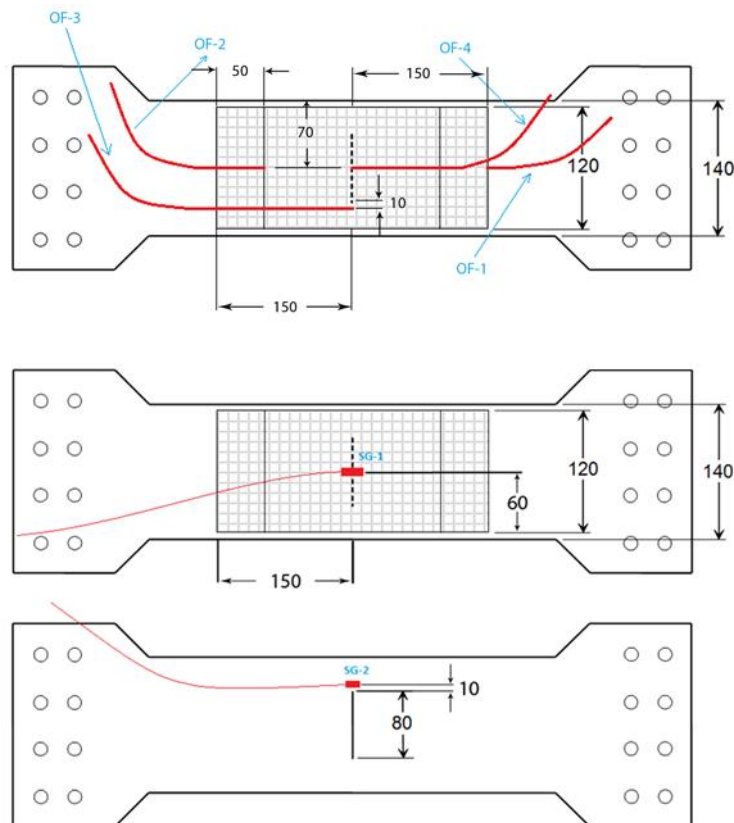


Figure 4.21: Instrumentation of the P1F specimen.

The diameter of the optical fibres was 0.88 mm including the protective layer which could not be removed without damaging the sensor. The steel surface was grit blasted to SA 2½ prior to the lamination and the achieved roughness was measured according to *ISO 4287:1997*. The value of the R_a parameter was equal to 4.49 μm and for the R_z equal to 30.28 μm . The surface was cleaned with the use of Loctite 7063 immediately prior to the lamination to remove any traces of dust or grease from handling the plate. The room temperature was 19.4 °C and the humidity 51% during lamination. The carbon fibre plies were divided in four groups with varying lengths to achieve the desired tapering. After lamination the patch was left to cure in ambient conditions for five days. To accurately position the optical fibres, two fixed laser pointers were used (Figure 4.22). The optical fibres were recording measurements during the lamination and curing processes. This served to detect whether any damage occurred to the fibres from the use of the laminating roller and

secondly to monitor the magnitude of the remaining strains in the laminate due to curing. The measurements indicated that no damage was done to the fibres during the lamination and handling of the specimen, the recorded remaining strains were compressive and ranging from $-60\mu\epsilon$ to $-90\mu\epsilon$. Unfortunately the acousto-ultrasonic equipment was not available at the time of testing and therefore the non destructive evaluation of the laminate/bondline was not possible. However, by using the hand lay-up technique the wetting of the laminates was easier to control compared to the vacuum infusion process. This ensured that no dry spots or poorly wetted areas existed.

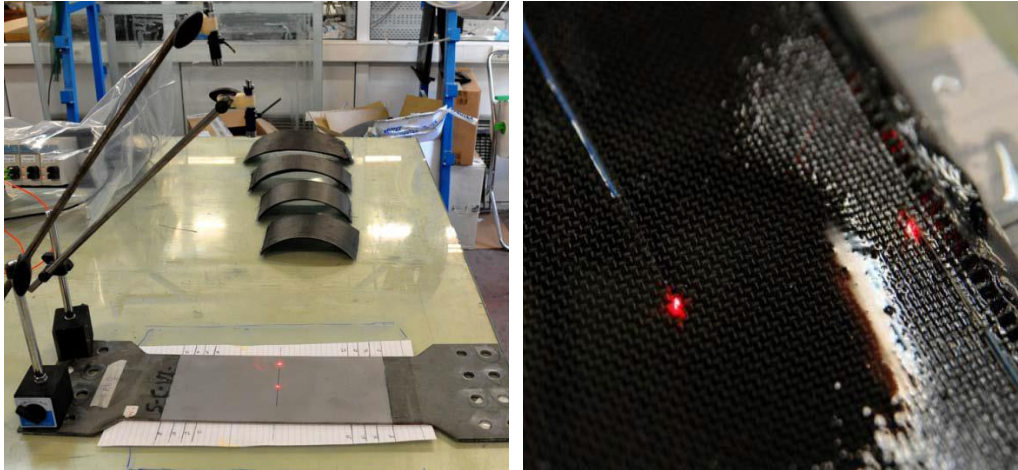


Figure 4.22: Positioning of the optical fibres with the aid of laser pointers.

Experimental Testing

A MTS hydraulic testing machine with a capacity of 250 kN was used for this additional test. A preloading of 25 kN was initially applied on the specimens, in order to minimize the specimen-fixtures assembly tolerances. This preloading was applied as a slow linearly increasing displacement with rate equal to 0.5 mm/min. Then, the specimens were unloaded and afterwards subjected to the final loading in the form of a linearly increasing tensile displacement with the same rate.

The applied force, the total specimen elongation and the longitudinal strains at various locations on the specimen were recorded during each test. In order to precisely measure the specimen's elongation, a LVDT transducer was placed alongside the length between the testing machine fixtures. For monitoring these parameters, the data acquisition system of the testing machine itself was used, together with an additional external Spider-8 system. Moreover a camera was recording the test procedure, focused on the notch area from the free side of the plate.

Results

The force displacement curve for the patched and the reference specimens are plotted in Figure 4.23. The force-strain measurements of both the optical fibres and the strain gages for P1F are concentrated in Figure 4.24. The yield load of the reference specimens and the ultimate load of P1F are listed in Table 4.6.

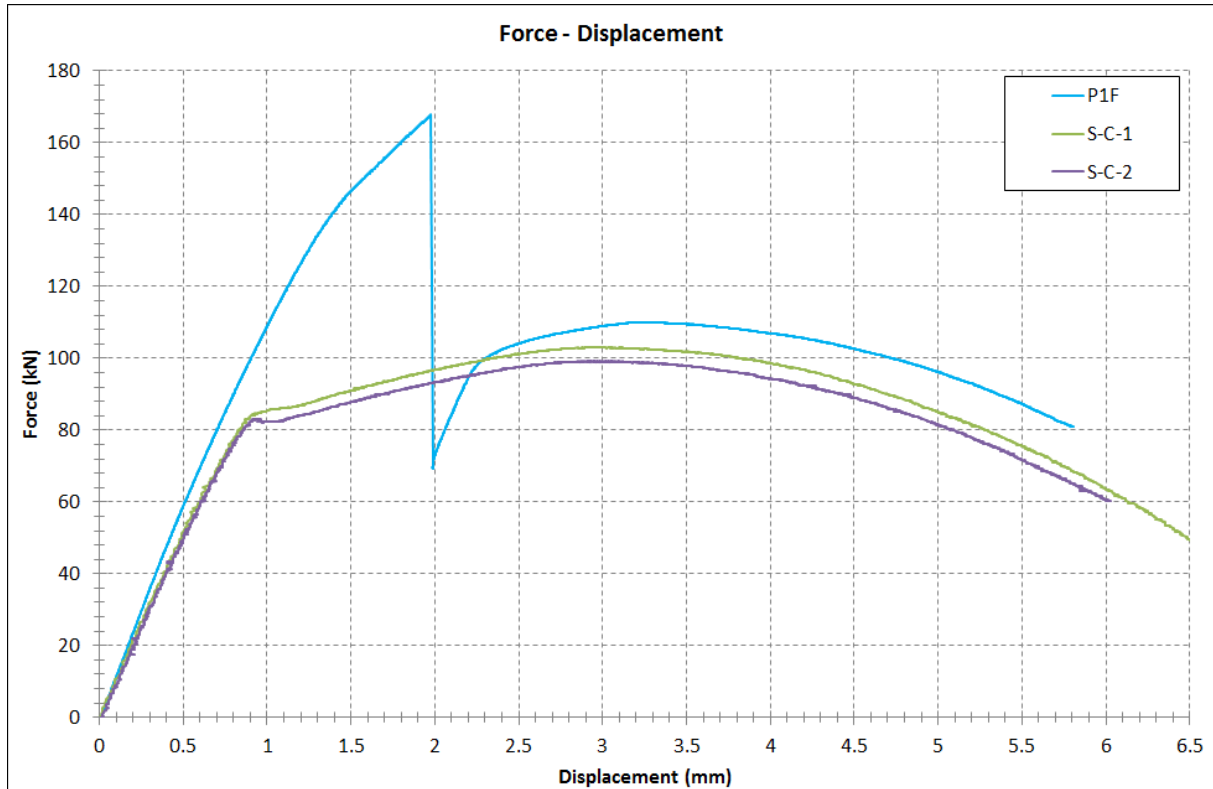


Figure 4.23: Force - displacement curve of the reference and P1F specimen.

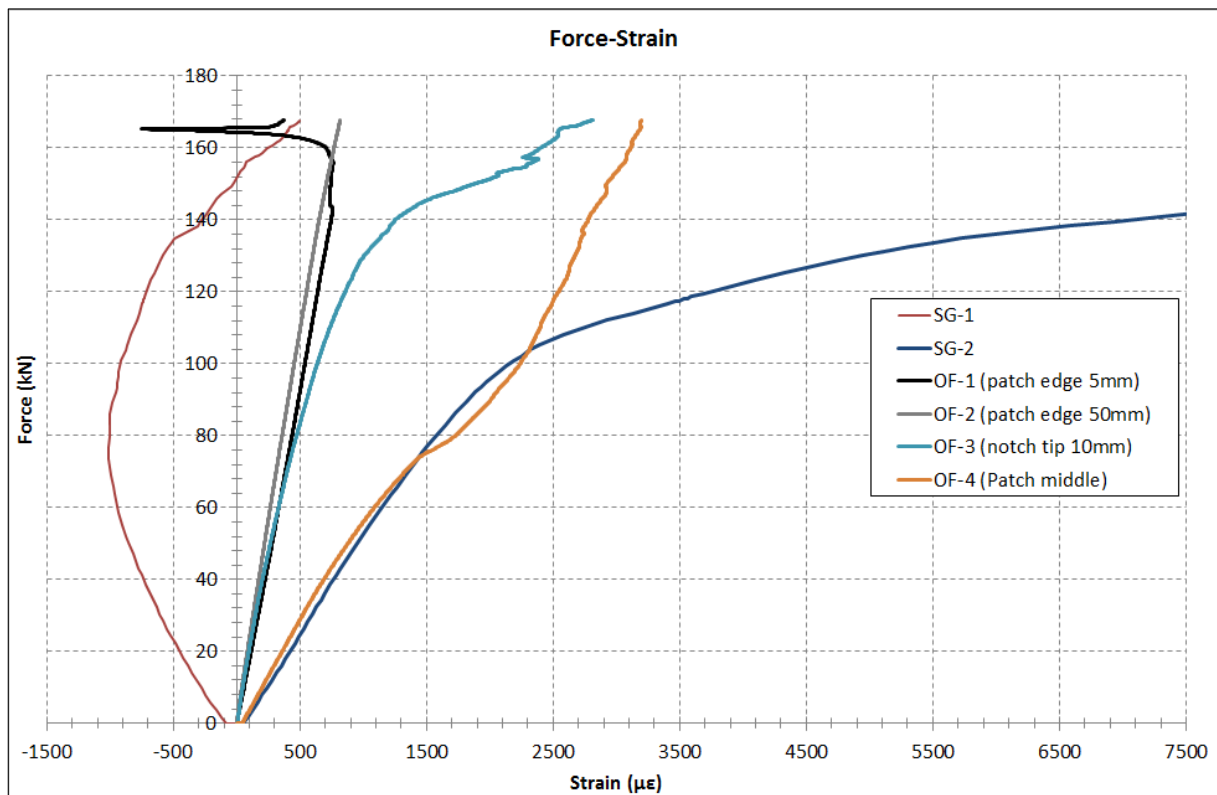
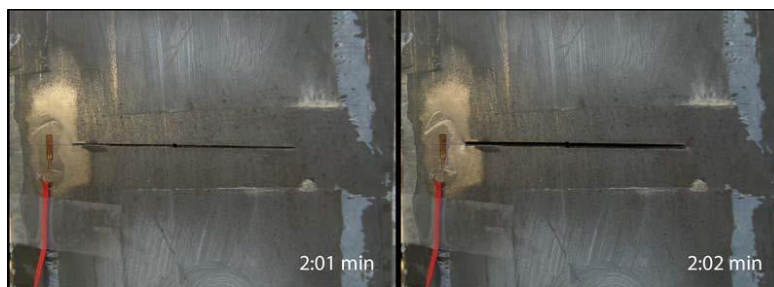
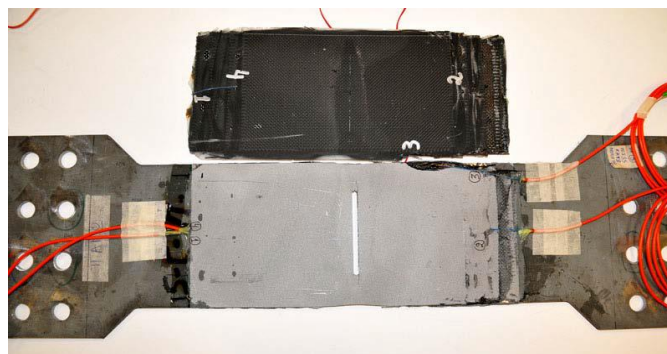


Figure 4.24: Force-strain measurements of P1F specimen.

Table 4.5: Results of reference and P1F specimens.

Specimen	Yield Load [kN]	Patch Debonding Load [kN]	Nominal Applied Stress [MPa]
<i>S-C-1</i>	84.6	-	151.1
<i>S-C-2</i>	82.5	-	147.3
<i>P1F</i>	-	167.7	299.5

The behaviour of the reference specimens is straightforward exhibiting a linear response until about 84 kN after which the specimens yield. Interpreting the force displacement diagram for P1F, the specimen's response is practically linear elastic up to the load of 80 kN. At this point the slope gradually changes assuming a non linear behaviour. The slope changes more notably around 140 kN. The maximum load is achieved at 167.7 kN, at which point the patch stops contributing to the load transfer due to extensive debonding from the steel. The latter leads to the abrupt change of the specimen's stiffness and the redirection of the exerted load in the steel substrate. This is reflected by the sudden drop in the measured load and is clearly visible also in the video frames exactly before and after the failure of the repair (Figure 4.25). Optical inspection and coin tapping of the debonded laminate revealed no visible damage at the composite substrate (Figure 4.26). The latter remark suggests that the evolution of damage was confined at the bimaterial interface between the composite and the metal substrate. Comparing the force displacement curves of the reference specimens to the one of P1F it is evident that the patch increases the load bearing capacity substantially.

**Figure 4.25:** Notch at the back side immediately before and after patch debonding.**Figure 4.26:** P1F specimen after testing.

The changes in the slope of the Force-Displacement curve of the specimen can be explained when combined with the measured strain data (Figure 4.24). The strain measurements after debonding have not been plotted to keep the graph legible. The interpretation of the behaviour of the specimen's strain sensors after patch debonding is straightforward with the strains dropping to zero in the patch and the strains in the steel rising dramatically due to the load redirection. Before analysing the results, an assessment of the position of the optical sensor's measuring gauge was performed where possible after testing, to see whether the fibres dislocated from their nominal positions during the lamination. The detection of the measuring tips was not possible for optical fibres 3 and 4, as these were embedded inside the laminate. Optical fibre 1 was in its predefined position (i.e. 5 mm from the tapered edge) with a slight inclination along the longitudinal axis. Optical fibre 2 was lying in the interface between the first ply and the steel as intended, but 4 mm towards the centre with respect to its predefined position, and slightly inclined. These dislocations (Figure 4.27) were caused by the roller used during lamination.

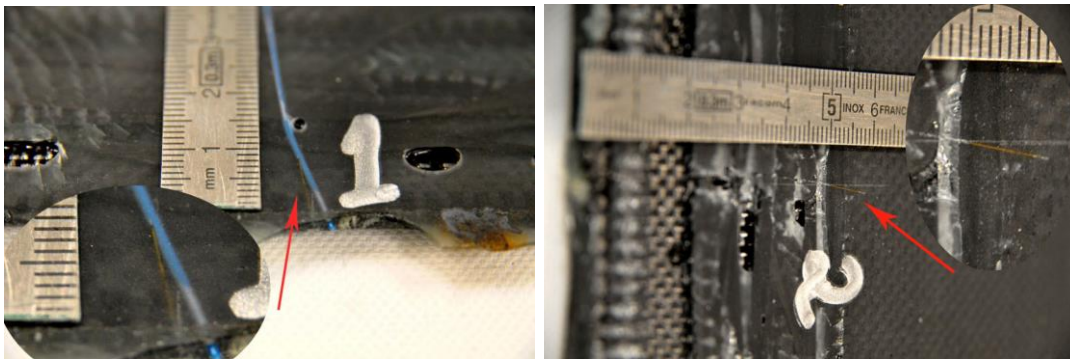


Figure 4.27: Position of optical fibres OF1 (left) and OF-2 (right).

The first inflection point at approximately 77.5 kN is the result of localized debonding between the steel and the composite substrate in the notch area. This is more pronouncedly reflected to the change in the readings of OF-4 which is embedded between the 4th and the 5th layer of the patch. The stiffness reduction of the specimen leads to the alleviation of the compressive bending effect and that is also reflected to the change of the slope of SG-1. This phenomenon has been already observed also in the case of the previously tested P1 plates and was correlated well with the findings of the non-destructive inspections. The effect of the secondary bending is more pronounced at the top of the composite plate (SG-1), as it is more remotely located with respect to the neutral axis. The effect of the load redistribution is also reflected in OF-3 with the slope gradually changing after 80 kN. Moreover, sensors OF-1, OF-3 and OF-4 demonstrated that they were able to capture the evolution of damage at higher loads. The reduction of the strain measured from OF-1 at 143 kN is attributed to the initiation of debonding at the edge of the patch which was also visually validated during the test. The increase of the applied loading led to further propagation of debonding which is signified by the substantial strain reduction from 158 kN until the ultimate load.

Assessing the position of the strain gage and the optical fibres, it appears that OF-1 and OF-4 reflect the evolution of damage more pronouncedly compared to the other positions, as they are positioned in the

vicinity of possible debonding initiation areas i.e. the edge of the patch and on the top of the notch. In particular debonding initiates at the vicinity of the notch and increases in size however at around 145 kN debonding initiates at the tapered edges of the patch as well. The unchanged behaviour of OF-2 and OF-3 denotes that total debonding occurred abruptly rather than progressively. Inflection points at the strain measurements mainly captured by OF-4 OF-3 and SG-1 are associated with the redistribution of the load due to the evolution of damage in the bondline, as the ultimate load is gradually reached.

4.5 Numerical simulations

Numerical simulations were performed based on the specifications of the last experimental test, due to the problems associated with the testing of the previous ones. For the simulations the commercial finite element Program ANSYS 15.0 was used and non-linear analyses were performed incorporating material and geometrical non-linearities. Moreover, to better correlate the numerical results with the experimental ones and in order to understand the damage initiation, evolution and how it affects the overall specimen response two different approaches were followed. The first one consisted of modelling the bondline using continuum elements and ignoring any damage mechanisms. Contrarily, in the second one the bondline was modelled using the cohesive zone modelling approach. Once again the cohesive properties were taken from the literature and were the ones used for the modelling of the P2 plates (Section 3.4), having already proven their validity. In the latter case, no strain results were available for the positions inside the bondline. The generated models were three dimensional and only $\frac{1}{4}$ of the actual specimen was modelled due to symmetry, using hexahedral 20 node elements (SOLID95), whereas the area inserted in the fixture was not included in the finite element analyses. The generated model geometry is illustrated in Figure 4.28, where the composite laminate is represented in blue and the steel in grey. The element edge length varied from 0.625 mm to 5 mm with the mesh being finer at the patch area and coarser at the steel area away from the repair to reduce the computational cost of the analyses.

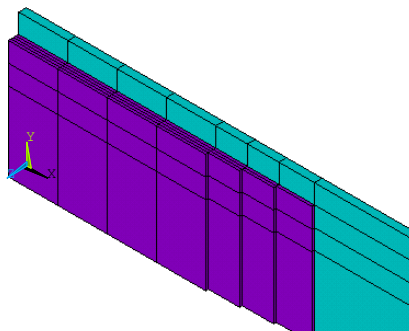
The displacements in the transverse (Y axis) and vertical/thickness (Z axis) directions were constrained at the end of the plate and a displacement in the longitudinal direction was applied. Symmetry boundary conditions were applied in the XY and YZ planes, except for the areas in the notch flanks which were left unconstrained.

The mechanical properties of the materials have been experimentally measured in a preceding experimental campaign. Material properties that were not measured experimentally were derived using data from the literature [Tsouvalis *et al*, 2009]. In the case of the non-linear analysis with no debonding modelling, the bondline was modelled as a separate linear isotropic layer with material properties equal to the unreinforced matrix of the laminate. The Young's modulus of elasticity of the adhesive was taken equal to 4500MPa and the Poisson's ratio equal to 0.25. The composite laminate was modelled as a linear orthotropic material, with properties shown in Table 4.5. Steel was modelled as bilinear elastic plastic with modulus of elasticity equal to 200 GPa and yield stress equal to 348 MPa. The hardening was taken equal to 0.015 times the Young's modulus.

Table 4.6: Patch material properties for the FE model of specimen P1F.

E_1 (MPa)	E_2 (MPa)	E_3 (MPa)	ν_{12}	ν_{23}	ν_{13}	G_{12} (MPa)	G_{23} (MPa)	G_{13} (MPa)
42950	42950	5000	0.30	0.02	0.30	2400	1600	2400

Convergence difficulties were encountered for the model where cohesive elements were employed. Different strategies were investigated to enhance convergence such as changing the element type, the mesh size and the minimum and automatic time stepping that is associated with non-linear analyses, to name but a few. However, it was not possible to obtain a fully converged solution up to the maximum patch failure load without significantly changing the tolerances for convergence. Therefore only partial data are available for the cohesive zone model. Nevertheless, the results obtained are in good accordance with the experimental results, validating the explanation given earlier for the force strain curves. This is further consolidated by comparing the results of the finite element model where no cohesive elements were employed. The comparison between the experimental and numerical results is presented in the following. No strain results were available for the positions inside the bondline for the model which encompassed cohesive elements.

**Figure 4.28:** FE model of the $\frac{1}{4}$ of the specimen.

In Figure 4.29 the force displacement curve is plotted. The behaviour of the continuum, non linear finite element model is straightforward as localised plasticity starts appearing at the notch area at 86 kN, but as the model does not account for debonding and the plastic zone is relatively small, there is no significant change in the slope of the curve. The curve changes slope at around 185 kN when the cross section of the steel plate beyond the patch yields. The results obtained from the finite element model which accounts for debonding are closer to the experimental measurements. Debonding initiates at 108 kN from the vicinity of the crack, but it does not affect the overall behaviour of the specimen as the debonded area is negligible. The slope of the curve starts changing with the propagation of debonding (Figure 4.30) rendering the specimen more compliant and closer to the experimental curve.

In addition, the von Mises stress on both sides of the steel plate are depicted in Figure 4.31 at 157 kN, illustrating that the steel areas have entered plasticity (depicted in grey colour) in the vicinity of the notch area in greater extent in the unpatched side, which is reasonable. Apart from the force displacement curves,

the force strain curves are depicted in Figure 4.32 to Figure 4.35. Comparing these, it is evident that the model encompassing the cohesive elements can represent accurately the experimentally recorded measurements.

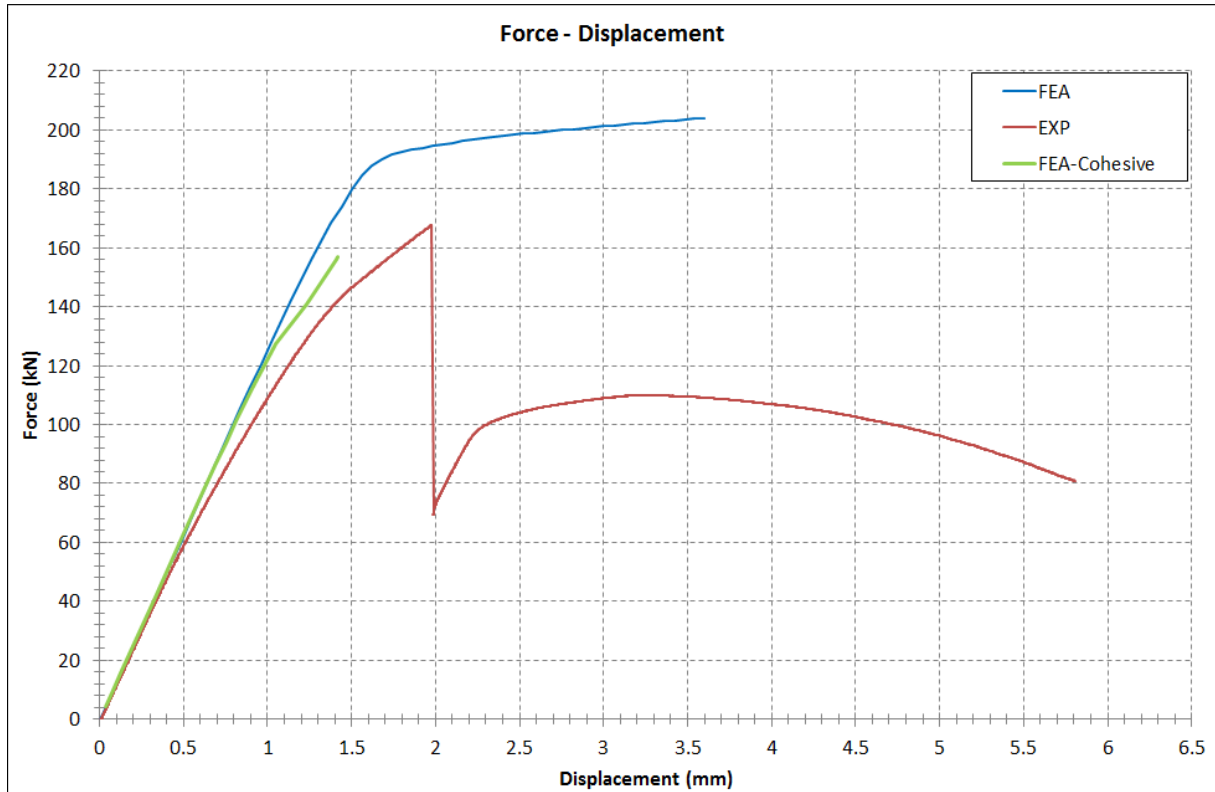


Figure 4.29: Force displacement curves.

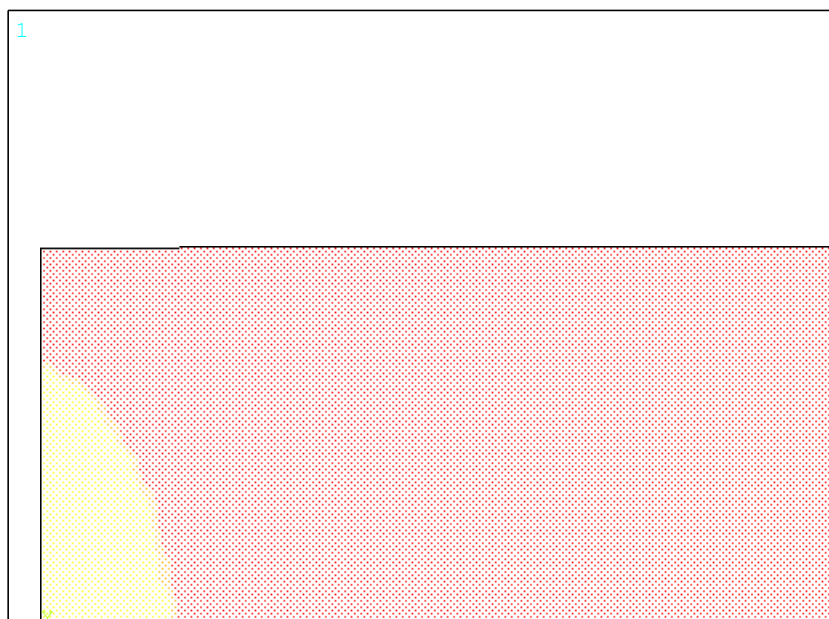


Figure 4.30: Debonding status at 157 kN.

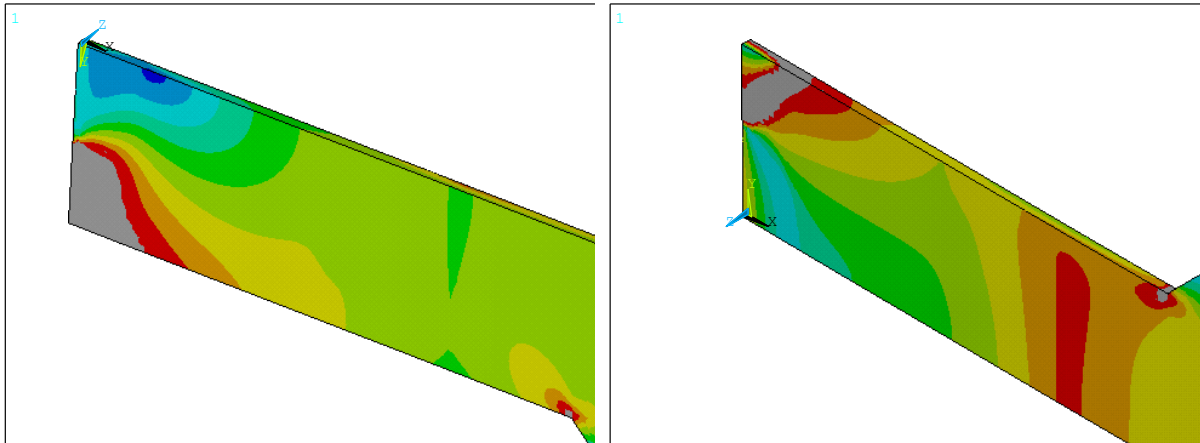


Figure 4.31: Von Mises stress distribution on the unreinforced side (left) and on the reinforced side (right) of the steel plate, at 157 kN.

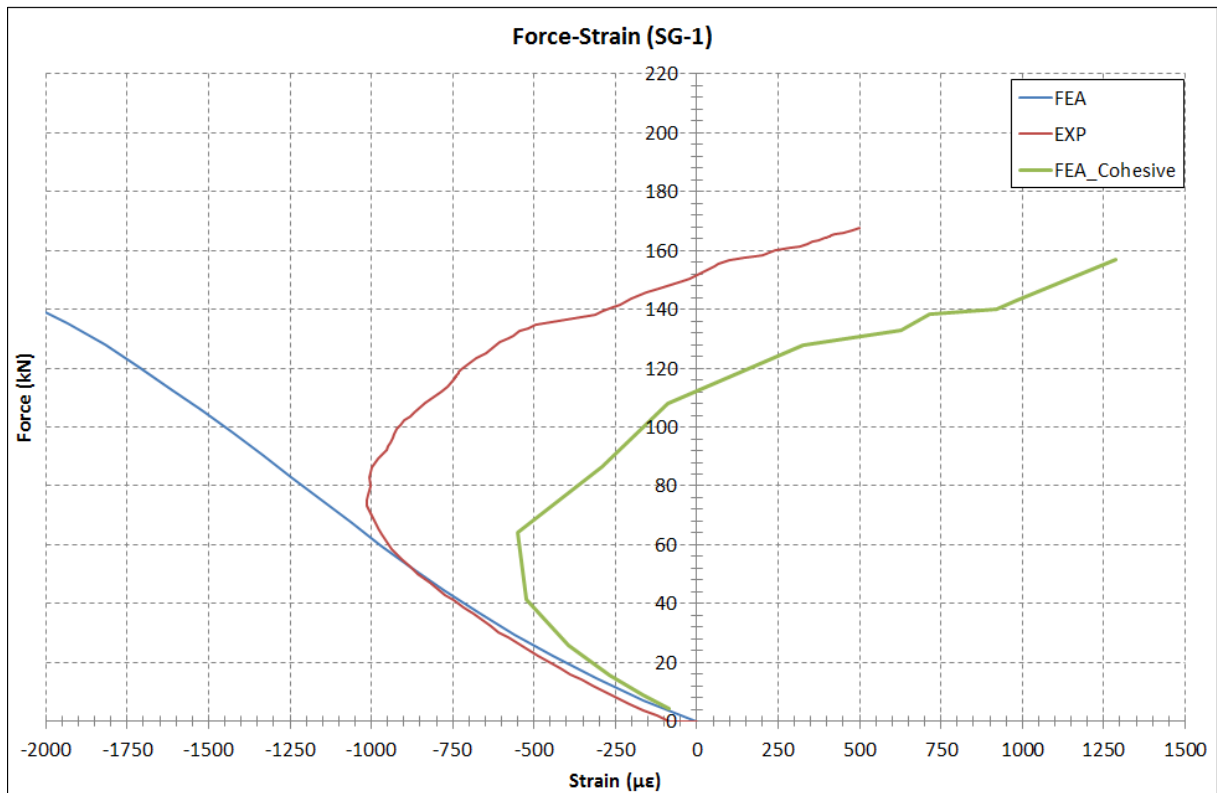


Figure 4.32: Strain gage-1 measurements.

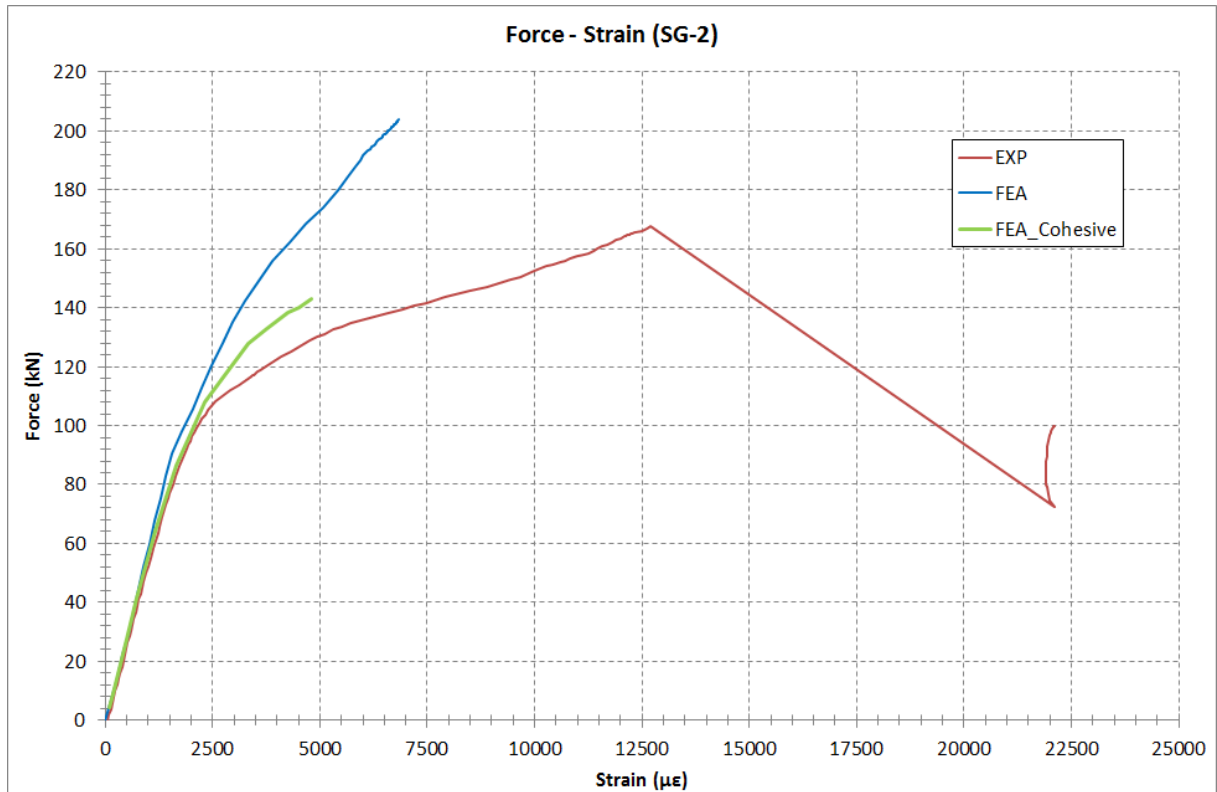


Figure 4.33: Strain gage-2 measurements.

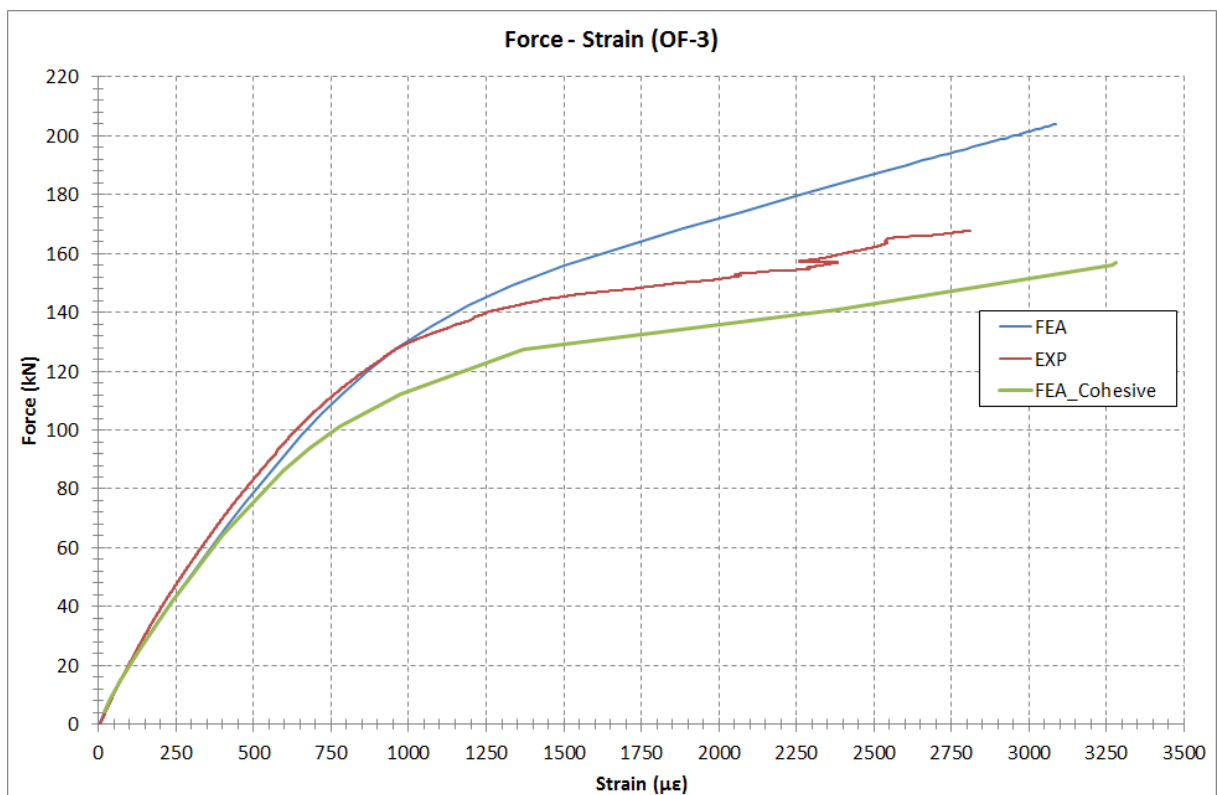


Figure 4.34: Optical fibre 3 measurements.

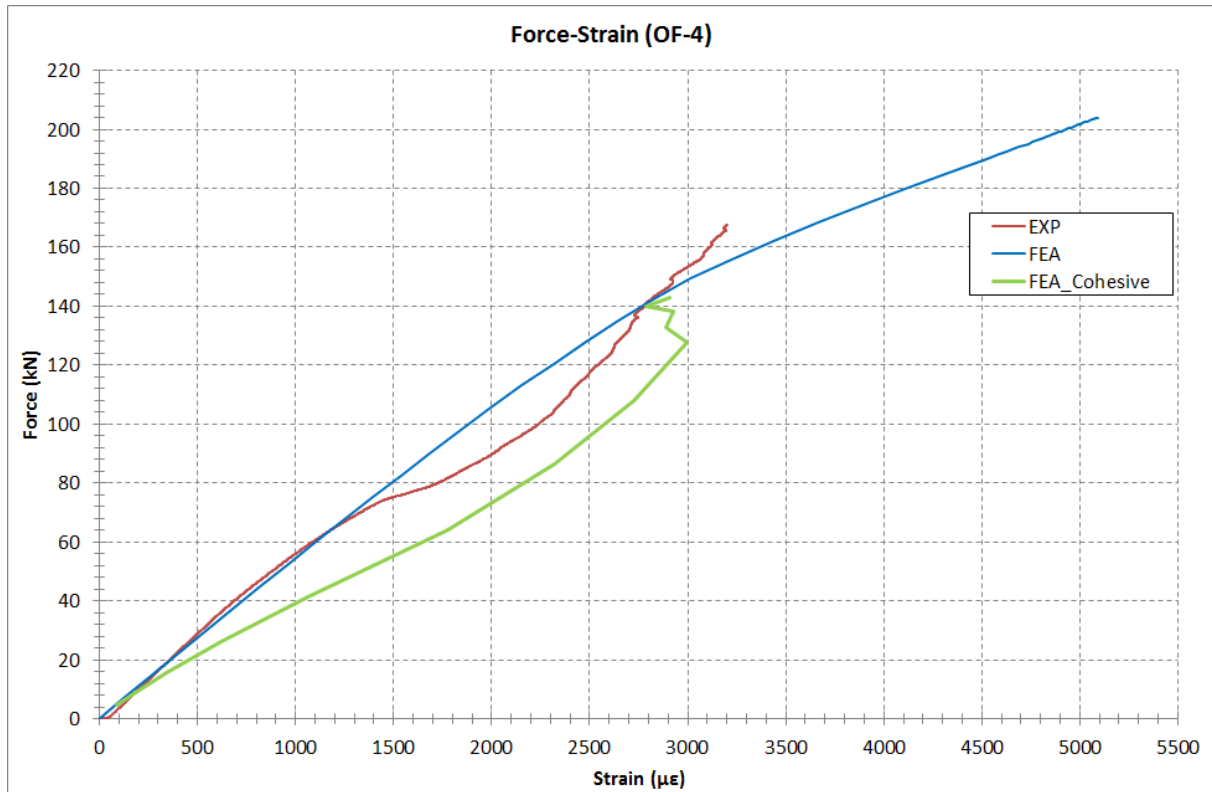


Figure 4.35: Optical fibre 4 measurements.

4.6 Conclusions

An experimental campaign was conducted to investigate the effectiveness of composite patch repairing on the rehabilitation of notched steel plates. Regarding the effectiveness of the patches on the static strength of cracked plates, it can be stated that it can be significant, given that a good bond is achieved and proper protection of the repair from the environment is applied. More specifically, comparing between the debonding loads of the patched plates to the maximum loads of the unpatched ones, the load increase was 2.9 times higher for the P1D1 specimens. Debonding initiated from the vicinity of the patch area in all cases which was also validated by the developed finite element models. Regarding the additional specimen in which optical fibres were placed, results indicate that a limited number of optical fibres embedded in suitable positions can provide sufficient structural health monitoring, detecting damage initiation which might potentially lead to catastrophic failure of the repair. Additionally, cohesive zone modelling was able to represent satisfactorily, although partially the behaviour recorded in the experimental procedure and validated the failure mechanisms. At the same time however, there are also some limitations with the use of cohesive elements, as they are more computationally expensive and might be subject to convergence difficulties as in the presented case.

5. Experimental investigation of repaired cracked plates subjected to fatigue loading

5.1 Introduction

This experimental program includes fatigue testing of plates with a central notch which were reinforced with a one-sided composite patch. This type of plates is denoted as P3 throughout this thesis. The main objective is to experimentally prove in a systematic way that the use of a composite patch increases the fatigue life of a defected steel structure. Another objective is to provide solid and systematic experimental data, which will be used to assess the effect of various patch design parameters. The tests are categorized taking into account the aging scenario and finally the surface preparation method.

5.2 General characteristics

Specimen Description

The geometry and the main dimensions of the specimen plates are presented in Figure 5.1. The nominal thickness of the steel plate, t_s , is 5 mm. The central orthogonal reference part of the steel plate has length L_s equal to 400 mm and width W_s equal to 200 mm. The total length of the plate is equal to 554 mm, which includes the fixtures areas. At the centre of this plate, there is a through thickness initial notch, having length 2α equal to 50 mm which has been opened using wire Electric Discharge Machining (EDM). On one of the plate's sides (front side) a composite patch with thickness t_p equal to 3.3 mm, effective length L_p equal to 200 mm and width W_p equal to 200 mm is installed. The total patch length (L_{pt}) is equal to 300 mm, since it additionally includes the tapered edges of the patch. A total of fifteen (15) specimens were tested. Twelve (12) of them were patch repaired, while the remaining three (3) were notched and not reinforced. The latter served as a reference and were used to assess the efficiency of the repair method. All specimens had the same nominal geometrical features.

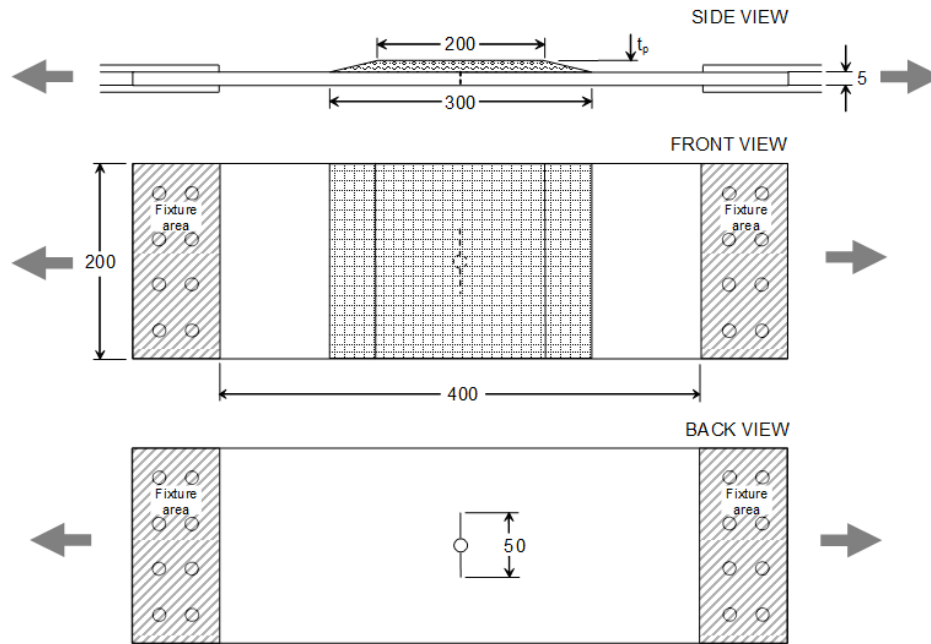


Figure 5.1: Geometry of P3 plates.

As with the previous specimens that were statically tested, the specimens' width exceeded that of the grips of the testing machine. Therefore in order to achieve the uniform loading of the specimens, the special steel fixtures that were described in the previous sections were used. The actual dimensions of all specimens are shown in Table 5.1.

Materials and Manufacturing Procedure

The composite patches used for the rehabilitation of the plates were manufactured by a carbon/epoxy system using the vacuum infusion method (VI-CE), and in all cases comprised of unidirectional plies that had the fibre direction normal to the crack length. The materials and manufacturing procedure used were the same followed for the P2 and P1D static specimens and were produced by AS2CON. Prior to the vacuum infusion process, the plates had their surface treated according to the selected methods described in the following section. The composite laminate was infused in two steps in an attempt to achieve better wetting of the fibres. The conditions during the manufacturing of the specimens were 35°C and 30% humidity for the first step and 35°C and 33% humidity for the second. The infusion process is depicted in Figure 5.2.

Table 5.1: Specimens' geometry

Specimen	Dimensions					
	W_s	L_s	t_s	L_{pt}	L_p	t_p^1
	[mm]	[mm]	[mm]	[mm]	[mm]	[mm]
P3A-C	199.0	399	5.1	-	-	-
P3A-D	199.5	399	5.1	-	-	-
P3A-E	200.0	399	5.1	-	-	-
P3D1-A	200.6	400	5.1	299.1	200.9	3.4
P3D1-B	201.0	400	5.1	300.6	201.0	3.3
P3D2-A	200.6	400	5.1	301.0	198.8	3.4
P3D2-B	200.7	400	5.1	299.5	200.6	3.3
P3D3-A	201.1	400	5.1	300.9	200.5	3.3
P3D3-B	201.0	399	5.1	301.0	201.2	3.4
P3D4-A	201.3	400	5.1	301.0	195.0	3.3
P3D4-B	200.3	400	5.1	297.7	202.3	3.2
P3D5-A	200.8	399	5.1	297.9	200.1	3.3
P3D5-B	200.9	400	5.1	301.9	199.5	3.3
P3D6-A	200.8	401	5.1	299.9	200.6	3.5
P3D6-B	200.7	400	5.0	299.3	200.3	3.2

¹ The full patch thickness was measured more accurately after testing and removal of the patch. Average values from nine measurements.

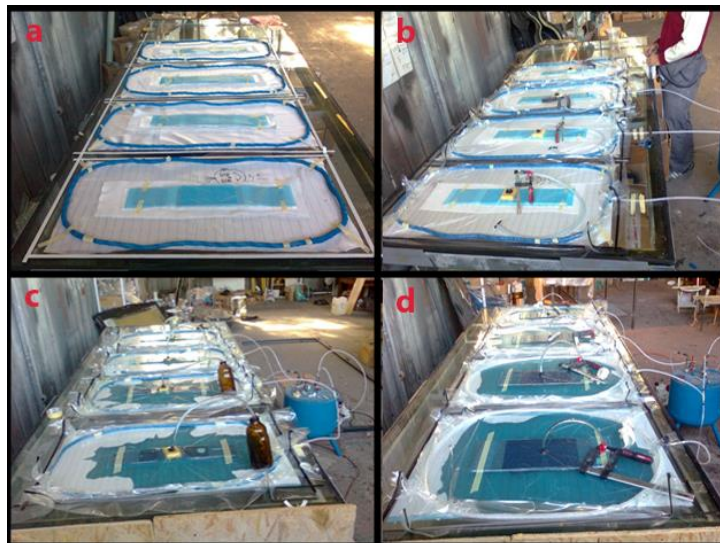


Figure 5.2: Specimens' manufacturing (Figure provided by AS2CON).

Surface Treatment

After proving that grit blasting ensures an efficient adhesion and performance of the composite repair from the previous static tests, it was decided to additionally investigate the effectiveness of an alternative surface preparation method. The second method consists of using a power tool. This was decided as, when due to safety or other constraints grit blasting is not possible, the use of power tools is more practical. In particular, treatment of the surface with a needle gun scaler (NG) was selected (Figure 5.3). The needle gun is typically used for the removal of old paint or/and rust from a surface, hence it was only logical to investigate whether the surface can be treated satisfactorily for bonding with the same tool employed for cleaning it. A needle gun has a set of very fine chisels known as needles; the tool forces these needles against a work surface at variable speeds up to around 5,000 times per minute. Different models offer choices of number of needles, operating speed, and power levels. Many models use compressed air, although electrical needle-guns do exist. The main advantage of the needle gun over other scaling tools is that the needles automatically adjust themselves to contours, making the tool a good choice for cleaning irregular surfaces. A needle gun can clean an area to bare metal in seconds, and compares well to other scaling tools in terms of accuracy and precision. Moreover, as with grit blasting, this surface preparation method is characterized by low cost, ease-of-use, and can be found in every shipyard.



Figure 5.3: Example of needle gun scaler.

Aging Process

After the curing of the patch laminate, some of the specimens were painted with a common marine paint and were subjected to accelerated aging conditions into an environmental chamber according to ISO 14993:2001 with 5% NaCl solution. The specimens subjected to the aging process were exposed for 300 cycles (100 days) and 450 cycles (150 days) under cyclic corrosion (including salt mist, dry and wet conditions in different temperatures), depending on the selected scenario and were subsequently tested. Details about the conditions of one accelerated corrosion cycle are presented in Table 2 in Chapter 2. The specimens were recursively repositioned inside the environmental chamber during aging, so as to ensure uniform exposure of the specimens to the environmental conditions, depending on the selected scenario and were subsequently tested in fatigue.

Specifically, specimens P3D2-A, B and P3D5-A, B were exposed for 100 days (300 aging cycles), while specimens P3D3-A, B and P3D6-A, B for 150 days (450 aging cycles). The areas that would subsequently enter the grips of the testing machine were protected from corrosion with vinyl tape. Specimens subjected to

the accelerated aging conditions inside the environmental chamber can be seen in Figure 5.4. The specimen nomenclature for their identification is listed in Table 5.2. Each specimen has its own code name depending on the category it belongs to. For example, specimen P3D2-B is the second specimen of the series of identical P3 plates that have a Carbon/Epoxy patch manufactured with the Vacuum Infusion method and the steel surface grit blasted prior to lamination. The specimens that had undergone aging are denoted with an (A) in the Aging column followed by the number of days exposed (100 or 150 days). Those that did not, are denoted with N/A. So, the specimen of the example above belongs to the category of specimens subjected to the aging procedure for 100 days. It is reminded at this point that a protective coating was applied on all specimens that underwent aging.

Table 5.2: Surface preparation and aging scenarios of P3 specimens.

SPECIMEN	Surface Preparation	Aging
P3D1-A	Grit Blasting	N/A
P3D1-B	Grit Blasting	N/A
P3D2-A	Grit Blasting	100 days
P3D2-B	Grit Blasting	100 days
P3D3-A	Grit Blasting	150 days
P3D3-B	Grit Blasting	150 days
P3D4-A	Needle gun	N/A
P3D4-B	Needle gun	N/A
P3D5-A	Needle gun	100 days
P3D5-B	Needle gun	100 days
P3D6-A	Needle gun	150 days
P3D6-B	Needle gun	150 days



Figure 5.4: Painted P3 specimens placed into the environmental chamber.

Specimens Instrumentation

In this series of experiments, the two magnitudes that were monitored were the crack propagation rate in the steel plate from the unreinforced side, and the evolution of debonding of the patch. To this end, strain gages were positioned on top of the patch in possible areas of debonding and crack gages were positioned near the notch tip so as to monitor the crack propagation rate in the steel substrate. More specifically, three strain gages were attached on the patch. Gages SG-1 and SG-2 were positioned at the edges of the full patch length, whereas gage SG-3 was positioned at the centre of the patch, over the notch, as shown in Figure 5.5. In the case of the reference specimens and the non-aged specimens P3D1-A and P3D4-B, two crack gages (CG-1 and CG-2) were bonded at the back side of the specimens. The crack gages were placed next to the notch tip, sequentially one after the other (Figure 5.6).

The instrumentation in the remaining specimens differed. On specimens P3D1-B and P3D4-A, two additional crack gages were placed as shown in Figure 5.7, so as to monitor the evolution of the crack in both sides of the initial notch. Crack gages on each side were positioned in contact with each other and in a short distance from the notch tip. After careful examination of the results of the aforementioned specimens, a different instrumentation was applied on the remaining specimens (namely P3D2-A, B, P3D3-A, B, P3D5-A, B and P3D6-A, B). In these specimens only two crack gages were placed as shown in Figure 5.8. CG-1 was placed closely to the notch tip while CG-2 at the end of the specimen's width, as it was considered more important to record the crack propagation at the final stages of crack growth. The gage length of the crack and strain gages was equal to 25 and 5 mm respectively. After the installation of the crack gages, the distances between the notch tip and CG-1 and between CG-1 and CG-2 were accurately measured using a stereoscope (see Figure 5.9). These two distances were used for the determination of the total crack length at each time step in the crack length to number of cycles (α -N) diagrams.

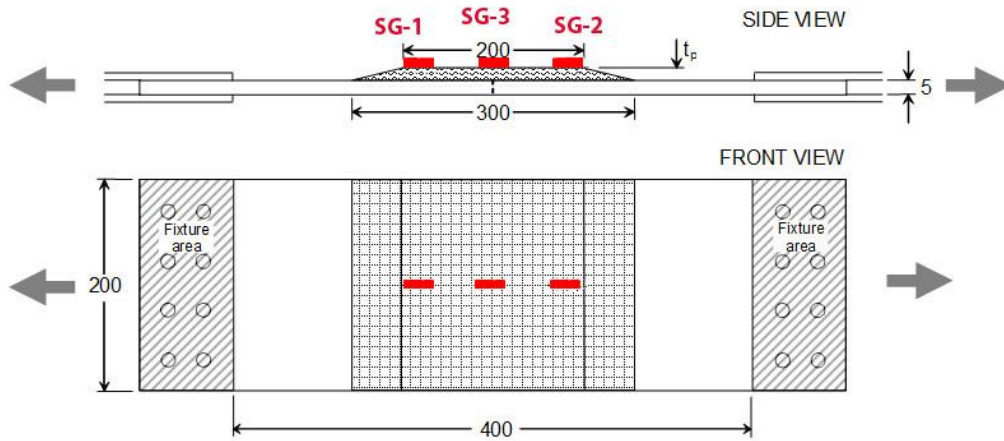


Figure 5.5: Position of strain gages on P3 specimens.

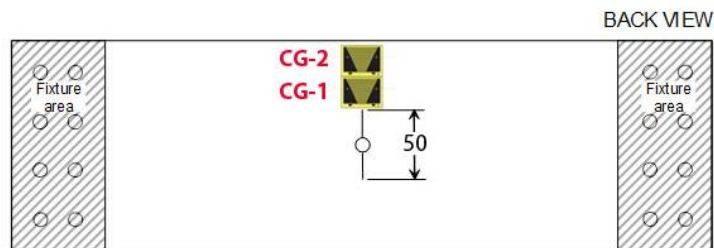


Figure 5.6: Instrumentation of specimens P3A-C, P3A-D, P3A-E, P3D1-A and P3D-B

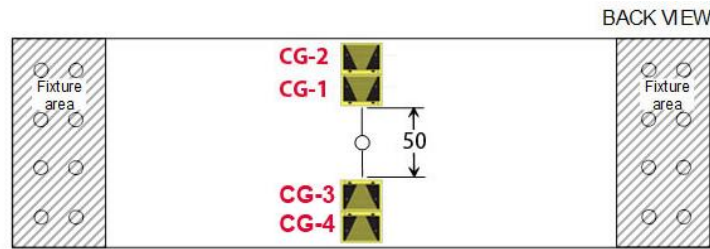


Figure 5.7: Instrumentation of specimens P3D1-B and P3D4-A.

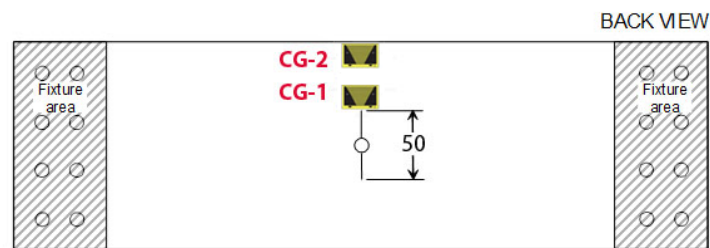


Figure 5.8: Instrumentation of specimens P3D2-A, B, P3D3-A, B, P3D5-A, B and P3D6-A, B.

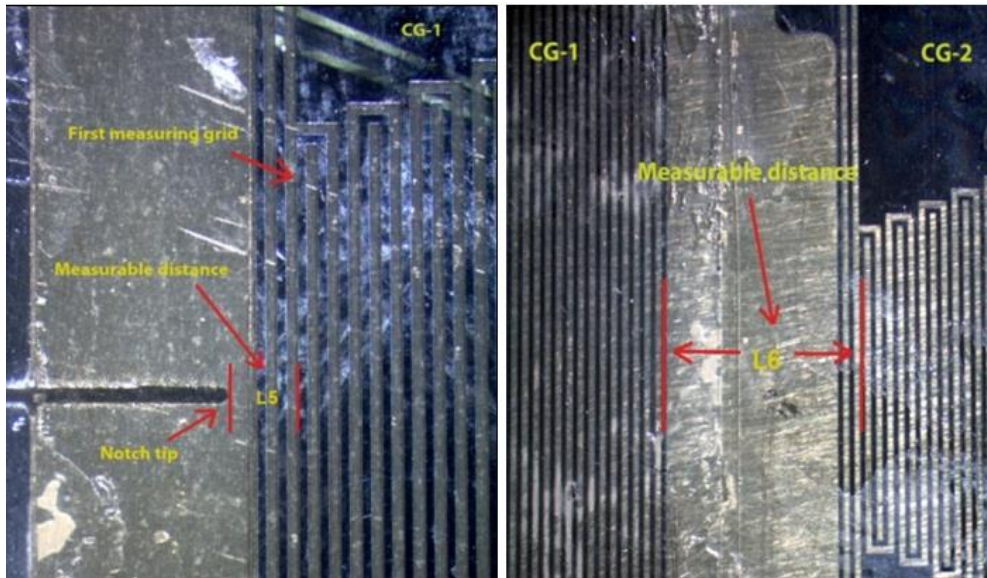


Figure 5.9: Definition of distances between notch tip and CG-1 and between CG-1 and CG-2.

5.3 Experimental testing and results

Test Parameters

A MTS hydraulic testing machine with a capacity of 250 kN was used for the fatigue tests of the specimens. In the case of the reference unpatched specimens P3A-C, D and E, a force controlled preloading was initially applied by a sinusoidal 5 kN to 105 kN force for 2 cycles (0.02 Hz loading frequency) in order to minimize the specimen-fixtures assembly tolerances and make sure that there was no problem with the experimental setup and the data acquisition system. Subsequently, the same loading (5 kN to 105 kN) was applied with a 2 Hz frequency until the specimen failed. In each P3A test, the applied force, total specimen elongation and number of loading cycles were measured, along with the measurements of the crack gages.

For the patched specimens, a force controlled preloading was initially applied by a sinusoidal ± 100 kN force for 2 cycles (0.02 Hz loading frequency) in order to minimize the specimen-fixtures assembly tolerances and make sure that there was no problem with the experimental setup and the data acquisition system. Subsequently, the same loading (± 100 kN) was applied with a 2 Hz frequency until specimens' failure. In Figure 5.10, specimen P3D4-B is depicted while being tested. The loading frequency of 2 Hz was decided in an attempt to reduce the required testing times.

The loading range differed between the reference and the repaired specimens. This difference was decided subsequently, as when the first P3A specimen was tested in the original range of ± 100 kN, buckling occurred during compression. Since a significant percentage of the patched specimens were already tested, an identical scenario could not be followed for all the specimens. However, taking into account that crack propagation is considered to advance only due to tension (*BS 7910:2005*), the results from the reference tests can be used, as the tensile stress amplitude for the specimens was the same and equal to $\Delta\sigma$. In reality, the patched specimens have been tested in a more punishing scenario as far as the bimaterial

interface crack is concerned due to the alternating out of plane movement caused by the secondary bending effect during the alternation of the load.

For the P3D specimens, once again the applied force, total specimen elongation, number of loading cycles, and the crack gage measurements were recorded during each test. In addition, strain measurements were recorded. More specifically, the strains were monitored every 2000 cycles for a duration of 6 cycles, whereas the crack length once every 200 cycles. To monitor these parameters, the data acquisition system of the testing machine itself was used, together with an additional external Spider-8 system, synchronized with each other.

In addition, an acousto-ultrasonic device (BONDMASTER 1000e) was employed prior and during testing to inspect possible debonding and/or delamination of/in the patch. The BONDMASTER findings prior to the fatigue testing (first inspection) were marked on the patch with a marker. In this way, an initial evaluation of the quality of the bond and the composite patches themselves was made in all P3D specimens. Additionally, the propagation of debonding was also monitored for the majority of specimens performing periodic inspections during testing, and marking the extent of debonding on the surface of the patch. In all cases, debonding started from the centre of the specimen above the notch and gradually extended to the edges along the width of the plate. Following the test results, an attempt was made to correlate the initial findings from the NDT method to the final number of cycles for each specimen.

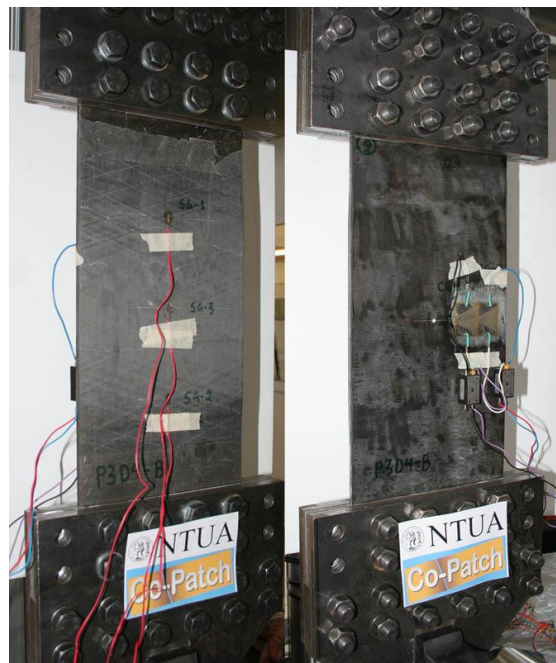


Figure 5.10: Both sides of specimen P3D4-B while tested in fatigue.

Results

In total fifteen (15) specimens have been tested in fatigue. In six of them the steel surface was grit blasted, on the other six the needle gun was used as the surface preparation method, while the remaining three were unpatched and served as a reference. Eight specimens (four grit-blasted and four needle gun treated) were

subjected to accelerated aging conditions into an environmental chamber, half of them for 100 and the other half for 150 days. Details of the aging scenario are listed in Chapter 2. All the fatigue experimental measurements are presented below in the form of tables and graphs. It must be reminded at this point that crack gages were not installed exactly on the same position in all specimens, as well as the fact that the number of cycles required for crack initiation varied unpredictably in each specimen, depending basically on the actual geometry and possible eccentricity of the notch, as well as on the specific shape of its tip. Therefore, in order to make a meaningful comparison between the fatigue life of the specimens, the number of cycles N_{36-83} from a crack length of $a = 36$ mm up to $a = 83$ mm was selected for comparison. These two values were selected as the minimum and maximum crack lengths for which we had measurements from the crack gages for the majority of the tested plates. Table 5.3 shows the percentage difference between the fatigue life N_{36-83} of the pairs of identical specimens, as an indication of the repeatability of the tests. Specimen P3D6-B failed prematurely due to buckling and therefore is not taken into account. Additionally, an error occurred during data logging of specimen P3D6-A which rendered the number of cycles that correspond to 83 mm crack unavailable. The total number of cycles up to fracture N_{25-f} and the number of cycles from a crack length $a=36$ mm up to fracture N_{36-f} are also listed for reasons of completeness. As it is shown from the results, in the cases of specimens P3D1 and P3D5, the difference in the fatigue life of the nominally identical specimens is significant. The results will be analysed in detail in the following.

Table 5.3: Fatigue results of P3D specimens.

Specimen	N_{25-f}	N_{36-f}	N_{36-83}	Difference
P3A-C	118615	49199	48917	
P3A-D	110401	43513	43175	
P3A-E	120607	45062	44989	
P3D1-A	183300	140738	102153	37.8%
P3D1-B	273756	196271	164160	
P3D2-A	343504	260024	241953	14.3%
P3D2-B	311460	235306	207333	
P3D3-A	117050	86405	83485	0.4%
P3D3-B	126799	85503	83132	
P3D4-A	121527	100520	99193	3.9%
P3D4-B	166193	107904	103220	
P3D5-A	53964	40561	39314	45.3%
P3D5-B	107380	73635	71823	
P3D6-A	97754	66672	-	-
P3D6-B	23843	N/A	N/A	-

Representative recordings of the strain gages versus time are depicted in Figure 5.11. However, unlike the case of the static tests, where strain gages provided insight in the failure mechanisms of the repair, in the

fatigue experiments they were only able to capture the overall increasing compliance of the specimen due to the crack growth and the evolution of damage in the bondline. This becomes apparent in the trends of the strain range measurements with SG-1 and SG-2, increasing at the latest stages of the test. This is caused by the substantial debonding at the interface which redistributes the load to the patch during tension. Contrarily, during compression the crack flanks come in contact and the part of the load is redistributed once again back to the steel specimen which practically resumes the original axial stiffness and therefore strains remain almost unchanged over time. Unlike SG-1 and SG-2, gage SG-3 measurements show a global increase of the compressive strains with the evolution of damage. In tension the decrease of strains is caused by the increasing contribution of the secondary bending. The compressive strains increase as the bending stiffness of the specimens at the crack plane is reduced leading to larger deflections.

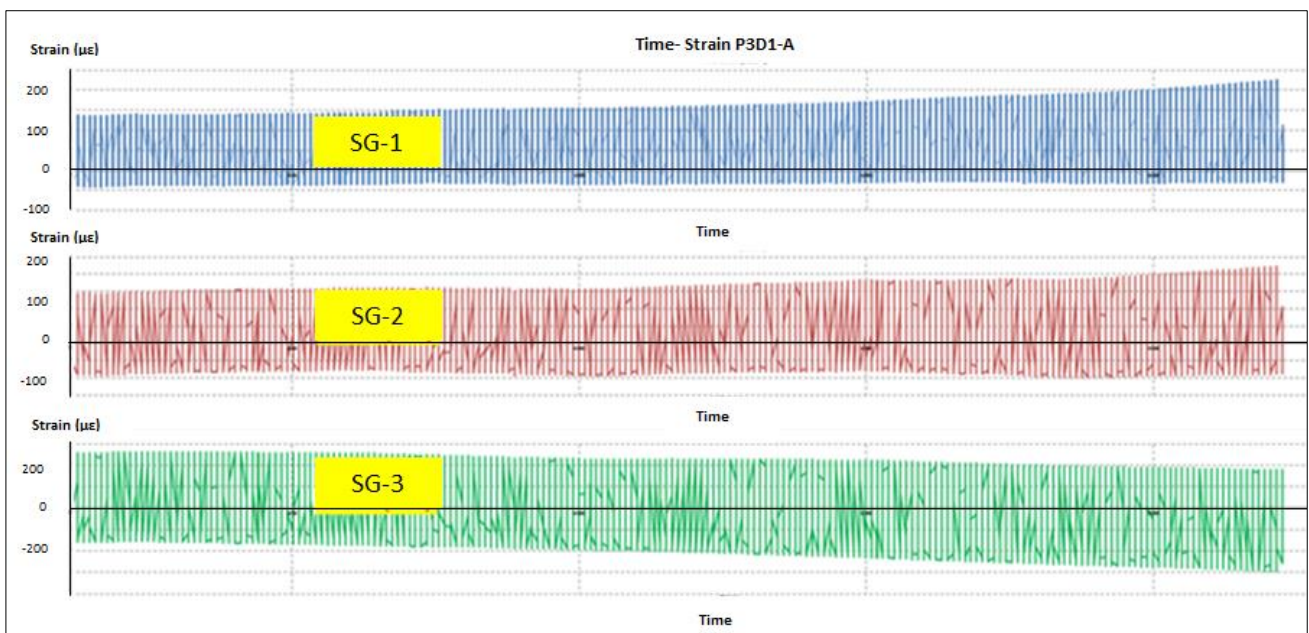


Figure 5.11: Indicative time strain measurements for specimen P3D1-A.

In Figure 5.12 and Figure 5.13 the crack length (a) versus the number of cycles (N_{36-f}) are presented for the reference and the repaired specimens, respectively. In both figures a crack length equal to 36 mm was taken as the starting point. As expected, the rate of crack propagation increases with increasing crack length and the curves exhibit an asymptotic behaviour from a certain crack length and until failure of the specimen. The curves of each specimen are not continuous due to the interposing space between the crack gages. Additionally, even in the specimens where the crack gages were placed at the end of the plate's width, the crack propagation rate at the point of failure could not be measured as yielding and eventually fracture occurred once the crack has propagated significantly. Thus, for reasons of completeness and clarity, the total number of cycles to failure N_{36-f} of each specimen is shown as a vertical line at the top of the figure, however it would be an oversight to consider these for the comparison of the performance of the specimens. In the case of specimens that four crack gages were installed (P3D1-B and P3D4-A), the presented measurements are those of the two crack gages placed at the side of the specimen on which the crack propagation was

faster. As it was mentioned earlier, specimen P3D6-B failed prematurely due to buckling and therefore it is not included in Figure 5.13.

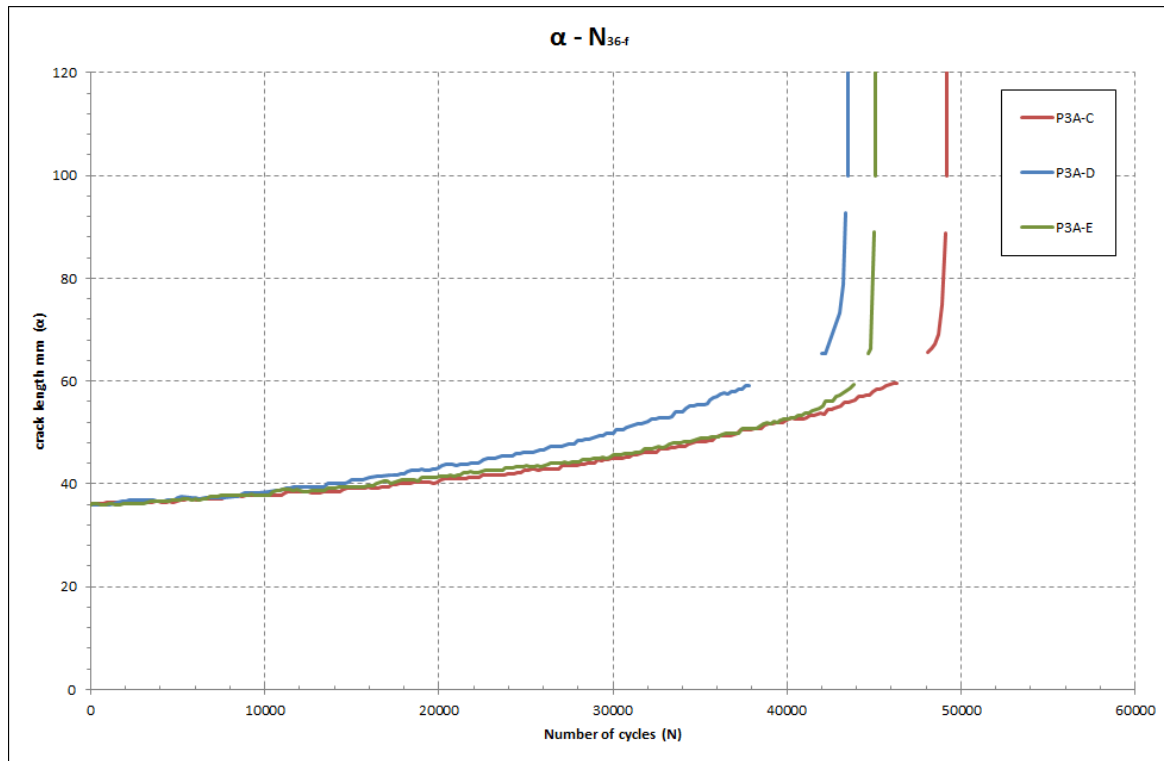


Figure 5.12: α -N curves of the reference P3A specimens.

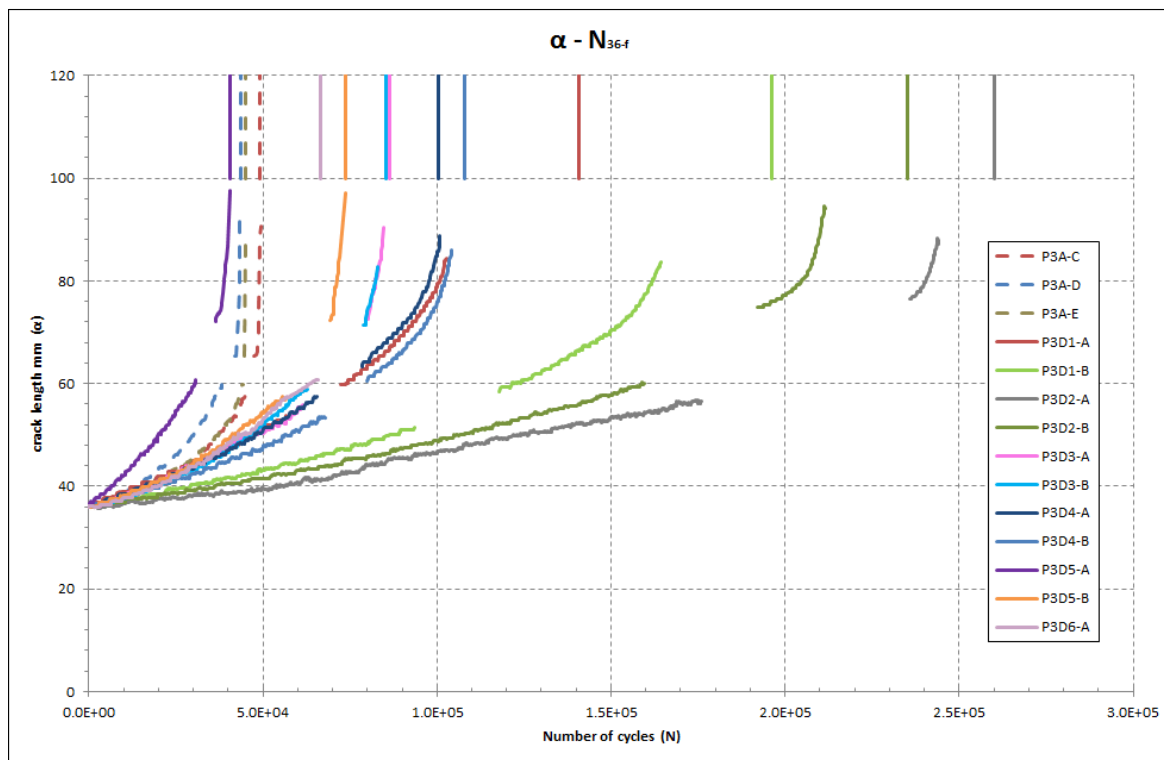


Figure 5.13: α -N curves of P3D specimens.

In some specimens, the initial notch was not exactly symmetrical with respect to the centre line of the specimen. In these specimens, the two crack gages of the configuration shown in Figure 5.8 were placed at the side where the distance between the notch tip and the edge of the plate's width was shorter. Stresses were expected to be higher in this side and, therefore, the crack was expected to propagate faster there. However, test results revealed that the crack didn't necessarily propagate faster in that side. The main reason that justifies this inconsistency is that the stresses in this area of the steel plate are largely affected by the quality of the bond between the patch and the steel plate, and therefore, by how much the steel stresses were alleviated by the existence of the patch. Thus, small eccentricities of the plates during their positioning inside the fixture along with possible variation of the bond quality across the specimens' width have potentially caused a non-uniform load distribution which thereafter affected the crack propagation rate.

In some cases, due to the distance between crack gages CG-1 and CG-2 (Figure 5.8) in combination with the fact that in some specimens the direction of the crack propagation was not exactly vertical to the applied load but oblique, the crack didn't propagate through CG-2 right from the first measuring grid as it should (Figure 5.14). Instead, the crack entered into CG-2 from a subsequent grid, resulting in fewer measurements from that crack gage.

The initial readings of the non-destructive evaluation are presented in Figure 5.15 and Figure 5.16 for the grit blasted and the needle gun treated specimens, respectively. The effect of the steel surface preparation method can be seen in Figure 5.17, where the same results as those in Figure 5.13 are presented, categorized with respect to the surface preparation method. Moreover, the fatigue life N_{36-83} of all specimens is shown as bar charts in Figure 5.18, where information about the aging scenario and the surface preparation method are also given for each specimen.

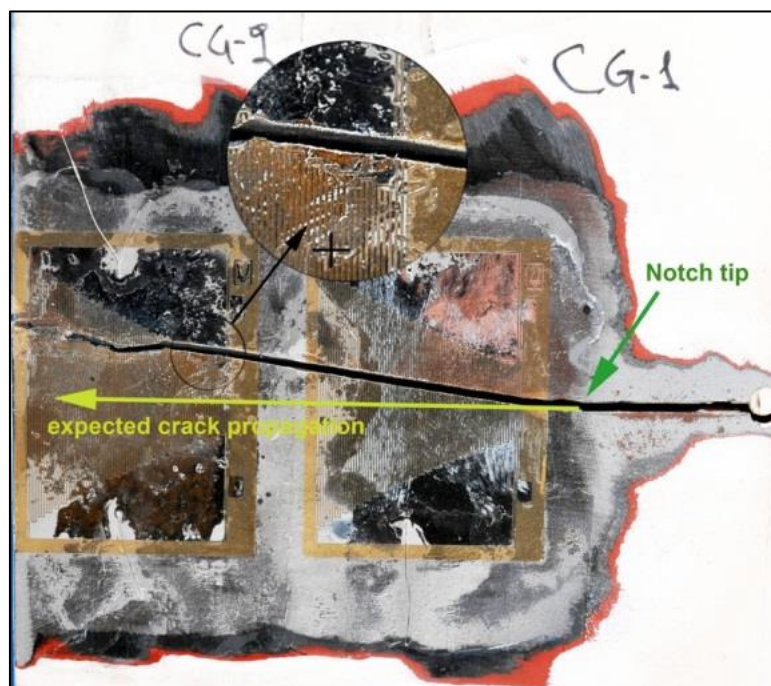


Figure 5.14: Oblique crack propagation that resulted in fewer measurements by CG-2.

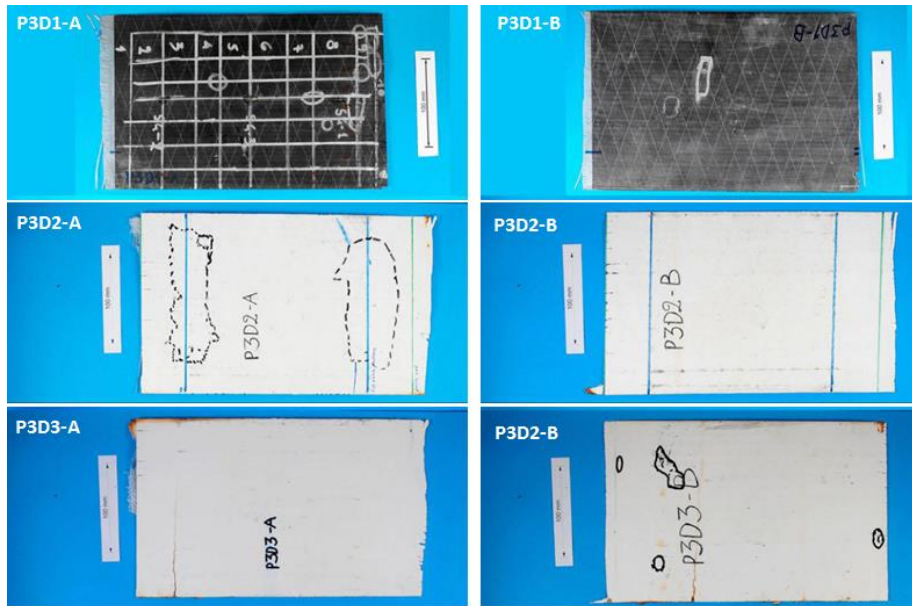


Figure 5.15: Findings of the initial NDE on the patch surface, for the grit blasted P3 specimens.

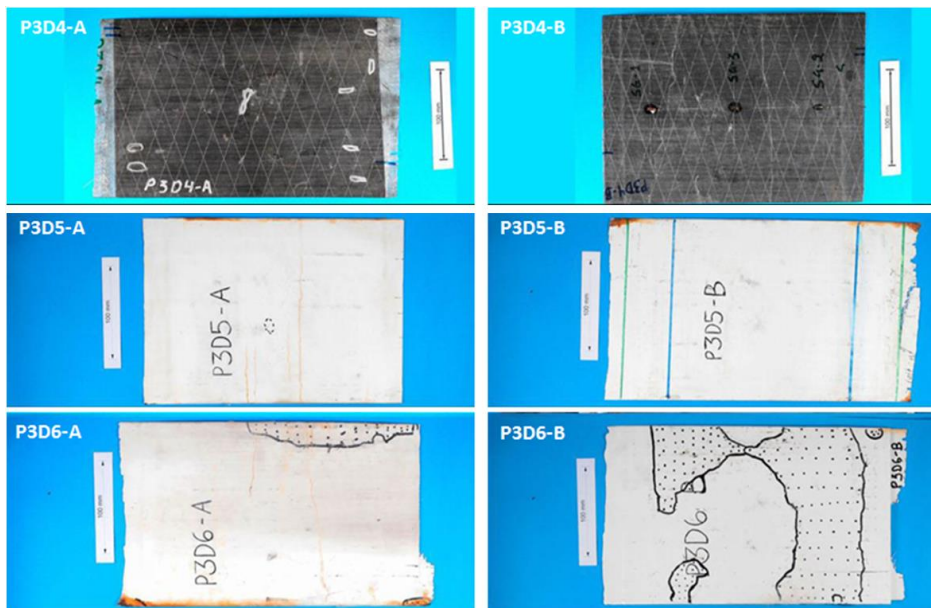


Figure 5.16: Findings of the initial NDE on the patch surface, for the needle gun treated P3 specimens.

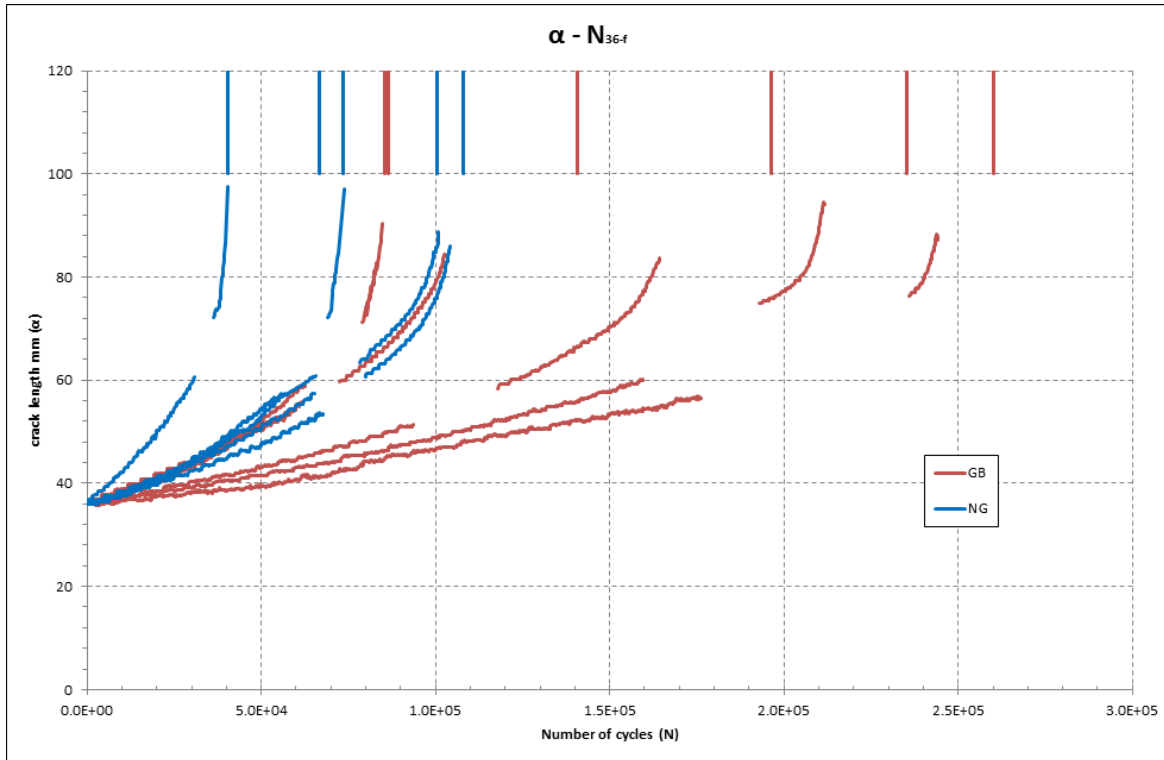


Figure 5.17: α -N curves of P3D specimens; comparison of surface preparation method.

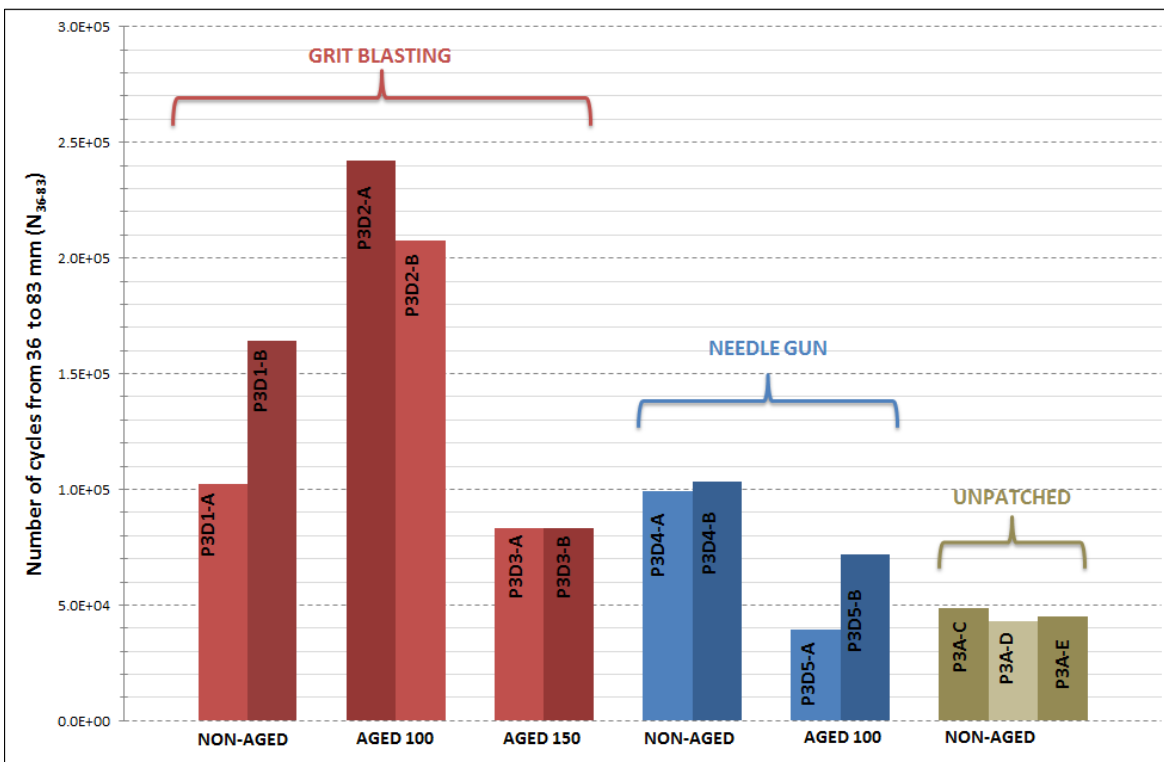


Figure 5.18: Fatigue life N_{36-83} of all specimens.

A combined study of Table, Figure 5.13, Figure 5.17 and Figure 5.18 draws some useful conclusions. The fatigue life and the repeatability of results for each pair of specimens vary, with nominally identical specimen pairs P3A, P3D2, P3D3 and P3D4 exhibiting less than 15 % difference. A notable difference of about 38% and 45% was presented in the case of specimens P3D1 and P3D5, respectively. These differences between otherwise nominally identical specimen pairs cannot be attributed to the flaws detected during the initial inspection. In particular, the difference of flaw size is less than 0.5 % for these specimens and the total extent of flaws was less than 1% of the patch area of these specimens. This observation implies that the performance of the repair is greatly influenced by the achieved bond strength, which is neither easily detectable nor quantifiable prior to testing. An attempt to assess the patch quality and thus justify the deviations of fatigue life between nominally identical specimens is given in the next section.

Regarding the effect of aging on the grit blasted specimens, pair P3D3 seems to have been affected by the aging scenario (150 days aging), exhibiting a significantly lower fatigue life compared to the rest of the grit blasted specimens. In contrast to this observation however, specimens P3D2 (100 days aging) exhibited the highest fatigue life, surpassing by far that of the non-aged specimens P3D1. Therefore, the results are inconclusive regarding the aging effect and the reasons for these fatigue life differences should be sought in other parameters like the quality of the patch and the bond and the surface preparation method. At specimens P3D1 and P3D2 it was observed that steel failure, in the form of complete rupture of the steel plate, occurred prior to patch debonding and that this happened earlier than the final failure of the specimen. This means that, for a significant number of cycles before the total failure, only the patch contributed to the load bearing capacity of the specimen. At specimens P3D3, the patch debonded first, quickly followed by the failure of the steel plate. This behaviour is possibly related to the inferior performance of P3D3 specimens compared to specimens P3D1 and P3D2. In all cases nonetheless debonding initiated at the vicinity of the notch region at the centre of the plate and gradually propagated towards the patch edges along the width direction.

The repeatability of results of the needle gun treated specimens is once more questionable, since the difference between the two P3D4 specimens was only 3.9% but the difference between the two P3D5 specimens was 45.3%. As mentioned before, the reasons that might have led to this deviation will be investigated in the following section. No results are given for specimen P3D6-B because, as stated previously, the patch debonded prematurely at the beginning of the fatigue scenario and was immediately followed by buckling of the steel plate. As it will be shown in the next section, the reason for this behaviour was the poor quality of the patch and of the adhesion between the composite and steel substrate.

Regarding the effect of aging on the needle gun treated specimens; the results are more consistent in this case, since the aged specimens exhibit a smaller fatigue life than the non-aged ones

Regarding failure modes, two different types were identified. In all grit blasted specimens except the P3D3 pair, the crack propagated throughout the whole width of the steel plate and complete steel failure occurred, while the patch was still bonded at its edges to the two separated steel parts. Thus, after the full separation of the steel plate, the patch was the only load transferring element, withstanding the fatigue loading for a considerable number of cycles beyond the steel plate's complete failure. This can be seen in Figure 5.19, where the final fatigue life N_{36-f} of each specimen is significantly higher than the expected one

by extrapolating the number of cycles measured using the crack gages. On the contrary, in the two P3D3 specimens and in all needle gun treated specimens, the patch debonding occurred first, and subsequently the crack propagated towards the edges of the steel plate and complete failure took place. This behaviour can be clearly seen in Figure 5.20, where the final fatigue life N_{36-f} of each specimen is the same to the number of cycles the α -N curve measured on the steel plate is converging at. The difference between the above two behaviours seems to be the key element for the fatigue strength of the patched specimens, since the specimens which exhibited the former failure mode sustained significantly more loading cycles than the specimens which exhibited the latter. The above difference in behaviours is furthermore supported by the type of the crack faces for the two groups of specimens. As shown in Figure 5.21 (top), the surface of the crack faces of the first group of specimens (P3D1 and P3D2) is typical of fatigue and relatively smooth all the way to the plate's edges, since the crack propagated up to the edges of the plate and patch debonding took place afterwards. For the second group of specimens however (P3D3, P3D4, P3D5 and P3D6, Figure 5.21-bottom), the crack faces are indicative of fatigue up to a certain limit, after which, because of the patch debonding and the subsequent overloading of the steel plate, a ductile failure took place rapidly. In all cases however, debonding started from the centre of the plate at the vicinity of the notch. A representative shape of the debonded area, as outlined by the non-destructive evaluation, is presented in Figure 5.22.

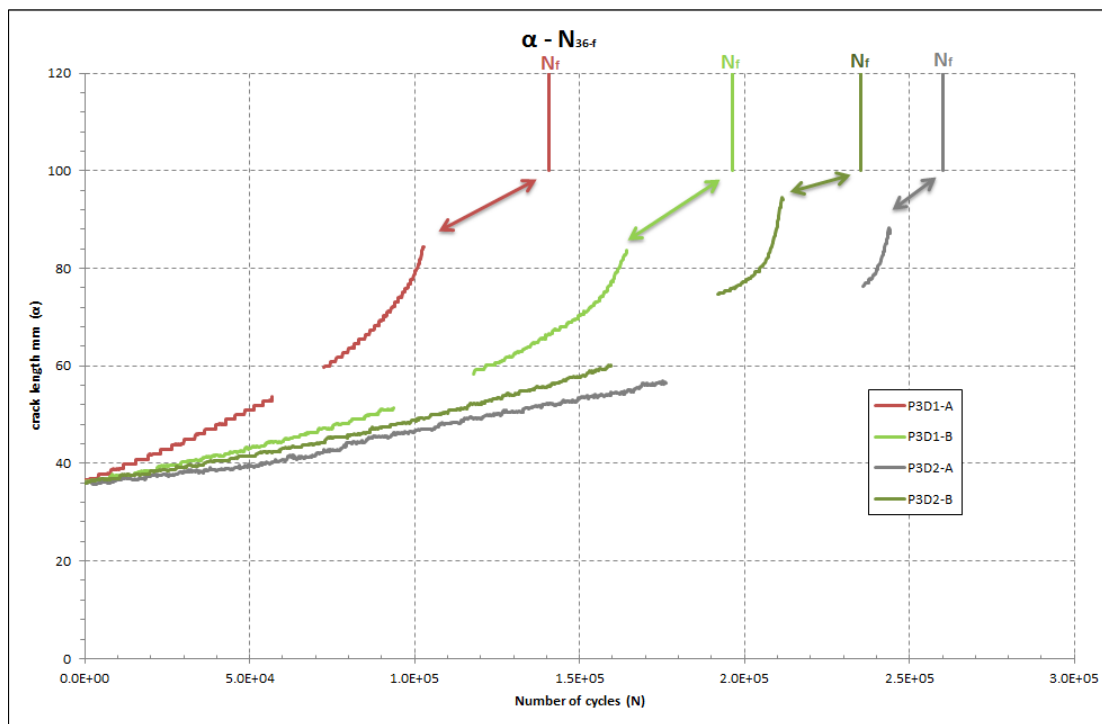


Figure 5.19: α -N curves of P3D1 and P3D2 specimens.

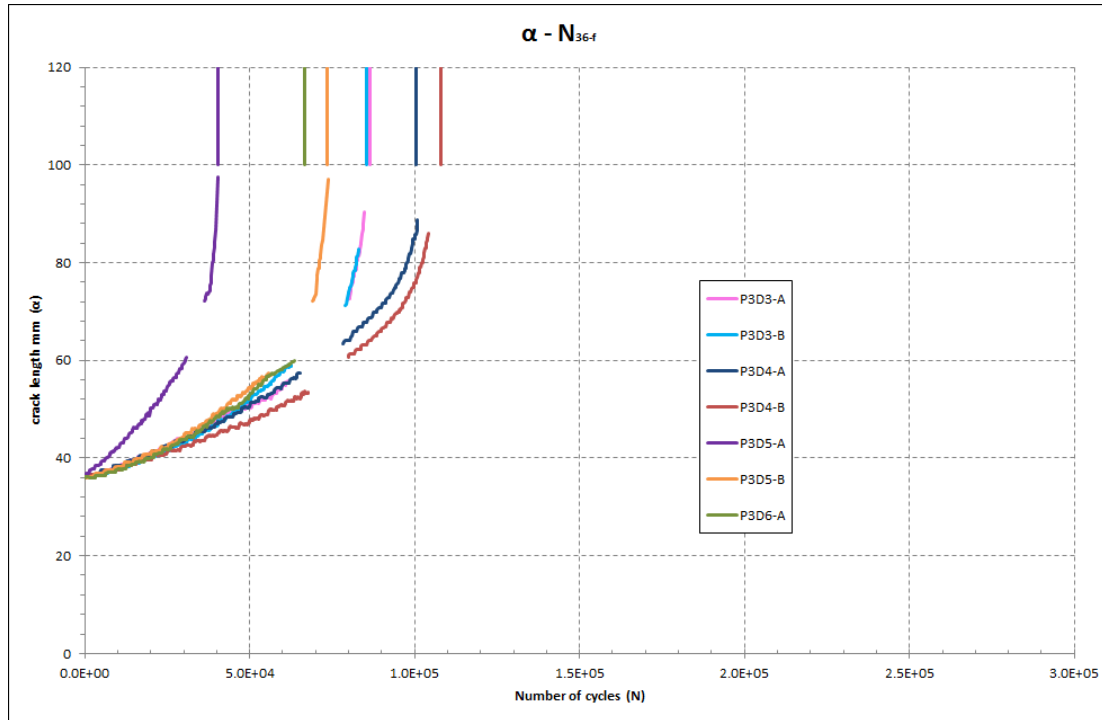


Figure 5.20: α -N curves of specimens P3D3, P3D4, P3D5 and P3D6-A.

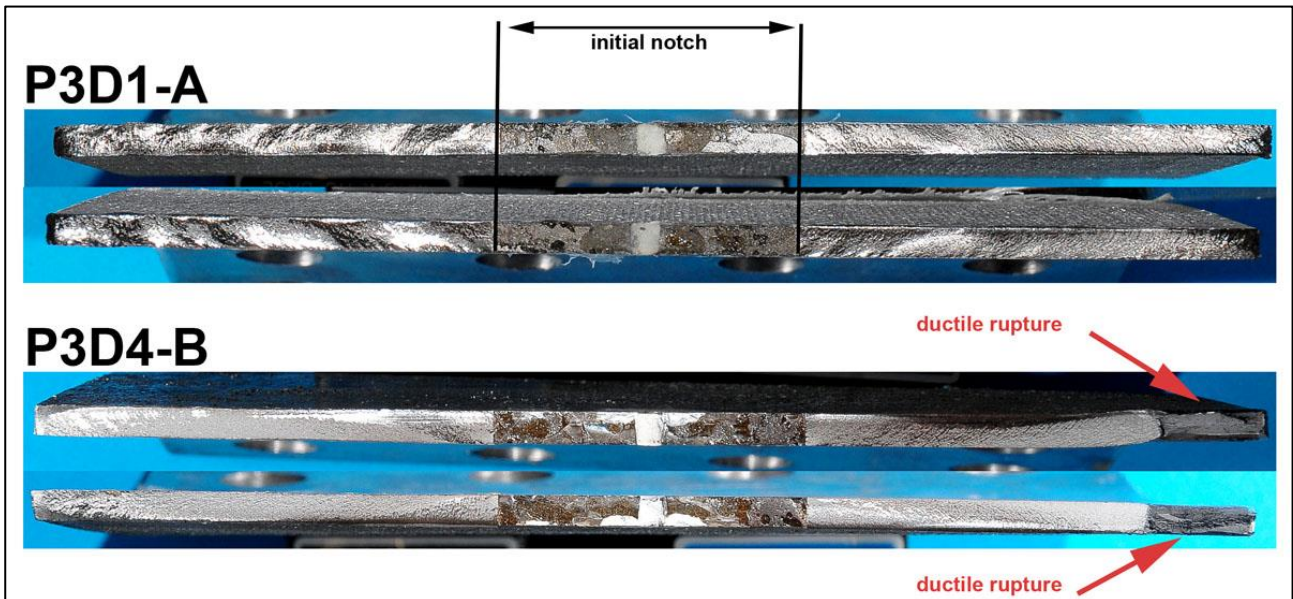


Figure 5.21: Crack faces of two representative specimens.

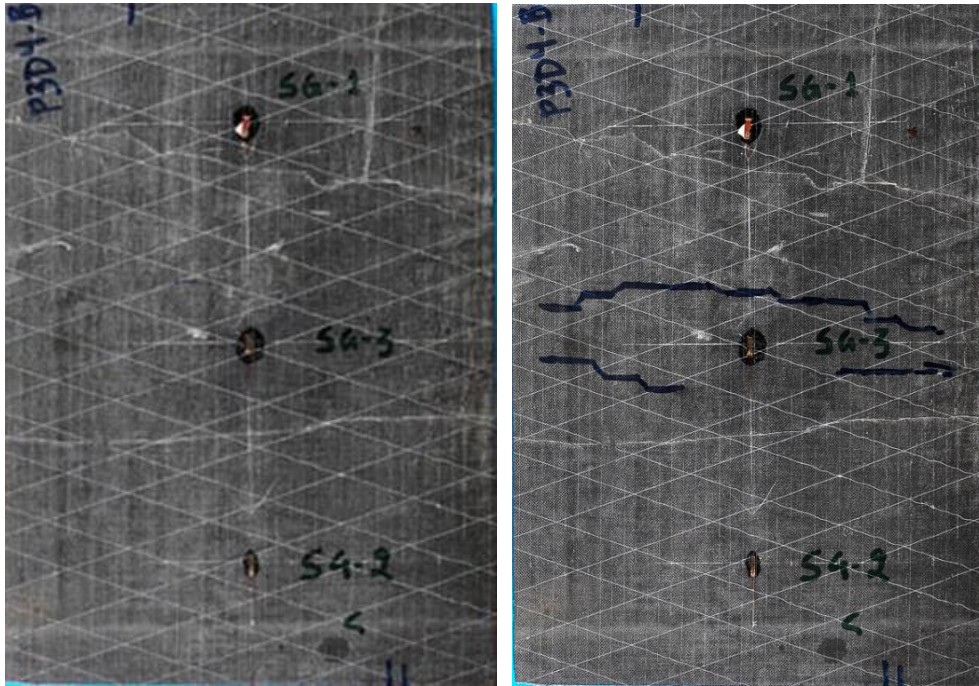


Figure 5.22: Initial non-destructive evaluation of the patch repair in P3D4-B (left) and evolution of debonding during fatigue testing (right).

5.4 Patch quality classification

In an effort to determine the reasons for the differences between the fatigue lives of the nominally identical specimens and to evaluate the influence of both the bond, and the patch qualities to the specimen's fatigue life, an attempt to classify the patches' quality was made. The main parameters of this study were the findings of the NDT inspection of the patches made before testing, the study of the debonded surfaces after testing, as well as the measurements, after testing, of some important characteristics of each specimen such as the patch thickness and the eccentricity of the notch.

The acousto-ultrasonic device used (BONDMASTER 1000e) was capable of detecting defects with a size greater than 10 mm, as this is the minimum flaw size that can be detected with the available transducer. These flaws may be either debonding of the patch-steel bonding layer or delamination of the patch itself Figure 5.23. However, the instrument does not provide information about the type of the defects, therefore only the extent and position of the defects were measured during initial inspection before testing were marked on the external surface of the patch with a marker. Any progression of damage detected at intermediate inspections during testing was marked on top of the existing ones. Identification of the type of flaws that were measured in the patch prior to testing was done post mortem by visual inspection of the interface and cutting of the laminate to inspect for dry/delaminated and/or debonded areas.

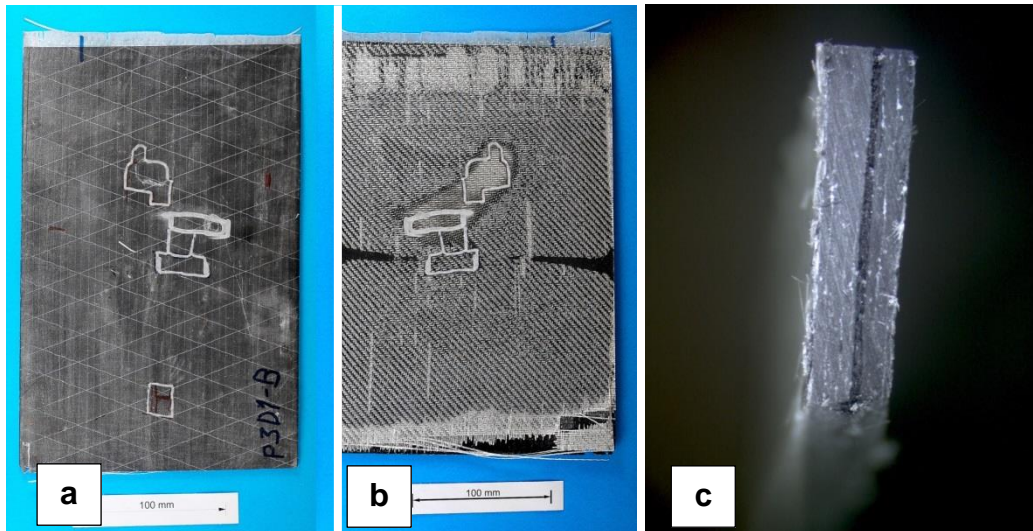


Figure 5.23: Initial findings (a) projection of findings matching the dry area at the interface (b), dry plies detected by the inspection revealed after cutting the laminate (c).

Initially, an attempt was made to assess the total quality of the patch repair, based on both the actual geometry of the repair and on the NDT findings before testing, without taking into account the test results (fatigue life, premature failures, etc.). Regarding the geometry of the repair, three parameters were taken into account, namely the (possible) eccentricity of both the notch and the patch and the patch thickness. Table 5.4 shows the measurements regarding the notch geometry. Magnitudes *b* and *c* are indicative of the deviation of the notch from being normal to the loading axis, whereas magnitudes *g* and *l* of the transverse eccentricity of the notch with respect to the loading axis. Magnitude *k* is the actual initial notch length. Table 5.4 includes also the ideal (nominal) values for each magnitude.

Table 5.4: Notch eccentricity measurements.

Specimen	Dimensions (mm)					
	a	b	c	g	l	k
P3D1-A	555.0	278.5	278.0	73.4	76.4	50.9
P3D1-B	555.0	280.0	281.5	74.1	76.0	49.1
P3D2-A	554.0	276.5	276.5	74.0	76.0	50.1
P3D2-B	555.0	277.5	277.5	75.5	74.5	50.0
P3D3-A	555.0	276.0	277.0	75.5	74.5	50.5
P3D3-B	555.0	276.5	277.5	74.5	75.0	50.5
P3D4-A	555.0	275.0	275.5	80.5	69.0	50.0
P3D4-B	555.0	276.5	276.5	75.0	75.0	50.3
P3D5-A	555.0	274.0	274.0	77.4	73.5	50.0
P3D5-B	555.0	276.5	277.0	75.0	75.5	50.5
P3D6-A	554.0	277.5	277.5	75.5	74.5	50.5
P3D6-B	554.0	277.5	277.5	76.0	74.0	50.5
IDEAL	555.0	277.5	277.5	75.0	75.0	50.0

Table 5.5 shows the measurements regarding the patch eccentricity. Magnitudes L1 and L2 are indicative of the longitudinal eccentricity of the patch with respect to the notch. Once more, the nominal values are listed. Table 5.6 presents the average patch thickness for each specimen, together with a qualitative assessment of both the notch and the patch eccentricities. The existence or absence of notch and/or patch eccentricity, is noted by *Yes* or *No*, respectively. Notch eccentricity is taken into consideration when the absolute value of the ratio $(g - l)/l$ surpasses 5%. Patch length eccentricity is considered to exist when the absolute value of the ratio $(L1 - L2)/L2$ is more than 5%.

Table 5.5: Patch eccentricity measurements.

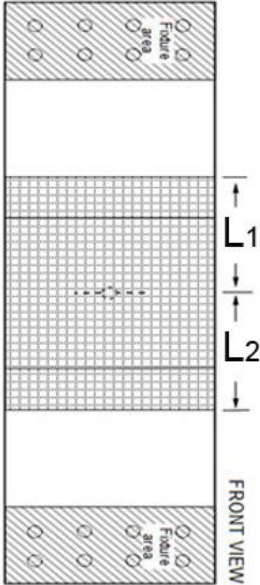
Specimen	Dimensions (mm)		
	L1	L2	
P3D1-A	N/A	N/A	
P3D1-B	144.0	157.0	
P3D2-A	147.0	154.0	
P3D2-B	144.0	153.0	
P3D3-A	147.0	152.0	
P3D3-B	139.0	161.0	
P3D4-A	149.0	151.0	
P3D4-B	150.0	149.0	
P3D5-A	147.0	151.5	
P3D5-B	149.0	153.0	
P3D6-A	150.0	149.0	
P3D6-B	150.0	150.0	
IDEAL	150.0	150.0	

Table 5.6: Specimens characteristics measurements.

Specimen	Patch thickness		Notch eccentricity	Patch eccentricity
	Average (mm)	Coefficient of Variance (%)		
P3D1-A	3.4	1.5	NO	N/A
P3D1-B	3.3	2.3	NO	YES
P3D2-A	3.4	2.3	NO	NO
P3D2-B	3.3	1.9	NO	YES
P3D3-A	3.3	1.7	NO	NO
P3D3-B	3.4	1.0	NO	YES
P3D4-A	3.3	1.3	YES	NO
P3D4-B	3.2	1.6	NO	NO
P3D5-A	3.3	5.2	YES	NO
P3D5-B	3.4	3.0	NO	NO
P3D6-A	3.5	2.3	NO	NO
P3D6-B	3.2	6.0	NO	NO

Regarding the NDT findings before testing, the existence, shape, size and position of any detectable defect of every specimen were evaluated and are presented in Table 5.7 (refer also to Figure 5.24 and Figure 5.25). More specifically, the “extent” values are the percentage of the area of the defect(s) with respect to the total area of the patch, whereas the shape of the defect is characterized as “oval”, “circular” and “rectangular”. Regarding the position of the defects, the following notation has been followed: M=Middle area, U=Upper area, B=Bottom area, R=Right side and L=Left side, looking at the external side of the patches, as shown in Figure 5.24 and Figure 5.25.

Table 5.7: Initial characteristics of patch or bond defects.

Specimen	Existence	Extent (%)	Position	Shape
P3D1-A	<i>N/A</i>	-	-	-
P3D1-B	<i>YES</i>	<i>0.8</i>	<i>M</i>	<i>RECTANGULAR</i>
P3D2-A	<i>YES</i>	<i>21.9</i>	<i>L,R</i>	<i>OVAL</i>
P3D2-B	<i>NO</i>	-	-	-
P3D3-A	<i>NO</i>	-	-	-
P3D3-B	<i>YES</i>	<i>1.2</i>	<i>L,R</i>	<i>CIRCULAR</i>
P3D4-A	<i>YES</i>	<i>1.3</i>	<i>L,R</i>	<i>CIRCULAR</i>
P3D4-B	<i>N/A</i>	-	-	-
P3D5-A	<i>YES</i>	<i>0.2</i>	<i>M</i>	<i>OVAL</i>
P3D5-B	<i>NO</i>	-	-	-
P3D6-A	<i>YES</i>	<i>6.2</i>	<i>U</i>	<i>RECTANGULAR</i>
P3D6-B	<i>YES</i>	<i>41.5</i>	<i>B,U,R,L</i>	<i>RECTANGULAR</i>

Taking into account the initial NDT findings of Table 5.7, a classification of the quality of the patch of each specimen is presented in Table 5.8. Specimens P3D1-A and P3D4-B were excluded from this classification as there was no initial NDT assessment prior to testing. The quality index in Table 5.8 is defined as 5 = good, 4 = above average, 3 = average, 2 = poor and 1 = bad and has been assigned to each specific specimen based on the aforementioned observations.

Table 5.8: Patch quality classification

Specimen	Quality Scale
P3D1-A	<i>N/A</i>
P3D1-B	4
P3D2-A	3
P3D2-B	5
P3D3-A	5
P3D3-B	4
P3D4-A	3
P3D4-B	<i>N/A</i>
P3D5-A	3
P3D5-B	5
P3D6-A	3
P3D6-B	1

After the tests, the internal surface of the patches that was bonded to the steel was examined (see Figure 5.24 and Figure 5.25). In some cases, like for specimens P3D1-A and B, there was poor local wetting of the insulating glass layer and therefore the poor bond quality was easily identifiable. These findings were also used in order to distinguish debonding from patch delamination in the initial NDT measurements. It is speculated that the white areas on the patch internal surface (see Figure 5.26) indicate a good bond between the patch and the steel substrate, as this whitish colour is attributed to a cohesive failure of the glass insulating layer due to the resin having good adhesion to the steel surface and thus failure did not take solely place at the resin/steel interface. On the contrary, dark areas (which are more notable in the needle gun treated specimens) correspond to at least a lower level of mechanical interlocking between the steel and the resin, as there is little or no exposure of the glass insulating layer meaning the resin failed adhesively (see Figure 5.26).

In specimens P3D2 and P3D3 there were no noteworthy findings; all these specimens had a uniform white debonding area indicating a strong bond (Figure 5.24). The total peel off and tearing of the glass insulating layer at the edges of the patch in these specimens was caused during the forced manual removal of the patch from the steel substrate after testing, and is not a result of the testing itself. In specimen P3D5-A, corrosion was observed in the centre of the patch, in the area over the notch. This occurred most likely due to the inadequate paint protection of the unpatched side of the specimen; moisture infiltrated from a gap in the notch during the accelerated aging tests, corroding locally the steel in that area.

In a similar way, a corroded area at the internal surface of the patch of specimen P3D6-A was found (Figure 5.25). Moisture entered from the side of the patch/steel interface, resulting in the corrosion of steel which in turn reduced the quality of the bond locally. This is probably the main reason why the crack in this specific specimen propagated faster on this side of the initial notch, as can be seen in Figure 5.27. This figure depicts the unpatched side of all specimens, where the full path of the developed crack can be clearly seen.

Regarding specimen P3D6-B, a massive area of dry layers was found, both in the bondline (insulating layer) and through the carbon plies of the laminate itself (Figure 5.25), which was the result of poor resin infusion during the lamination manufacturing. Due to these defects, in combination with possible inadequate paint protection of the specimen at the bottom side of the patch, moisture infiltrated through the carbon plies and spread to the steel substrate.

Finally, because not all NDT findings could be explained and verified by examining the bonded surface of the patches, these were cut in strips using a cutting wheel (see for example specimen P3D1-A in Figure 5.24, where the strips to be cut are marked) and were examined again at the points of interest. In these cases the findings were associated with poor wetting during the infusion process which is assumed similar to the existence of delamination between the patch layers. More specifically, in the majority of these cases, poor wetting took place in the mid-thickness of the patch, a fact indicating problematic resin infusion during the second lamination step. The delamination of the glass insulating fibres of specimens P3D2 and P3D3 in Figure 5.24 was caused during the removal of the patch from the steel plate.

At this point it must be noted that the existence of delamination or debonding, as well as their extent, were successfully detected using the specific NDT device.

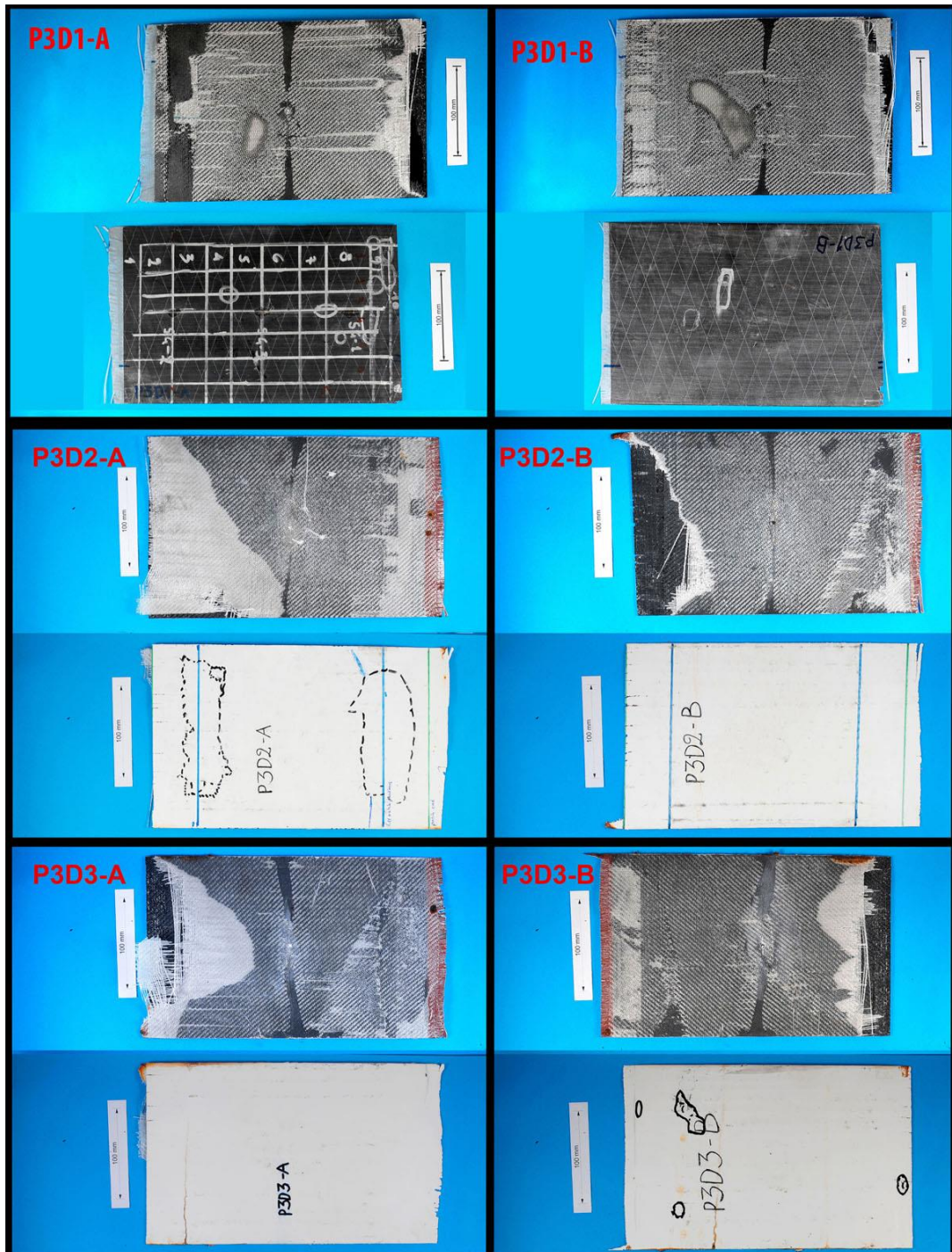


Figure 5.24: Internal and external patch surfaces of P3 grit blasted specimens. The initial findings were marked on the external surfaces.

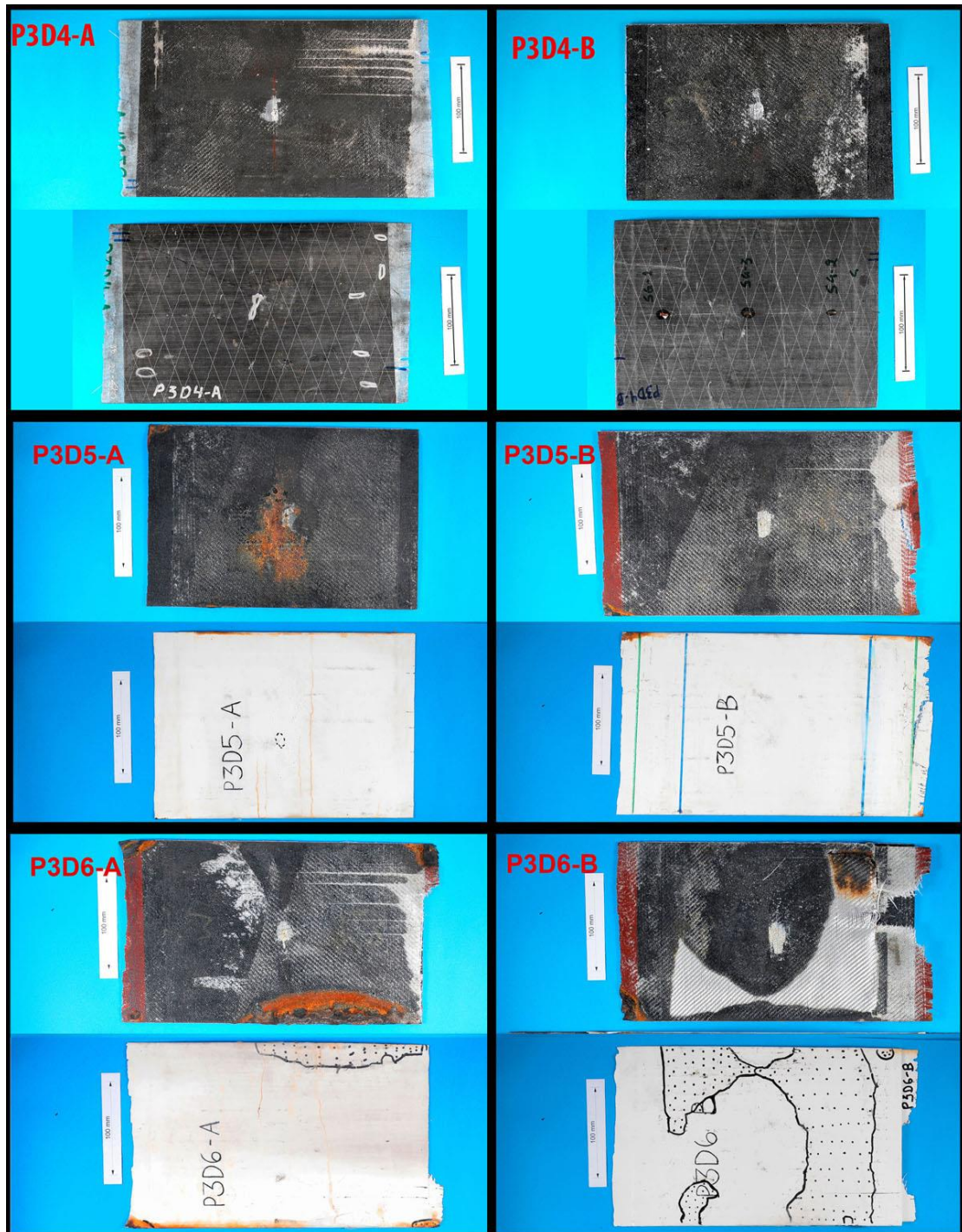


Figure 5.25: Internal and external patch surfaces of P3 needle gunned specimens. The initial findings were marked on the external surfaces.

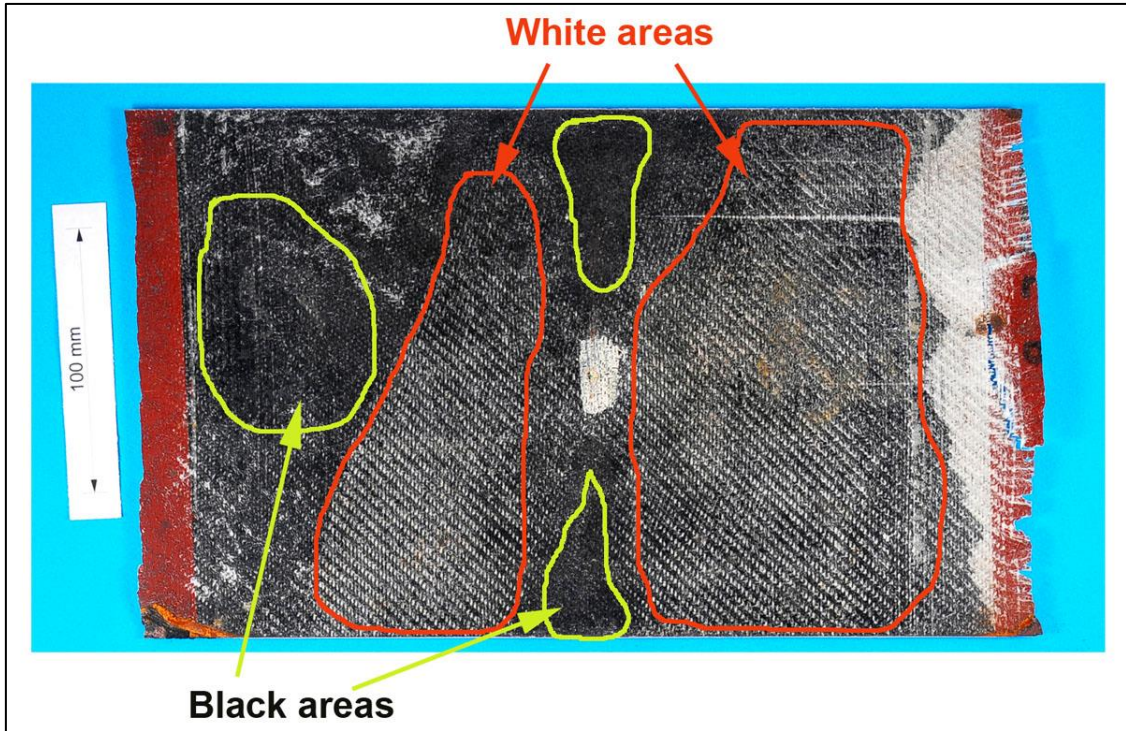


Figure 5.26: Distinction between white and black areas on the internal surface of P3D5-B patch.

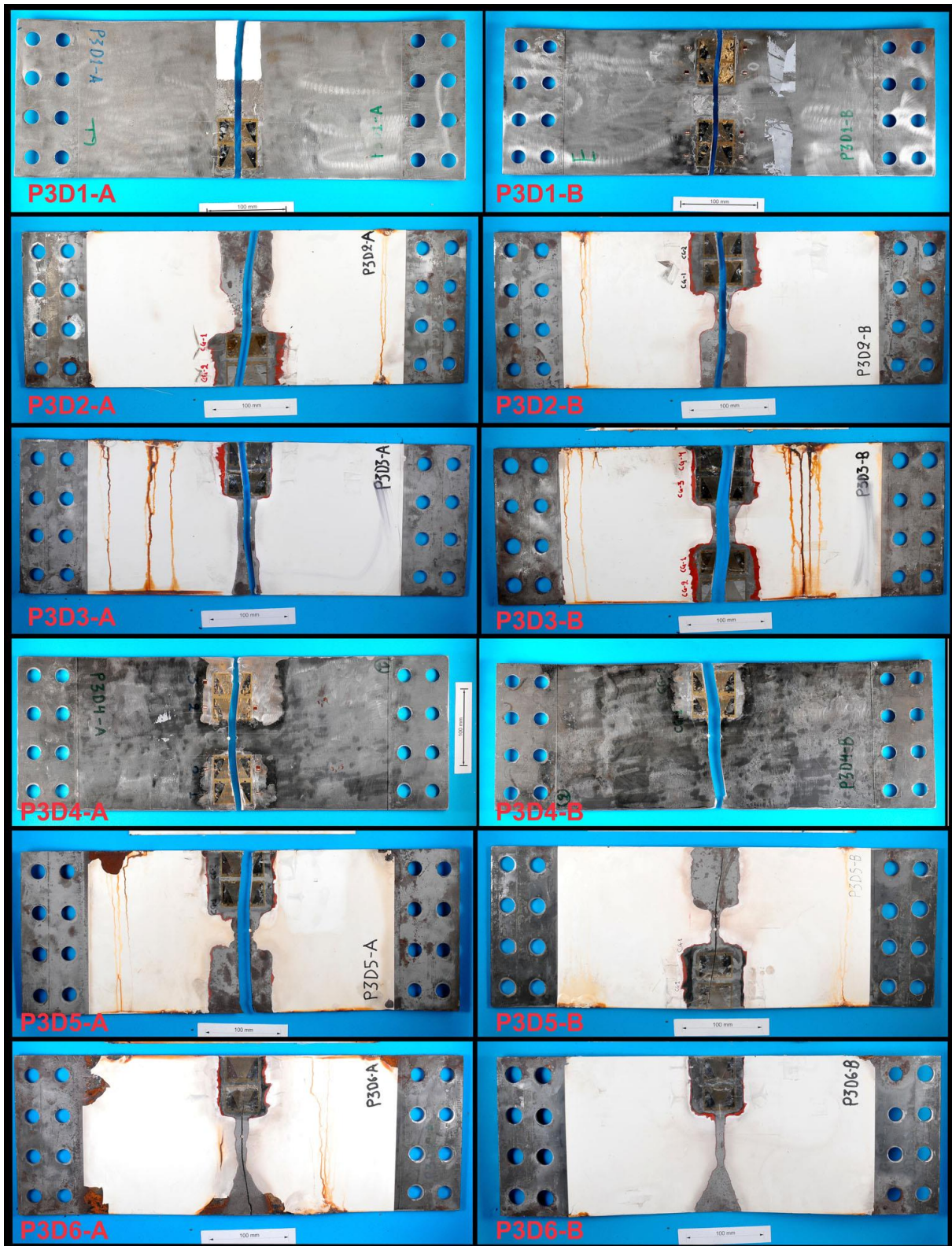


Figure 5.27: Unpatched side of steel, showing the crack paths.

The quality index of the patches (see Table 5.8), the patch thickness, the type of defect, as identified after testing and the fatigue life N_{36-f} of each specimen, are presented in Table 5.9.

Table 5.9: Comparison of repair characteristics and fatigue life.

Specimen	Quality Scale	Patch thickness (mm)	Type of defect	Fatigue Life (N_{36-f})
P3D1-A	N/A	3.4	-	140738
P3D1-B	4	3.3	Debonding	196271
P3D2-A	3	3.4	Delamination	260024
P3D2-B	5	3.3	None	235306
P3D3-A	5	3.3	None	86405
P3D3-B	4	3.4	Delamination	85503
P3D4-A	3	3.3	Debonding	100520
P3D4-B	N/A	3.2	-	107904
P3D5-A	3	3.3	Debonding	40561
P3D5-B	5	3.4	None	73635
P3D6-A	3	3.5	Debonding	66672
P3D6-B	N/A	3.2	Del. + Deb.	N/A

The following conclusions can be drawn out concerning the quality assessment attempt. The initial quality assessment of the patch doesn't seem to correlate well with the fatigue life of each specimen. This indicates that more parameters, which were not quantified, should be considered for the lifetime estimation. The estimation of the patch efficiency based on the initial NDT findings, although meaningful, is not the only affecting parameter. The patch thickness differences are very small and normally they should not have affected the fatigue life of the specimens. In general, a thicker patch, although may alleviate more the stresses passing through the steel plate, produces at the same time larger eccentricity due to the non-symmetry of the repair cross-section, a fact which could potentially lead to earlier patch debonding initiation.

It appears that the effect of the existence of delamination between the patch layers due to poor wetting is not as detrimental as debonding between the patch and the steel substrate. Finally, considering the fatigue life results as well as the NDT findings prior to testing, it can be stated that the quality of the bond area around the notch is of great importance. As it is well known, in most cases the composite patch will not completely arrest the crack growth on the steel, but it will greatly delay its propagation. Defects in the middle of the patch (above the notch) can possibly lead to faster debonding in that area, thus undermining the repairs' effectiveness and viability (see results for specimens P3D4-A and P3D5-A and their internal surface in Figure 5.25).

5.5 Conclusions

The present experimental study investigated the efficiency of composite patch repaired cracked steel plates under fatigue loading. Emphasis was given to techniques and service conditions met in marine applications.

Starting from the experimental response of the specimens, two different failure modes were identified. The first one was patch debonding followed by the complete rupture of the steel plate. The second one was the opposite, with a large extent of the patch remaining bonded to the steel surface even after the propagation of the crack throughout the steel plates' width. In both cases debonding of the patch initiated from the centre of the plate, from the notch area. In some cases, large differences in the number of cycles were presented for nominally identical specimens. This is attributed to variations at the surface preparation quality which in turn affected the quality of the bond and consequently the performance of the repair.

The specimens whose surface was grit blasted prior to bonding proved to be more efficient at the retardation of the crack growth rate, extending the fatigue life of the cracked specimens from 1.7 up to 5.6 times. The number of cycles exhibited from the needle gun treated specimens was up to 2.4 times that of the unpatched ones. In general, with the exception of one specimen, the repair was able to significantly decrease the crack propagation rate.

The assessment of the quality of the repair with the use of the acousto-ultrasonic device was successful, providing insight for the extent of the defect. Nonetheless, results indicated that there are many parameters that affect the quality of the repair, such as the position and type of flaw and the quality of the formed bond, which are not possible to identify a priori with the used technique and which consists an interesting subject for future studies.

Concerning the aging effect of the repair, results are inconclusive, with the 100 days aged, grit blasted specimens exhibiting the greatest number of cycles. In respect to the marine paint applied to protect the specimens, it was shown that it was sufficient to at least partially protect the repair, as the effect of the aging procedure was evident in the bondline in the cases where the marine paint was mechanically damaged or not applied properly.

Further experimental studies are needed in order to investigate additional parameters that have not been addressed in this study, extending in this way the understanding of the key mechanisms that affect the efficiency of the patch repair under fatigue loading.

6. Numerical simulations employing a three compartment model

6.1 Introduction

The sustainability of the global maritime industry depends on enhancing ship safety and mitigating the consequences of ship incidents and accidents. To a very large extent, a comprehensive system of international rules covers every conceivable aspect of the construction and use of ships, including their safe navigation and the welfare of their crew members.

Nevertheless there are reports (*Bloor et al. 2006, Papanikolaou et al. 2006, Papanikolaou et al. 2007, Knudsen and Hassler 2011, Eliopoulou et al. 2012*) showing that vessels continue to sail with grave irregularities and defects even after recent inspections (*Knudsen and Hassler 2011*). For example, in the case of Double Hull Tankers, non-accidental structural failures appear frequently (*Eliopoulou et al. 2012*), in ships 0-5 years old. Although critical damages require immediate rectification actions, non-critical damages might be underestimated and in such cases develop into critical ones. The aforementioned issue becomes more prominent in the light of studies (*IACS 2010, Hamann et al. 2011*) that show significant underreporting of relevant non-serious accidents.

Among the most common non-accidental structural failures found in ship structures, which potentially could lead to critical loss of structural integrity, are cracks. Cracks are formed predominantly due to low stress-high cycle fatigue loading of the structure during its operational life as well as by various other causes, such as harbour operations during cargo loading/unloading, poor initial design of structural details, overloading due to extreme sea conditions and dormant defects caused by inefficient workmanship during repairs, to name but a few. Hitherto the detection of cracks in a ship leads inevitably to its immediate repair which in most cases means the cease of operation for the ship. Therefore there is an increasing interest in developing the means and technology to address both the creation of cracks in the ship's structure and finding alternative ways to arrest already existing cracks.

A step that would facilitate the wide acceptance of the aforementioned trend is the use of existing rules and regulations for the preliminary study of cracks on a case by case basis, aimed at assessing the most suitable course of action. Within this framework, a platform was developed and is described in this section for the implementation of proper fatigue loads. A methodology is proposed that can be used as a common base for evaluating different crack arrest technologies. In this work the proposed methodology was employed for the comparative study of two cracks in an Aframax tanker following a simple approach. The stress intensity factors were derived at the crack tips under different loading conditions and compared for each loading case. This well-known method is simple, straightforward and can serve as a first step for the assessment of the criticality of cracks given that enough time is available for the generation of the finite element model.

Subsequently, the same methodology is expanded to quantify the efficiency of composite patch repairing as the selected crack arresting technology. To this end, multiple scenarios at different crack locations have been investigated. The patch material, geometry and configuration have been varied. The reduction of the

stress intensity factor along the thickness of the steel plate was then calculated for each case. The investigation of the effectiveness of the patch was carried out within the framework of the Diploma Thesis of E.I. Avgoulas, under main supervision and guidance from the author.

6.2. Description of Finite Element model

In marine applications the total loading acting on the structure is a combination of different loads (cargo, wave induced loads etc.) which is impossible to reproduce in controlled conditions. Therefore the use of the Finite Element Method (FEM) represents the most appealing alternative for the assessment of structural elements under complex loadings. Another characteristic of marine vessels is that their structural response due to the loads exerted from the marine environment, varies greatly, depending on ship type and its operating conditions. To this end, the classification societies have developed the Common Structural Rules (CSR) for certain ship-types, which are the most widely accepted rules for the structural assessment of ships.

This work is the result of the further development of a tool that integrates the prescribed CSR into the FE analyses of an oil tanker's structure. Originally this tool was developed for the strength assessment of the ship's structure (Zilakos *et al.* 2011); subsequently it was enriched including also fatigue loads. The methodology used for the FE modelling and the loading scheme is in full accordance with the CSR. The ship used in this study is an Aframax tanker; the principal dimensions of the ship are presented in Table 6.1.

Table 6.1: Principal characteristics of study case.

L_{BP}	239.0 m
B_{MLD}	44.0 m
D_{MLD}	21.0 m
$T_d=T_{sc}$	14.6 m
Δ	130882.9 t
DWT	112700 t

The modelled section of the ship is shown in Figure 6.1. The three-compartment model consists of the cargo tank amidships, along with two adjacent cargo tanks.

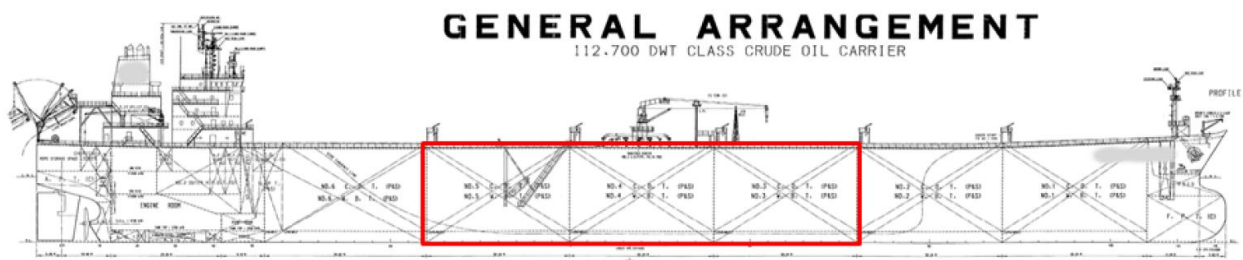


Figure 6.1: Aframax tanker depicting the modelled section.

The cargo holds No. 3, 4 and 5 have been modelled using the commercial finite element software ABAQUS 6.10. For its creation fully integrated shell elements (referred to as S3 and S4) were used. In order to reduce the complexity of the geometry and meshing, it has been decided to model the stiffeners of the bulkhead and stringers with Euler-Bernoulli beam elements (Figure 6.2) which are referred as B33 in ABAQUS manuals. The rest of the stiffeners and stringers were modelled using shell elements. A global element length of approximately 200 mm has been chosen for the mesh generation. This value ensured that the web and flange of the T-profile stiffeners were meshed with at least two shell elements (Figure 6.3), as the height of the web of the stiffeners of the ordinary section range from 300 mm to 450 mm, according to the available drawings.

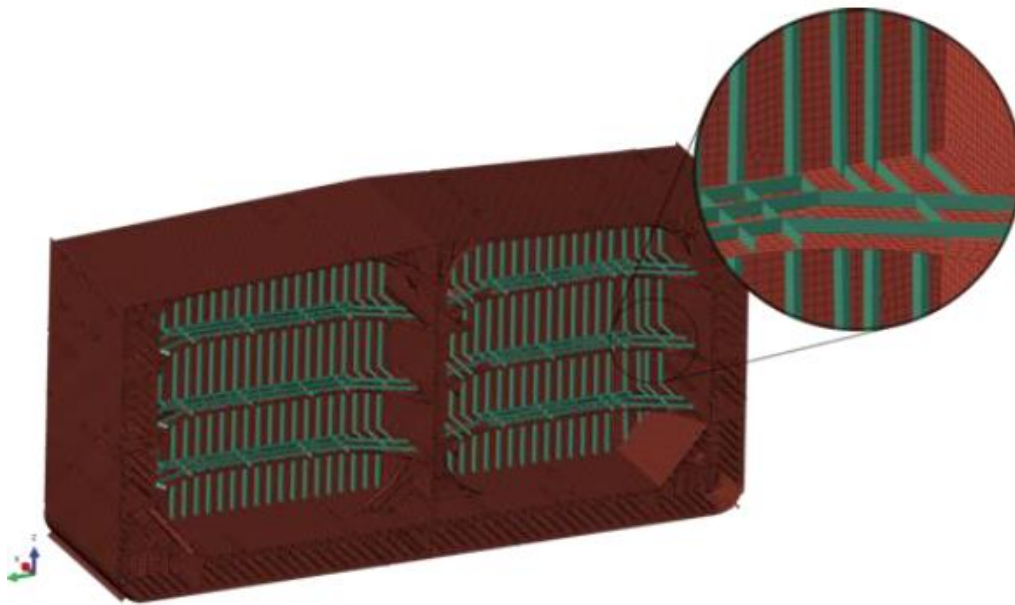


Figure 6.2: Bulkhead stiffeners modelled using shell elements (red) and Euler-Bernoulli beams (green).

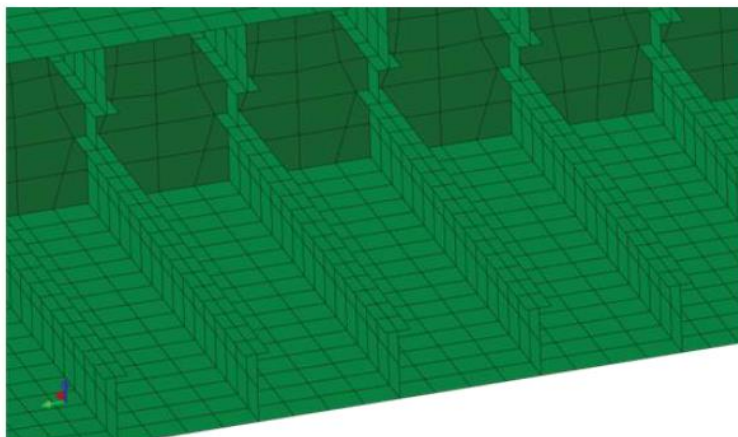


Figure 6.3: Stiffeners' mesh size.

The thicknesses of the shell elements are in accordance with the actual thicknesses of the structure. The material used in the analysis is high strength steel AH36 according to the ABS classification rules. The mechanical properties of the AH36 steel are: Young's Modulus $E=207$ GPa; Poisson's ratio $\nu=0.3$ and yield stress $=355$ MPa.

The types of loads that were imposed on the three-compartment model for the fatigue analysis are both static and dynamic (*IACS 2010*). Analyses were carried out for two representative loading conditions, according to the intended ship's operation as prescribed by the CSR, namely, for oil tankers, for the full load departure (FLD) condition and for the water ballast departure condition (WBD). The implementation of the aforementioned loads was achieved using a subroutine that was written in FORTRAN and was called by ABAQUS during the FE analysis of the three-compartment model (DLOAD subroutine). The boundary conditions imposed on the model were in full accordance with the requirements of the CSR and comprised of a series of spring elements with stiffness dependent on the geometry and materials of the model.

According to CSR, the shear forces and the vertical bending moment have to achieve certain values. The necessary procedure for adjusting the loads is explained in the following and it requires the creation of a beam model. The beam model represents the three compartment of the vessel. For the creation of the beam model, ANSYS 12.0 was selected due to its capability of creating easily free body diagrams of beam models. The approximate global size of the beam elements was also 200 mm each. Thus, the total number of subdivisions along the longitudinal axis was the same in both the 3D model and the beam model. Since the only outputs of interest were the static equilibrium of reaction forces and moments acting on the model, the section properties of the beam elements did not affect the values of the required results. The boundary conditions imposed on the beam model were simple supports at both ends, as dictated by the CSR. The following local loads were to be applied on the beam model for the calculation of hull girder shear forces and bending moments:

- (a) Ship structural weight distribution over the length of the 3-tank model (static loads).
- (b) Weight of cargo and ballast (static loads).
- (c) Static sea pressure, dynamic wave pressure and, where applicable, green sea load.
- (d) Dynamic tank pressure load for Design Load Combination Static and Dynamic (seagoing load cases).

After the implementation of the aforementioned loads, the shear forces and bending moment distributions were produced. A check was made if these satisfied the prescribed values required by the regulations. As there were deviations between the achieved and the prescribed values, corrections were implemented by the application of distributed uniform loading along the beam model's length, as defined by the regulations. Having adjusted the shear force distribution, the new bending moment distribution was calculated and compared with the designated values from the regulations. Once again, an adjustment had to be made to comply with the regulations' moment requirement and therefore a constant moment across the length of the beam model was added. The applied bending moment is depicted in Figure 6.4.

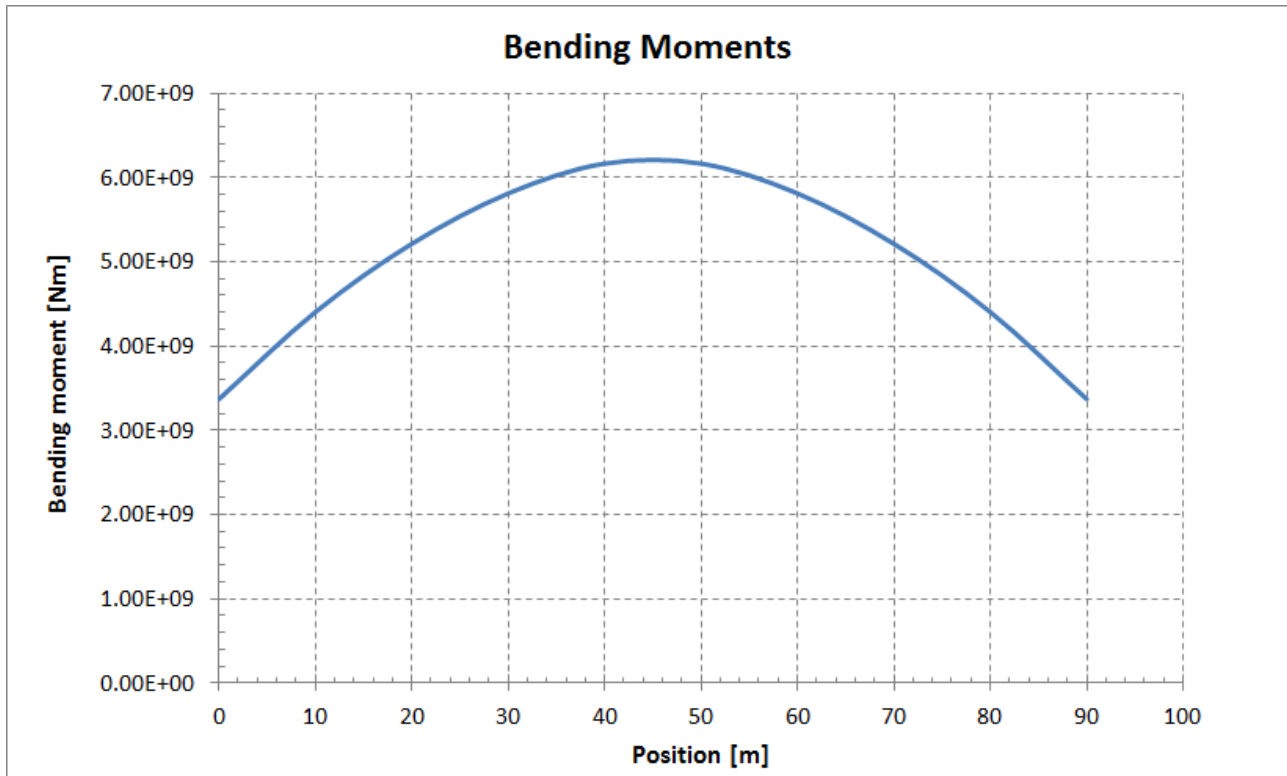


Figure 6.4: Distribution of bending moment in the model after the adjustment.

Depending whether a structural strength assessment or a fatigue assessment analysis is sought, the magnitude of the applied load varies, being overall lower in the case of the fatigue assessment.

6.3. Employment of the model for crack assessment

Description of Studied Cases

The aforementioned procedure, related to the beam model and the evaluation of the loads applied on it, has to be followed for each load case prescribed by the CSR. As mentioned earlier, in the selected study case and for the implementation of the developed methodology, analyses were carried out for two representative loading conditions, according to the intended ship's operation as prescribed by the CSR. Namely, for oil tankers, for the full load departure (FLD) condition and for the water ballast departure condition (WBD). The implementation of the calculated loads was achieved using a subroutine that was written in FORTRAN and was called by ABAQUS during the FE analysis of the three-compartment model (DLOAD subroutine). In summary the loads taken into consideration are:

- weight of the structure and the cargo/ballast
- static sea pressure
- dynamic wave pressure
- dynamic tank pressure

- hull girder vertical/horizontal bending moments

In all studied cases, linear analyses were conducted. At this point it must be underlined that the proposed methodology could also take into consideration non-linearities. In total four indicative analyses have been conducted to demonstrate the potential of the aforementioned methodology. These cases consist of the ship operating in FLD and WBD (Figure 6.5) in hogging and sagging. The fatigue loading of these cases consists of cyclic alternation between hogging and sagging. However the aforementioned methodology provides the ability to study a vast combination of loading scenarios for several loading patterns.

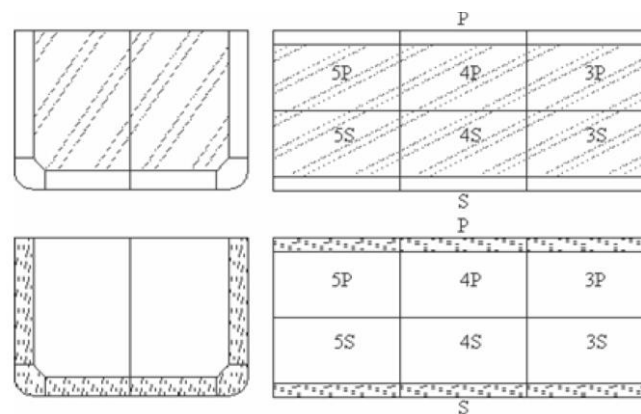


Figure 6.5: the FLD (top) and WBD (bottom) conditions

All four analyses were performed to the intact ship structure. Subsequently, and aimed at minimizing the computational cost, a sub-model of the structural member where the cracks were to be introduced was subtracted from the three-compartment model. Another reason that favours the proposed submodelling technique, in addition to the flexibility provided considering the mesh refinement and element type, is the modelling of details that might have been omitted in the three-compartment model.

The web floor located amidships and starboard was selected for the introduction of cracks. The selection of this particular structural member was based on existing surveys' data for oil tankers. These reports indicate that openings or/and manholes in that region are prone to the development of cracks (*Larsen et al. 2010*).

Two crack scenarios were envisaged, with respect to the position of the cracks. Both cracks had a total length equal to 300 mm, originating from the flange stiffener of the lightening hole and extending to the web plate. To this end, the 200 mm flange was interrupted in both crack locations and a 100 mm crack length was also modelled on the web plate. Both cracks were inclined at 45° with respect to the vertical axis of the structure. Their location is depicted in Figure 6.6

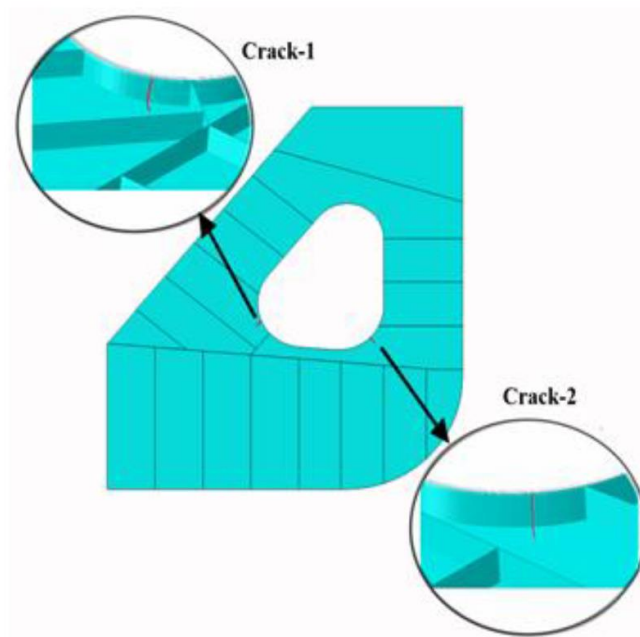


Figure 6.6: Regions where the cracks were introduced.

The boundary conditions that were imposed on the sub-model were, for each scenario, derived from the three-compartment model. The displacements and rotations were extracted from the web floors boundary regions. Since the mesh refinement level between the three-compartment model and the submodel will in most cases differ, it is essential to express the displacements and rotations of the boundary analytically. In order to acquire these analytical expressions, polynomial fitting was performed to the initial values extracted from the three-compartment model. An indicative figure depicting one of the displacements in the hopper plate boundary is depicted in Figure 6.7. The values of the rotational degrees of freedom at the web floor boundary were negligible and therefore omitted in the present analyses. A representative example is given in Figure 6.8.

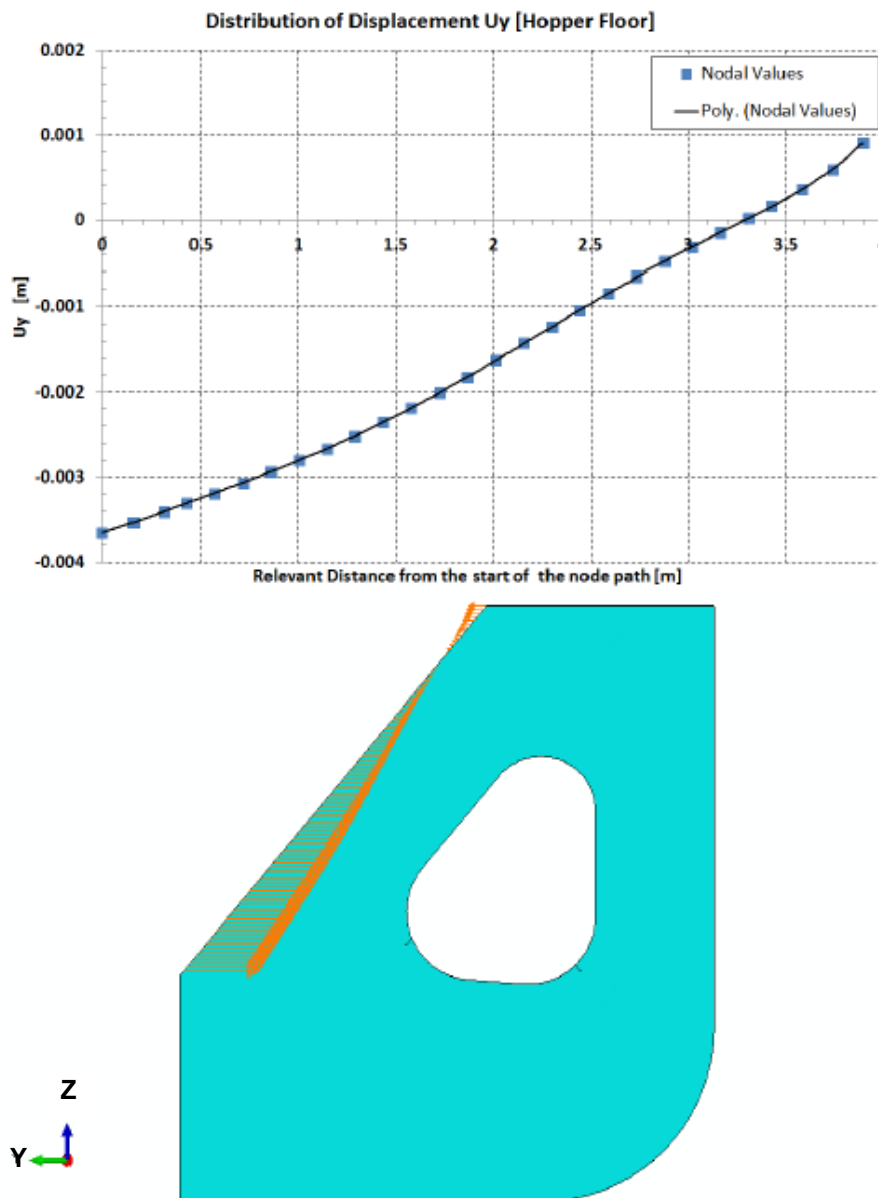


Figure 6.7: Derivation of the U_y displacement analytical field at the hopper floor boundary.

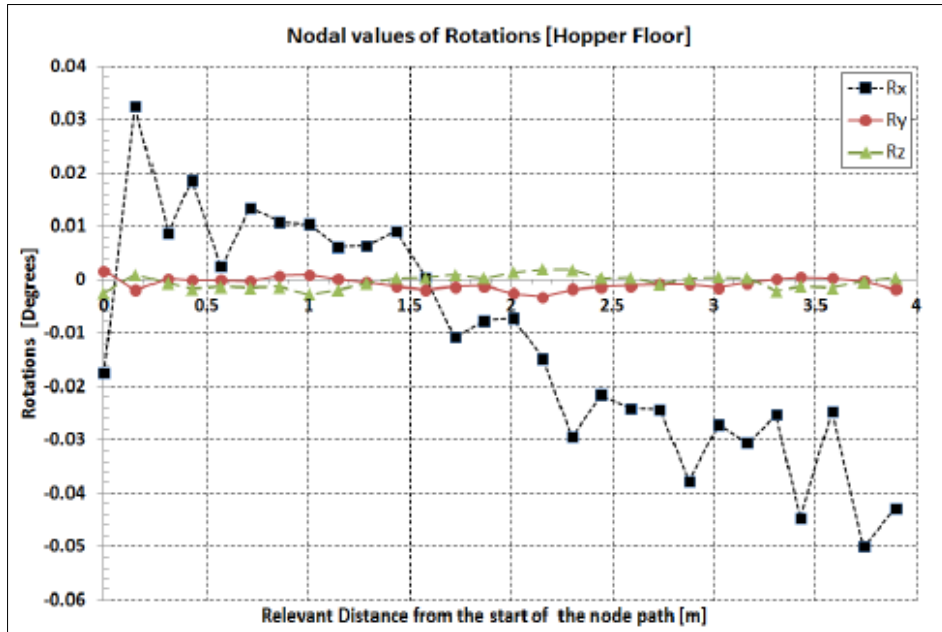


Figure 6.8: Distribution of the nodal rotations for the hopper floor boundary.

Crack Assessment and Results

The evaluated von Mises stresses were significantly lower than the yield stress of the AH36 steel (355 MPa). The region in the vicinity of the crack tip that had surpassed the yield stress can be characterized as highly local (grey area in Figure 6.9), compared to the size of the crack. Therefore the assumption of linear elastic analysis is valid and subsequently the use of linear elastic fracture mechanics (LEFM) can be applied. The value of the J integral was derived only for Crack-1 for all loading cases. In the following the stress intensity factor (SIF) was calculated with the use of the following well-known LEFM formula (Equation 6.1):

$$J = G = \frac{K^2}{E} \quad (6.1)$$

where G is the strain energy release rate, K is the SIF and E is the Young's Modulus of Elasticity. The J integral value of Crack-2 was not taken into account, as this crack did not exhibit mode-I opening. This is justified by the distribution of stresses that are normal to the crack edges (S11). As depicted in Figure 6.10, the stress distribution is virtually uniform for both sides of the crack edges and remains constant for hogging and sagging.

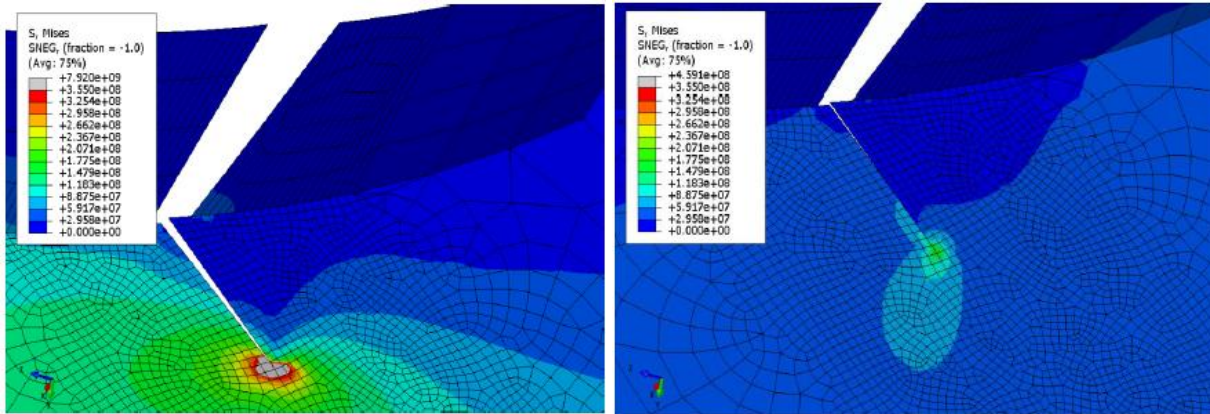


Figure 6.9: Von Mises stress distribution near crack-1 for hogging (left) and sagging (right).

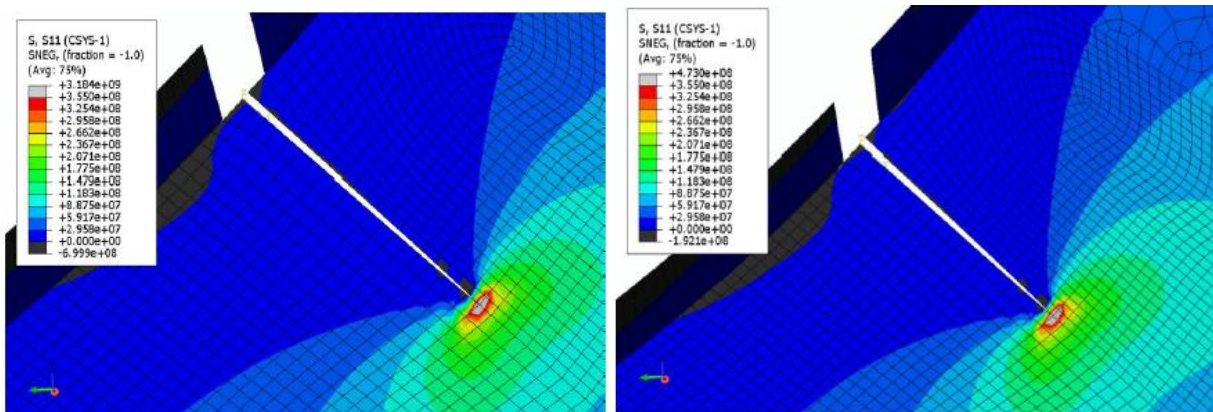


Figure 6.10: Distribution of stresses normal to crack-2 edges for hogging (left) and sagging (right).

Reviewing the results, it can be concluded that although the hopper tank floor is subjected to fatigue loading, the area around Crack-2 is in effect experiencing static loads. This is also indicated by the almost identical von Mises stress distribution around the crack area for both hogging and sagging (Figure 6.10).

As mentioned earlier, the crack locations were selected according to reports that cite the most commonly encountered crack locations in oil-tankers (*Larsen et al. 2010*). The fact that Crack 2 is in reality not subjected to fatigue for the specific loading patterns, indicate that cracks at this location could have been formed due to different loading patterns of the ship. Additionally, since a linear analysis cannot employ any contact algorithms, it is possible that element penetration at the crack edges may occur. This was indeed observed in the FLD condition and in these cases the J integral was not calculated (Figure 6.11).

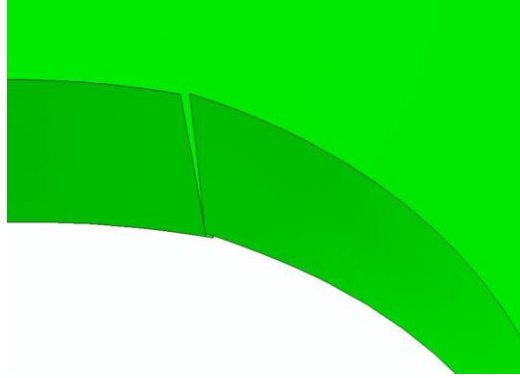


Figure 6.11: Indicative figure showing the crack-2 edge penetration.

On the contrary this was not observed in the WBD Crack-1 case. In Table 6.2 the SIF value is listed for the Crack-1 WBD case where the J integral could be evaluated. Once the K value was derived, an estimation of the Crack-1 growth rate was accomplished, based on the Paris law:

$$\frac{da}{dN} = C(\Delta K)^m \quad (6.2)$$

where:

ΔK is the difference of the SIF in hogging and sagging

$C = 2.3E-12$

$m = 3$

The values for the material constants C and m in the fatigue crack growth expression were taken from the British standard *BS 7910:2005*. The values of ΔK and crack growth rate of Crack-1 for the WBD scenario are listed in Table 6.3.

Table 6.2: Value of K and J for the WBD.

Crack Case	Loading Case	J Integral J/m ²	K MPa m ^{1/2}
Crack-1	WBD Hogging	10611.40	46.41 m
	WBD Sagging	1428.82	17.03

Table 6.3: Calculated ΔK and crack growth rate

Crack Case	Loading Case	ΔK MPa m ^{1/2}	da/dN mm/cycle
Crack-1	WBD Hogging	29.38	0.00184
	WBD Sagging		

In order to assess the criticality of the crack, the evaluated $(\Delta K, da/dN)$ point was plotted on a logarithmic chart along with the crack propagation curve of the AH-36 steel (Figure 6.12). The crack propagation curve of AH36 steel was assumed to be equal to the one described in *BS 7910:2005* for marine steels. Furthermore, the ΔK_{th} value was chosen equal to $2 \text{ MPa m}^{1/2}$, according to the same standard, and the value of K_{IC} of AH36 was selected equal to $170 \text{ MPa m}^{1/2}$ (*Sielski 1992*). The ΔK_{max} is:

$$\Delta K_{max} = K_{max} - K_{min} = (1 - R)K_{max} = 107.37 \text{ MPa m}^{\frac{1}{2}} \quad (6.3)$$

where $K_{max} = K_{IC}$ and R is the loading ratio taken as constant and equal to the ratio of $K_{WBD-Hogging}$ to $K_{WBD-Sagging}$ which gives $R = 0.37$.

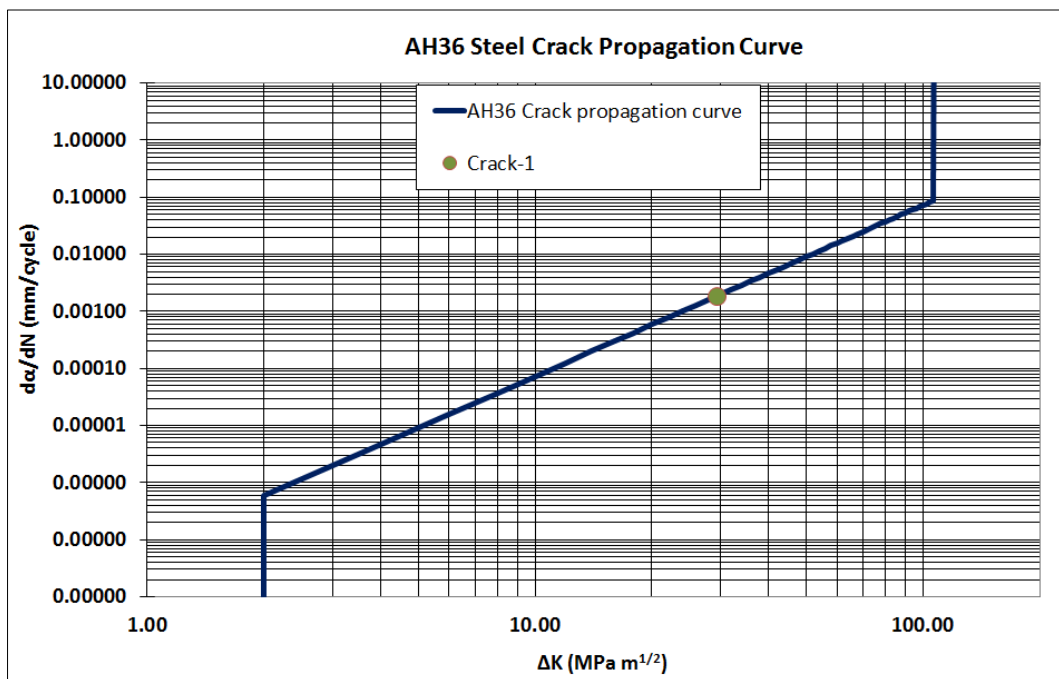


Figure 6.12: Crack propagation curve of AH36 steel along with the evaluated point for Crack-1.

As observed in Figure 6.12, the $(\Delta K, da/dN)$ point of Crack-1 is further away from the midpoint of the AH36 steel's Paris law curve, thus indicating that Crack-1 will propagate rapidly and rectification measures have to take place. The difference in the exhibited response of the cracks for WBD condition is significant, especially when considering the fact that the studied cracks have the same characteristics, are located in the same structural member and in close proximity between each other. From the findings of the results, the need for a case by case approach of cracks in marine structures is once again being pointed out, due to the complexity of the structure and the constantly varying acting loads.

6.4. Crack rectification using composite patches

Description of the Studied Cases

The previously described three compartment model was employed to investigate the effectiveness of the installation of composite patches for the rehabilitation of the structure enquiring into the effect of different parameters (Avgoulas *et al*, 2013). The same web floor located amidships and starboard was selected for the introduction of cracks and all analyses were performed using the submodelling technique. The difference however is that in the following analyses the web floor was modelled using 20-node hexahedral elements using reduced integration (referred as C3D20R in ABAQUS) with an average mesh size of 50mm and eight elements along the plating's thickness. The number of the selected through thickness elements was decided after a mesh convergence study which proved that eight elements were adequate to represent the thickness variation of the stress intensity factor accurately. The reason for the use of solid elements was to obtain a good representation of the SIF variation across the thickness of the plating, as it is well documented in the literature that the SIF in cracks that have been covered with composite patches varies through the thickness when the patch is applied on one side of the plate.

Moreover, the loading pattern of the ship was different from the one selected in the previous case (Figure 6.13). Unlike the previous section, static loads used for the strength assessment of the ship were considered for the investigation presented below. This decision was based on the fact that the loads prescribed by the regulation for strength assessment are more severe compared to the loads applied for fatigue assessment. Additionally, it would be very cumbersome to investigate all the varying patch configurations for all the possible fatigue load combinations. Therefore this approach serves as a demonstration of the effectiveness of the patch as a crack retardant under severe loading conditions.

The boundary conditions were extracted from the three compartment model along the shell edges of the web floor. To confirm that these would induce the desired loading in the solid submodel, a shell submodel was also created with a coarse mesh and the same boundary conditions were exacted in the form of displacements using the analytical filed option in ABAQUS. The reason for this investigation is because the element type is different and the mesh is significantly finer in the case of the solid model. It was reckoned that these differences might affect the response of the web. This comparison revealed that the results between the two sub models and the three compartment model are in excellent agreement with each other. Indicative results are shown in Figure 6.14.

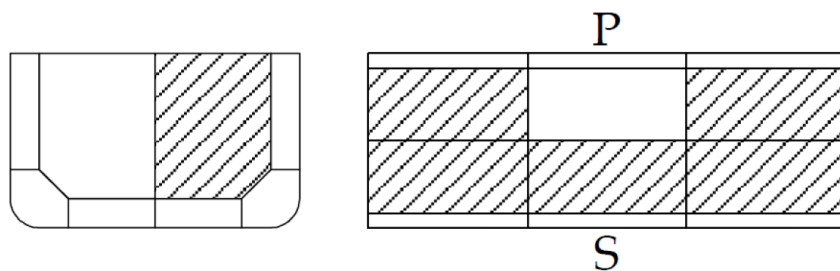


Figure 6.13: Cargo loading considered in the three compartment model.

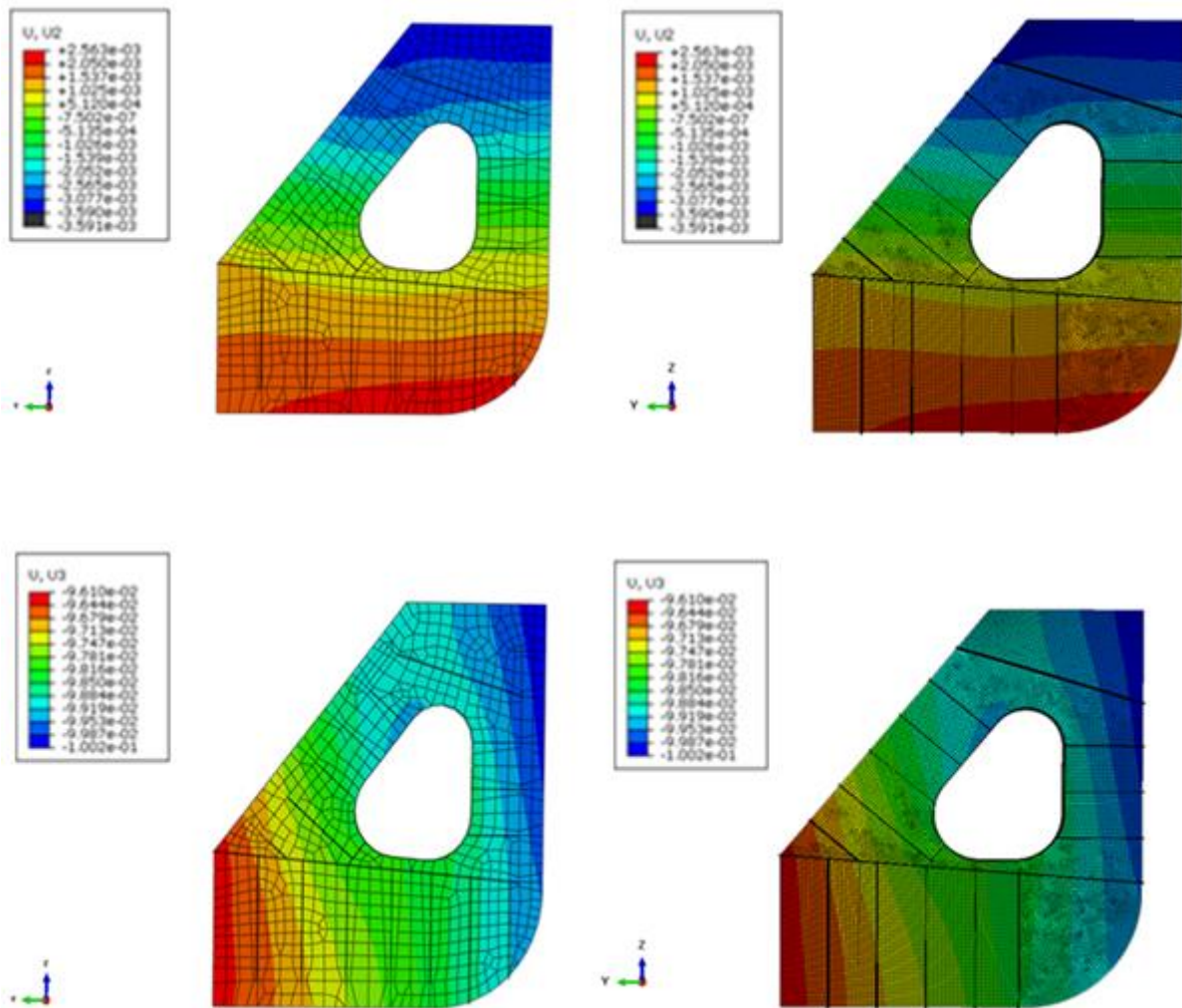


Figure 6.14: Displacement field along the Y (top) and Z (bottom) direction in the shell (left) and the solid (right) sub model.

Three different crack scenarios were considered with respect to the crack length and location. The cracks were introduced in regions 1 and 2 as shown in Figure 6.15, originating from the openings' circumferential flange stiffener. The cracks were inclined by 45° with respect to the vertical axis Z. The crack locations were once again selected based on existing surveys' data for oil tankers which indicate that openings and lightening holes in that region are prone to the development of cracks. In addition, the work presented here was focused on calculating the SIF under mode I loading and, to this end, different crack locations around the opening were examined and the ones that would exhibit a dominant mode I behaviour were selected to proceed with the analyses. The crack lengths in the web floor plate were considered equal to 200 mm and 400 mm. The edge length of the elements around the crack tip was equal to 2 mm. It must be noted that cracks were considered extending both in the flange around the opening and in the web frame plate.

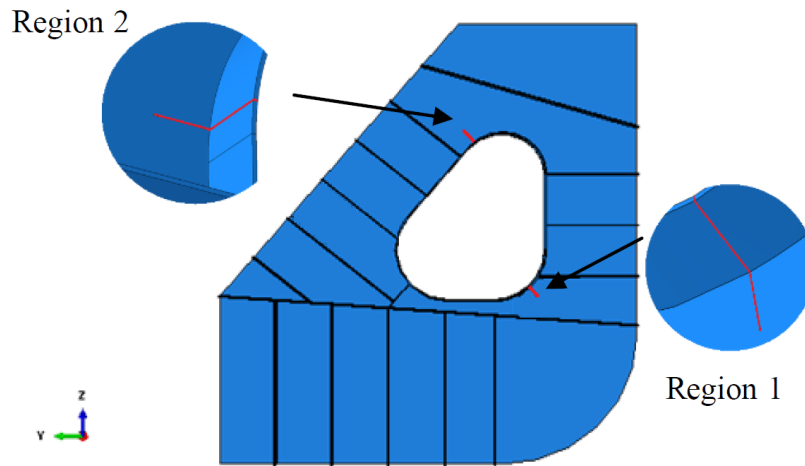


Figure 6.15: Crack locations.

Two different composite systems were selected for the patch, namely Carbon/Epoxy using the hand-layup method (HLU-CE) and Carbon/Vinylester using the vacuum infusion method (VI-CV). The mechanical properties of the materials have been measured from a preceding series of characterization tests and are listed in Appendix A. The composite patches were modelled using four conventional, continuum solid finite elements through thickness. The patches were modelled as homogeneous orthotropic, with a linear elastic response. The adhesive layer was considered to be in all cases the resin of the composite system and was modelled as an isotropic linear elastic material, using one continuum solid element through thickness. Possible failure mechanisms were not taken into consideration in the analysis.

A numerical parametric analysis was undertaken investigating the effect of the geometry, material and the thickness of the composite patch. The material properties of the steel and the adhesive layers are listed in Table 6.4, where E = Young's modulus and ν = Poisson ratio.

Table 6.4: Material properties of resin and steel.

Material	E (MPa)	ν
Steel	207000	0.33
Vinylester	3050	0.35
Epoxy	3450	0.35

For each one of the two materials, two different thicknesses were considered. The thicknesses were selected to reflect realistic manufacturing limitations and were decided based on preselected values of the axial stiffness ratio between the base steel plate and the composite patch. The stiffness ratio is defined as:

$$SR = \frac{E_1 t_p}{E_s t_s} \quad (6.3)$$

where:

E_1 is the composite laminate's Young modulus in the principal direction

t_p is the laminate thickness

E_s is the young's modulus of steel, equal to 207 GPa

t_s is the steel plate's thickness, equal to 14mm.

The stiffness ratio values of 0.4 and 0.6 were selected for the VI-CV case, while values 0.2 and 0.4 were selected for the HLU-CE. Rearranging the stiffness ratio formula, the patch thickness for each case was calculated. Three different geometries were selected for the repairs, denoted as geometries A, B and C (Figure 6.17). Cases A and B were applied for the rehabilitation of Crack-1, while case C was implemented on Crack-2. These geometries were selected based on the available space between the stiffeners. Specifically, for cases A and B the edges AB and CD were selected to be as close as possible to the transverse stiffeners and parallel to them. Moreover, the distance of the crack tip (point G) from the edge BC was taken as approximately equal to three times the crack length for case A and equal to two times the crack length for geometric case B. Finally, edges AF and EF were approximately equal. As previously, for geometry case C, the patch edge AB was parallel and as close as possible to the existing stiffener. The length of the edges AB and CD were equal to three times the length of the crack. Finally, the dimension AD is equal to BC. The dimensions for all cases are listed in Table 6.5.

Table 6.5: Patch dimensions.

Dimensions [m]			
Edges	Crack-1		Crack-2
	Case A	Case B	Case C
AB	0.561	0.361	0.600
BC	0.587	0.587	0.460
CD	0.898	0.698	0.600
DE	0.187	0.187	-
EA	0.472	0.472	-
AD	-	-	0.460

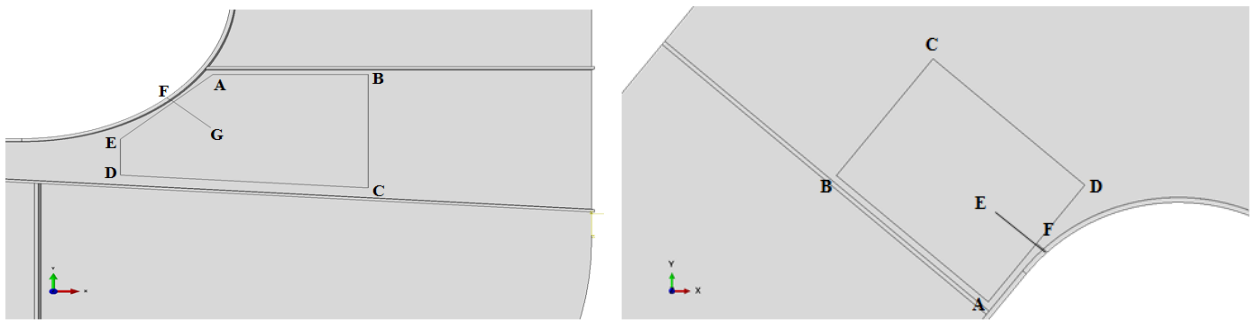


Figure 6.17: Patch geometries cases A and B (left) and case C (right).

Table 6.6: Studied cases.

Region	Geometry	Crack Case	Material	Stiffness Ratio	Patch Thickness [mm]	Configuration
1	A	Crack-1/200	VI-CV	0.4	11.3	One-sided
1	A	Crack-1/200	VI-CV	0.6	17.0	One-sided
1	A	Crack-1/200	HLU-CE	0.2	15.0	One-sided
1	A	Crack-1/200	HLU-CE	0.4	30.0	One-sided
1	B	Crack-1/200	VI-CV	0.4	11.3	One-sided
1	B	Crack-1/200	VI-CV	0.6	17.0	One-sided
1	B	Crack-1/200	HLU-CE	0.2	15.0	One-sided
1	B	Crack-1/200	HLU-CE	0.4	30.0	One-sided
2	C	Crack-2/200	VI-CV	0.4	11.3	One-sided
2	C	Crack-2/200	VI-CV	0.6	17.0	One-sided
2	C	Crack-2/200	HLU-CE	0.2	15.0	One-sided
2	C	Crack-2/200	HLU-CE	0.4	30.0	One-sided
2	C	Crack-2/400	VI-CV	0.4	11.3	One-sided
2	C	Crack-2/400	VI-CV	0.6	17.0	One-sided
2	C	Crack-2/400	HLU-CE	0.2	15.0	One-sided
2	C	Crack-2/400	HLU-CE	0.4	30.0	One-sided
2	C	Crack-2/200	VI-CV	0.4	11.3	Double sided
2	C	Crack-2/200	VI-CV	0.6	17.0	Double sided
2	C	Crack-2/200	HLU-CE	0.2	15.0	Double sided
2	C	Crack-2/200	HLU-CE	0.4	30.0	Double sided

Results of Parametric Study

Crack-1

Initially the redistribution of the von Mises stress due to the existence of the patch was evaluated for the

different cases. Results indicated that the stress distribution was similar for all cases with no major variations and that in all cases lead to the significant stress reduction at the crack tip area. Figure 6.16 depict the von Mises stress distribution around crack-1 before and after the application of the composite patch.

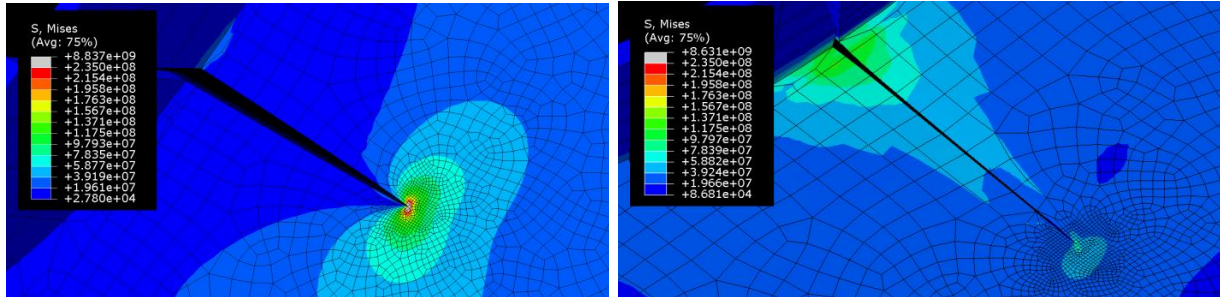


Figure 6.16: Von Mises stress in the steel before (left) and after repair (right).

Figure 6.17 presents the through thickness variation of the SIF, at the crack tip of crack-1/200, for the unpatched case and for the four different cases of geometry A. The zero thickness value corresponds to the unpatched side of the steel plate, whereas the 100 thickness value corresponds to the patched side.

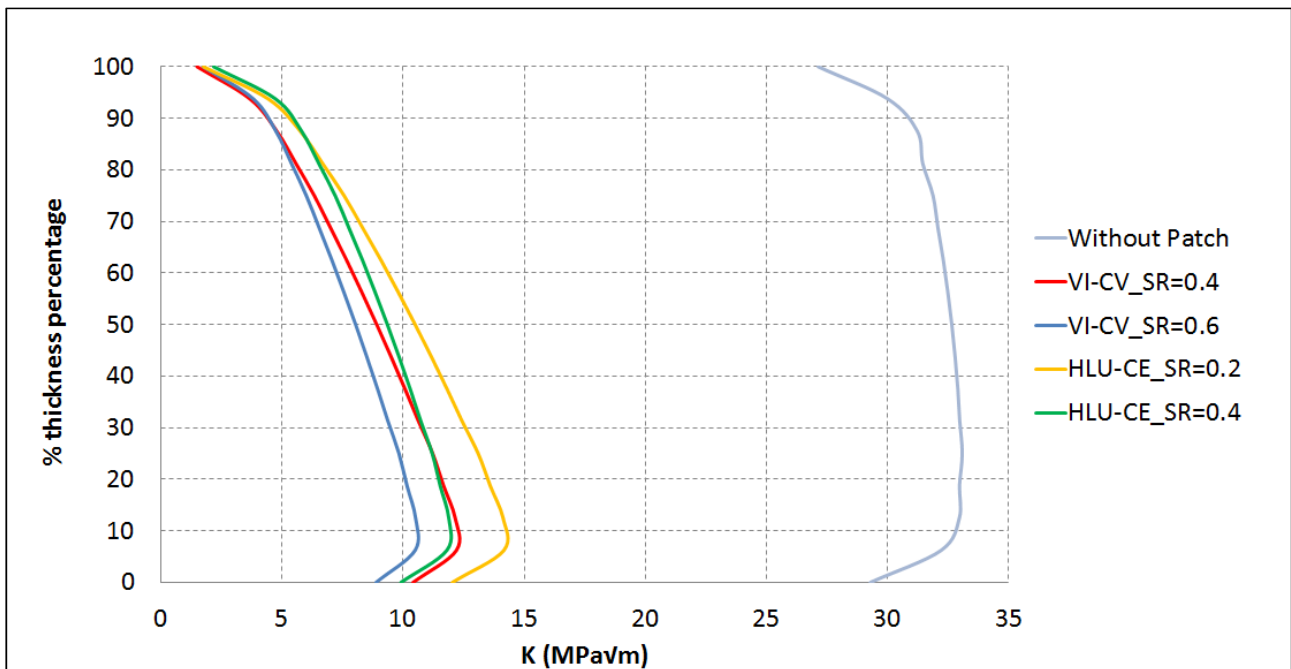


Figure 6.17: Stress intensity factor across the thickness.

The SIF variation of the unpatched plate is slightly tilted due to some bending loading that develops on the steel plate, originating from the global loading of the ship. Figure 6.18 however shows also a substantially inclined SIF variation for all patched cases, which owes to the inherent bending of the plate and to the induced secondary bending. Reviewing the results, it is obvious that for both reinforced and unreinforced cases there is an inflection on the curves depicting the stress intensity factor distribution across

the thickness of the plate. The change in the slope of the curve occurs near the edges of the free, unreinforced surface. This behaviour is attributed to the fact that because of the high stresses that develop perpendicular to the crack plane at the crack front, the surrounding material tries to contract in the remaining two directions due to the well-known Poisson phenomenon. However, it is prohibited to do so by the surrounding material, causing a triaxial stress state near the crack tip. The stress triaxiality becomes lower near the surface reaching plane stress on the surface of the plate, as the material is not constrained by its surrounding and is free to retract (Anderson 2005).

It is evident from this figure that the application of a patch results in a remarkable reduction of the SIF values. Comparing the maximum values of SIF for the unpatched and the patched cases, a reduction of 57%, 64%, 63% and 68% was observed in the patched cases for the composite systems HLU-CE (SR=0.2), HLU-CE (SR=0.4), VI-CV (SR=0.4) and VI-CV (SR=0.6), respectively. The higher difference in the reduction of SIF (11%) was observed between the HLU-CE (SR=0.2) and the VI-CV (SR=0.6) cases. Moreover, negligible difference in the SIF reduction was observed between the two different composite systems with the same SR (0.4).

Regarding the different patch geometry (case B), results indicated that no differences were marked in the SIF variations from those of the geometry A patch. This is attributed to the fact that by varying the length of the patch after a certain point the stress field around the crack tip is not affected. Thus, it can be stated that, in this specific case, the use of the smaller geometry B patch is equally effective.

Consequently the length of the patch does not affect the distribution of the stress intensity factor along the crack tip. However, in the case where the crack is advancing, a larger patch is more favourable as the crack length will have to grow to larger lengths in order to get past the repair.

Crack-2

Similar results were obtained for crack-2, with comparable stress redistribution in the vicinity of the crack, regardless of the patch thickness and material system. This is reflected, as expected, in the values of the stress intensity factor, as shown in Figure 6.18.

The results of Figure 6.18 refer to both crack-2/200 (dash lines) and to crack 2/400 (solid lines). The differences of the results between the two crack lengths are in general small, indicating that the geometry C patch is equally efficient in decreasing the stress state at the tip of either crack-2/200 or crack-2/400. Comparing the maximum values of SIF of Figure 6.19 for the unpatched and the patched cases of Crack-2/200, a reduction of 51%, 60%, 57% and 62% is observed in the patched cases for the composite systems HLU-CE (SR=0.2), HLU-CE (SR=0.4), VI-CV (SR=0.4) and VI-CV (SR=0.6), respectively. For the Crack-2/400 case, the corresponding reductions are 58%, 69%, 64% and 71%, slightly higher than in the previous case. In both crack cases, the higher difference in the reduction of SIF between the composite systems of the same crack case was 11% for Crack-2/200 and 13% for Crack-2/400. This difference was observed between HLU-CE (SR=0.2) and VI-CV (SR=0.6) composite systems. Finally, small differences in the SIF reduction (3% and 5%) are observed between the two different composite systems with the same SR (0.4).

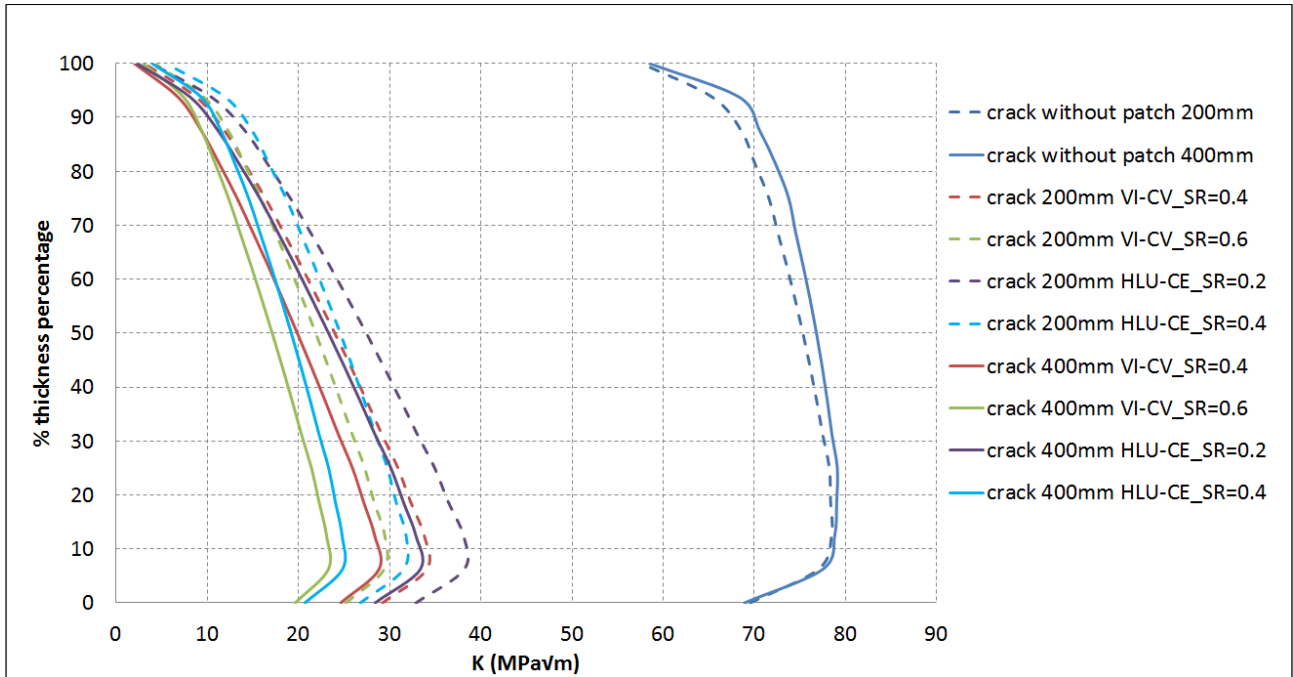


Figure 6.18: Distribution of stress intensity factor in crack-2.

Crack-2 bilateral patch configuration

A bilateral patch (applied on both sides of the steel plate) was modelled for the crack-2/200 case. Both patches were modelled according to geometry C and taking into account the different composite systems. The application of a bilateral patch results in the development of very low stresses, both near the crack tip and in the crack front along the plate's thickness. This was expected as, due to symmetry, no eccentricity is presented. Additionally, the stresses are uniformly redistributed on both sides of the plate. The SIF distribution for both the one sided (solid lines) and the double sided patch configurations (dashed lines) are listed in Figure 6.19. Results demonstrate that in the case of the bilateral patch configuration, the SIF variation is approximately constant through the thickness of the steel plate, a fact owing to the lack of secondary bending since the cross section of the reinforcement is now symmetric but most importantly at the redirection of the stresses from the steel to the composite substrate. In the case of the bilateral patch, a SIF reduction of 86%, 89%, 91% and 93% is observed in the patched cases with respect to the unpatched one, for the composite systems HLU-CE (SR=0.2), HLU-CE (SR=0.4), VI-CV (SR=0.4) and VI-CV (SR=0.6), respectively.

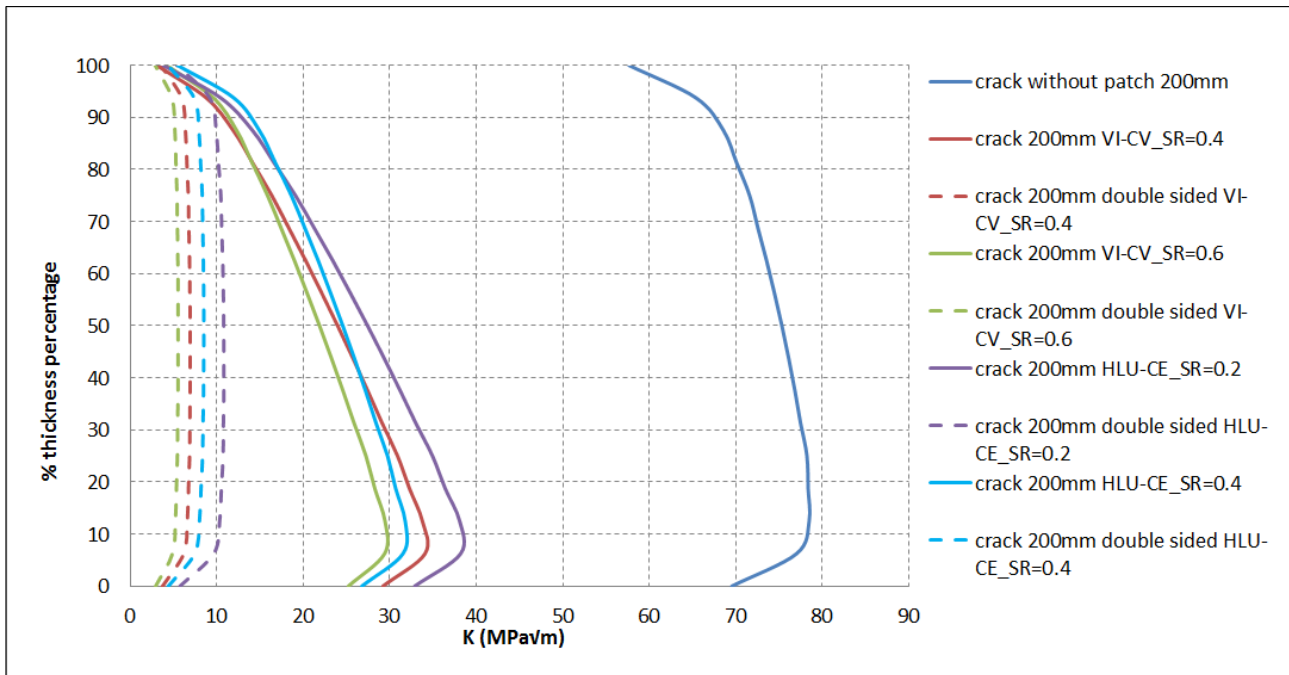


Figure 6.19: One sided versus double sided patch configuration.

6.5. Conclusions

A methodology based on the implementation of the fatigue loadings prescribed by CSR in finite element analysis has been presented. This methodology is proposed as a common base for the implementation of proper fatigue loads in the study of the effectiveness of different crack arrest technologies on real applications in marine structures. A platform was developed and a demonstration of its potential was presented through the introduction of two cracks with the same characteristics, in neighbouring positions in the floor of a web frame of an Aframax oil tanker. The response of the two considered cracks under hogging and sagging loading was evaluated for the FLD and WBD conditions. It was observed that for different loading patterns (FLD, WBD), the response of the modelled cracks was different. Furthermore under the same loading pattern (WBD), the two cracks exhibited different results, as Crack-1 would propagate while Crack-2 remained stationary. This remark underlines once again the necessity of a case by case study of cracks and the importance of creating a common base concerning the fatigue loading of structures operating in the marine environment.

Subsequently the efficiency of the composite patch repair technology for the rectification of cracked structural members of marine structures was demonstrated using the same platform. Different repair configurations were investigated to study the effectiveness of the material geometry and thickness of the composite patch. Analyses showed that in all cases the application of a composite patch led to the significant reduction of the stress intensity factor across the thickness of the plate. In general, the effectiveness of the configurations was comparable for the types of repairs that were considered. The patches which had a length equal to two times the crack length proved to be equally effective with the larger patches, which had a

length equal to three times the crack length. However a fatigue analysis incorporating damage models is required to provide a better understanding on how the patch length truly affects the crack growth rate as possible damage mechanisms at the bondline were not implemented in the conducted analyses.

7. Parametric investigation for the design of composite patches

7.1. Introduction

Having proven their efficiency, composite patch repairs have started being implemented in the marine and offshore field, as mentioned in the first chapter of this thesis. Nonetheless, unlike other fields, such as pipe repairing, where eventually an ISO has been developed (*ISO 24817:2015*), rules and guidelines have not yet been introduced for the composite patch rehabilitation of marine and offshore structures. A first step towards this direction is the development of a recommended practice for “Design Fabrication, Operation and Qualification of Bonded Repair of Steel structures: *DNV-RP-C301* by Det Norske Veritas, based on the experience gained from both laboratory and field applications (*McGeorge 2009, 2010*). A brief description of the recommended practice and its application areas is presented in the paper of *Echtermeyer et al (2014)*. The recommended practice lists several issues associated with composite patch repairing, starting from decision making regarding the performance of the repair, up to inspection and qualification testing. But, due to the nature of this document, it serves more as a starting step and several of the issues are addressed inadequately providing little practical help on how to adequately design and evaluate a composite patch repair. A similar guidance note has been issued by Bureau Veritas (*Guidance note NI613-DT-R00-E, 2015*) providing requirements and recommendations for the assessment of composite patch repairs. Once again, this document does not sufficiently address the design a composite patch repair.

In this section a methodology for the assessment of composite patch repairs is proposed. This methodology is principally based on the theory of linear elastic fracture mechanics for bimaterial surfaces, as described in Chapter 2.

In most occasions the available time window for the conduction of repairs do not allow for extensive Finite Element Analyses. In addition, cohesive zone modelling, although proven very effective for the description of the patch debonding mechanisms, constitute an advanced finite element modelling techniques which necessitate difficult to find data related to the characteristics of the cohesive law, might be prone to convergence difficulties and give rise to unacceptably long computational time.

Taking these factors into account, emphasis has been given in providing a robust, fast and simple approach, employing mainly analytical formulas in conjunction with simple finite element modelling, if necessary, for the design of composite patch repairing. The method is predominantly based on the work of *Suo and Hutchinson (1990)* and the employment of the Crack Surface Displacement Extrapolation method. This method was implemented with the use of a user subroutine in ANSYS which extracts the magnitudes that are necessary for the analytical calculation of the phase angle. Having quantified the values of these parameters for different material systems, a simple analytical approach can be followed for the calculation of both the energy release rate and the mode mixity of each given configuration for various loading conditions.

7.2 Crack Surface Displacement Extrapolation method and enhanced Virtual Crack Closure Technique

Williams, by using analytical models to examine two distinct isotropic media with an interface crack between them, found that the energy-release rate and phase angle exhibit an oscillatory behaviour closer to the crack tip (*Williams 1959*). This sharp oscillatory behaviour is in reality not physically possible as it implies that, in that region, the upper and lower crack faces will interpenetrate one another. Due to this oscillatory behaviour, the strain energy release rate and the mode mixity cannot be directly measured at the crack tip. In the isotropic bimaterial case it is well established that most interfacial fracture problems are weakly dependent on the ε or the related second Dundurs parameter β (see section 2.4 for nomenclature). Therefore, in most analyses, it is possible to set $\varepsilon = 0$ without significantly altering the physics of the analysis. However, an analogous role for the orthotropic case has not yet been established.

There are several methods available in the literature for the extraction of the energy-release rates and mode-mixity phase angles of bimaterial interfaces using finite element analysis. From these, one of the most widely used for isotropic materials is the virtual crack closure technique (VCCT). The VCCT involves expressing the mode I and mode II components of the total energy release rate in terms of nodal forces ahead of the crack tip and nodal displacements behind the crack tip (Equation 7.1).

$$\begin{aligned} G_I &= \frac{1}{2\Delta} \sum_{j \text{ nodes}} F_{12j} \delta_{2j} \\ G_{II} &= \frac{1}{2\Delta} \sum_{j \text{ nodes}} F_{22j} \delta_{1j} \end{aligned} \quad (7.1)$$

where F_{22j} and F_{12j} are, respectively, the normal and shear nodal forces per unit thickness over a distance Δ ahead of the crack tip and δ_{2j} , δ_{1j} are corresponding nodal crack opening and sliding displacements over distance Δ behind the crack tip. In applying the classical VCCT method, only the total energy release rate reaches a limiting value, as the virtual crack extension length Δ is decreased and the implementation of VCCT is made possible by choosing values of Δ significantly larger than the oscillatory region. This places a limit on how close to the crack tip the VCCT can be applied. To circumvent this limitation, *Beuth (1996)* proposed the enhanced VCCT. The enhanced VCCT's formulation expresses the nodal forces and displacements in complex forms and in this way allows the extractions of the aforementioned energy release rates despite the oscillatory behaviour. An alternative attractive method to circumvent the problems related to the oscillatory region is the Crack Surface Displacement Extrapolation technique (CSDE). This method is based on the observation that the mode-mixity phase angle and energy-release rate G vary linearly for a short distance in the region preceding the oscillatory behaviour. This region is referred to as the K-dominated zone and the developed stress, is proportional to $1/(r^{1/2})$. Taking into consideration the existence of this linearity, the CSDE method calculates the slope of the energy release rate and the mode mixity between the

boundaries of the K dominated zone and subsequently, using the calculated slopes, performs an extrapolation to the crack tip. The method is illustrated in Figure 7.1. The CSDE is implemented by the use of a user subroutine written in ANSYS parametric design language script (APDL), which seeks the boundaries of the K-dominated zone, calculates the slope and in the following performs the extrapolation.

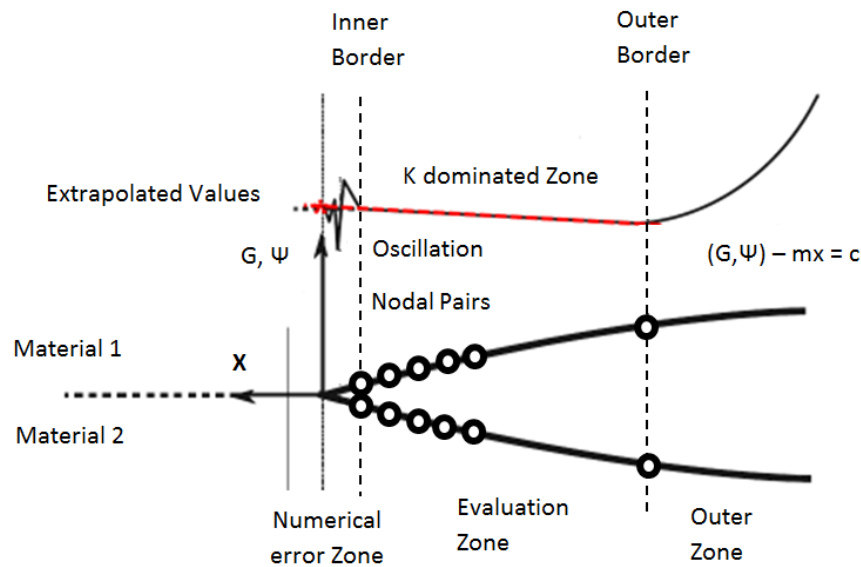


Figure 7.1: Representation of the CSDE method.

The advantages of the CSDE method against other existing methods for the calculation of the energy release rates and mode mixity have been reported in *Berggreen (2004)* and *Saseendran (2014)* focusing on skin core debonding problems in sandwich constructions.

There are though some significant differences between a sandwich construction and a composite to steel bimaterial interface, as in the latter the thickness ratio and the Young modulus of the constituent materials are significantly higher. As there is a lack in the literature concerning suitable experimental results, the CSDE method is compared to the enhanced VCCT method and the J integral for different bimaterial configurations and loading ratios, to investigate the suitability of the selected method. To the best of the author's knowledge, there is no publicly available research employing the CSDE method for the investigation of a composite to steel bimaterial, with the composite being modelled as an orthotropic material. This makes the need for benchmarking the method against the enhanced VCCT method even greater.

Finite Element Formulation: 2-D CSDE Method

Prior to comparing the CSDE method to the enhanced VCCT, a mesh convergence study was conducted to study the effect the near tip mesh size can have on the CSDE subroutine results. To this end, different near-tip mesh densities were evaluated. The mesh discretization was performed for a single configuration for the same load case. After the analyses the energy-release rate G and the mode-mixity phase angle were compared for different mesh densities.

The ANSYS model consisted of two-dimensional quadratic 8 node elements (PLANE82). Four-node planar linear elements were used near the crack tip (PLANE42 in ANSYS). This element type was chosen at the crack tip as it shows higher tolerances to large deformations that might be experienced at the crack-tip. The linear elements are present around the crack tip for a distance of three times the element edge length. A highly refined mesh is used to model the crack region extending one time the thickness of the composite material. It must be noted that the choice of elements near the crack-tip has no influence on the CSDE method, as the calculated values are obtained from the extrapolation from the inner boundary of the K-dominant zone. The parabolic elements outside the linear region have been modelled with high mesh density to capture the relative crack flank displacements. Six elements were used through the thickness of the composite substrate and 12 through the steel one, resulting in a global element size equal to approximately 0.85mm outside the highly refined region at the crack tip.

The considered scenario consisted of a 500 mm long bimaterial interface with thicknesses equal to 5 and 10 mm for the composite and steel substrates respectively. The crack length in the interface was equal to 200 mm. The composite substrate consisted of vacuum infused carbon epoxy laminate (refer to Appendix A for the mechanical properties), while the tensile modulus of the steel was taken equal to 203 GPa and the Poisson ratio 0.3. In all cases, the composite material is modelled as orthotropic, while the metallic substrate as linear elastic isotropic.

Pure moments were applied at the free ends of each substrate (Figure 7.2), while all degrees of freedom are constrained in the opposing side. Moment acting on the composite substrate is considered positive acting clockwise, while the moment acting on the steel substrate is positive when it is counter clockwise. Figure 7.2 illustrates the selected case focusing on the debonded region up to the crack tip. The magnitudes of the applied moments were 800 Nmm/mm and 200 Nmm/mm acting on the steel and composite substrate respectively. The finite element model mesh is depicted in Figure 7.3. Elements in light blue correspond to the composite material, while in dark blue to the steel. The element arrangement and mesh density around the crack tip is presented in Figure 7.4, where the linear element area is outlined in green.

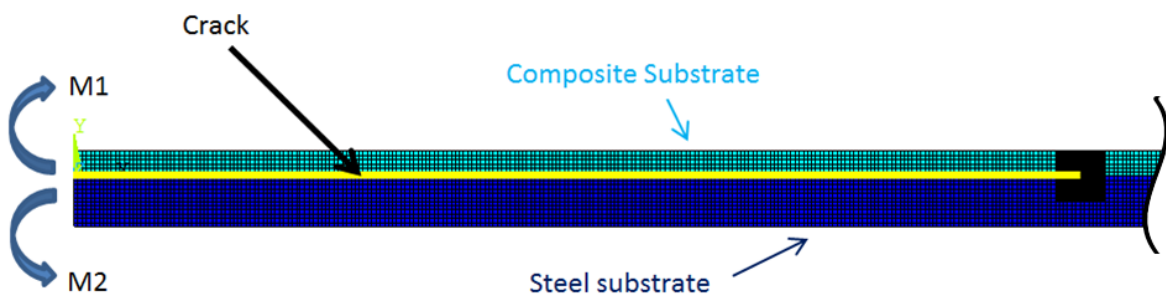


Figure 7.2: Illustration of the crack region of studied bimaterial interface.

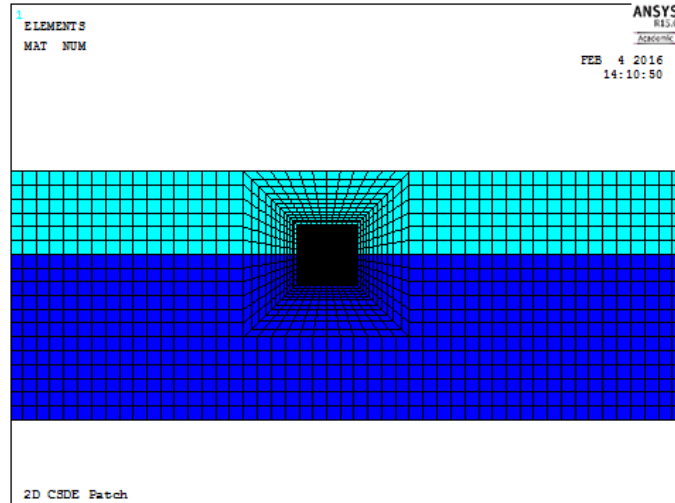


Figure 7.3: Mesh size of the FE model for the implementation of the CSDE method.

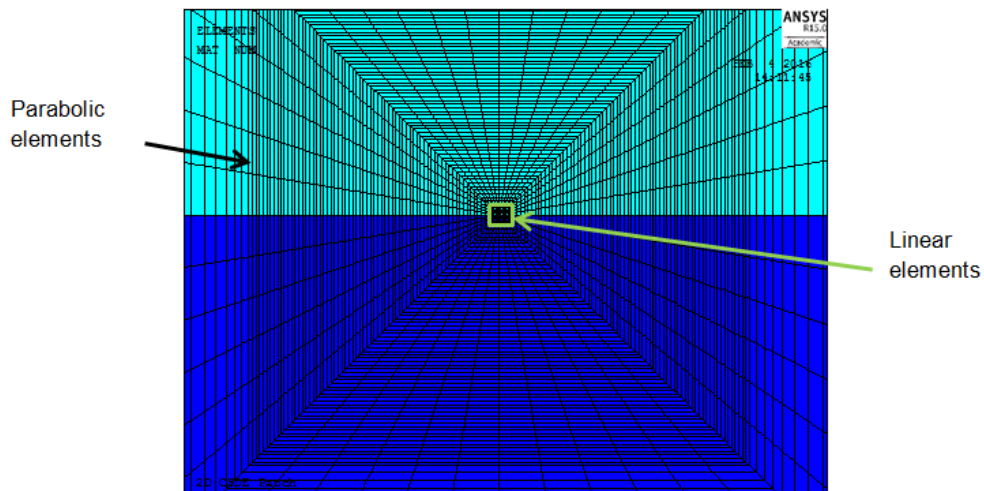


Figure 7.4: Element arrangement and mesh density at the crack tip.

The mesh sensitivity investigation initially started out from a near tip element size of $1.786\text{E-}02$ mm. It was observed that making the mesh denser at crack-tip beyond the size of $3.571\text{E-}03$ leads to insignificant variation of G and ψ (Table 7.1). Therefore a near-tip element edge length of $3.571\text{E-}03$ mm is used in all subsequent models.

Table 7.1: Crack tip convergence CSDE.

Element size [mm]	G [N/mm]	$\psi_{\text{fullformulation}}$ [degrees]
$1.786\text{E-}02$	$2.9251\text{E-}2$	-1.990
$7.143\text{E-}03$	$2.9597\text{E-}2$	-1.999
$3.571\text{E-}03$	$2.9651\text{E-}2$	-2.013
$1.786\text{E-}03$	$2.9651\text{E-}2$	-2.027

Figure 7.5 and Figure 7.6 illustrate the energy release rate and mode mixity obtained with the CSDE method for the described configuration with a selected near-tip element edge length of $3.571\text{E-}03$ mm. The

horizontal axis marks the distance from the crack tip in both cases. The vertical dashed line denotes the inner boundary of the linear, K-dominated zone as defined by the energy release rate readings and the prescribed tolerance after which the linear behaviour is assumed to stop. It is evident that moving closer to the crack tip beyond the inner boundary, the calculated values deviate from the linearity and eventually start to oscillate as described earlier in this section. The way the CSDE circumvents this oscillatory behaviour is depicted by the green line, whose slope is defined by the linear K-dominated region and is subsequently extrapolated to the crack tip to obtain the correct values for both the energy release rate and the mode mixity. It must be noted that this is the first time to the best of the author's knowledge that the CSDE method has been used for the calculation of the energy release rate at a steel composite bimaterial interface with the composite substrate modelled as an orthotropic material.

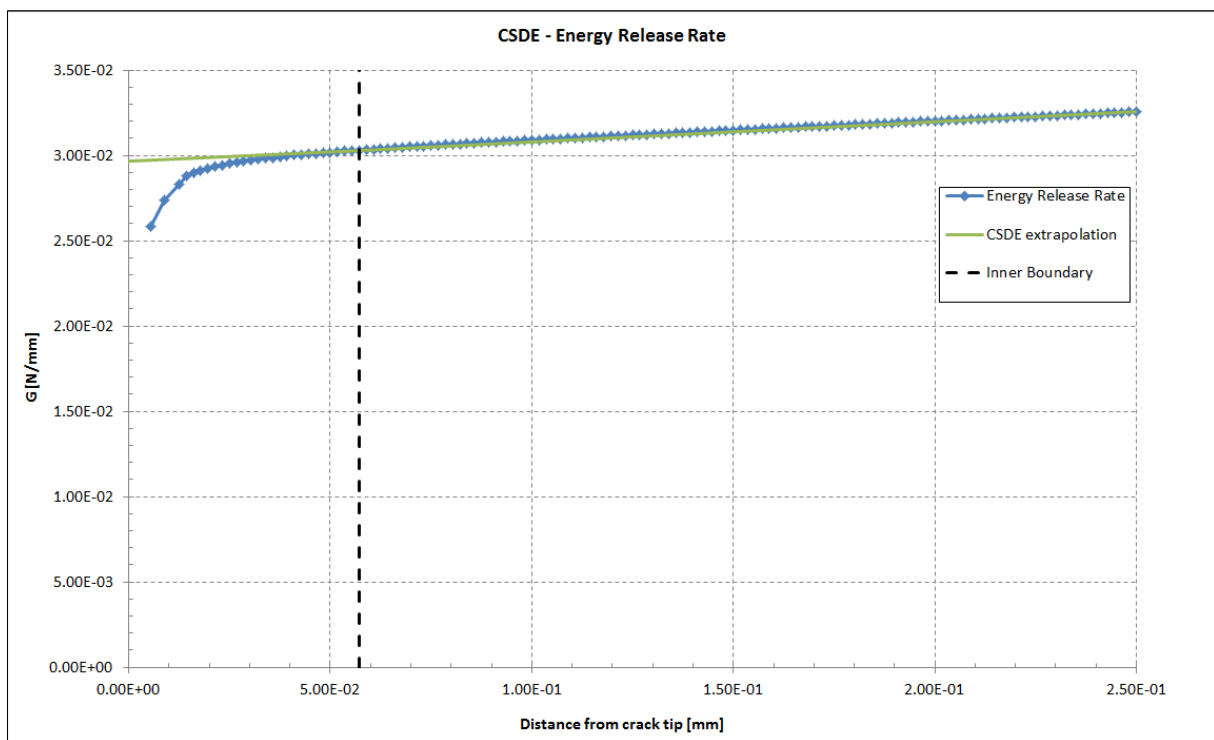


Figure 7.5: Extrapolation of the energy release rate.

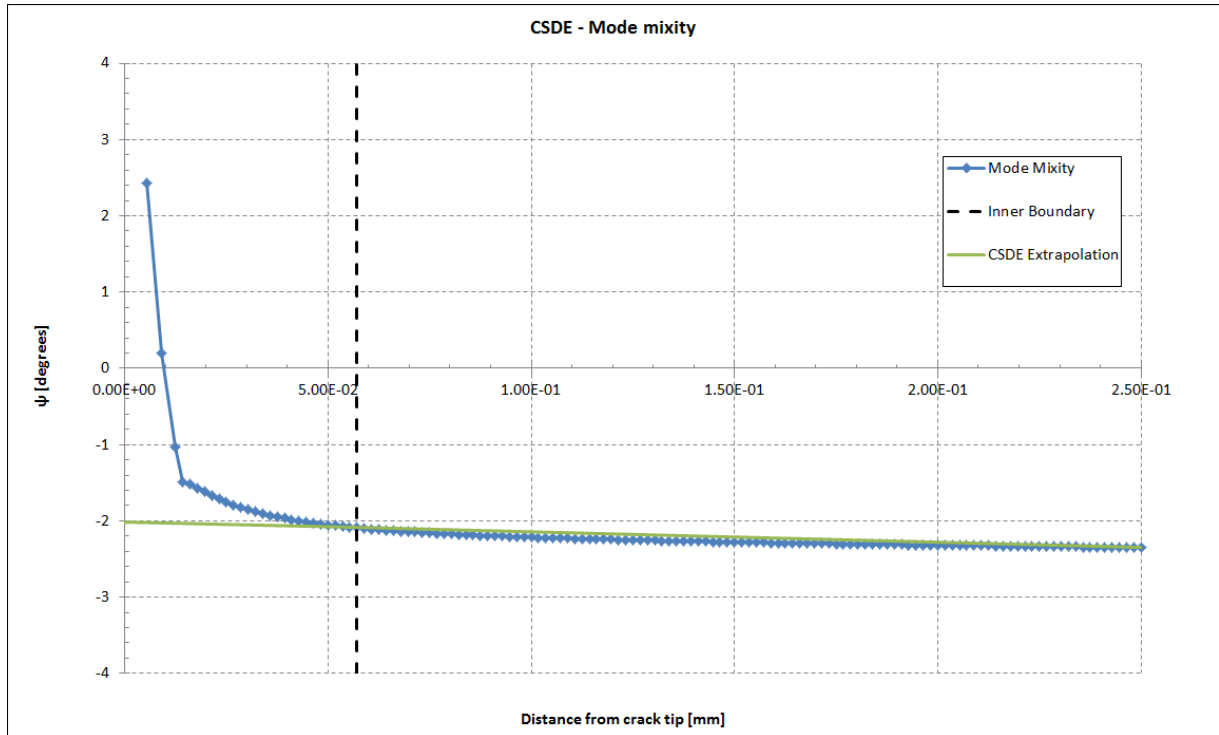


Figure 7.6: Extrapolation of the mode mixity.

Comparison of the CSDE Method to the Enhanced VCCT

In the following the results from the CSDE method were compared to the ones obtained using the enhanced VCCT method. The enhanced VCCT method was implemented using ABAQUS 6.14-2, as this method is already incorporated in the software. Hence, a geometrically identical model with the one presented earlier was generated in ABAQUS using 4 node bilinear planar elements with reduced integration. The global mesh density was the same for both cases, however as the computational time for the enhanced VCCT increased significantly, the fine mesh area around the crack tip was set equal to 0.1mm for the ABAQUS model.

Three different loading combinations were considered and the results obtained with the CSDE and enhanced VCCT methods as well as the J-integral are presented in Table 7.2. Additionally, the mode mixities calculated by the enhanced VCCT and the CSDE method are listed in the same table. It must be mentioned that only the reduced formulation of the mode mixity can be calculated by the enhanced VCCT method (Equation 2.31). Following the definition of the aforementioned equation, only the absolute value of the mode mixity can be calculated, unlike the VCCT method where both full and reduced formulations can be calculated, with the respective signs. The loading combinations were selected so as to achieve different values of the strain energy release rate and mode mixity. It is reminded that moments acting on the composite substrate are considered positive when they are acting clockwise, while the moments acting on the steel substrates are positive when they are acting counterclockwise (Figure 7.2).

Table 7.2: Comparison of the CSDE to the enhanced VCCT and the J-integral.

Cases	G_{CSDE} [N/mm]	$G_{enhanced\ VCCT}$ [N/mm]	J-integral [N/mm]
$M_1 = 1000$ Nmm/mm $M_2 = 1000$ Nmm/mm	0.44492	0.44625	0.44525
$M_1 = 200$ Nmm/mm $M_2 = 800$ Nmm/mm	0.02965	0.03016	0.03035
$M_1 = 50$ Nmm/mm $M_2 = 1200$ Nmm/mm	0.02502	0.02664	0.024923
	Ψ_{full_CSDE} [degrees]	$\Psi_{reduced_CSDE}$ [degrees]	$\Psi_{reduced_enhanced_VCCT}$ [degrees]
1 st case	-26.998	-47.979	44.794
2 nd case	-2.013	-23.490	22.767
3 rd case	33.677	11.529	14.771

The results obtained from the CSDE and the enhanced VCCT methods are overall in good agreement between each other, with the energy release rate difference being below 1.8% for the first and second case and 6.5% for the last case. In addition, the maximum difference in the calculated mode mixity for the two methods is 3 degrees which is reasonable. Comparing the two methods to the results of the J-integral, it is evident that the CSDE method is overall in better agreement with the J-integral. This observation along with the reduced computational time made the CSDE more appealing. Additionally the fact that the CSDE subroutine is written in APDL and not built in in the software allowed for the in depth understanding and control of the implementation of the method. These reasons led to the selection of the CSDE over the enhanced VCCT for all subsequent calculations.

7.2. Analytical approach

In this section, a semi-analytical approach based on bimaterial linear elastic fracture mechanics and the implementation of the CSDE method is proposed. The scope is to provide a practical and easy design method for composite patch repairs. Suo and Hutchinson (1990) analysed interface cracks between linear elastic isotropic planar substrates under fairly general loading conditions. The first step into achieving this, was expressing any general loading case, involving axial loads and bending moments acting on each one of the substrates on a cracked bimaterial interface, as a combination of loads acting on the fully bonded bimaterial and on a cracked bimaterial. By using the principle of superposition, they proved that only four out of the six load parameters are independent and that the Griffith energy of the bimaterial can be expressed as a function of these parameters. In Figure 7.7 the superposition principle for a cross-section of an infinite bilayer with an interface crack is illustrated. It is considered that the undamaged interface is perfectly bonded and therefore the displacements and tractions are continuous. Additionally, their approach is valid

considering that the crack is sufficient long, meaning at least three times the minimum thickness h and that there is no friction at the crack flanks when in contact. Taking these considerations into account, the overall equilibrium provides that the Equations 7.2 and 7.3 are valid. The moments and forces in the subsequent equations are per unit width.

$$P_1 - P_2 - P_3 = 0 \quad (7.2)$$

$$M_1 - M_2 - M_3 + P_1 \left(\frac{h}{2} + H - \delta \right) + P_2 \left(\delta - \frac{h}{2} \right) = 0 \quad (7.3)$$

The superposition shows that the number of load parameters that control the crack tip can be reduced to only two, namely P and M , given by Equations 7.4 and 7.5. The variables C_1, C_2, C_3 are geometric factors that are equal to (Equations 7.6 to 7.8)

$$P = P_1 - C_1 P_2 - C_2 \frac{M_3}{h} \quad (7.4)$$

$$M = M_1 - C_3 M_3 \quad (7.5)$$

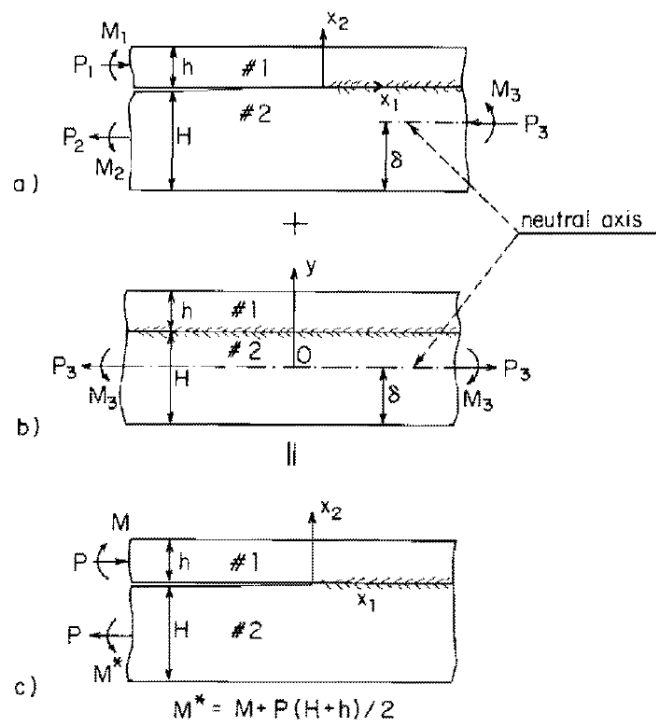


Figure 7.7: Superposition technique (Suo 1990).

$$C_1 = \frac{\Sigma}{A_0} \quad (7.6)$$

$$C_2 = \frac{\Sigma}{I_0} \left(\frac{1}{\eta} - \Delta + \frac{1}{2} \right) \quad (7.7)$$

$$C_3 = \frac{\Sigma}{12I_0} \quad (7.8)$$

In the unbonded part, the position of the neutral axis of the bimaterial is given by Equation 7.9:

$$\frac{\delta}{h} = \Delta = \frac{1 + 2\Sigma\eta + \Sigma\eta^2}{2\eta(1 + \Sigma\eta)} \quad (7.9)$$

where magnitudes A_0 , η and I_0 are given in Equations 7.10 and 7.11

$$\Sigma = \frac{1 + \alpha}{1 - \alpha}, \quad A_0 = \frac{1}{\eta} + \Sigma, \quad \eta = \frac{h}{H}, \quad (7.10)$$

$$I_0 = \frac{1}{3} \left\{ \Sigma \left[3 \left(\Delta - \frac{1}{\eta} \right)^2 - 3 \left(\Delta - \frac{1}{\eta} \right) + 1 \right] + 3 \frac{\Delta}{\eta} \left(\Delta - \frac{1}{\eta} \right) + \frac{1}{\eta^3} \right\} \quad (7.11)$$

α and β are the first and second Dundurs parameters respectively, which for isotropic materials are given by Equations 7.12 and 7.13:

$$\alpha = \frac{G_{(1)}(\kappa_2 + 1) - G_{(2)}(\kappa_1 + 1)}{G_{(1)}(\kappa_2 + 1) + G_{(2)}(\kappa_1 + 1)} \quad (7.12)$$

$$\beta = \frac{G_{(1)}(\kappa_2 - 1) - G_{(2)}(\kappa_1 - 1)}{G_{(1)}(\kappa_2 + 1) + G_{(2)}(\kappa_1 + 1)} \quad (7.13)$$

The parameters $G_{(1)}$ and $G_{(2)}$ are the shear moduli of materials 1 and 2. The variables κ_i depend on whether the problem is under a plane strain or a plane stress state and take the form $\kappa_i = 3 - 4\nu_i$ for plane strain and $\kappa_i = (3 - \nu_i)/(1 + \nu_i)$ for plane stress, with ν_i being the Poisson's ratio for each material. It should be pointed out that the generalised Dundurs parameter expressed in Equations 2.20 and 2.21 are simplified to those of Equations 7.12 and 7.13 for isotropic bimaterials. The energy release rate of the superimposed figure can be computed exactly as follows (Equation 7.14), by taking the difference between the energy stored far ahead and far behind the crack tip and is a function of P and M , calculated in Equations 7.4 and 7.5.

$$G = \frac{1}{2\bar{E}_{(1)}} \left(\frac{P^2}{Ah} + \frac{M^2}{Ih^3} + 2 \frac{PM}{h^2\sqrt{AI}} \sin\gamma \right) \quad (7.14)$$

where $\bar{E}_{(1)}$ is the efficient Young's modulus in the longitudinal direction of material 1, A , I are positive dimensionless numbers and the angle γ is restricted such that $|\gamma| \leq \pi/2$. These quantities are given by Equations 7.15 to 7.17. Suo and Hutchinson originally developed their formulas considering that $h < H$ for the thicknesses of the individual substrates, nevertheless with a simple transformation the opposite case can be accounted for.

$$A = \frac{1}{1 + \Sigma(4\eta + 6\eta^2 + 3\eta^3)}, \quad I = \frac{1}{12(1 + \Sigma\eta^3)} \quad (7.15)$$

$$\sin\gamma = 6\Sigma\eta^2(1 + \eta)\sqrt{AI} \quad (7.16)$$

$$\bar{E}_{(1)} = \frac{E_{(1)}}{1 - \nu_{zx}^{(1)}\nu_{xz}^{(1)}} \text{ for plane strain,} \quad \bar{E}_{(1)} = E_{(1)} \text{ for plane stress} \quad (7.17)$$

The complex stress intensity factor is also discussed in the same paper, and when contact is ignored, takes the form of Equation 2.22. The real and imaginary parts of the complex stress intensity factor can be expressed as functions of the geometry, loading and material properties of the bimaterial interface (Equation 7.18 to 7.19)

$$Re|Kh^{ie}| = \frac{\sqrt{1-a}}{\sqrt{2(1-\beta^2)}} \left[\frac{P}{\sqrt{Ah}} \cos\omega + \frac{M}{\sqrt{Ih^3}} \sin(\omega + \gamma) \right] \quad (7.18)$$

$$Im|Kh^{ie}| = \frac{\sqrt{1-a}}{\sqrt{2(1-\beta^2)}} \left[\frac{P}{\sqrt{Ah}} \sin\omega + \frac{M}{\sqrt{Ih^3}} \cos(\omega + \gamma) \right] \quad (7.19)$$

The mode mixity is defined as (Equation 7.20):

$$\psi = \arctan \left[\frac{Im(Kh^{ie})}{Re(Kh^{ie})} \right] = \arctan \left[\frac{\lambda \sin\omega - \cos(\omega + \gamma)}{\lambda \cos\omega + \sin(\omega + \gamma)} \right] \quad (7.20)$$

In the aforementioned equations, λ measures the loading combination as (Equation 7.21)

$$\lambda = \sqrt{\frac{I Ph}{A M}} \quad (7.21)$$

The real angular quantity ω depends on the Dundurs parameters α, β and the thickness ratio η . In their work, Suo and Hutchinson used integral equation methods and calculated the ω values for different values of Dundurs parameters and for thickness ratio η ranging from 0 to 1, allowing in that way the calculation of the strain energy release rate and the mode mixity of an interface crack in a linear elastic bimaterial under general loading conditions. By following the same approach, it can be proven that in the case of orthotropic bimaterials the energy release rate formula remains unchanged (*Kardomateas et al 2012*).

To investigate whether the analytical solutions provided by Suo and Hutchinson for the ω parameter for isotropic bimaterial configurations can be employed for the calculation of the mode mixity in the case of orthotropic materials, a numerical approach was adopted. This approach is based on the implementation of the CSDE method for the extraction of the ω parameter, by calculating the mode mixity angle ψ for different material and geometric configurations and, subsequently, by rearranging Equation 7.20 to take the form presented in Equation 7.22:

$$\omega = \arctan \left[\frac{\cos \gamma + (\lambda + \sin \gamma) \tan \psi}{\lambda + \sin \gamma - \cos \gamma \tan \psi} \right] \quad (7.22)$$

This approach has been used in *Kardomateas et al (2012)* for the case of isotropic trimaterials and bimaterials and yielded promising results. In the same work, it was argued that the values of ω are nearly constant under different loading combinations and consequently should be treated independent of loading. This signifies that the parameter can be assumed as independent of the loading applied to the bimaterial system and as such needs to be calculated only for one loading for the given geometry. To verify that this is also valid for the orthotropic bimaterial case, different cases were investigated in the present study. Simultaneously, the energy release rate was compared to the energy release rate values obtained with the CSDE method for different mode mixities. The finite element model was identical to the one described earlier in this chapter and the positive load notation is in accordance with the one illustrated in Figure 7.1.

The main objectives of this work were to verify the load independency that was referenced earlier and foremost to investigate whether the values of the parameter ω in the case of orthotropic materials can be correlated to the ones listed by *Suo and Hutchinson (1990)*. To this end the CSDE method was implemented and the reduced ($\psi_{Reduced\ CSDE}$) and full formulation for mode mixity $\psi_{full\ CSDE}$ were calculated. For both formulations, the respective ω values were extracted, denoted as $\omega_{Reduced\ CSDE}$ and $\omega_{full\ CSDE}$. These values were in the following compared to the ones listed from Suo and Hutchinson using the generalised expression of the Dundurs parameters ($\omega_{generalized}$). For all cases the full formulation with the CSDE method was calculated by choosing the thickness of the thinner substrate as the characteristic length.

A total of eight cases were examined. In cases 1 to 5, the loading combination is varied to prove that the ω value is independent of the loading configuration, whereas the thickness ratio and material configuration is

kept identical in these cases. The remaining cases were selected to allow for a more extensive comparison between the ω values listed by Suo and Hutchinson with the ones extracted using the CSDE method. To this end the thickness ratio is varied. Additionally, the energy release rate calculated with the CSDE was compared to the analytical calculation (Equation 7.14) in all cases. The results and relative information for each studied case are presented in Table 7.3

Table 7.3: Extraction of ω values for different cases

Case	1	2	3	4	5	6	7	8
Material	VI-CE	VI-CE	VI-CE	VI-CE	VI-CE	VI-CE	VI-CE	VI-CE
h (Composite)	5	5	5	5	2.5	1	3	9
H (Steel)	10	10	10	10	5	10	10	10
η	0.5	0.5	0.5	0.5	0.5	0.1	0.3	0.9
M_1 [Nmm/mm]	1000	200	50	0	100	0	0	0
M_2 [Nmm/mm]	1000	800	1200	0	100	500	500	500
P_1 [N/mm]	0	0	0	100	-50	0	0	0
P_2 [N/mm]	0	0	0	150	100	0	0	0
$G_{analytical}$ [Nmm/mm ²]	4.51E-01	3.02E-02	2.51E-02	5.89E-03	4.08E-02	1.00E-03	2.73E-03	5.31E-03
G_{CSDE} [Nmm/mm ²]	4.45E-01	2.97E-02	2.50E-02	5.78E-03	4.08E-02	1.00E-03	2.72E-03	5.28E-03
% G difference	1.43%	1.82%	0.48%	1.81%	-0.06%	-0.26%	0.47%	0.65%
$\Psi_{ReducedCSDE}$	-47.98	-23.49	11.53	40.94	-29.56	26.96	24.17	21.29
$\Psi_{fullCSDE}$	-27.00	-2.01	33.68	62.41	-8.15	48.83	46.13	43.25
$\omega_{ReducedCSDE}$	31.33	31.35	30.99	30.25	29.89	32.80	30.46	29.89
$\omega_{fullCSDE}$	52.31	52.99	53.14	51.72	51.30	51.67	52.42	51.85
$\alpha_{generalised}$	-0.756							
$\beta_{generalised}$	-0.169							
$\omega_{generalised}$	52.62					53.96	53.29	52.43

Interpreting the results of the presented cases, it is demonstrated that the analytical and numerical results of the energy release rate are in excellent agreement between each other, with the difference between the two being lower than 2% in all cases. Comparing cases 1 to 5 it is verified that the extracted values of the ω parameter are virtually independent of the applied loading with the maximum difference noted being equal to 1.84 degrees for the $\omega_{fullCSDE}$. This difference is smaller than the one calculated by *Kardomateas et al*, where a maximum difference of 4 degrees was noted.

Comparing the ω_{Full} values extracted from the full formulation of the mode mixity with those that Suo and Hutchinson listed ($\omega_{generalized}$), it can be concluded that they are practically the same, with the larger difference being equal to 2.3 degrees for case 6. This signifies that the original table listed from Suo and Hutchinson can be employed, provided that the generalized expression of the Dundurs parameters is used as input.

The populated tables from Suo and Hutchinson do not cover the whole range of values for the Dundurs parameters as, for isotropic materials, the physically admissible values of α and β are restricted to a

parallelogram enclosed by $\alpha = \pm 1$ and $\alpha - 4\beta = 1$ in the α, β plane. Contrarily, in orthotropic bimetals the values of the generalized Dundurs parameters are no longer constrained by the same boundaries. Therefore material combinations exist that do not befall within the original boundaries. The angular parameter values in these cases can be extracted employing the approach described above.

It should be noted that, by extracting the angular parameter from the calculated reduced formulation, a new set of values is generated. These values will provide input for the analytical calculation of the reduced formulation. In each case, it is important that the analytically calculated mode mixity is consistent with the one associated to the experimental procedures for the definition of the critical energy release rate under different loading combinations.

Based on the findings of the aforementioned investigation, the ω values were calculated for the HLU-CE, VI-CE and PP-CE composite systems described in Appendix A, using the procedure described above for both the reduced and full formulation. In the case of the full formulation the angular values for the PP-CE and VI-CE systems were already available from the table provided by Suo and Hutchinson. For each material case the thickness ratio was varied between 0.1 and 1. This procedure was implemented for both the composite substrate being thinner than the steel and for the opposite case. The latter can be achieved easily by reassigning the material properties in the substrates in the already given formulas in such a way that the steel substrate represents material number 1 and the composite lamina material number 2. In this way the original assumption that $h/H \leq 1$ is preserved. This inversion leads to Dundurs parameters with opposite signs between the two cases. The generalized Dundurs parameters that correspond to the selected bimaterial systems are listed in Table 7.4. The calculated values of the phase angle parameter for both the reduced and full formulation are concentrated in Table 7.5 and Table 7.6 respectively for thickness ratios 0.1, 0.5 and 1.0. Table 7.6 additionally includes the ones originally calculated by Suo and Hutchinson in the case of the full formulation. The values that correspond to the selected bimaterial systems are coloured for the reader's convenience. For the reduced formulation, all values were extracted from the finite element models. Intermediate values of the thickness ratio can be calculated using linear interpolation.

Table 7.4: Generalised Dundurs parameters for the studied bimaterial systems.

Bimaterial system	Generalised Dundur's Parameter	
	α	β
HLU-CE / Steel	-0.8450	-0.1860
VI-CE / Steel	-0.7565	-0.1690
PP-CE / Steel	-0.6905	-0.2198

Table 7.5: ω values table for the reduced formulation.

$\eta =$		0.1				
$\beta \backslash \alpha$	-0.845	-0.7565	-0.6905	0.6905	0.7565	0.845
-0.2198	-	-	26.8	-	-	-
-0.186	28.1	-	-	-	-	-
-0.169	-	31.8	-	-	-	-
0.169	-	-	-	-	76.2	-
0.186	-	-	-	-	-	83.3
0.2198	-	-	-	75.2	-	-
$\eta =$		0.5				
$\beta \backslash \alpha$	-0.845	-0.7565	-0.6905	0.6905	0.7565	0.845
-0.2198	-	-	28.7	-	-	-
-0.186	27.9	-	-	-	-	-
-0.169	-	30.6	-	-	-	-
0.169	-	-	-	-	72.1	-
0.186	-	-	-	-	-	77.9
0.2198	-	-	-	72.6	-	-
$\eta =$		1				
$\beta \backslash \alpha$	-0.845	-0.7565	-0.6905	0.6905	0.7565	0.845
-0.2198	-	-	28.7	-	-	-
-0.186	26.4	-	-	-	-	-
-0.169	-	29.7	-	-	-	-
0.169	-	-	-	-	68.8	-
0.186	-	-	-	-	-	73.8
0.2198	-	-	-	69.5	-	-

Table 7.6: ω values table for the full formulation.

Full Formulation															
$\eta =$	0.1														
$\beta \backslash \alpha$	-0.845	-0.8	-0.7565	-0.6905	-0.6	-0.4	-0.2	0	0.2	0.4	0.6	0.6905	0.7565	0.8	0.845
-0.4		64.5			65.2										
-0.3		59.9			60.5	61.5	64.0								
-0.2198				56.6											
-0.2		55.2			56.0	56.9	58.1	61.5	63.6						
-0.186	52.4														
-0.169			53.9												
-0.1		50.6			51.5	52.5	55.4	57.1	59.1	61.3	64.4				
0		46.0			49.0	50.9	52.7	54.6	56.5	58.9	62.0			64.0	
0.1						43.4	44.7	42.3	50.4	53.2	56.5			60.9	
0.169													57.7		
0.186															58.8
0.2								44.0	46.4	49.1	52.4			57.7	
0.2198												54.0			
0.3										44.7	48.4			53.9	
0.4														49.9	
$\eta =$	0.5														
$\beta \backslash \alpha$	-0.845	-0.8	-0.7565	-0.6905	-0.6	-0.4	-0.2	0	0.2	0.4	0.6	0.6905	0.7565	0.8	0.845
-0.4		64.1			64.5										
-0.3		59.3			59.8	60.6	61.6								
-0.2198				55.4											
-0.2		53.3			55.2	56.1	57.1	58.4	59.9						
-0.186	52.4														
-0.169			52.6												
-0.1		50.0			50.8	51.5	52.8	54.1	55.6	57.5	59.7				
0		45.3			46.1	47.2	48.4	49.8	51.4	54.6	56.8			59.2	
0.1						43.0	43.9	45.6	47.3	49.4	51.8			55.2	
0.169													51.8		
0.186															53.5
0.2								41.2	43.0	45.1	47.8			51.4	
0.2198												48.6			
0.3										40.7	43.6			47.4	
0.4														43.2	
$\eta =$	1														
$\beta \backslash \alpha$	-0.845	-0.8	-0.7565	-0.6905	-0.6	-0.4	-0.2	0	0.2	0.4	0.6	0.6905	0.7565	0.8	0.845
-0.4		63.7			64.6										
-0.3		58.5			59.5	60.8	62.1								
-0.2198				55.1											
-0.2		53.7			54.5	55.8	57.2	58.7	60.3						
-0.186	50.8														
-0.169			52.4												
-0.1		48.9			49.7	51.0	52.3	53.8	55.4	57.2	59.6				
0		44.2			44.9	46.2	47.6	49.1	50.8	52.6	55.0			57.2	
0.1						41.6	42.9	44.4	46.0	47.8	49.8			52.4	
0.169													48.5		
0.186															49.4
0.2								39.5	41.2	43.0	45.1			47.6	
0.2198												45.3			
0.3										38.0	40.1			42.8	
0.4														37.6	

7.3 General considerations regarding composite patch repairing

Loading Definition

The analytical formulation described in the previous section enables the investigation of numerous loading combinations consisting of bending moments and axial loads acting on the bimaterial interface. This analytical approach will be extensively employed in this section to investigate how the thickness ratio and of

the material properties of the composite material system affect the energy release rate in the case where a crack has formed at the bimaterial interface. Additionally, special considerations regarding the load application and the repair configuration are addressed through the selection of representative load cases without loss of generality.

Composite patches provide an alternative loading path, alleviating the defected substrate. In the case of planar repairs and if there are no external loading applied to the composite substrate, the loads acting on the laminate are the ones transmitted from the metal substrate through the interface. In other words, if we consider that a crack has formed at the edges of the bimaterial interface, the unbonded part of the repair will be in most cases free of loads. This signifies that only combinations of forces and bending moments acting on the steel substrate should be considered in that case.

However, as it has been experimentally observed, in the case where the composite patches are used for the rehabilitation of defected structures, debonding will initiate in the bondline area either at the edges of the patch or in the vicinity of the crack in the metallic substrate. In the latter case, the force and moment equilibrium Equations 7.1 to 7.4 can be employed to calculate the energy release rate and compare it to the one obtained by considering a crack laying at the edges of the patch. Bearing the previous observations in mind, the following loading cases can be identified.

- 1) Axial forces acting on the steel substrate
- 2) Bending moment acting on the steel substrate
- 3) Combination of axial forces and bending moments acting on the steel substrate

Examining the selected cases in conjunction with Equation 7.13, it appears that if only axial loads or only bending moments are acting on the steel substrate, according to the analytical formula the sign of these loads does not affect the critical energy release rate nor the mode mixity. However, this is not true. This error stems from the fact that the analytical model does not account for the contact between the crack flanks in the case when load lead to the crack closing. This deficiency in the analytical formula can be easily tackled by correctly recalculating the applied moments and forces to take into account the contact boundary condition. The method is explained for the case where only pure bending moments are applied without loss of generality. Friction between the crack flanks has not been taken into account.

Let us consider that an interface crack with sufficient length lies in the interface at the edge of the bimaterial and a constant moment M_2 is acting clockwise on the steel substrate beyond the repair. Equilibrium enforces that the sum of all loads in a given section, before and after the crack, is zero (Equations 7.2 and 7.3).

Therefore the moment M_3 after the crack in the bonded section (Figure 7.8) should be equal and opposite of moment M_2 . In the area of the bimaterial section that has been disbonded, contact enforces that a portion of the imposed moment M_2 is transferred to the substrate number 1. By denoting this moment as M_0 , the equilibrium equation can be rewritten as:

$$(M_2 - M_0) + M_0 = M_3 \quad (7.23)$$

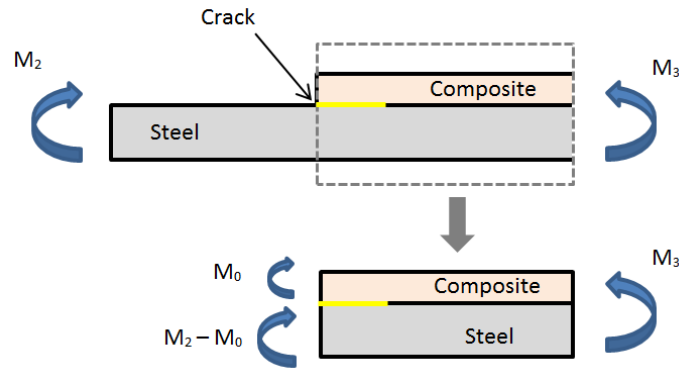


Figure 7.8: Moment equilibrium due to contact at the crack tip.

Additionally, the contact condition in the cracked part means that both substrates follow the same curvature κ . This boundary condition is expressed mathematically in Equation 7.24:

$$\kappa_{(1)} = \kappa_{(2)} \Rightarrow \frac{(M_2 - M_0)}{\bar{E}_{(2)} I_{(2)}} = \frac{M_0}{\bar{E}_{(1)} I_{(1)}} \quad (7.24)$$

where $I_{(1)}$, $I_{(2)}$ the moment of inertia of substrates 1 and 2, respectively. Rearranging this equation, the magnitude of the moment M_0 can be calculated as:

$$M_0 = \frac{\bar{E}_{(1)} I_{(1)}}{\bar{E}_{(2)} I_{(2)}} (M_2 - M_0) \quad (7.25)$$

$$M_0 \left(1 + \frac{\bar{E}_{(1)}}{\bar{E}_{(2)}} \left(\frac{h_1}{h_2} \right)^3 \right) = M_2 \frac{\bar{E}_{(1)}}{\bar{E}_{(2)}} \left(\frac{h_1}{h_2} \right)^3 \quad (7.26)$$

$$M_0 = M_2 \frac{\frac{\bar{E}_{(1)}}{\bar{E}_{(2)}} \left(\frac{h_1}{h_2} \right)^3}{\left(1 + \frac{\bar{E}_{(1)}}{\bar{E}_{(2)}} \left(\frac{h_1}{h_2} \right)^3 \right)} \quad (7.27)$$

Therefore, attention should be paid on how the acting loads on the base substrate beyond the bimaterial interface are transmitted to the substrates in the cracked region. One case has been selected to serve as an example. In this case two moments M_2 of equal magnitude but opposing signs acting on the steel substrate (substrate number 2) beyond the interface were considered. The material combination and the geometry

were identical for both cases. The two cases are presented in Table 7.7. Comparing the obtained results, it is evident that the moment which causes opening of the crack produces higher energy release rate and lower mode mixity which are more unfavourable for the repair.

Table 7.7: Results for bending moments with different signs.

Case	Opening	Closing
Material	HLU-CE	HLU-CE
h (Composite)	3	3
H (Steel)	5	5
η	0.6	0.6
M_1 [Nmm/mm]	0	36.9
M_2 [Nmm/mm]	-1000	-963.1
M_3 [Nmm/mm]	1000	1000
$G_{\text{analytical}}$ [Nmm/mm ²]	9.40E-02	8.61E-02
$\Psi_{\text{ReducedCSDE}}$	17.9	34.80
Ψ_{fullCSDE}	43.4	59.28

As stated earlier, the analytical formulas assume that a crack of sufficient length has already formed in the bimaterial interface. These cracks form where free edges exist, i.e. in the edges of the patch or in the vicinity of existing cracks/notches/holes in the metal substrate. Hence, when free edges are present where cracks may form, the energy release rate has to be assessed. In effect, in the area of the patch above the crack the geometrical configuration resembles the one of a single strap joint with equilibrium enforcing that the forces and moments acting on the steel substrate are the same at the composite patch repair above the crack. Representing a composite patch repair as a single strap joint in the case of cracked substrates is quite conservative. In real applications the width of the laminate will sufficiently exceed the width of the damaged area and, depending on the configuration and loading, will allow for the redistribution of forces in the areas beyond the damage. Nevertheless, the single strap joint is significantly simpler, and hence can be analytically analysed with little required effort, which makes this simplified approach appealing.

The problem can be decoupled in two separate cases as shown in Figure 7.9, which makes the implementation of Equation 7.13 for each case more straightforward. In Figure 7.9, the sign of the applied moment leads to contact in the crack flanks at the edge of the patches, without loss of generality.

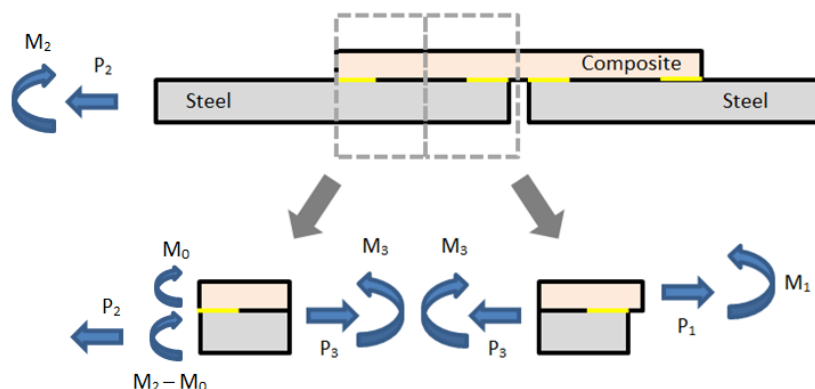


Figure 7.9: Axial force and moment equilibrium in a single strap joint.

Force equilibrium dictates that $|P_1| = |P_2| = |P_3|$. Similarly, moment equilibrium dictates that $|M_1| = |M_2| \pm |P_2| \times (h + H)/2$ and $|M_3| = |M_2| \pm |P_2| \times (H/2 - \delta)$, where δ is the position of the neutral axis as depicted in Figure 7.7. The energy release rate and mode mixity on both locations can be calculated analytically. To this end, two different configurations have been investigated, namely carbon epoxy laminated with the hand-lay-up method to steel and pre-preg carbon epoxy to steel. In the first case only axial loading is applied, while in the second one both axial loads and bending moments have been applied. The results are listed in Table 7.8. For the first case, the energy release rate is three orders of magnitude higher at the free edge at the vicinity of the crack at the steel plate compared to the patch edges, denoting that debonding would start from the former location. The mode mixity is higher at the vicinity of the steel crack. In the second case the energy release rates between the two areas are of the same order of magnitude with the one at the steel crack area being three times larger compared to the energy release rate at the edge of the patch. However the mode mixity is higher at the vicinity of the steel crack which corresponds to higher fracture toughness compared to the edge of the patch. In general, the location of debonding is case dependent and as such has to be investigated when designing repairs for the rehabilitation of structural members where free edges are present.

Table 7.8: Edge versus crack debonding in cracked cases.

Case	1		2	
	Patch Edge	Above steel Crack	Patch Edge	Above steel Crack
Material	HLU-CE	HLU-CE	PP-CE	PP-CE
h (Composite)	3	3	3	3
H (Steel)	5	5	5	5
η	0.6	0.6	0.6	0.6
P_1 [N/mm]	0	-300	0	-300
P_2 [N/mm]	300	0	300	0
P_3 [N/mm]	-300	-300	-300	-300
M_1 [Nmm/mm]	0	1200.0	0	200.0
M_2 [Nmm/mm]	0	0.0	1000	0.0
M_3 [Nmm/mm]	115.3	115.34	-884.66	-884.66
$G_{analytical}$ [Nmm/mm ²]	2.27E-03	8.44E+00	1.25E-01	4.73E-01
$\Psi_{ReducedCSDE}$	34.78	71.20	20.15	77.37
$\Psi_{fullCSDE}$	59.26	46.72	44.63	78.02

Geometrical considerations

The following recommendations can be made based on the findings of this study and the general knowledge obtained from the Shipbuilding Technology Laboratory.

The two-sided reinforcement is clearly superior compared to the one-sided one and should be preferred when there are no prohibitive restrictions or access difficulties to both sides of the metal plate. The reason for this is that a one-sided patch leads to an asymmetric cross-section of the reinforced metal plate, resulting in the appearance of bending towards the steel adherent, even when purely coplanar axial loads are imposed. This induced bending leads to the development of additional bending stresses in the patched region. Attention should be paid to the fact that, due to the consequent bending, the installation of one-sided patch reinforcement may lead to plastic yield of the metallic plate in areas near the edges of the patch, away from the area of the defect. This is more likely to happen when the patch has a high stiffness ratio. Patch reinforcements with a high stiffness ratio relieve more the defected area from the applied loading; however at the same time high stiffness ratio can potentially lead to the attraction of loads at the edges of the patch. This could initiate debonding of the repair or/and cause undesirable overloading of the metallic substrate at these areas. Consequently, it may be preferable to choose a patch with a lower stiffness ratio, which, although carries less loading and therefore relieves less the metal substrate at the defected area, it does not overload the surrounding structure, resulting in longer life for the patch reinforcement.

A rectangular shaped patch seems advantageous over other circular or elliptical shaped patches with similar dimensions. Further improvement can be achieved by cutting the corners of the rectangular shape so as to create an octagonal shaped patch. This improves the stress state at the edges of the patch.

The minimum recommended length of the patch (normal to the crack) must be equal to 1.5 to 2.0 times the length of the crack. The aforementioned length refers to the active length of the patch, i.e. the length along which the patch has its full thickness. Similarly, the minimum recommended width of the patch (parallel to the crack) is equal to 1.75 to 2 times the length of the crack or 1.5 to 2 times the width of the corroded area.

To avoid high peeling stresses at the edges of patch, it is recommended to gradually decrease its thickness towards the edges, making the edges tapered. This is easily achieved by gradually varying the length of the layers of the patch. The recommended tapering angle at the edges is 3° to 5° . Subsequent layers should overlap the first ones, i.e. the first layers laminated onto the metal plate should be shorter than those that follow.

Previous experience has shown that it is a good practice to seal the entire tapering area of the patch with an additional glass tape, in order to better protect the bondline at the patch edges from external effects (environment, wear, etc.).

7.4. Parametric study

Description of the Study

Having extracted the ω values, a parametric study was conducted to investigate how the energy release rate and the mode mixity are affected by the composite substrate and the thickness ratio for representative types of loading. To use the analytical formulations, once again a pre-existing crack was considered at the

edges of the bimaterial interface. The loading was applied in the metallic substrate outside the bimaterial region following the remarks made earlier.

The composite material systems selected were HLU-CE, VI-CE and PP-CE accounting for low, average and high stiffness composite systems. The metallic substrate was typical marine grade steel with Young's modulus equal to 203 GPa and 235 MPa yield strength. The thickness of the metallic substrate was kept constant and equal to 5mm, while the one of the composite substrate was varied, resulting in different thickness ratios. The ply lay-up orientation of the composite patch is out of the scope of the present study.

Two different loadings were considered, namely, axial loading and pure bending. The direction of the loads was taken so as to cause opening of the crack flanks, as it has proven to be more detrimental for the integrity of the bimaterial system. The magnitude of each loading case was equal to the one required to cause yielding of the steel substrate. The rationale behind this decision is that a properly designed structural element should operate well below its yield load during service. Therefore, if only the type of loading is known, a conservative approach would be to consider that the acting load is equal to the yield load of the steel substrate and investigate if that could lead to debonding. This approach has been adopted in the presented parametric study. For the case of the axial loading the induced secondary bending effect for each case was also considered in this study, to represent the actual loads that would be imposed to an unsymmetrical repair.

The reduced formulation was used in this investigation for two reasons. The first one is that the fracture toughness values used from the literature (*Lee et al 2010*) correspond to the reduced formulation. The second one is that, as mentioned in Chapter 2, the reduced formulation is more tangible and easier to physically interpret compared to the full formulation. A total of 60 cases were investigated, the details of which are presented in Table 7.9.

Table 7.9: Cases of the parametric study.

Materials	HLU		VI		PP		Thickness Ratio
	Bending Moment	Axial Load	Bending Moment	Axial Load	Bending Moment	Axial Load	
Loading Cases	980 [Nmm/mm]	1175 [N/mm]	980 [Nmm/mm]	1175 [N/mm]	980 [Nmm/mm]	1175 [N/mm]	Composite / Steel
Composite Thickness [mm]	1.25						0.25
	2.50						0.50
	3.75						0.75
	5.00						1.00
	7.50						1.50
	10.00						2.00
	12.50						2.50
	15.00						3.00
	20.00						4.00
Steel Thickness [mm]	30.00						6.00
	5.00						
Total number of cases	60						

In addition to the calculated energy release rates and mode mixity, the corresponding fracture toughness was calculated and plotted. The fracture toughness dependency on the mode mixity was calculated following the phenomenological model that Suo and Hutchinson proposed (*Hutchinson et al, 1992*) (Equation 7.28).

$$\Gamma(\psi) = G_{Ic}\{1 + \tan^2[(1 - \lambda)\psi]\} \quad (7.28)$$

where G_{Ic} is the fracture toughness in pure mode I and ψ the mode mixity. The parameter λ adjusts the influence of the mode II contribution in the criterion. The limit $\lambda = 1$ is the "ideally brittle" interface with initiation occurring when $G = G_{Ic}$ for all mode combinations. This limit coincides with the classical surface energy criterion. When $\lambda = 1$, crack advancement depends only on the mode I component. On the contrary, when $\lambda \ll 1$, significant mode dependence exists. The critical energy release variation used for the implementation of this criterion is achieved by setting $\lambda = 0.5$. Additionally the fracture toughness as a function of the mode mixity by linear extrapolation as proposed by Lee et al (*2010*) is plotted. The fracture energy ratio G / G_{Ic} as a function of the reduced formulation of mode mixity is given in Figure 7.10. The linear model leads to higher values of the critical fracture energy when compared to the phenomenological model. The deviation between the two ranges up to 20% which is significant. In praxis, the relationship between the mode mixity and the critical strain energy release rate should be defined by performing appropriate experiments which represent a satisfactory range of the phase angle. At this study, it was decided to proceed with the linear model as due to the lack of experimental data, the values listed by Lee et al have been used throughout the thesis. Additionally in the preceding cohesive zone modelling with ANSYS the linear model was employed, yielding satisfactory results.

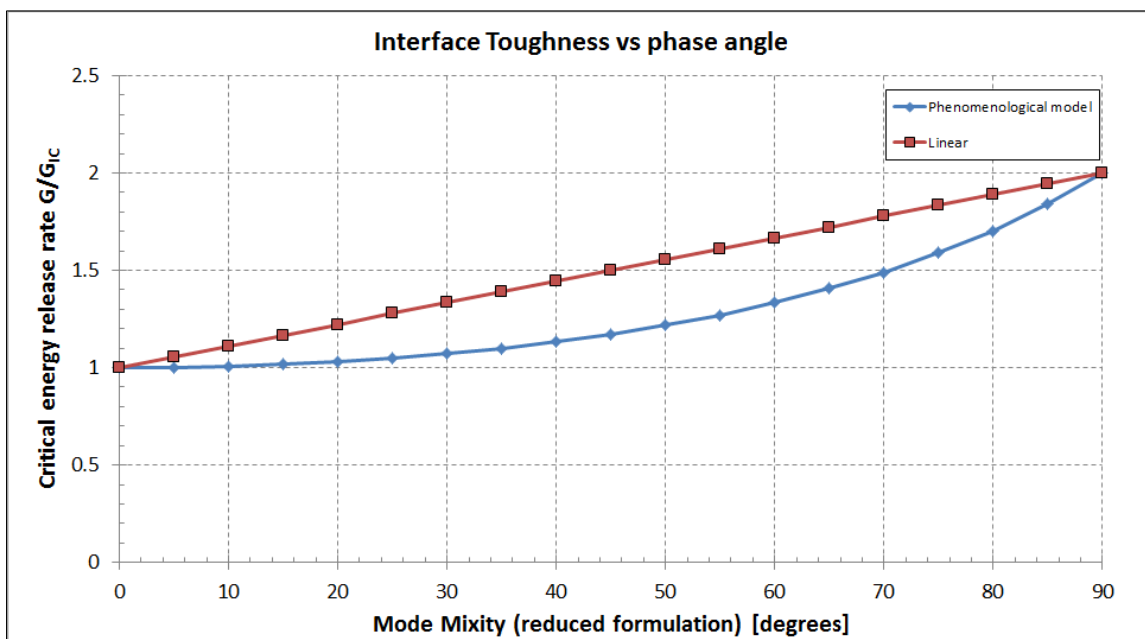


Figure 7.10: Critical energy release rate models as a function of mode mixity.

Results of the Parametric Study

The results of the parametric study are presented in Figure 7.11 to Figure 7.18. To better interpret the results, the calculated energy release rates, mode mixity and fracture toughness have been plotted as a function of the thickness ratio as well as of the stiffness ratio. By the term stiffness ratio, the bending stiffness ratio is implied for the case where a pure moment is acting and the axial stiffness ratio for the case of the axial load. The formulas corresponding to each case are presented in Equations 7.29 and 7.30 respectively.

$$\text{Bending } S.R. = \frac{E_c}{E_s} \left(\frac{t_c}{t_s} \right)^3 \quad (7.29)$$

$$\text{Axial } S.R. = \frac{E_c}{E_s} \frac{t_c}{t_s} \quad (7.30)$$

where E_c is the young modulus of the composite substrate in the longitudinal direction, E_s is the Young's modulus of the steel and t_c , t_s are the thicknesses of the composite and steel substrates respectively.

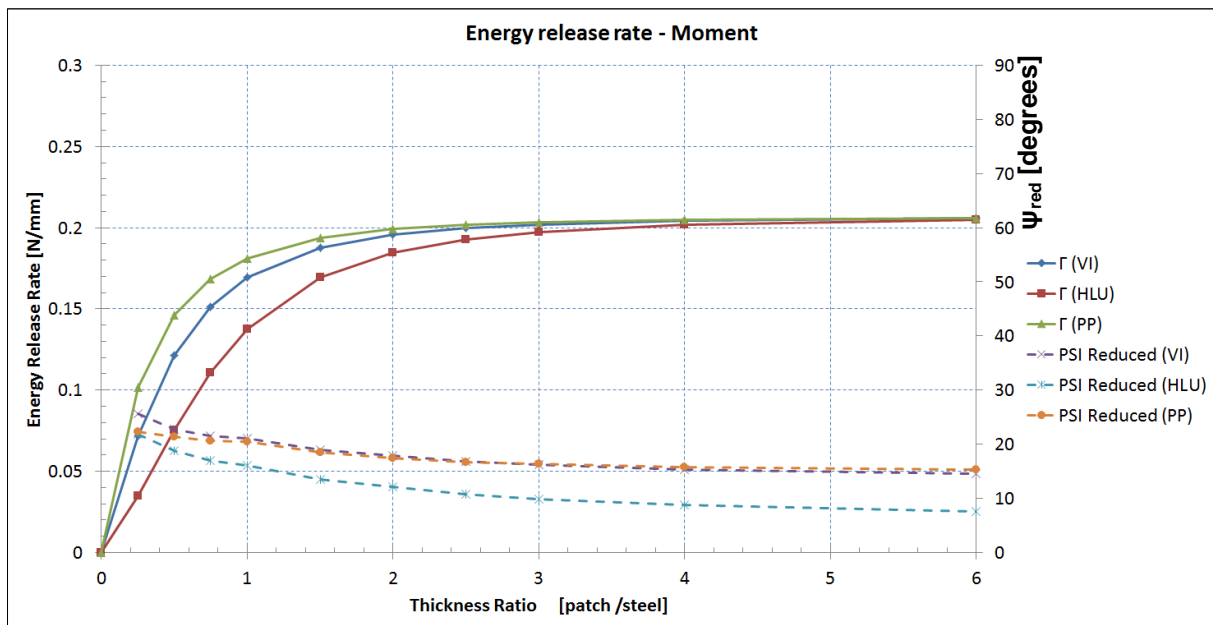


Figure 7.11: Strain energy release rate and mode mixity versus thickness ratio (bending load).

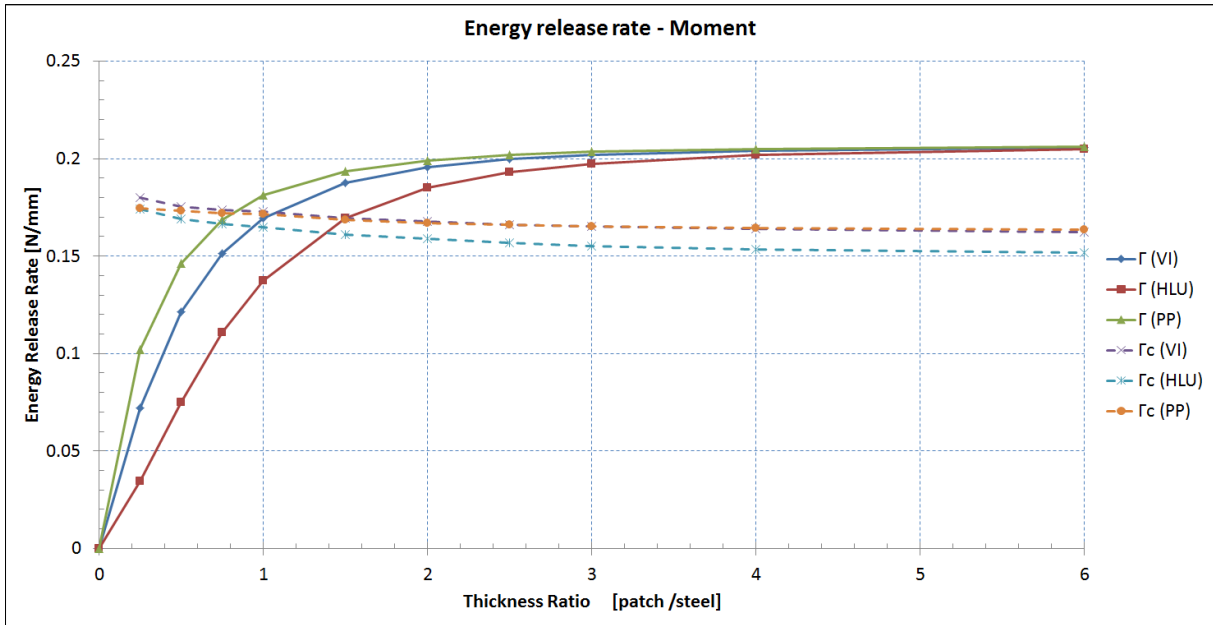


Figure 7.12: Strain energy release rate and fracture toughness versus thickness ratio (bending load).

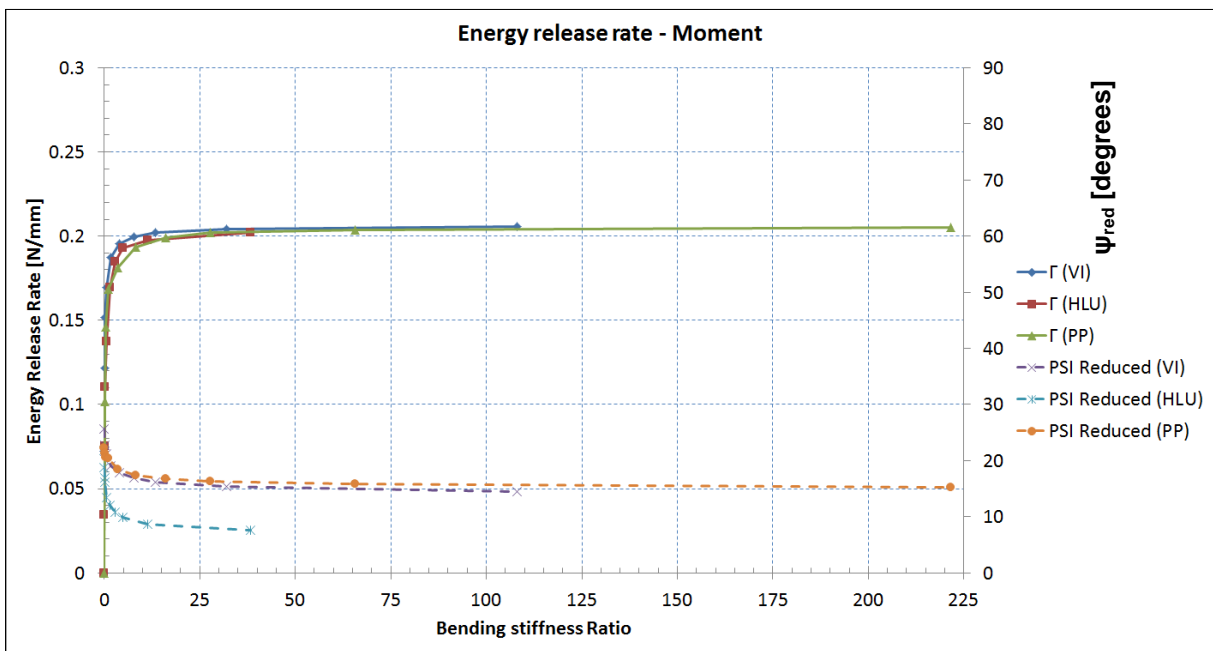


Figure 7.13: Strain energy release rate and mode mixity versus bending stiffness ratio (bending load).

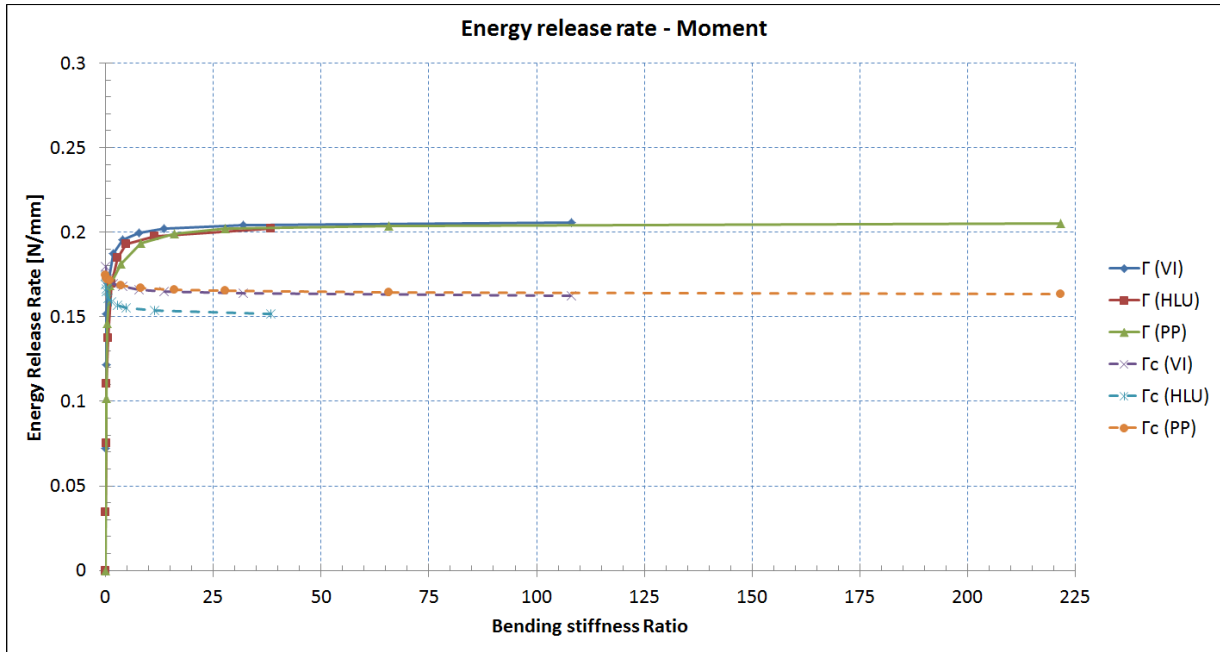


Figure 7.14: Strain energy release rate and fracture toughness versus bending stiffness ratio (bending load).

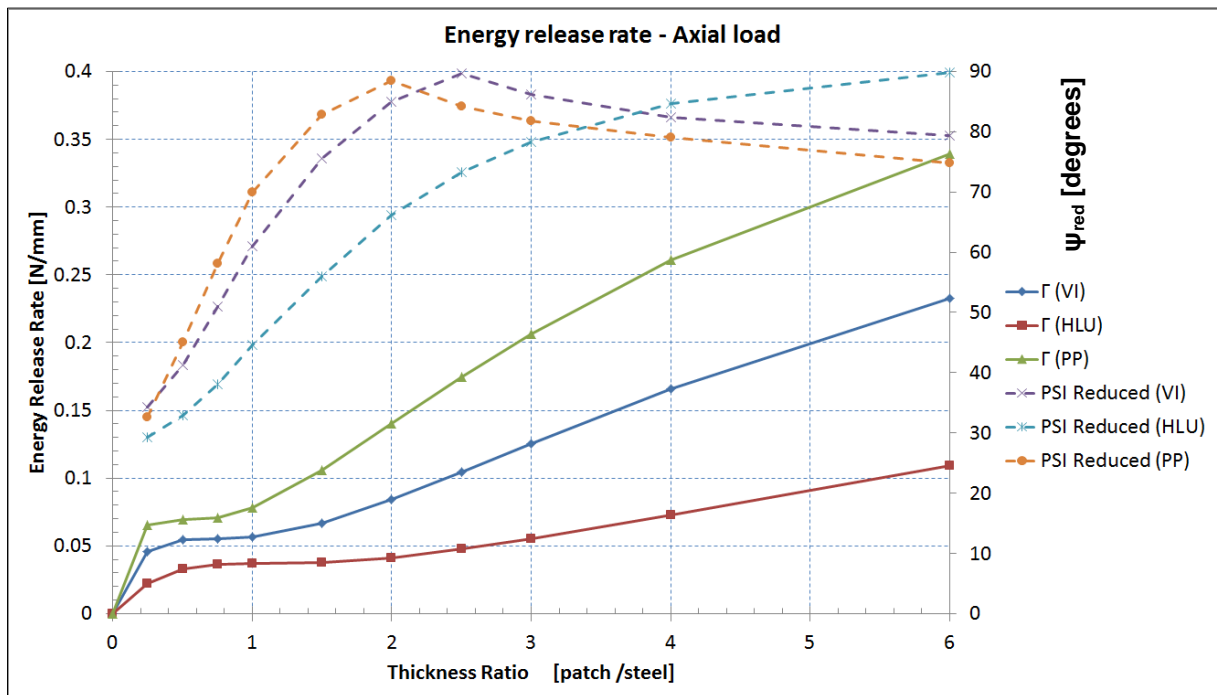


Figure 7.15: Strain energy release rate and mode mixity versus thickness ratio (axial load).

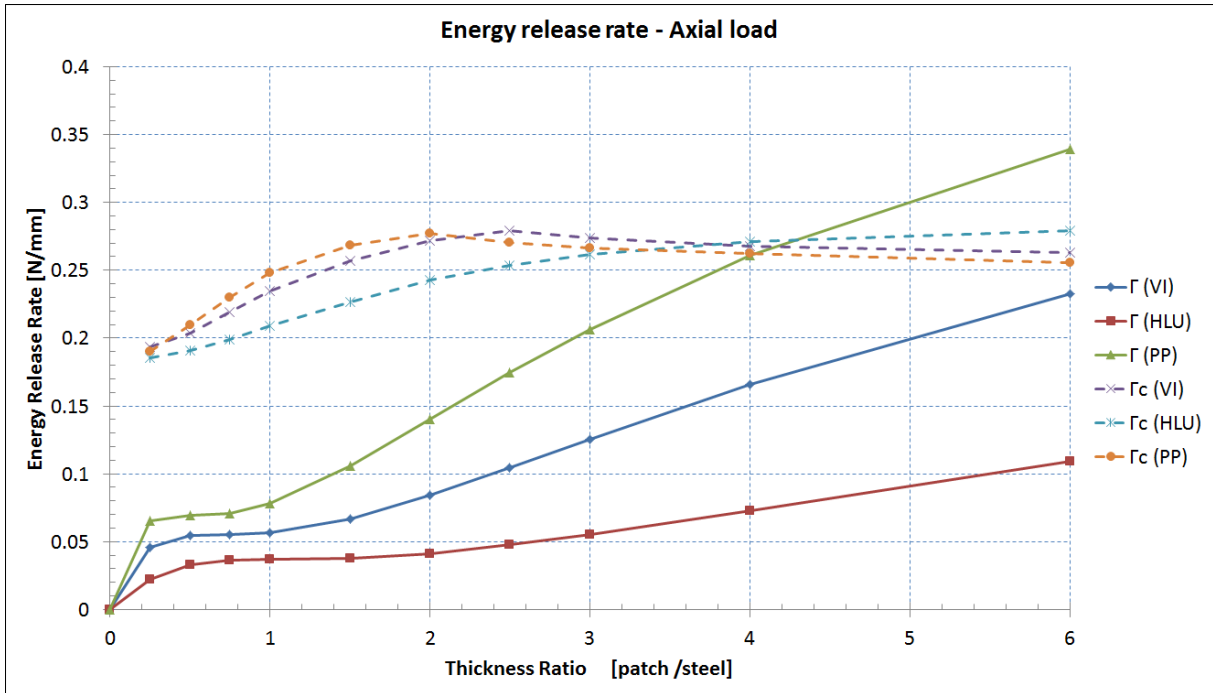


Figure 7.16: Strain energy release rate and fracture toughness versus thickness ratio (axial load).

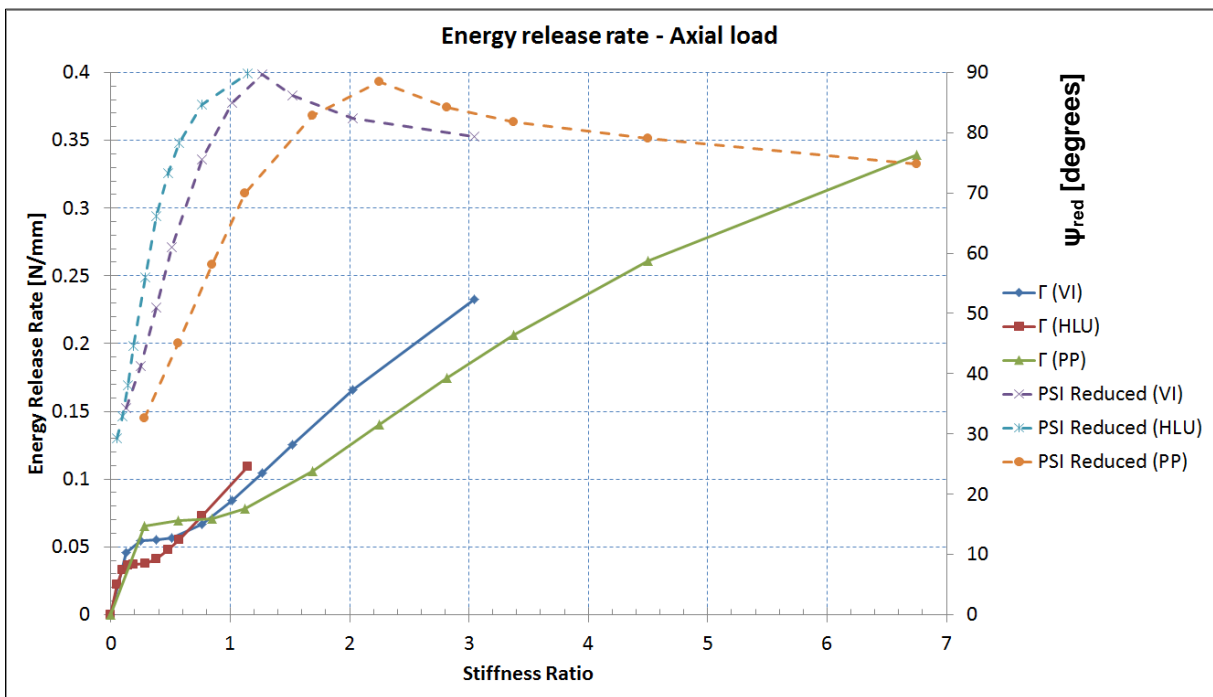


Figure 7.17: Strain energy release rate and mode mixity versus axial stiffness ratio (axial load).

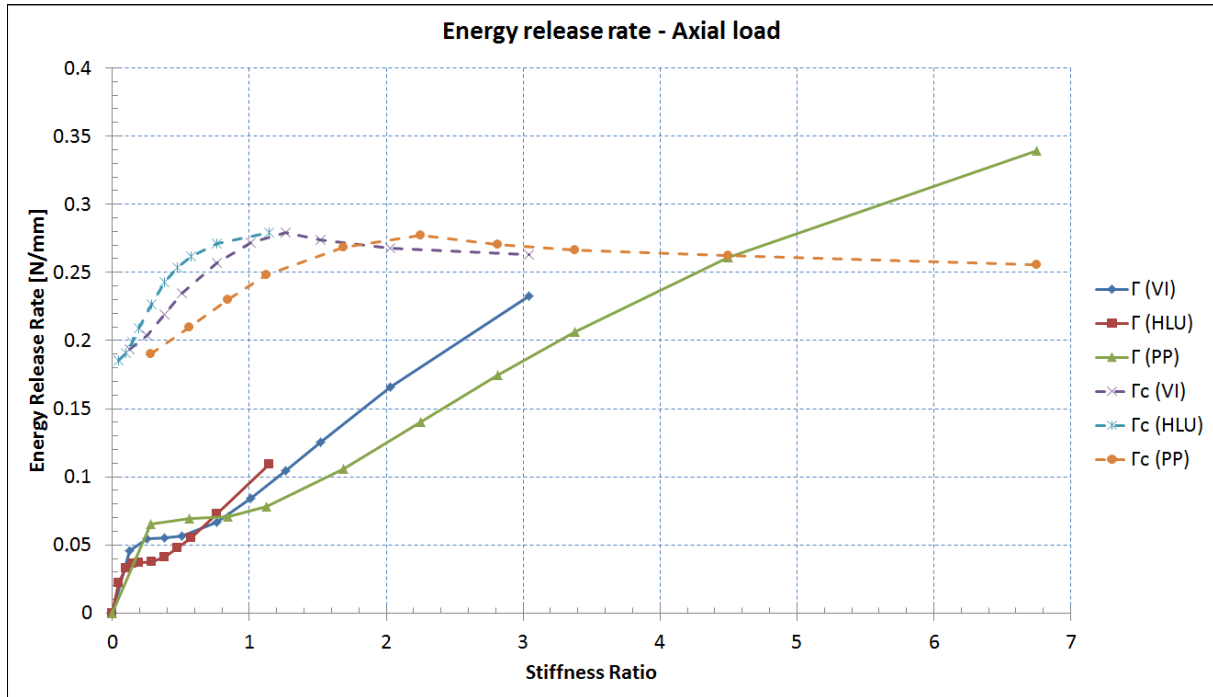


Figure 7.18: Strain energy release rate and fracture toughness versus axial stiffness ratio (axial load).

For the cases where bending moment was applied, results indicate that in all cases the energy release rate increases with increasing thickness ratio, and composite material systems with larger Young's modulus in the main direction result in greater energy release rate values for the same thickness ratio. The values of the energy release rate increase until a plateau value is reached at different thickness ratios for each case. Specifically, the larger the Young's modulus the lower the thickness ratio the plateau value is reached. After that point, further increasing the thickness ratio does not affect the strain energy release rate (Figure 7.11).

Regarding the mode mixity a similar trend is observed with the mode mixity being mode I dominant in all cases. The HLU exhibited the lower values, while the VI and PP material systems yielded practically the same results. However, the difference between the HLU case and the remaining two materials does not lead in practice to significantly different fracture toughness (Figure 7.12). The mode mixity becomes more mode I dominant with increasing thickness ratio until once again a plateau is reached.

Plotting the results as a function of the bending stiffness ratio allows for a more clear interpretation. Examining Figure 7.13 and Figure 7.14 it appears that the curves of the energy release rate for the three different bimaterial systems are identical, signifying that the governing parameter is the value of the bending stiffness ratio, as after it reaches a value of twenty, further increasing the bending stiffness ratio does not affect the energy release rate neither the mode mixity.

Interpreting the axial loads cases, it is evident that the results differ significantly compared to the bending loading cases.

Three different regions can be identified at the curves of the energy release versus the thickness ratio for each bimaterial case (Figure 7.15). The first region consists of the gradual increase of the energy release rate with increasing thickness ratio. After a certain thickness ratio value, the behaviour changes and the

energy release rate is almost constant with increasing composite thickness. This region differs for each material case, ranging up to 0.8 for the PP and 1.5 for the HLU. From that point forward, there is an almost linear increase of the energy release rate with increasing composite thickness. For all thickness ratios the stiffer the Young's modulus, the larger the value of the energy release rate.

Interpreting the mode mixity as a function of the thickness ratio, no apparent correlation exists between the selected material cases as the PP and VI cases present a similar behaviour with the mode mixity increasing until reaching a pure mode II loading i.e. $\psi = 90^\circ$. From that point forward, the mode mixity decreases in a logarithmic fashion, contrarily, the mode mixity of the HLU case keeps increasing with increasing thickness ratio and reaches pure mode II for a thickness ratio equal to 6. The mode mixity trend is reflected less pronouncedly to the fracture toughness (Figure 7.16).

Plotting the energy release rate as a function of the axial stiffness ratio, no obvious correlation exists between the two, unlike the pure bending load where the results coincided when plotted against the stiffness ratio. Looking at the mode mixity versus thickness ratio, the variation of the mode mixity is more consistent.

Its values increase until a stiffness ratio of about 1.2 is reached for the HLU and VI bimaterial cases where the mode mixity is pure mode II. The mode mixity for the VI bimaterial subsequently decreases logarithmically. To investigate whether further increasing the stiffness ratio for the HLU case leads to a similar decrease in the mode mixity values, some additional cases were considered with composite substrate thicknesses equal to 50 and 60mm. Plotting the results including these cases (Figure 7.19) shows the declining trend, although less pronounced compared to the other two bimaterial configurations. Similar behaviour is noted for the PP bimaterial, albeit the axial stiffness ratio needed to achieve the pure mode II loading condition is higher than the other material systems (axial S.R.=2.3).

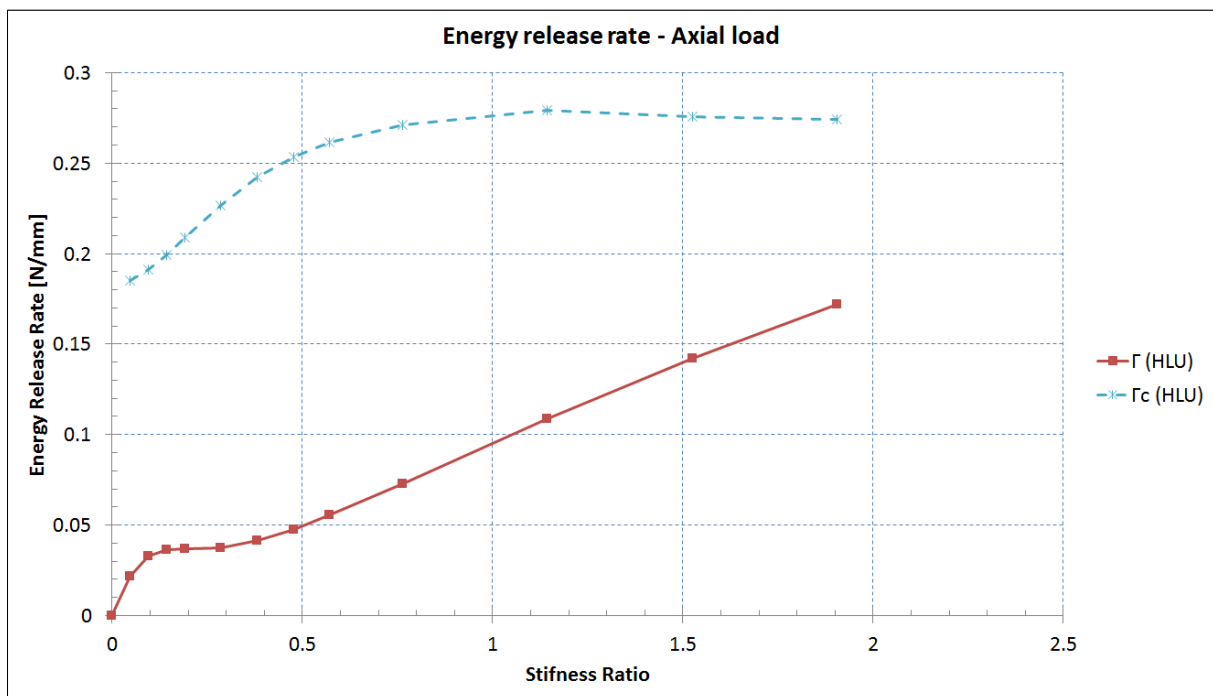


Figure 7.19: Strain energy release rate and mode mixity versus axial stiffness ratio (axial load) for the HLU

At this point it must be emphasized that it is very unlikely that the thickness of a composite patch will exceed a value of 10 mm, as there are several practical limitations. In addition, in this study we were only interested to investigate how the material properties and thickness ratios affect the energy release rate and the mode mixity in the bimaterial. The structural integrity has not been taken into account except for the definition of the applied loading. This should be thoroughly considered when designing an actual repair, as the secondary bending effect or/and excessive local stiffening may prove detrimental to the repair and the structure itself if not properly accounted for.

The following interesting conclusions can be drawn from the parametric study. The first one is that the bending loading led to higher energy release rates and more mode I dominant mode mixities compared to the axial one, constituting this type of loading more dangerous for the integrity of the repair. Additionally it has been demonstrated that increasing the bending stiffness ratio to values beyond twenty, induces no change in the energy release rate and the fracture toughness of the case. Regarding the axial load, overall mode II dominant mode mixity was observed. More importantly, it has been demonstrated that even by disregarding the structural capacity of the substrates, it is not possible to reach debonding of the repair from the free edges. The only case where the energy release rate exceeded the fracture toughness was for unrealistically thick pre-preg carbon composite substrates.

7.5 Design assessment procedure

Based on the general considerations listed earlier and the findings of the parametric study, a suitable procedure focusing on the analysis and design of composite patch repairs is suggested, once the criticality of the damage has been assessed.

In general, the decision whether the damage is critical or not needs to be determined based on the existing standards or codes. In the case of non-critical damage, the existing regulatory frame will not require any rectifications, however repairing the damage in the non-critical stage should ensure that the damage growth is arrested and the critical situation which requires a costly traditional repair will not be reached (*Echtermeyer 2014*). This decision process is illustrated in DNV's recommended practice and is presented in Figure 7.20.

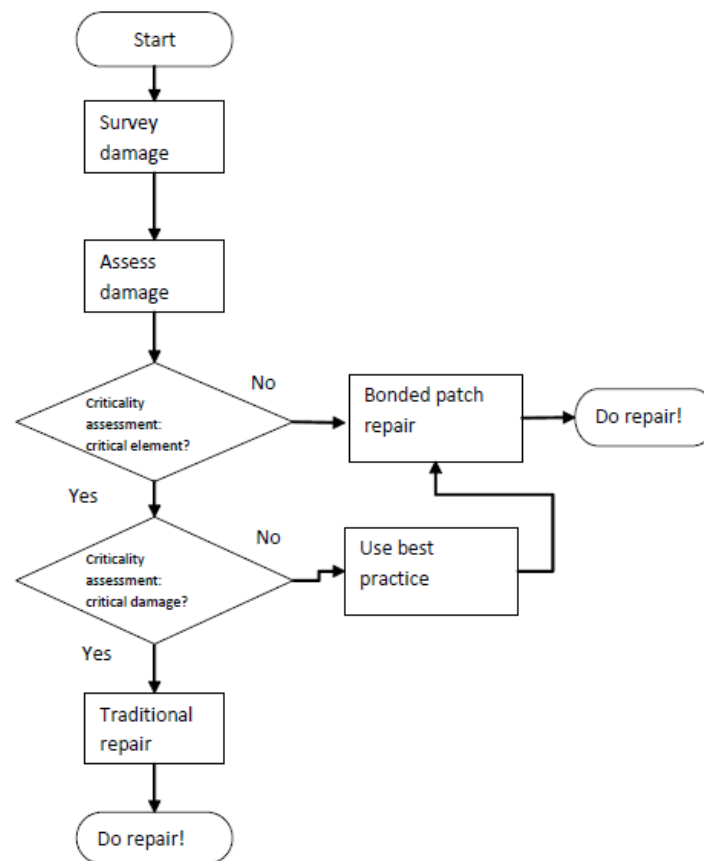


Figure 7.20: Outline of repair assessment and decision making process (DNV-RP-C301).

The approach suggested below is to be used in conjunction with the repair decision process of Figure 7.20. Its scope is the assessment of a composite patch repair using the simple analytical formulas described above, enabling the designer to compare alternative configurations and choose the most advantageous one. A purely analytical approach or a combination of analytical formulas and simple finite element modelling can be employed for the implementation of the method depending on the criticality and complexity of the case. In this way, a fast and efficient analytical way to choose the best repair strategy is provided. The process can be summarized in the following steps:

1st step:

Identification of the operational loading of the intact structural member. The operational loading can be defined either directly, in the case where the acting loads on the structure are known, or, alternatively, by the maximum allowable operational load, as prescribed from the regulation requirements.

2nd step:

Application of the operational loads defined from step 1 to the defected geometry to identify the structural response of the defected element.

3rd Step

Definition of the design constraints and selection of candidate patch configurations

4th step

Analysis of the repaired structure to investigate whether the selected configuration can reach the prescribed operational performance criteria.

5th step

Expression of the acting loading at appropriate locations near the free edges of the bimaterial as a combination of axial loads and bending moments by integrating the stresses through the plate thickness (Equations 7.31 and 7.32).

$$P = \int \sigma dy \quad (7.31)$$

$$M = \int \sigma y dy \quad (7.32)$$

If the maximum stresses are not prescribed, the yield load can be taken as the acting load for the calculations, representing a conservative approach.

6th Step

Calculation of the energy release rate and comparison to the experimentally measured fracture toughness for the corresponding mode mixity. Suitable safety factors will have to be defined depending on the criticality of the structural element and the type of repair, i.e. temporary or permanent

This procedure is illustrated in the form of a flowchart in Figure 7.21.

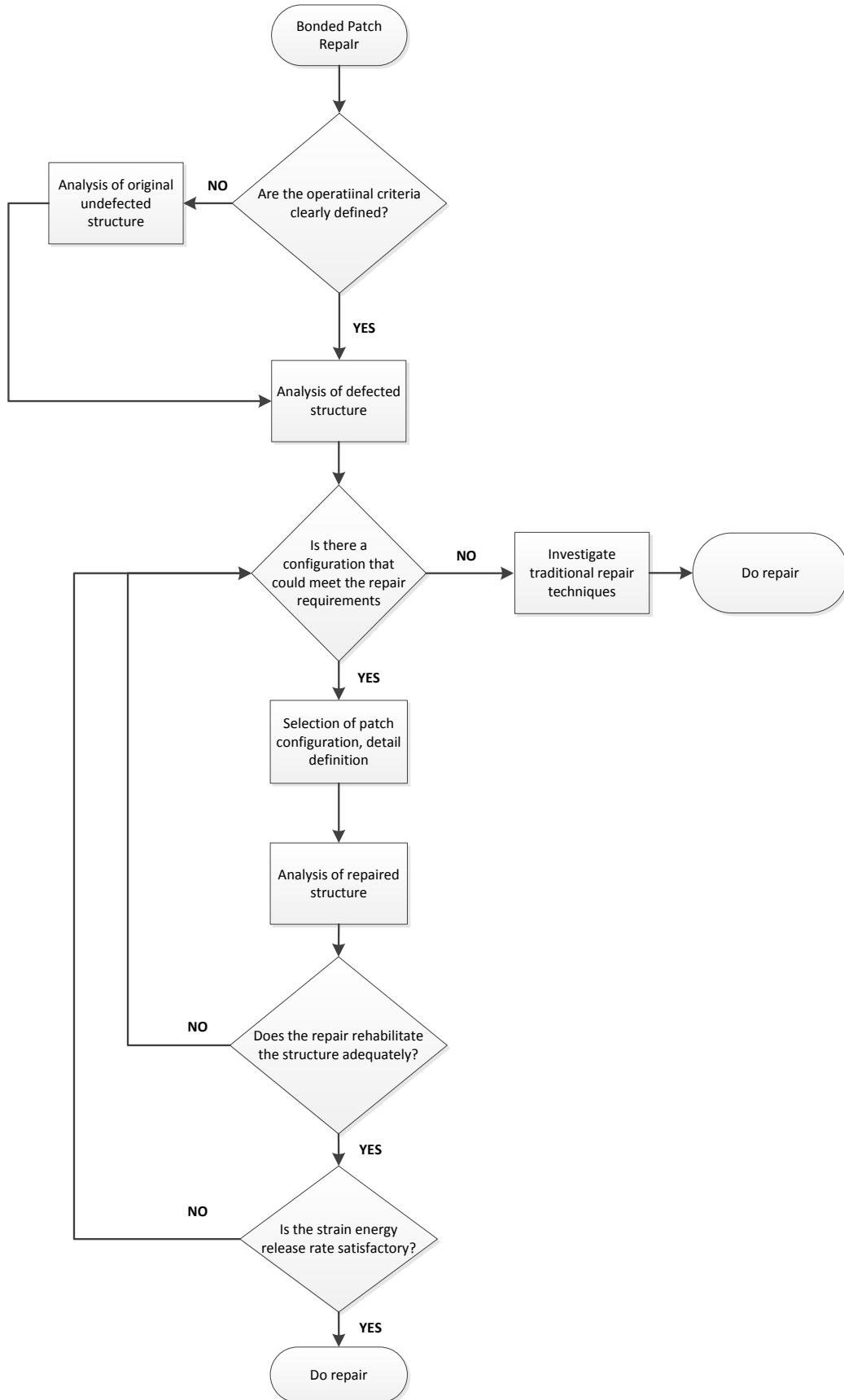


Figure 7.21: Patch assessment and decision making procedure.

7.6 Implementation of assessment methodology

To demonstrate the suggested procedure, one case study is considered dealing with the repair of a corroded deck in a Floating Production Storage and Offloading (FPSO) vessel. The plating's original thickness is 20 mm, whereas localized corrosion has been detected at the plating of the deck. The corrosion extended to an area of 500 mm x 300 mm and the average plate thickness diminution was 2 mm. The thickness reduction is 10% of the original plate's thickness which is within the allowable diminution margins for longitudinal strength members according to DNV's guideline (*DNVGL-CG-0172*). Composite patch repairing is considered as a preemptive measure to repair the damage at this non critical stage in order to avoid renewal of the plating due to further thickness diminution. The deck panel's dimensions are 4800x4260mm and the deck is reinforced by T-profile longitudinal stiffeners with 13x300mm web and 90x17mm flange. The frame spacing is equal to 855mm. The steel used is typical marine grade steel with Young's modulus equal to 203 GPa. The maximum in-plane tensile load acting on the structure is equal to 100 MPa. Assessment of two different composite patch designs will be performed following the suggested methodology.

1st step

The operational load is known and equal to 100 MPa.

2nd step

The damaged case was analysed using the finite element modelling software ABAQUS. A panel with dimensions of 4800x4260mm was considered. All degrees of freedom are constrained at the fore end of the panel, while the other end is constrained only to the vertical direction (Y-axis). These boundary conditions simulate the existence of the stiff transverse web at the panel's ends. The structure was modelled using reduced integration 8 node quadratic brick elements Solid Elements (C3D20R in ABAQUS) with an average element size of 25 mm. Four elements were assigned through the thickness of the steel plating. The loading was 100 MPa acting in the longitudinal direction (Z axis). The thickness reduction at the corroded area was taken as uniform and equal to 2 mm. The longitudinal stress field for the corroded case is depicted in Figure 7.22.

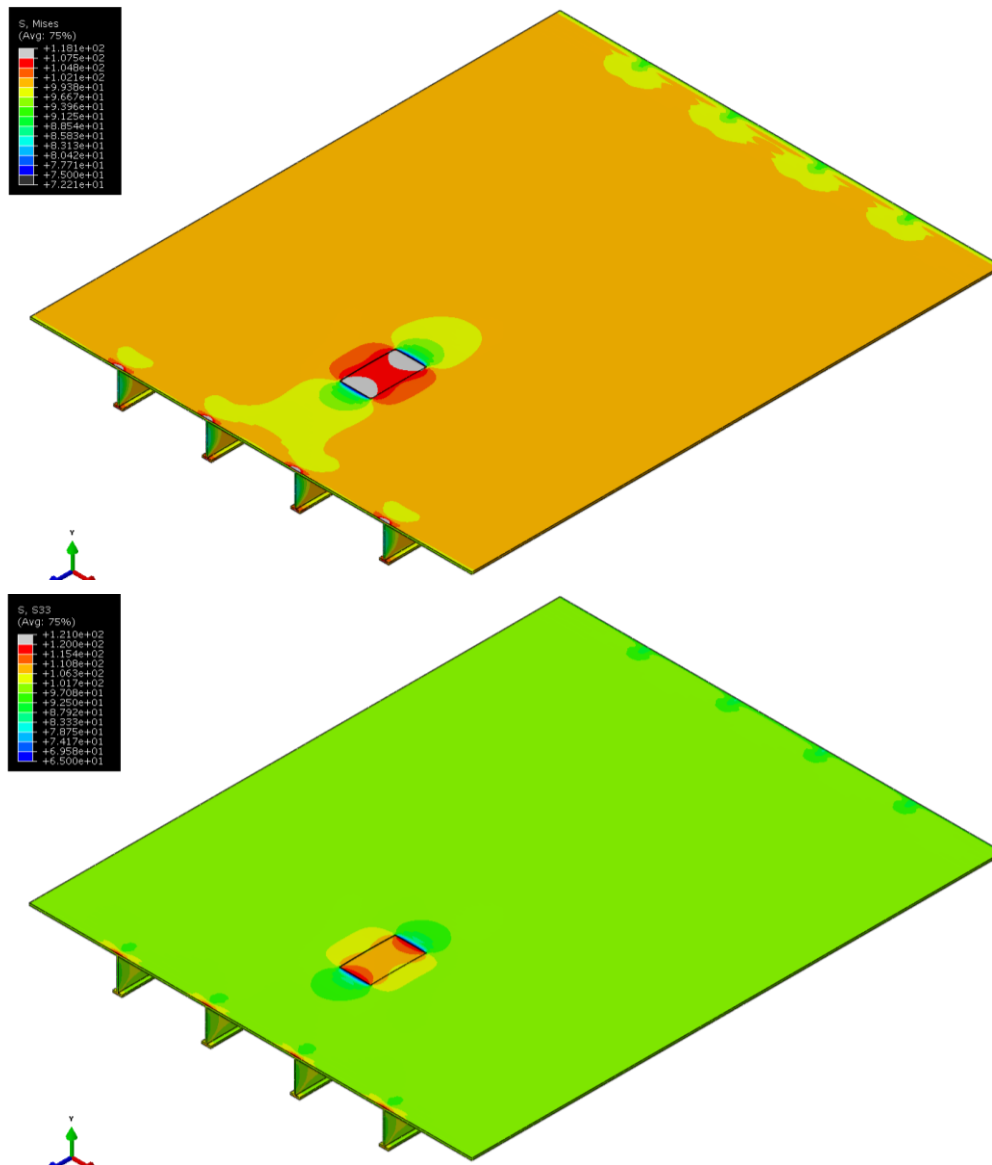


Figure 7.22: von Mises stress distribution (top) and longitudinal stresses (σ_z) in defected structure (bottom).

As it was expected, the thickness reduction led to increased stress levels at the corroded area with the von Mises stress ranging up to 115 MPa.

3rd step and 4th step

Two different materials were considered for the repair, namely HLU-CE and VI-CE. The composite patch was 850mm long, 550 mm wide including the tapered edges, whereas the thickness was considered to be equal to 4mm. In the finite element model the tapered edges were ignored and the dimensions of the patch were 750 x 450 x 4mm. The analytical formula used for the calculation of the strain energy release rate is valid only if a crack of sufficient length is already present in the bondline. To comply with this condition we can assume that cracks have formed between the patch and the steel substrate throughout the tapered area. Taking into consideration that no loads are carried by the debonded part of the composite patch, the tapered

edges can be ignored, simplifying the modelling procedure. This hypothesis is more conservative and allows the implementation of the analytical approach described earlier, in which a crack preexists between the two substrates. Given that there are no available data and methods regarding the formation of cracks, it is safe to assume that a crack preexists and check if the strain energy release rate reaches its critical value for each studied case. The imposed loading and boundary conditions were identical both for the intact and for the damaged models. Figure 7.23 and Figure 7.24 illustrate the stress distribution in the steel structure for the HLU-CE and VI-CE cases, respectively. The von Mises stress distribution is plotted ranging from 75 MPa up to 107.55 MPa for reasons of clarity. The longitudinal stress in the Z direction is additionally presented. The stress range plotted for the latter is from 65 MPa to 120 MPa. The patch should be able to alleviate the stresses from the damaged area and rehabilitate the structure.

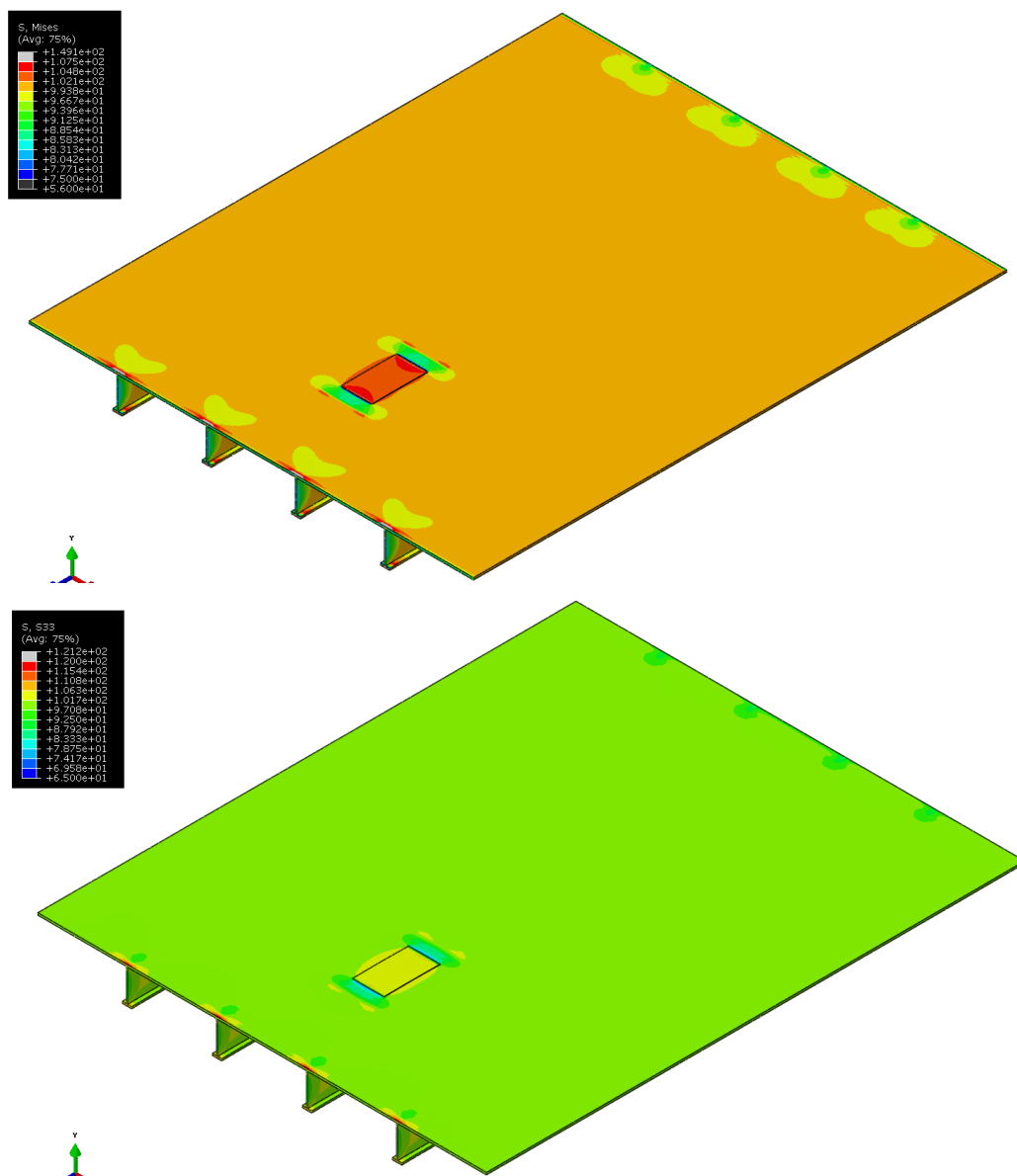


Figure 7.23: von Mises stress distribution (top) and longitudinal stresses (σ_z) on the steel structure after the application of a HLU-CE patch.

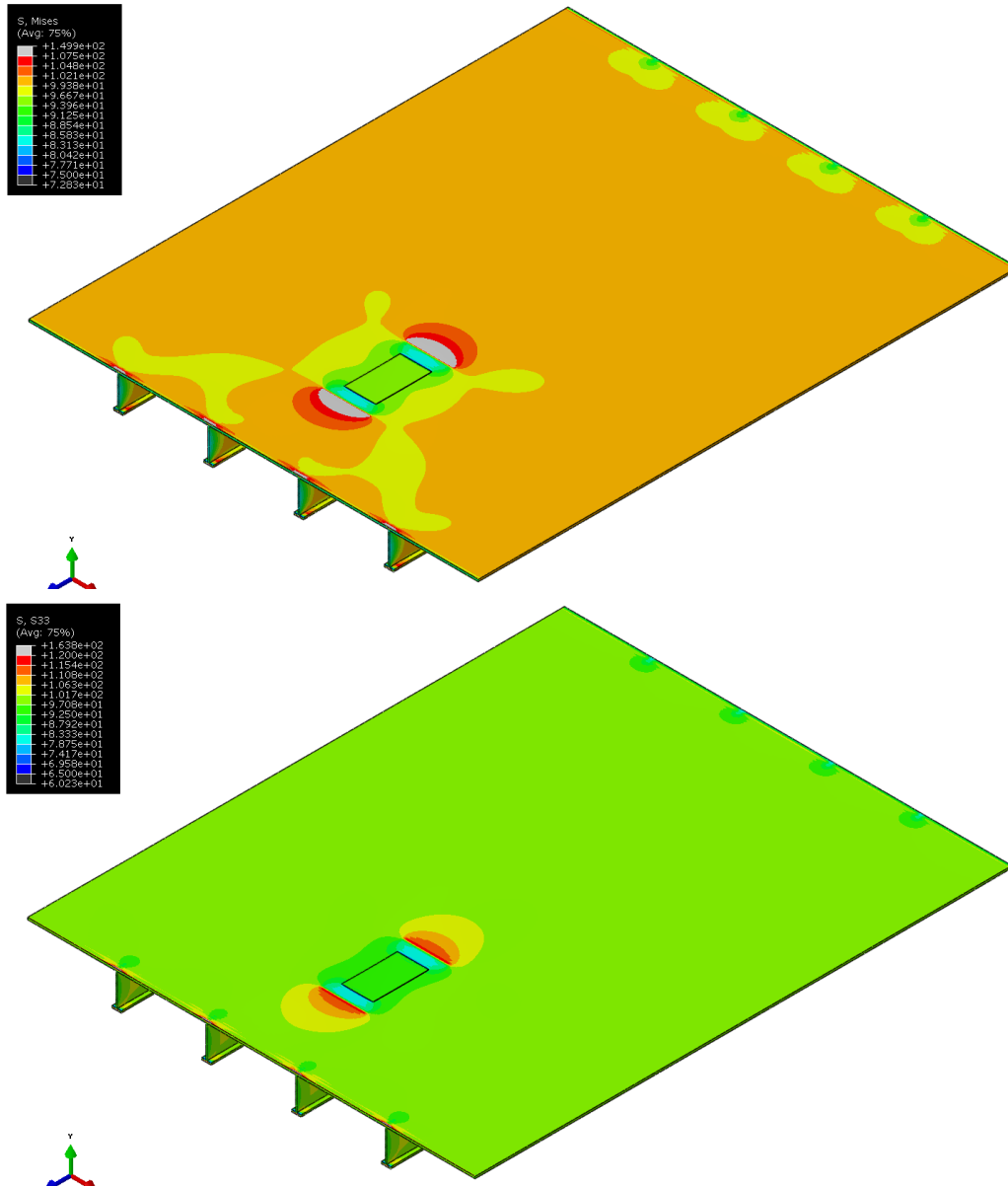


Figure 7.24: von Mises stress distribution (top) and longitudinal stresses (σ_z) on the steel structure after the application of a VI-CE patch.

Results indicate that both material configurations are able to reduce the stresses acting at the damaged area and its vicinity. In particular the HLU-CE patch leads to a reduction of the stresses from 115 MPa to 105 MPa at the corroded area. The VI-CE leads to a more pronounced and uniform reduction of the stresses at the damaged area with the values being around 95 MPa. However, the latter configuration leads to the increase of stresses at the patch edges with the stress being about 113 MPa. Based on the results of the analyses, the HLU-CE option is deemed more suitable for this particular application, as it leads to the alleviation of stresses at the damaged region and at the same time does not introduce stresses in different areas of the structure.

5th step

Having selected the patch configuration for the repair, the longitudinal stresses acting on the steel substrate along the composite patch edge are plotted for the outer surfaces of the steel plate (Figure 7.25). The stresses vary along the edge, however, for reasons of simplicity, they can be assumed as uniform considering the worst case scenario. Based on the results of the parametric study, it can be argued that generally the bending component is more detrimental for the repair. Bearing this in mind, the magnitude of the uniform stresses were selected in the location where the resulting bending moment would be higher, i.e. where the difference in the longitudinal stresses between the top and bottom surface of the steel substrate was higher. The magnitudes of the uniform stresses are 105.07 MPa at the top of the plate and 99.07 MPa at the bottom. The stress distribution is plotted in Figure 7.25.

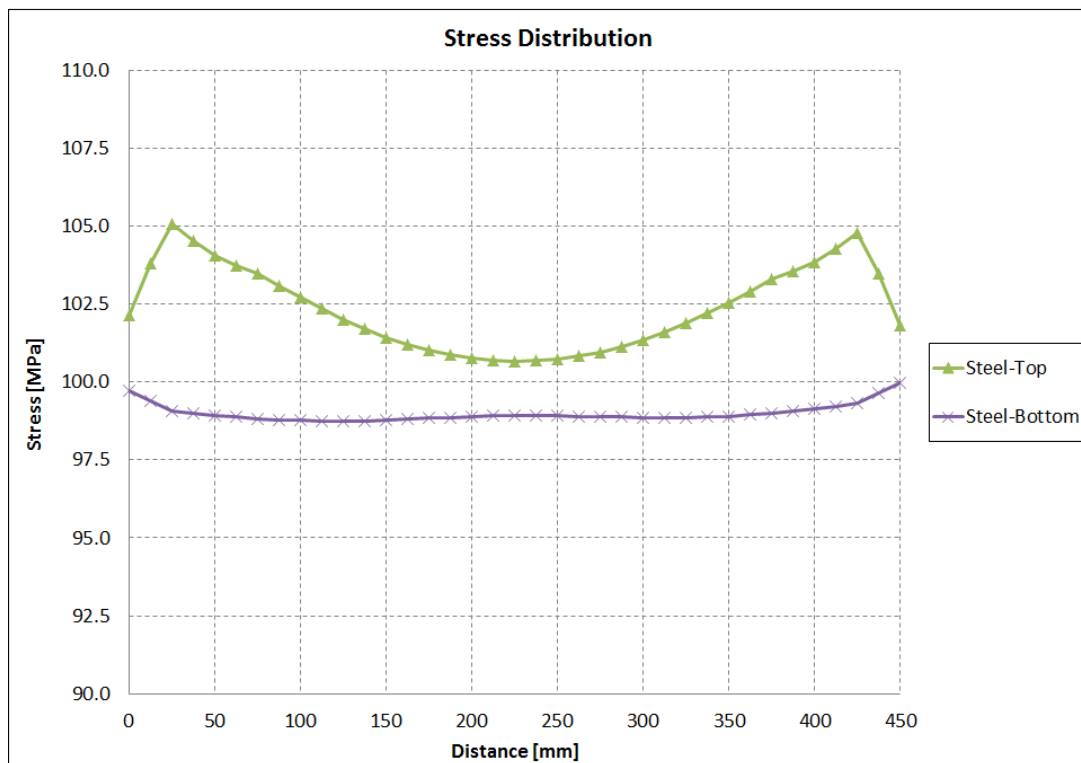


Figure 7.25: Stress distribution in the reinforced and unreinforced sides of the steel at the patch edge

The corresponding axial load and bending moment per unit width were calculated employing Equations 7.31 and 7.32 yielding $P_2=2041.4$ N/mm and $M_2=340.23$ Nmm/mm. The signs follow the notation of Figure 7.7. Having defined all the required parameters, the energy release rate was calculated and found equal to $\Gamma = 0.0157$ N/mm, while the reduced formulation of the mode mixity yielded $\psi = 35.24^\circ$. Considering the same fracture toughness as the one mentioned in the parametric study, the corresponding critical energy release rate is $\Gamma_c = 0.195$ N/mm. The calculated energy release rate is significantly lower than the fracture toughness, ensuring that there is no risk of debonding due to the acting loads.

7.7 Conclusions

In this chapter a comparison between the CSDE and the enhanced VCCT method and an analytical solution for steel to composite bimetals has been presented. Subsequently, an analytical approach for the calculation of the energy release rate and the mode mixity on orthotropic bimetals subjected to axial and bending loads was presented with special considerations on the case of composite patch repairs.

Through selected cases representing different material and geometrical combinations, it was demonstrated that the angular parameter values ω proposed by Suo and Hutchinson for isotropic bimetals can be used for the calculation of the full formulation of the mode mixity on orthotropic bimetals. For material combinations outside the range of the ones considered by Suo and Hutchinson, an extraction method based on the CSDE method was implemented. Additionally, it was verified that the extracted ω values were practically independent of the applied loading.

In the following, three different bimaterial systems were selected with the metallic substrate being steel in all cases and with a constant thickness of 5mm. Furthermore, a parametric study was conducted for various thickness ratios for two different loadings employing the analytical formula. Results indicated that in the case of the bending load, the energy release rate and mode mixity are identical for all material systems when expressed as a function of the bending stiffness ratio. Moreover, increasing the bending stiffness ratio beyond the value of twenty has no effect on the energy release rate and the mode mixity. The mode mixity, as expected, is mode I dominant for the selected case. Under axial loading the energy release rate increases with increasing Young's modulus. Additionally increasing the thickness ratio beyond the value of one, leads to an almost linear increase of the energy release rate. In spite of that the energy release rate, for realistic thickness ratios is significantly lower than the fracture toughness remains. The mode mixity is increased with increasing thickness ratios and the Young's modulus of the composite leading to mode II dominant phase angles.

Concatenating the aforementioned findings, a design assessment procedure for composite patch repairing is proposed. This methodology can be implemented either entirely analytically or in conjunction with simple finite element modelling enabling fast and precise evaluation of composite patch repairs. A realistic damage case was selected as a study case for the implementation of the method.

8. Conclusions and scientific novelties

The composite patch repairing method is very promising and has demonstrated its effectiveness in the aerospace industry where it is a standard practice. However, there is a lack in the literature regarding such applications in marine and offshore structures which has inhibited the adaptation and acceptance of this method in naval structures.

The motivation of the current PhD thesis has been to investigate critical aspects associated with the performance, inspection and evaluation of such repairs in marine structures. For this purpose a multidisciplinary approach has been adopted combining experimental, numerical and analytical aspects. In detail, a series of static and fatigue tests were conducted focusing on the rehabilitation of commonly defected parts (i.e. cracked and corroded). Additionally emphasis has been given to different surface preparation procedures and aging scenarios, in an effort to represent realistic operational conditions. Different non-destructive evaluation and structural health monitoring techniques have been successfully implemented during testing which provided valuable information on the initiation and evolution of damage. The experimental results were interpreted and reproduced successfully with the use of advanced finite element modelling techniques, which take into account debonding, providing insight in the failure mechanisms that govern the integrity of such repairs.

Finally, having demonstrated the effectiveness of composite patch repairing, emphasis has been given in developing methodologies for the assessment of the damage and the repair itself. This has been achieved with the use of advanced numerical modelling and analytical formulas befalling in the fields of damage mechanics and fracture mechanics. Critical issues related to the design and evaluation of such repairs in an accurate, practical and efficient way were investigated aiming at bringing this repair method one step closer to its implementation.

The general conclusions and novelties of the present work are as follows:

1. Extension of the analytical work of Suo and Hutchinson (1990) for the analysis of interface cracks to include orthotropic bimetals, thus enabling its application on steel-composite patch interfaces. Association of the phase angle parameter ω to orthotropic bimetals, originally postulated for the calculation of the mode mixity of isotropic bimetals. Calculation of additional values for bimaterial systems not included in the original table, and extraction of similar quantities to account for the reduced formulation of the mode mixity.
2. Development of a novel assessment methodology for different designs of these repairs, addressing the integrity of the bimaterial interface and the surrounding steel structure.
3. Performance of a parametric study using an analytical approach investigating three representative bimaterial systems under a wide range of thickness ratios subjected to axial loading and pure bending. Proof that bending constitutes a more detrimental loading condition for the integrity of the repair, and identification of the effect of the thickness ratio and material properties for the selected loading cases.

4. Comparison of the CSDE method to the enhanced VCCT and to analytical formulas for an orthotropic bimaterial interface comprising of composite and metal which has not been performed before, to the best of the author's knowledge.
5. Development of a methodology for the assessment of the criticality of cracked elements on tanker vessels, based on the implementation of the Common Structural Rules.
6. Comparison of the effect of two different surface preparation methods on the fatigue life of cracked steel plates indicating that the correct surface preparation of the metallic substrate is vital for the efficiency of the repair.
7. Provision of additional proof of the effectiveness of the composite patch method for the repair of marine structures' representative defects, i.e. corrosion and cracks. Addressing the existing gap in the literature and contributing to the field, by testing under laboratory conditions and implementing the method in real applications. Emphasis has been given in aspects associated with the durability of the repair and non-destructive inspection and health monitoring techniques.
8. It was shown that Cohesive Zone Modelling is able to represent the experimentally observed types of damage and provides significant insight on the mechanisms governing its evolution. The numerical results are in good agreement with the ones obtained from the experiments. However, this method is prone to convergence difficulties resulting in partial solutions.

9. Suggestions for Future Work

This PhD Thesis focused on several critical aspects associated with the efficiency and the design procedure of composite patches as a rectification method of defected steel structures. Nevertheless, there are still several issues associated with this type of repairs which consist interesting areas for further study. Some of these are:

1. Formulation of an analytical or numerical method to account for the effect of fatigue loads at the bondline between the composite and the metallic substrate
2. Investigation of the effect of alternating loading during curing of the patch at the fracture toughness of the bondline
3. Investigation of the degradation mechanisms due to the exposure of the bondline to environmental conditions
4. The conduction of experiments to measure the critical energy release rate of composite to steel biomaterials under a wide range of mode mixities and material combinations under both static and fatigue loading
5. The effect of thermal stresses at the fracture energy of the bondline during the curing of the laminate

References

- ABAQUS 2010. Theory Manual, Version 6.10, Dassault Systèmes Simulia Corp. Providence: RI, USA BS 7910:2005. Guide to methods for assessing the acceptability of flaws in metallic structures
- Achour, T., Bouiadjra B.B., and Serier B., Numerical analysis of the performances of the bonded composite patch for reducing stress concentration and repairing cracks at notch. *Computational Materials Science*, 2003. 28(1): p. 41-48.
- Alfano, G. and M.A. Crisfield, Finite element interface models for the delamination analysis of laminated composites: Mechanical and computational issues. *International Journal for Numerical Methods in Engineering*, 2001. 50(7): p. 1701-1736.
- Alfano, G., On the influence of the shape of the interface law on the application of cohesive-zone models,(2006) *Composites Science and Technology* vol. 66 (6) p. 723-730
- Allix, O., Corigliano, A., 1996. Modelling and simulation of crack propagation in mixed-modes interlaminar fracture specimens. *International Journal of Fracture* 77: 111-140.
- Anderson, T.L. *Fracture Mechanics: Fundamentals and Applications*, Third Edition. CRC Press, 2005
- Andresen, H.W. and A.T. Echtermeyer, Critical energy release rate for a CSM reinforced carbon fibre composite/steel bonding. *Composites Part A: applied science and manufacturing*, 2006. 37(5): p. 742-751.
- Anyfantis K. *Analysis and Design of Composite-to-Metal Adhesively Bonded Joints*, National Technical University of Athens, 2012, PhD Thesis.
- Avdelidis, N.P., Ibarra-Castanedo C., Maldague X., Marioli-Riga Z.P. and Almond D.P., A thermographic comparison study for the assessment of composite patches. *Infrared Physics and Technology*, 2004. 45(4): p. 291-299.
- Avgoulas E., Karatzas V., Zilakos E., and Tsouvalis N., "Numerical analysis of cracked marine structures repaired with composite patches", *4th International Conference on Marine Structures, MARSTRUCT 2013*, Espoo, Finland, March 2013
- Baker A, McKenzie I ,Jones R. Development of life extension strategies for Australian military aircraft, using structural health monitoring of composite repairs and joints. *Composite Structures* 2004;66:133–143.
- Baker A, Rose L, Jones R, Editors, "Advances in the Bonded Composite Repair of Aircraft Structure", Elsevier 2002
- Baker A, Structural health monitoring of a bonded composite patch repair on a fatigue cracked F-111C wing, 2008
- Baker A., Jones R, *Bonded repair of aircraft structures* , Martinus Nijhoff, 1988
- Baker, A., Bonded composite repair of fatigue-cracked primary aircraft structure. *Composite Structures*, 1999. 47(1-4): p. 431-443.

- Baker, A., N. Rajic, and C. Davis, Towards a practical structural health monitoring technology for patched cracks in aircraft structure. *Composites Part A: applied science and manufacturing*, 2009. 40(9): p. 1340-1352.
- Baker, A.A.; Chester, R.J.; Davis, M.J.; Roberts, J.D.; Retchford, J.A., Reinforcement of the F-111 wing pivot fitting with a boron/epoxy doubler system—materials engineering aspects (1993) *Composites* vol. 24 (6) p. 511-521
- Baker, A.A.; Callinan, R.J.; Davis, M.J.; Jones, R.; Williams, J.G. (1984), Repair of mirage III aircraft using the BFRP crack-patching technique, *Theoretical and Applied Fracture Mechanics* vol. 2 (1) p. 1-15
- Banks-Sills, L., Bortman, Y., 1986. A mixed-mode fracture specimen: analysis and testing. *Int. J. Fract.* 30 (3), 181–201
- Belhouari, M., et al., Comparison of double and single bonded repairs to symmetric composite structures: A numerical analysis. *Composite Structures*, 2004. 65(1): p. 47-53.
- Benzeggagh, M.L., Kenane, M., 1996. Measurement of mixed-mode delamination fracture toughness of unidirectional glass/epoxy composites with mixed- mode bending apparatus. *Compos. Sci. Technol.* 56 (4), 439–449
- Berggreen. C., *Damage Tolerance of Debonded Sandwich Structures*. PhD thesis, Technical University of Denmark, 2004.
- Bloor, M., Datta, R., Gilinskiy, Y. and Horlick-Jones, T. 2006. Unicorn among the cedars: On the possibility of effective 'smart regulation' of the globalized shipping industry. *Social and Legal Studies* 15:534-551.
- Bortolotti P., Berggreen C., Anyfantis K., Pure Moment Approach to Determine Mixed-Mode Fracture Toughness of Sandwich Face/Core Interfaces. In 19th International Conference on Composite Materials, 2013.
- Bouiadjra, B.B., Ouinas D., Serier B. and Benderdouche N., Disbond effects on bonded boron/epoxy composite repair to aluminium plates. *Computational Materials Science*, 2008. 42(2): p. 220-227.
- Bouiadjra, B.B., Belhouari M., and Serier B., Computation of the stress intensity factors for repaired cracks with bonded composite patch in mode I and mixed mode. *Composite Structures*, 2002. 56(4): p. 401-406.
- BS 7910:2005, Guide to methods for assessing the acceptability of flaws in metallic structures
- Campilho, R.D.S.G., de Moura, M.F.S.F. and Domingues, J.J.M.S., Stress and failure analyses of scarf repaired CFRP laminates using a cohesive damage model. *Journal of Adhesion Science and Technology*, 2007, 21: 855- 970.
- Campilho, R.R.D.S.G., M.M.F.S.F. de Moura, and J.J.M.S. Domingues, Modelling single and double-lap repairs on composite materials. *Composites Science and Technology*, 2005. 65(13): p. 1948-1958.
- Carlsson, L., Berggreen C., Kardomateas, G., Pure Moment Approach to determine Mixed-Mode Fracture Toughness of Sandwich Face/Core Interfaces. In 19th International Conference on Composite Materials, 2013.

- Chai, H., 1988. Shear fracture. *International Journal of Fracture* 37, 137–159.
- Chai, H., 1995. Deformation and fracture of particulate epoxy in adhesive bonds. *Acta Metallurgica Materialia* 43, 163–172.
- Chandra, N., Li, H., Shet, C., Ghonem, R., Some issues in the application of cohesive zone models for metal-ceramic interfaces. *International Journal of Solids and Structures*, 2002. 39:2827-2855.
- Chen, J., Predicting progressive delamination of stiffened fibre-composite panel and by decohesion models. *Journal of Thermoplastic Composite Materials*, 2002.15: 429-441.
- Chung, K.H. and W.H. Yang, A study on the fatigue crack growth behaviour of thick aluminium panels repaired with a composite patch. *Composite Structures*, 2003. 60(1): p. 1-7.
- Chung, K.H. and W.H. Yang, Mixed mode fatigue crack growth in aluminium plates with composite patches. *International Journal of Fatigue*, 2003. 25(4): p. 325-333.
- Dalzel-Job, J., S. JDG, and L. F, Composite Patch Repair of Steel Ships, *Proceedings of Advanced Marine Materials: Technology and Applications*. RINA Conference, London, 2003.
- Davis, M. J. and Bond, D. Principles and practice of adhesive bonded structural joints and repairs. *Int. J. Adhesion Adhes.*, 1999, 19(3), 91–105.
- Det Norske Veritas, Design, fabrication, operation and qualification of bonded repair of steel structures, 2012, Recommended Practice, DNV-RP-C301
- Det Norske Veritas, Thickness diminution for mobile offshore units, Class Guideline, July 2015, DNVGL-CG-0172
- Dundurs, J, Some properties of elastic stresses in a composite, A.C. Eringen (Ed.), *Recent advances in engineering science*, vol. 5, Gordon and Breach Science Publishers, New York. 1970, pp 203-216
- Echtermeyer A., Mc George D., Grave J.H.L. and Weitzenbock J. Bonded patch repairs for metallic structures – A new recommended practice, *Reinforced plastics & composites*. 2014, vol.33(6) 597-585
- Eliopoulou, E., Papanikolaou, A., Diamantis, P. and Hamann, R. 2012. Analysis of tanker casualties after the Oil Pollution Act (USA, 1990). *Proceedings of the Institution of Mechanical Engineers, Part M: Journal of Engineering for the Maritime Environment* 226:301-312.
- Eshelby, J. D., W. T. Read, and Shockley W.. Anisotropic elasticity with applications to dislocation theory, *Acta metallurgica* 1.3 (1953): 251-259.
- Gieske, J.H., D.P. Roach, and P.D. Walkington. Ultrasonic inspection technique for composite doubler/aluminium skin bond integrity for aircraft. 1998.
- Grabovac, I. and D. Whittaker, Application of bonded composites in the repair of ships structures - A 15-year service experience. *Composites Part A: applied science and manufacturing*, 2009. 40(9): p. 1381-1398.
- Grabovac, I., Bonded composite solution to ship reinforcement. *Composites Part A: applied science and manufacturing*, 2003. 34(9): p. 847-854.
- Grabovac, I., P.J. Pearce, and A. Camilleri, Are composites suitable for reinforcement of ship structures? In: *Proceedings of ICCM-12 Conference*, Paris, France; July 5-9 1999.

- Grabovac, I., R.A. Bartolomeusz, and A. Baker, Carbon fibre composite reinforcement of a ship structure - project overview. *Composites* 1993. 24(6): p. 501-509.
- Grant L.D.R., Adams R.D., DaSilva L.F.M., Experimental and numerical analysis of single lap joints for the automotive industry, *International Journal of Adhesion & Adhesives*, 29, 2009, 405-413.
- Griffith, A.A., "The Phenomena of Rupture and Flow in Solids." *Philosophical Transactions, Series A*, Vol. 221, 1920, pp. 163–198.
- Hamann, R., Eliopoulou, E. and Konovessis, D. Standard risk models for collision and grounding events of passenger vessels. Document Deliverable 5.1, GOAL Damage Stability, DG Research- FP7 2nd call. 2011
- Hollaway L.C., Applications of advanced fibre-reinforced polymer (FRP) composites in bridge engineering: rehabilitation of metallic bridge structures, all-FRP composite bridges, and bridges built with hybrid systems. (2013) *Advanced Fibre-Reinforced Polymer (FRP) Composites for Structural Applications* p. 631-661
- Hosseini-Toudeshky, H. and B. Mohammadi, A simple method to calculate the crack growth life of adhesively repaired aluminium panels. *Composite Structures*, 2007. 79(2): p. 234-241.
- Hosseini-Toudeshky, H. and B. Mohammadi, Mixed-mode numerical and experimental fatigue crack growth analyses of thick aluminium panels repaired with composite patches. *Composite Structures*, 2009. 91(1): p. 1-8.
- Hosseini-Toudeshky, H., B. Mohammadi, and H.R. Daghyani, Mixed-mode fracture analysis of aluminium repaired panels using composite patches. *Composites Science and Technology*, 2006. 66(2): p. 188-198.
- Hughes O F, Paik J K, Ship structural design and analysis, (2010). The Society of Naval Architects and Marine Engineers.
- Hutchinson and Allen. *ADVANCES IN APPLIED MECHANICS*, Volume 29. Academic Press, 1992.
- Hutchinson J. W., Mear M. E, and Rice J. R.. Crack Paralleling an Interface Between Dissimilar Materials. *Journal of Applied Mechanics*, 54(4):828, December 1987. ISSN 00218936.
- Hutchinson J. W., Mear M. E, and Rice J. R. Crack Paralleling an Interface Between Dissimilar Materials. *Journal of Applied Mechanics*, 54(4):828, December 1987
- Hutchinson, J.W., Suo Z., Mixed Mode Cracking in Layered Materials. 1991, p. 63-191.
- IACS. 2010. International Association of Classification Societies. Common Structural Rules for Double Hull Tankers
- IACS. 2010. International Association of Classification Societies. General cargo ship safety FSA study - step 2 (Risk Analysis). Document MSC 87/INF.4. Maritime Safety Committee, International Maritime Organization, London, UK, 2010.
- Ikegami, K., Takeshita T., Matsuo, K., Sugibayashi, T. Strength of adhesively bonded scarf joints between glass fibre-reinforced plastics and metals. *International Journal of Adhesion and Adhesives*. 1990, 10, 385-400

- Irwin, G.R., "Fracture Dynamics." *Fracturing of Metals*, American Society for Metals, Cleveland, OH, 1948, pp. 147–166.
- ISO 24817:2015, Petroleum, petrochemical and natural gas industries – composite repairs for pipework – qualification and design, installation testing and inspection
- ISO 4287:1997, Geometrical Product Specifications (GPS) -- Surface texture: Profile method -- Terms, definitions and surface texture parameters
- Jack L. Beuth. Separation of crack extension modes in orthotropic delamination models. *International Journal of Fracture*, 77(4):305-321, 1996. ISSN 0376-9429.
- Jones, R. and Galea S., Health monitoring of composite repairs and joints using optical fibres. *Composite Structures*, 2002. 58(3): p. 397-403.
- Jones, R.; Chiu, W.K., Composite repairs to cracks in thick metallic components. *Composite Structures*. 1999, vol. 44 (1) p. 17-29
- Kafkalidis, M.S. and M.D. Thouless, The effects of geometry and material properties on the fracture of single lap-shear joints. *International Journal of Solids and Structures*, 2002. 39(17): p. 4367-4383.
- Kardomateas G., Berggreen C., and Carlsson L. Energy-Release Rate and Mode Mixity of Face/Core Debonds in Sandwich Beams. *AIAA Journal*, 51(4):885-892, April 2013. ISSN 0001-1452.
- Katnam, K.B., Da Silva, L.F.M. and Young, T.M, Bonded repair of composite aircraft structures: A review of scientific challenges and opportunities. 2013, *Progress in Aerospace Sciences* vol. 61 p. 26-42
- Kawashita LF, Kinloch AJ, Moore DR, Williams JG, The influence of bond line thickness and peel arm thickness on adhesive fracture toughness of rubber toughened epoxy-aluminium alloy laminates, *International Journal of Adhesion & Adhesives*, 28, 2008, 199-210.
- Knudsen, O. F. and Hassler, B. IMO legislation and its implementation: Accident risk, vessel deficiencies and national administrative practices. *Marine Policy*. 2011, 35:201-207.
- Koventarou E., Kotsidis E., Karatzas V., and Tsouvalis N., A Parametric Numerical Study of Corroded Steel Plates Repaired with Composite Patches, *Shipbuilding Technology Laboratory (N.T.U.A.)*, Report No. STL 336-F-13, 2013
- Kotsidis, E., Use of Fibre Optics Sensors for Measuring Strains in Composite Materials and adhesive Joints, Diploma Thesis, National technical University of Athens, School of Naval Architecture and Marine Engineering, 2012 (in Greek).
- Kubair, D. and Geubelle, P. Comparative analysis of extrinsic and intrinsic cohesive models of dynamic fracture *International Journal of Solids and Structures*. 2003, 40, 3853.
- Lam, A.C.C., et al., Study of stress intensity factor of a cracked steel plate with a single-side CFRP composite patching. *Journal of Composites for Construction*, 2010. 14(6): p. 791-803.
- Larsen, A.T. and Wilson, E.D. 2010. "Definition of Application Cases (Marine)", Co-Patch Project Report, Composite Patch Repair for Marine and Civil Engineering Infrastructure Applications.
- Lee M.J., Cho T.M., Kim W.S., Lee B.C. and Lee J.J., Determination of cohesive parameters for a mixed mode cohesive zone model. *International Journal of Adhesion & Adhesives*. 2010, 30:322-328.

- Lee, D.B., Ikeda, T., Miyazaki, N., Choi, N.S., 2004. Effect of bond thickness on the fracture toughness of adhesive joints. *Journal of Engineering Materials and Technology* 126, 14–18.
- Lee, W.Y. and J.J. Lee, Successive 3D FE analysis technique for characterization of fatigue crack growth behaviour in composite-repaired aluminium plate. *Composite Structures*, 2004. 66(1-4): p. 513-520.
- Lekhnitskii, S. G. *Of an anisotropic elastic body*. Vol. 525. San Francisco: Holden-Day, 1963.
- Liu, H., R. Al-Mahaidi, and X.L. Zhao, Experimental study of fatigue crack growth behaviour in adhesively reinforced steel structures. *Composite Structures*, 2009. 90(1): p. 12-20.
- Liu, X. and G. Wang, Progressive failure analysis of bonded composite repairs. *Composite Structures*, 2007. 81(3): p. 331-340.
- Mall S, Ramamurthy G, Effect of bond thickness on fracture and fatigue strength of adhesively bonded composite joints, *Int J. Adhesion & Adhesives*, 9, 1, 1989, 33-37.
- Mall, S. and D.S. Conley, Modelling and validation of composite patch repair to cracked thick and thin metallic panels. *Composites Part A: applied science and manufacturing*, 2009. 40(9): p. 1331-1339.
- McGeorge, D., et al., Repair of floating offshore units using bonded fibre composite materials. *Composites Part A: applied science and manufacturing*, 2009. 40(9): p. 1364-1380.
- McGeorge, D., Inelastic fracture of adhesively bonded overlap joints. *Engineering Fracture Mechanics*, 2010. 77(1): p. 1-21.
- McKenzie, I., et al., Optical fibre sensors for health monitoring of bonded repair systems. *Composite Structures*, 2000. 50(4): p. 405-416.
- Megueni, A. and A. Lousdad, Comparison of symmetrical double sided and stepped patches for repairing cracked metallic structures. *Composite Structures*, 2008. 85(1): p. 91-94.
- Megueni, A., B. Bachir Bouiadjra, and B. Boutabout, Computation of the stress intensity factor for patched crack with bonded composite repair in pure mode II. *Composite Structures*, 2003. 59(3): p. 415-418.
- Megueni, A., The effect of a bonded hygrothermal aged composite patch on the stress intensity factor for repairing cracked metallic structures. *Composite Structures*, 2003. 62(2): p. 171-176.
- Mirisiotis LS, Tsouvalis NG. Experimental investigation of a composite patch reinforced cracked steel plate in static loading. In: *FAST 2007: proceedings of the 9th international conference on fast sea transportation*, Shanghai, China; September 2007.
- Molent, L., Callinan, R.J., and Jones, R., Design of an all boron/epoxy doubler reinforcement for the F-111C wing pivot fitting: Structural aspects *Composite Structures* vol. 11. 1989, (1) p. 57-83
- Needleman, A. A Continuum Model for Void Nucleation by Inclusion Debonding. *Journal of Applied Mechanics* 1987, Transactions of the ASME 54- 525.
- Papanikolaou, A., Eliopoulou, E. and Mikelis, N. 2006. Impact of Hull Design on Tanker Pollution. 9th International Marine Design Conference, Ann Arbor- Michigan.

- Papanikolaou, A., Eliopoulou, E., Alissafaki, A., Mikelis, N., Aksu, S. and Delautre, S., Casualty analysis of Aframax tankers. Proceedings of the Institution of Mechanical Engineers, Part M: Journal of Engineering for the Maritime Environment. 2007, 221:47-60.
- Papanikos, P., Tserpes K.I., Labeas G., and Pantelakis S., Progressive damage modelling of bonded composite repairs. Theoretical and Applied Fracture Mechanics, 2005. 43(2): p. 189-198.
- Papanikos, P., Tserpes K.I., and Pantelakis S.. Initiation and progression of composite patch debonding in adhesively repaired cracked metallic sheets. Composite Structures, 2007. 81(2): p. 303-311.
- Pardoën, T., Ferracin, T., Landis, C.M., Delannay, F. Constraint effects in adhesive joint fracture. Journal of the Mechanics and Physics of Solids. 2005, 53, 1951– 1983.
- Park S.W., Kim H.S., Lee D.G. Optimum design of the co-cured double lap joint composed of aluminium and carbon epoxy composite. Composite Structures, 2006. 75, pp. 289-297
- Philipiddis T.P and Theocaris P. S., The transverse Poisson's ratio in fibre reinforced laminae by means of a hybrid experimental approach, Journal of Composite Materials, 1994. Vol.28. No 3
- QinetiQ, Patching it up. Reinforced Plastics, 2004(July-August): p. 42-45.
- Reeder, J.R. and Crews Jr., J.H., Mixed-mode bending method for delamination testing. AIAA J, 1990. 28 (7), 1270–1276.
- Rice, J.R., A Path Independent Integral and the Approximate Analysis of Strain Concentration by Notches and Cracks. Journal of Applied Mechanics, Vol. 35, 1968, pp. 379–386.
- Russo A. and Zuccarello B. Influence of the Resin Layer Thickness at the Interface of Hybrid Metal-composite Co-cured Joints. Procedia Engineering, 2011. 10, pp. 3775–3786.
- Saseendran V., Fracture Mechanical Testing of Sandwich Composites A Numerical & Experimental Campaign, Technical University of Denmark 2014 , master thesis
- Seo, D.C. and J.J. Lee, Fatigue crack growth behaviour of cracked aluminium plate repaired with composite patch. Composite Structures, 2002. 57(1-4): p. 323-330.
- Shin K.C., Lim J., Lee J. The manufacturing process of co-cured single and double lap joints and evaluation of the load-bearing capacities of co-cured joints. Journal of Materials Processing Technology, 2003. 138, pp. 89-96.
- Siddaramaiah, et al., Tensile behaviour of composite patched cracked metallic structures. Journal of Applied Polymer Science, 1998. 68(13): p. 2063-2068.
- Sielski, R.A., Fracture mechanics of ship structures, Naval Engineers Journal, 1992. 104 36-45
- Stroh, A. N. Dislocations and cracks in anisotropic elasticity. Philosophical magazine 3.30 (1958): 625-646.
- Song M.G., Kweon J.H., Choi J.H., Byun J.H., Song M.H., Shin S.J. and Lee T.J. Effect of manufacturing methods on the shear strength of composite single-lap bonded joints. Composite Structures, 2010. 92, pp. 2194–2202.
- Sørensen, B.F., Jacobsen, T.K., 2009. Characterizing delamination of fibre composites by mixed mode cohesive laws. Composites Science and Technology 69, 445-456.

- Sørensen, B.F., Jørgensen, K., Jacobsen, T.K., Østergaard, R.C., 2006. DCB-specimen loaded with uneven bending moments. *International Journal of Fracture* 141:159–72.
- Sørensen, B.F., Kirkegaard, P., 2006. Determination of mixed mode cohesive laws. *Eng. Fract. Mech.* 73, 2642–2661.
- Suo Z., and Hutchinson J. W., Interface crack between two elastic layers, *International Journal of Fracture*, 1990. 43, 1-18
- Suo Z., Singularities, Interfaces and Cracks in Dissimilar Anisotropic Media. *Proceedings of the Royal Society A: Mathematical, Physical and Engineering Sciences*, 427(1873):331{358, February 1990. ISSN 1364-5021.
- Takeda, S., et al., Debonding monitoring of composite repair patches using embedded small-diameter FBG sensors. *Smart Materials and Structures*, 2007. 16(3): p. 763-770.
- Tamblin J.S., Yang C., and Harter P. Investigation of thick bond line adhesive joints, DOT/FAA/AR-01/33, June 2001.
- Tsamasphyros, G.J., et al., Selection of optical fibres paths and sensor locations for monitoring the integrity of composite patching. *Applied Composite Materials*, 2003. 10(6): p. 331-338.
- Tsouvalis, N.G. and L.S. Mirisiotis, Experimental investigation of the static behaviour of a hole drilled steel plate reinforced with a composite patch. *Strain*, 2008. 44(2): p. 133-140.
- Tsouvalis, N.G., L.S. Mirisiotis, and D.N. Dimou, Experimental and numerical study of the fatigue behaviour of composite patch reinforced cracked steel plates. *International Journal of Fatigue*, 2009. 31(10): p. 1613-1627.
- Turton, T.J., Dalzel-Job J., and Livingstone F., Oil platforms, destroyers and frigates - Case studies of QinetiQ's marine composite patch repairs. *Composites Part A: applied science and manufacturing*, 2005. 36(8): p. 1066-1072.
- Tvergaard, V. and Hutchinson J.W., The influence of plasticity on mixed mode interface toughness. *Journal of the Mechanics and Physics of Solids*, 1993. 41(6): p. 1119-1135.
- Tvergaard, V. and Hutchinson, J.W., 1992. The relation between crack growth resistance and fracture process parameters in elastic-plastic solids. *Journal of the Mechanics and Physics of Solids* 40: 1377-1397.
- Umamaheswar, T.V.R.S. and Singh R., Modelling of a patch repair to a thin cracked sheet. *Engineering Fracture Mechanics*, 1999. 62(2-3): p. 267-289.
- Wang, Q.Y. and Pidaparti R.M., Static characteristics and fatigue behaviour of composite-repaired aluminium plates. *Composite Structures*, 2002. 56(2): p. 151-155.
- Wang, S.; and Harvey, C.M. Mixed mode partition theories for one dimensional fracture *Engineering Fracture Mechanics*, 2012. vol. 79 p. 329-352
- Williams M. L., The stresses around a fault or crack in dissimilar media. *Bulletin of the Seismological Society of America*, 49(2):199{204, April 1959.

- Xiong, J.J. and Shenoi R.A., Integrated experimental screening of bonded composites patch repair schemes to notched aluminium-alloy panels based on static and fatigue strength concepts. *Composite Structures*, 2008. 83(3): p. 266-272.
- Yang, C., Huang, H., Tomblin, J.S. and Sun, W., 2004. Elastic–plastic model of adhesive-bonded single-lap composite joints. *Journal of Composite Materials* 38, 293–309.
- Yang, Q.D. and M.D. Thouless, Mixed-mode fracture analyses of plastically-deforming adhesive joints. *International Journal of Fracture*, 2001. 110(2): p. 175-187.
- Yang, Q.D., M.D. Thouless, and S.M. Ward, Numerical simulations of adhesively-bonded beams failing with extensive plastic deformation. *Journal of the Mechanics and Physics of Solids*, 1999. 47(6): p. 1337-1353.
- Yang, Q.D., Thouless, M.D., Ward, S.M., 1999. Numerical simulations of adhesively-bonded beams failing with extensive plastic deformation. *Journal of the Mechanics and Physics of Solids* 47: 1337-1353.
- Yang, Q.D., Thouless, M.D., Ward, S.M., 2000. Analysis of the symmetrical 90° peel test with extensive plastic deformation. *Journal of Adhesion* 72: 115- 132.
- Yang, Q.D., Thouless, M.D., Ward, S.W. 2001. Elastic-plastic mode-II fracture of adhesive joints. *International Journal of Solids and Structures* 38: 3251-62.
- Zhao, X.L. and L. Zhang, State-of-the-art review on FRP strengthened steel structures. *Engineering Structures*, 2007. 29(8): p. 1808-1823.
- Zilakos I.K., Karatzas V.A., Chatzidouros E.V. and Papazoglou V.J.. Simulation of External Application of SuSy devices on an Aframax Tanker that has been Structurally Compromised, 2011 RINA, Royal Institution of Naval Architects - International Conference on Design and Operation of Tankers, Proceedings , pp. 121-130.

List of PhD Publications

Journal papers relevant to the PhD work

1. Karatzas V., Kotsidis E. and Tsouvalis N., “Experimental Fatigue Study of Composite Patch Repaired steel plates with Cracks”, *Applied Composite Materials*, 22(5), pp 507-523, 2015 (online 2014) (<http://dx.doi.org/10.1007/s10443-014-9420-5>).

Contribution: The PhD candidate was involved in all the aspects of the paper i.e. in the design and performance of experiments, the post-processing of results and the non destructive testing evaluation. The candidate was the corresponding author.

2. Tsouvalis, N.G., Karatzas, V.A., “An Investigation of the Tensile Strength of a Composite-to-Metal Adhesive Joint”, *Applied Composite Materials*, 18(2), pp 149-163, 2011 (<http://dx.doi.org/10.1007/s10443-010-9137-z>).

Contribution: The PhD candidate was involved in the specimens manufacturing procedure, the design and conduction of experiments, the expansion of the already existing finite element model and the post processing of the results.

Fully reviewed conference papers

1. Karatzas V., Kotsidis E. and Tsouvalis N., “An Experimental and Numerical Study of Corroded Steel Plates Repaired with Composite Patches”, *4th International Conference on Marine Structures, MARSTRUCT 2013*, Espoo, Finland, March 2013.

Contribution: The PhD candidate was involved in the design and conduction of the experiments, the generation of the finite element models, the post processing and evaluation of the results. The paper has been written and presented by the PhD candidate.

2. Zilakos I., Karatzas V., Chatzidouros E., Papazoglou V. and Tsouvalis N., “A FE based numerical tool for crack assessment in ship structures employing the CSR loading scheme”, *4th International Conference on Marine Structures, MARSTRUCT 2013*, Espoo, Finland, March 2013.

Contribution: The PhD candidate was involved in the concept of the idea, the generation of the three compartment model, the implementation of the common structural rules in FORTRAN, and the interpretation of the results. The PhD candidate contributed to the writing of the paper.

3. Avgoulas E., Karatzas V., Zilakos E., and Tsouvalis N., “Numerical analysis of cracked marine structures repaired with composite patches”, *4th International Conference on Marine Structures, MARSTRUCT 2013*, Espoo, Finland, March 2013.

Contribution: This publication is based on the diploma thesis of E. Avgoulas. The PhD candidate was responsible for the supervision and guidance of the student through his project. Moreover the work performed here was largely based on the already generated three compartment model. Additionally the PhD candidate participated in the crack and patch geometry definition and the evaluation of the results. Part of the paper was written by the PhD candidate.

Conference papers with Abstract review

1. Zilakos I., Karatzas V., Chatzidouros E., Papazoglou V., “Simulation of external application of SuSy devices on an Aframax tanker that has been structurally compromised”, RINA, Royal Institution of Naval Architects, International Conference on Design and Operation of Tankers, Proceedings, pp121-130, Athens, Greece, June 2011.

Contribution: The work performed here was largely based on the generated three compartment model. Additionally the PhD candidate participated in the evaluation of the results.

2. Karatzas V., Zhang Y., Tsouvalis N., and Chryssanthopoulos M., “A parametric Investigation of the response of directly laminated composite-to-metal single lap Joints”, *15th European Conference on Composite Materials, ECCM15*, Venice, Italy, June 2012.

Contribution: This publication deals with the performance of static tensile tests on single lap joints with different overlap lengths and materials. The PhD candidate was responsible for the conduction of the experiments for two different material configurations, the post processing and evaluation of the results and the overall comparison between all the different test series. The candidate was responsible for writing and presenting the paper.

3. Frydas J. Karatzas V., Kotsidis E. and Tsouvalis N., “A parametric numerical study of the fatigue behaviour of cracked steel plates repaired with composite patches”, *17th International Conference on Composite Structures ICCS-17*, Porto, Portugal, June 2013.

Contribution: This publication is based on the diploma thesis of J. Frydas. The PhD candidate was responsible for the supervision and guidance of the student through his project. The PhD candidate contributed at the evaluation of the results and some aspects of the finite element modelling. The paper was written and presented by the PhD candidate.

4. Skampis E., Karatzas V., and Tsouvalis N., "Effect of delamination on the bending response of composite materials", *16th International conference on Experimental Mechanics, ICEM-16*, Cambridge, UK, July 2014.

Contribution: This publication is based on the diploma thesis of E. Skampis. The PhD candidate was responsible for the supervision and guidance of the student through his project. The PhD candidate contributed at the creation of the finite element model which was used to validate the experimental results and the evaluation of the results.

Technical Reports

1. V. Karatzas, "Composite Patch Repair for marine engineering infrastructure applications: Literature Survey, Shipbuilding Technology Laboratory (N.T.U.A.), Report No STL-315-F-11, January 2011.
2. V. Karatzas, N. Tsouvalis, "Composite Materials Characterization Tests", Program entitled: "Composite Patch Repair for Marine and Civil Engineering Infrastructure Applications (Co-Patch)", 2010-2012, funded by the European Commission (FP7), Shipbuilding Technology Laboratory (N.T.U.A.), Report No. STL 337-F-13, February 2011.
3. V. Karatzas, N. Tsouvalis, "Bond Strength Tests", Program entitled: "Composite Patch Repair for Marine and Civil Engineering Infrastructure Applications (Co-Patch)", 2010-2012, funded by the European Commission (FP7), Shipbuilding Technology Laboratory (N.T.U.A.), Report No. STL 341-F-13, May 2012.
4. S. Paboeuf, V. Karatzas, N. Tsouvalis, M. Codda, G. Risso, J. Harald Grave, D. Polic, "Report on the comparison of the numerical and experimental results for the bond strength tests", Program entitled: "Composite Patch Repair for Marine and Civil Engineering Infrastructure Applications (Co-Patch)", 2010-2012, funded by the European Commission (FP7), Shipbuilding Technology Laboratory (N.T.U.A.), Report No. STL 342-F-13, June 2012.
5. N. Tsouvalis, V. Karatzas, "Bond Strength Tests: Specimens Geometry and Fabrication Guidelines", Program entitled: "Composite Patch Repair for Marine and Civil Engineering Infrastructure Applications (Co-Patch)", 2010-2012, funded by the European Commission (FP7), Shipbuilding Technology Laboratory (N.T.U.A.), Report No. STL 336-F-13, October 2010.
6. E. Koventarou, E. Kotsidis, V. Karatzas, N. Tsouvalis, "A Parametric Numerical Study of Corroded Steel Plates Repaired with Composite Patches", Program entitled: "Composite Patch Repair for Marine and Civil Engineering Infrastructure Applications (Co-Patch)", 2010-2012, funded by the European Commission (FP7), Shipbuilding Technology Laboratory (N.T.U.A.), Report No. STL 336-F-13, May 2013.
7. A. Echtermeyer, V. Karatzas, "Integrated monitoring and data transmission systems for the automated monitoring of a patched structure", Program entitled: "Composite Patch Repair for Marine

- and Civil Engineering Infrastructure Applications (Co-Patch)", 2010-2012, funded by the European Commission (FP7).
8. E. Kotsidis, V. Karatzas, N. Tsouvalis, "Failure criteria implementation on mid-scale short term specimens", Program entitled: "Composite Patch Repair for Marine and Civil Engineering Infrastructure Applications (Co-Patch)", 2010-2012, funded by the European Commission (FP7), Shipbuilding Technology Laboratory (N.T.U.A.), Report No. STL 345-F-13, July 2012.
 9. E. Kotsidis, V. Karatzas, N. Tsouvalis, "Manufacturing and short-term tests results of plate specimens", Program entitled: "Composite Patch Repair for Marine and Civil Engineering Infrastructure Applications (Co-Patch)", 2010-2012, funded by the European Commission (FP7), Shipbuilding Technology Laboratory (N.T.U.A.), Report No. STL 345-F-13, January 2013.
 10. J. Frydas, E. Kotsidis, V. Karatzas, N. Tsouvalis, "A Parametric Numerical Study of the Fatigue Behaviour of Cracked Steel Plates Repaired with Composite Patches", Program entitled: "Composite Patch Repair for Marine and Civil Engineering Infrastructure Applications (Co-Patch)", 2010-2012, funded by the European Commission (FP7), Shipbuilding Technology Laboratory (N.T.U.A.), Report No. STL 347-F-13, March 2013.

Appendix A

Introduction

A large series of laboratory tests were performed at AIMEN, NTNU and NTUA from September 2010 to January 2011 for the characterization of the material properties of different composite material systems. Five different composite materials configurations were examined, depending on the material selection and the fabrication method. In particular, the composite systems tested were the following:

- carbon/epoxy using the hand-lay-up method, denoted as HLU C/E,
- carbon/vinylester using the hand-lay-up method, denoted as HLU C/V,
- carbon/epoxy using the vacuum infusion method, denoted as VI C/E,
- carbon/vinylester using the vacuum infusion method, denoted as VI C/V and
- carbon/epoxy pre-preg, denoted as PP C/E

Carbon fibres were selected, instead of glass, as they result to thin, high moduli composites. This means that a high stiffness ratio can be attained when they are used as reinforcing patches. Concerning the selection of resin, vinylester and epoxy resins are predominant for the fabrication of high-performance structural composite systems in both the civil and marine structures. It is well known that the achieved material properties of composites greatly rely on the manufacturing procedure. Each manufacturing procedure has different attributes concerning the quality of the composite system, the overall cost for its production, the level of specialization needed and the conditions required for their correct application. Therefore three different configurations were examined, namely hand-lay-up, vacuum infusion and pre-preg which consist well-known and mature methods for the fabrication of composites. The specimens provided for testing were manufactured by AS2CON, ENP, NTNU and UM.

Test standards applied

The following four standards, commonly used for fibre-reinforced materials, have been applied for the materials characterization testing:

- ASTM D3039M standard ¹
 - Tension at 0° for measuring:
 - Tensile modulus in the fibre direction E_{1t}
 - Poisson's ratio ν_{12}
 - Maximum tensile stress in the fibre direction X_{1t}

¹ American Society for Testing and Materials (ASTM) - *Standard test method for tensile properties of polymer matrix composite materials* - D 3039/D 3039M.

- Tension at 90° for measuring:
 - Tensile modulus in the transverse direction E2t
 - Poisson's ratio ν_{21}
 - Maximum tensile stress in the transverse direction X2t
- ISO 14126 standard 2
 - Compression at 0° for measuring:
 - Compressive modulus in the fibre direction E1c
 - Maximum compressive stress in the fibre direction X1c
 - Compression at 90° for measuring:
 - Compressive modulus in the transverse direction E2c
 - Maximum compressive stress in the transverse direction X2c
- ASTM D3518 standard 3
 - Tensile test of a $\pm 45^\circ$ laminate for measuring:
 - Shear modulus G12
 - Maximum shear stress S
- ASTM D3171 standard 4
 - Test methods for measuring:
 - Fibre weight fraction

The fibre weight fraction of the specimens was measured according to the formula cited in ASTM D3171. This was decided after testing two specimens in nitric acid solution. The results showed that the nitric acid solution failed to completely dissolve the resin.

Nomenclature

The following names have been assigned to the material systems reflecting the composite configuration and the method used for their manufacture, that is:

- **HLU-C/E** for the carbon/epoxy composite produced with the hand-lay-up method
- **HLU-C/V** for the carbon/vinylester composite produced with the hand-lay-up method
- **VI-C/E** for the carbon/epoxy composite produced using the vacuum infusion method
- **VI-C/V** for the carbon/vinylester composite produced using the vacuum infusion method

² International Standards Organisation (ISO) - *Fibre-reinforced plastic composites - Determination of compressive properties in the in-plane direction* - ISO 14126:1999(E).

³ American Society for Testing and Materials (ASTM) - *Standard Test Method for In-Plane Shear Response of Polymer Matrix Composite Materials by Tensile Test of a $\pm 45^\circ$ Laminate* - D 3518/D 3518M.

⁴ American Society for Testing and Materials (ASTM) - *Standard Test Methods for Constituent Content of Composite Materials*- D 3171

- **PP-C/E** for the Pre – Preg

Hand lay-up carbon/epoxy

The Hand-Lay-Up Carbon/Epoxy specimens were fabricated by ENP using CST 200 carbon fibres with area density equal to 200 g/m² provided by SGL GROUP. The matrix system consists of LH 160 133 epoxy resin and H 138 hardener, provided by HAVEL.

Hand lay-up carbon/vinylester

The Hand-Lay-Up Carbon/Vinylester specimens were fabricated by ENP using *L(X) 440-C10 [0]₂* carbon fabric. The two layers are stitched together and the individual weight density of each layer is 208 g/m². The carbon fabric is provided by AMT DEVOLD. The resin selected was *DION 9500-M800* vinylester resin provided by REICHHOLD.

Vacuum infusion carbon/epoxy

The Vacuum Infusion Carbon/Epoxy specimens were fabricated by AS2CON using CST 200 carbon fibres with area density equal to 200 g/m² provided by SGL GROUP. The matrix system consists of LH 160 133 epoxy resin and H 138 hardener, provided by HAVEL. Four and eight layers of *CST 200* were used for the fabrication of the tensile specimens in the 0° and 90° direction accordingly. For the compression tests, eight layers of the same material were used for the manufacturing of the VI-C/E-C-0 specimens while for the VI-C/E-C-90 specimens sixteen layers were used. For the shear specimens twenty layers were used. After the plies configuration of each laminate was set up, they were infused with resin.

Before the production of the laminates, all materials were heated to ambient temperature. The environmental conditions recorded during the manufacturing of the laminates were 20°C. The vacuum pressure was equal to -0.75 bar. No post-curing of the laminates was considered necessary. The tabs were fabricated using 5 layers of E-glass woven roving, with twill weave oriented in ±45°. The epoxy resin system used was the same (LH 160 133 epoxy resin). The adhesive system used for bonding the tabs to the laminate was once again the same epoxy with microspheres added to ensure a stronger bond. The specimens were cut using water-jet cutting.



Figure A.1: Vacuum infusion of laminate (provided by AS2CON).

Vacuum infusion carbon/vinylester

The Vacuum Infusion Carbon/Vinylester specimens were fabricated by UM using $L(X) 440-C10 [0]_2$ carbon fabric. The two layers are stitched together and the individual weight density of each layer is 208 g/m^2 . The carbon fabric is provided by AMT DEVOLD. The resin selected was *DION 9500-M800* vinylester resin provided by REICHHOLD.

Two and four layers of $L(X) 440-C10 [0]_2$ were used for the fabrication of the tensile specimens in the 0° and 90° direction accordingly. For the compression tests, four layers of the same material were used for the manufacturing of the VI-C/V-C-0 specimens while for the VI-C/V-C-90 specimens eight layers were used. For the shear specimens, ten layers of DB420 – C05 [$\pm 45^\circ$], each weighing 201 g/m^2 were used. After the plies configuration was set up, the vacuum infusion took place.



Figure A.2: Layer configuration used for each specimen type (provided by UM).



Figure A.3: Plies configuration prior to infusion (provided by UM).

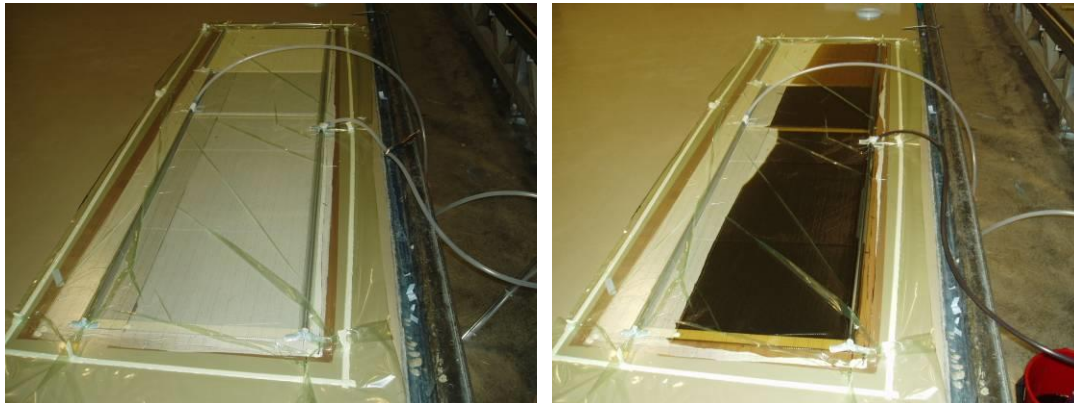


Figure A.4: Sealing and Vacuum Infusion of laminates (provided by UM).

The environmental conditions measured during the specimens' production were: 19°C temperature and 31% relative humidity. The vacuum pressure was equal to -0.7 bar during the infusion of the resin and -0.3 bar during the curing. The filling time was between 15 and 30 minutes for each type of specimen. The post-curing of the laminates was performed at 50° C for 24 hours.

The tabs were manufactured using 3 layers of chopped strand mat with area weight equal to 300 g/m² with DION 9500 – 501 vinylester resin and glued using ARALDITE 2015 to the specimen laminates according to the geometric specifications. Following the adhesion of the tabs and the post-curing of ARALDITE 2015 for 16 hours in approximately 45° C the specimens were cut using a cooled wheel saw.

Pre-Preg carbon/epoxy

The Pre-Preg Carbon/Epoxy specimens were manufactured by NTNU using *HS 40* ultra high modulus carbon fibres, *one layer weighing 300 g/m²*, carbon fibres provided by GRAFIL Inc. and SE84LV low temperature cure epoxy resin provided by SP GURIT with a 32% content of resin before curing. This Pre-Preg configuration was chosen as it allows curing and post curing in low temperature (less than 100°C).

For the manufacturing of the PP-C/E-T-0 specimens four layers were used. The number of layers for the PP-C/E-T-90 and PP-C/E-C-0 specimens was seven, while for the PP-C/E-C-90 fourteen layers were used. For the shear specimens twenty layers were used.

For the manufacturing of the laminates, the Pre-Preg was taken out of the freezer (-18°C) and was left to thaw for ten hours before it was taken out of the bag in order to prevent the Pre-Preg from condensing. Afterwards it was cut according to the specified dimensions dictated by the testing standards. A release film and a peel ply were placed on a stainless steel plate followed by the stacking of the plies. On top of the plies a sheet of peel-ply and a sheet of breather were placed and afterwards the system was sealed by the vacuum bag using sticky tape. The set-up is presented in Figure A.5.

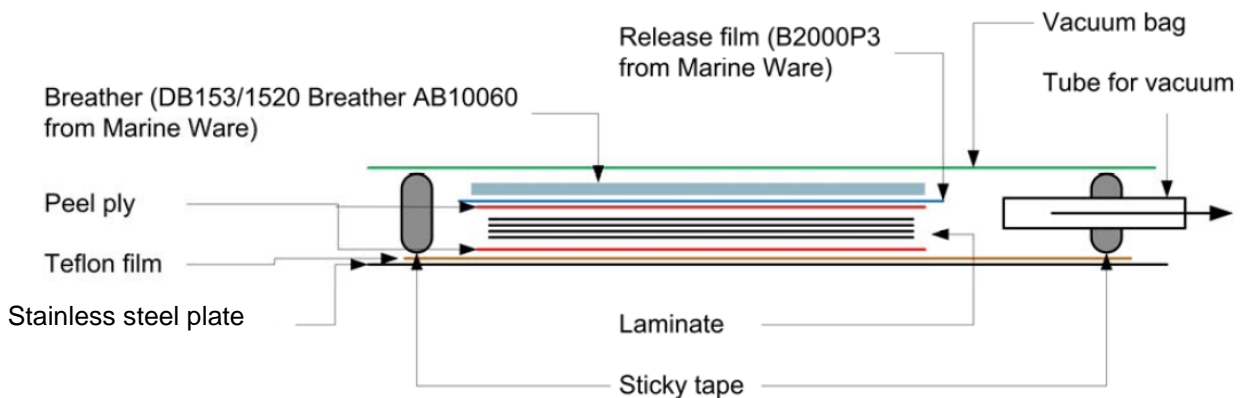


Figure A.5: Set-up of pre-preg prior to curing (provided by NTNU).

The vacuum pressure achieved was -0.95 bar and was kept constant during the whole process. The pressure was released when the temperature was down to 30°C after curing. The laminates were placed in the oven for curing. The curing process had a heat-up cycle between $0.3^{\circ}\text{C}/\text{min}$ and $2^{\circ}\text{C}/\text{min}$ starting from 20°C until 85°C temperature was reached. The laminates were cured for ten hours before the fan cooled them down to 25°C with a rate of $1^{\circ}\text{C}/\text{min}$. Post curing of the laminates was not required. The environmental temperature during the manufacture and curing of the laminates was between 22 and 23.5°C . The relative humidity varied from 36 to 41%.

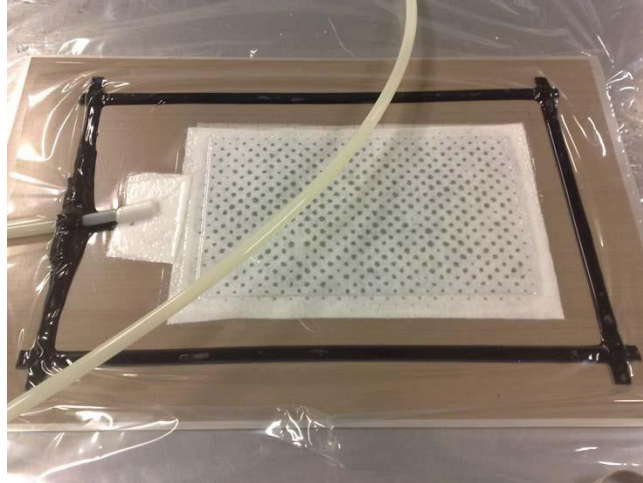


Figure A.6: PP-C/E-T-0 laminate after curing (provided by NTNU).

The material used for the tabs was $\pm 45^\circ$ double biaxial E-glass fibres with MGS RIMR135 Epikote resin provided by Hexion. The tabs were 1 mm thick and were glued to the tensile and compression specimens with the use of a SA 70 adhesive film provided by SP GURIT. No tabs were required for the shear specimens. The specimens were cut by the use of a cooled diamond saw.

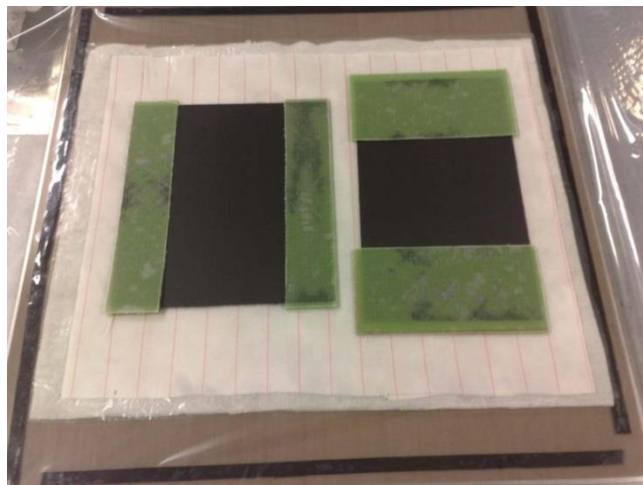


Figure A.7: PP-C/E-T-0 and PP-C/E-T-90 laminates with tabs prior to tab-adhesive curing (provided by NTNU).



Figure A.8: PP-C/E-T-0 and PP-C/E-T-90 laminates with tabs after tab-adhesive curing (provided by NTNU).

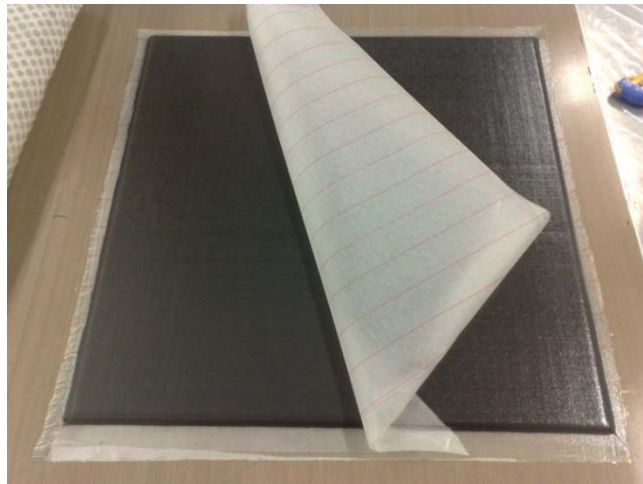


Figure A.9: PP-C/E-S laminate after curing (provided by NTNU).

Material Properties

Table A.1 lists the average values of all material properties measured for the 5 materials. Having measured these material properties the engineering constants needed for the numerical modelling are listed in Table A.2. The Poisson's ratio in the transverse direction was calculated based on the formula listed in *Philippidis et al (1993)*.

Table A.1: Experimentally measured material properties.

Properties	HLU-C/E	HLU-C/V	VI-C/E	VI-C/V	PP-C/E
E_{1T} [GPa]	38.7	74.0	112.3	102.6	228.4
E_{2T} [GPa]	6.5	5.1	5.5	7.6	6.5
X_{1T} [MPa]	660.1	999.1	972.7	1691.6	2254.1
X_{2T} [MPa]	-15.1	16.0	-14.4	15.0	20.7
ν_{12}	0.355	0.385	0.376	0.388	0.249
W_{fT}	44.2%	47.8%	52.8%	62.7%	87.6%
E_{1C} [GPa]	80.7	67.1	-	83.2	196.9
E_{2C} [GPa]	4.9	5.2	3.9	6.3	6.8
X_{1C} [MPa]	453.3	511.4	-	557.6	882.3
X_{2C} [MPa]	85.4	71.8	76.3	107.0	133.2
W_{fC}	36.2%	53.8%	48.1%	58.6%	78.9%
G_{12} [GPa]	1.7	2.5	2.0	4.5	4.5
S [MPa]	33.5	41.3	42.4	51.0	63.4
W_{fS}	30.0%	50.6%	50.4%	-	72.6%

Table A.2: Engineering Constants.

Properties	HLU-C/E	HLU-C/V	VI-C/E	VI-C/V	PP-C/E
E_1 [GPa]	38.7	74.0	112.3	102.6	228.4
E_2 [GPa]	6.5	5.1	5.5	7.6	6.5
E_3 [GPa]	6.5	5.1	5.5	7.6	6.5
ν_{12}	0.355	0.385	0.376	0.388	0.249
ν_{13}	0.355	0.385	0.376	0.388	0.249
ν_{23}	0.518	0.609	0.592	0.534	0.329
G_{12} [GPa]	1.7	2.5	2.0	4.5	4.5
G_{13} [GPa]	1.7	2.5	2.0	4.5	4.5
G_{23} [GPa]	2.1	1.6	1.7	2.3	2.4